sensors

Special Issue Reprint

Advances in the Monitoring, Diagnosis, and Optimisation of Water Systems

Edited by
Miquel À. Cugueró-Escofet and Vicenç Puig

mdpi.com/journal/sensors

MDPI

Advances in the Monitoring, Diagnosis, and Optimisation of Water Systems

Advances in the Monitoring, Diagnosis, and Optimisation of Water Systems

Editors

Miquel À. Cugueró-Escofet
Vicenç Puig

MDPI

Basel • Beijing • Wuhan • Barcelona • Belgrade • Novi Sad • Cluj • Manchester

Editors
Miquel À. Cugueró-Escofet
Polytechnic University of Catalonia
(UPC-BarcelonaTech)
Terrassa
Spain

Vicenç Puig
Institut de Robòtica i Informàtica Industrial
CSIC-UPC
Barcelona
Spain

Editorial Office
MDPI
St. Alban-Anlage 66
4052 Basel, Switzerland

This is a reprint of articles from the Special Issue published online in the open access journal *Sensors* (ISSN 1424-8220) (available at: https://www.mdpi.com/journal/sensors/special_issues/Optimisation_Water_Systems).

For citation purposes, cite each article independently as indicated on the article page online and as indicated below:

Lastname, A.A.; Lastname, B.B. Article Title. *Journal Name* **Year**, *Volume Number*, Page Range.

ISBN 978-3-0365-9594-8 (Hbk)
ISBN 978-3-0365-9595-5 (PDF)
doi.org/10.3390/books978-3-0365-9595-5

Cover image courtesy of Miquel À. Cugueró-Escofet

Contents

About the Editors . . . . . **vii**

Miquel Àngel Cugueró-Escofet and Vicenç Puig
Advances in the Monitoring, Diagnosis and Optimisation of Water Systems
Reprinted from: *Sensors* **2023**, *23*, 3256, doi:10.3390/s23063256 . . . . . **1**

Ildeberto Santos-Ruiz, Francisco-Ronay López-Estrada, Vicenç Puig, Guillermo Valencia-Palomo and Héctor-Ricardo Hernández
Pressure Sensor Placement for Leak Localization in Water Distribution Networks Using Information Theory
Reprinted from: *Sensors* **2022**, *22*, 443, doi:10.3390/s22020443 . . . . . **5**

Débora Alves, Joaquim Blesa, Eric Duviella and Lala Rajaoarisoa
Robust Data-Driven Leak Localization in Water Distribution Networks Using Pressure Measurements and Topological Information
Reprinted from: *Sensors* **2021**, *21*, 7551, doi:10.3390/s21227551 . . . . . **17**

Adrián Navarro-Díaz, Alejandro Delgado-Aguiñaga, Ofelia Begovich and Gildas Besançon
Two Simultaneous Leak Diagnosis in Pipelines Based on Input–Output Numerical Differentiation
Reprinted from: *Sensors* **2021**, *21*, 8035, doi:10.3390/s21238035 . . . . . **37**

Ramon Pérez, Albert Martínez-Torrents, Manuel Martínez, Sergi Grau, Laura Vinardell, Ricard Tomàs, et al.
Chlorine Concentration Modelling and Supervision in Water Distribution Systems
Reprinted from: *Sensors* **2022**, *22*, 5578, doi:10.3390/s22155578 . . . . . **53**

Fatiha Nejjari, Boutrous Khoury, Vicenç Puig, Joseba Quevedo, Josep Pascual and Sergi de Campos
Economic Linear Parameter Varying Model Predictive Control of the Aeration System of a Wastewater Treatment Plant
Reprinted from: *Sensors* **2022**, *22*, 6008, doi:10.3390/s22166008 . . . . . **67**

David Palma-Heredia, Marta Verdaguer, Vicenç Puig, Manuel Poch and Miquel Àngel Cugueró-Escofet
Comparison of Optimisation Algorithms for Centralised Anaerobic Co-Digestion in a Real River Basin Case Study in Catalonia
Reprinted from: *Sensors* **2022**, *22*, 1857, doi:10.3390/s22051857 . . . . . **83**

Ivan Pisa, Antoni Morell, Ramón Vilanova and Jose Lopez Vicario
Transfer Learning in Wastewater Treatment Plant Control Design: From Conventional to Long Short-Term Memory-Based Controllers
Reprinted from: *Sensors* **2021**, *21*, 6315, doi:10.3390/s21186315 . . . . . **103**

Meng Zhou, Yinyue Zhang, Jing Wang, Yuntao Shi and Vicenç Puig
Water Quality Indicator Interval Prediction in Wastewater Treatment Process Based on the Improved BES-LSSVM Algorithm
Reprinted from: *Sensors* **2022**, *22*, 422, doi:10.3390/s22020422 . . . . . **129**

Pavel P Fil, Alla Yu Yurova, Alexey Dobrokhotov and Daniil Kozlov
Estimation of Infiltration Volumes and Rates in Seasonally Water-Filled Topographic Depressions Based on Remote-Sensing Time Series
Reprinted from: *Sensors* **2021**, *21*, 7403, doi:10.3390/s21217403 . . . . . **153**

Jaime Lloret, Sandra Sendra, Laura Garcia and Jose M. Jimenez
A Wireless Sensor Network Deployment for Soil Moisture Monitoring in Precision Agriculture
Reprinted from: *Sensors* **2021**, *21*, 7243, doi:10.3390/s21217243 . . . . . **171**

Liping Yang, Joshua Driscol, Sarigai Sarigai, Qiusheng Wu, Christopher D. Lippitt and Melinda Morgan
Towards Synoptic Water Monitoring Systems: A Review of AI Methods for Automating Water Body Detection and Water Quality Monitoring Using Remote Sensing
Reprinted from: *Sensors* **2022**, *22*, 2416, doi:10.3390/s22062416 . . . . . **195**

About the Editors

Miquel À. Cugueró-Escofet

Miquel À. Cugueró-Escofet is Assistant Professor at the Automatic Control Department of the Universitat Politècnica de Catalunya (UPC-BarcelonaTech) and Researcher at the Advanced Control Systems Research Group (SAC-UPC). His research interests are on the field of systems fault diagnosis and control, with a strong focus on data analysis, including system modelling and supervision, optimisation, adaptive control, robust control, sensor placement, and sensor data validation, reconstruction, and forecasting in different applications such as water systems management or active noise control. He has co-authored over 45 publications including JCR-indexed journals, international conference papers, and book chapters, and participated in over 30 EU and national R&D projects in collaboration with multidisciplinary scientific teams in different countries. His current research area is related to supervision, fault diagnosis, and the optimisation of critical infrastructure systems such as water sanitation systems, with a special focus on trying to reduce the gap between theory and practice.

Vicenç Puig

Vicenç Puig is Full Professor at the Automatic Control Department of the Universitat Politècnica de Catalunya (UPC-BarcelonaTech) and a Researcher at the Institut de Robòtica i Informàtica Industrial (IRI), CSIC-UPC. He is the Director of the Automatic Control Department and Head of the research group on Advanced Control Systems (SAC) at UPC. He has made important scientific contributions in the areas of fault diagnosis and fault-tolerant control using interval and linear parameter-varying models adopting set-based approaches. He has also developed important scientific contributions in the areas of monitoring, control, and supervision of large-scale systems with particular applicability to systems in the water cycle (drinking water networks, sewage/drainage networks, irrigation networks, and waste treatment plants). He has participated in more than 20 European and national research projects in the last decade. He has also led many private contracts with several companies and has published more than 140 journal articles, as well as over 400 contributions in international conference/workshop proceedings. He has supervised over 25 PhD dissertations and over 50 master's theses/final projects. He is currently Chair of the IFAC Safeprocess TC Committee 6.4 and served as Vice Chair from 2016 to 2019. He was the general chair of the 3rd IEEE Conference on Control and Fault-Tolerant Systems (SysTol 2016) and IPC Chair of IFAC Safeprocess 2018.

sensors

MDPI

Editorial

Advances in the Monitoring, Diagnosis and Optimisation of Water Systems

Miquel Àngel Cugueró-Escofet [1,*] and Vicenç Puig [1,2]

[1] Advanced Control Systems (SAC) Research Group, Polytechnic University of Catalonia (UPC-Barcelo-naTech), Terrassa Campus, Gaia Research Bldg, Rambla Sant Nebridi, 22, 08222 Terrassa, Spain
[2] Institut de Robòtica i Informàtica Industrial (CSIC-UPC), 46 Llorens i Artigas Street, 08028 Barcelona, Spain
* Correspondence: miquel.angel.cuguero@upc.edu

In the context of global climate change, with the increasing frequency and severity of extreme events—such as draughts and floods—which will likely make water demand more uncertain and jeopardise its availability, those in charge of water system management face new operational challenges because of increasing resource scarcity, intensive energy requirements, growing populations (especially in urban areas), costly and ageing infrastructures, increasingly stringent regulations, and rising attention towards the environmental impact of water use. The shift from a linear to a circular economy and the need for a transition to a low-carbon production system represents an opportunity to address these emerging challenges related to water, energy, and the efficient use of resources. These challenges impel network managers to improve their methods and techniques for the monitoring, diagnosis, prognosis, supervision, and optimisation of the performance of water-related systems to adhere to the current sustainability agenda.

In this context, the increasing number of advanced installed sensors—and the corresponding increase in available data—allow for the implementation of Industry 4.0 (I4.0) techniques, which are strongly focused on interconnectivity, automation, artificial intelligence (AI), and real-time data acquisition, and will facilitate the development of intelligent tools to tackle such challenges. Within this framework, the successful implementation of I4.0 techniques in water-cycle-management facilities may prompt a breakthrough in improving the processes involved, drastically increasing their performance.

In this Special Issue, a selection of these techniques applied to the integral water cycle—i.e., water distribution and water sanitation—is introduced to address different current water-management challenges. These challenges may be classified as water-quantity challenges and water-quality challenges. On the water-distribution side, these challenges may include fault detection—namely, leak localisation—in water-distribution networks (WDNs), e.g., in [1], where a process prior to the actual leak localisation—i.e., sensor placement—is carried out using information-theory simulation-based methodology; or in [2], where a new data-driven method for leak location considering pressure measurements and network topological information is presented; or in [3], where simultaneous leak detection and isolation is applied to real data. All these methodologies contribute to reducing water loss due to leaks, which may account for up to 65% of the total water depending on the network [3] and, hence, impact water-quantity-management challenges. WDNs are also the focus in [4], where a challenge from the water-quality side—particularly, the water-disinfection process in water distribution—is addressed, providing a water-quality model by an online chlorine-decay-model calibration method, which has a strong impact on human health, since its correct concentration is paramount to ensure safe water disinfection.

Work presented in [5–8] discusses the water-sanitation side. In this field, there is a growing interest in the adaptation and use of technologies related to the circular economy which promote environmental sustainability, where resource recovery is a key issue for industrial and environmental processes and involves a wide spectrum of study possibilities.

Citation: Cugueró-Escofet, M.À.; Puig, V. Advances in the Monitoring, Diagnosis and Optimisation of Water Systems. *Sensors* **2023**, *23*, 3256. https://doi.org/10.3390/s23063256

Received: 1 March 2023
Revised: 8 March 2023
Accepted: 11 March 2023
Published: 20 March 2023

In water sanitation, wastewater treatment plants (WWTPs) offer a wide range of possibilities for resource recovery, mainly related to sludge-treatment processes such as biogas generation via the substrate codigestion process, which can be an alternative source for thermal and electrical energy production. This potential for biogas generation could become a source of renewable natural gas, which has specific composition requirements that demand high-tech sensors to assure its quality no matter its origin. Due to their potential for resource recovery and the further implications in the water–food–energy nexus, WWTPs have been a research focus in different areas of expertise: from modelling and engineering design to process dynamics, simulation, and integration. This line of work is introduced in [6], where resource recovery—namely biogas in the latter reference—is optimised by a centralised codigestion method considering real data from a WWTP network. Different nature-inspired optimisation algorithms are compared in the performance of this task, providing potential dramatic improvement when compared with actual nonoptimised operation. The improved operation of WWTP is also sought in [5,7] by means of improving the controllers involved in the operation of certain key processes of the WWTP, e.g., the aeration process of biological reactors. Classic proportional-integral (PI) controllers have been traditionally considered as the control strategy for such processes; however, improved performance may be achieved with more complex structures and techniques, e.g., model predictive-control (MPC) schemes or artificial neural network (ANN) approaches. In [5], an economic MPC (EMPC) considering a linear parameter-varying (LPV) model is proposed to control dissolved oxygen concentration in the WWTP biological reactors. Since the MPC technique requires a model of the process involved for its control, in the latter reference, a reduced model of the complex nonlinear plant is represented in a quasilinear parameter-varying (qLPV) form to reduce the computational burden—enabling the real-time operation—and applied in a real facility. This model, however, may be not available or may be difficult to obtain since the processes involved in the WWTP include nonlinear relations. ANN schemes may provide an alternative to this issue since they are well suited to deal with such processes. In this line of work, [7] considers transfer-learning (TL) methods to train ANN nets supporting control operations in WWTPs, and compares this approach with traditional control schemes, providing improved control performance while reducing control-design complexity and time invested in the ANN training process, which can be considerably time-demanding. Last but not least, in this Special Issue collection, a soft-sensing approach to predict key performance indicators (KPIs) in water-quality monitoring and control of WWTPs—such as effluent biochemical oxygen demand (BOD) or ammonia nitrogen (NH3-N)—is presented in [8]. Water-quality KPIs in WWTPs are traditionally subject to nonautomated lab-based offline monitoring approaches. Instead, in the latter reference, a method to perform accurate predictions of these KPIs, aiming for online operation, is introduced.

Further work in this area is included in the Special Issue, e.g., in [9], where remote sensing (RS) image-based time series are considered to obtain mass balances and estimate the unfiltered volumes in topographic depressions which are seasonally filled with water in a real area; or in [10], where a soil-moisture monitoring technique in precision agriculture—which is becoming key to providing food sustainably in the context of world's increasing population and natural resource scarcity—is provided using a low-cost wireless sensor network in order to help farmers optimise the irrigation process, and is tested in a real plot of land. Finally, a comprehensive review of AI and computer-vision methods for intelligent water monitoring—namely, water-body extraction and water-quality monitoring—using RS techniques is presented in [11], discussing the main challenges of using AI and RS for water-information extraction, as well as pointing out research priorities in this area. Hence, all the contributions in this Special Issue have an impact on the advances in the monitoring, diagnosis, and optimisation of water systems and, overall, cover a wide and complete sector of knowledge within this area.

Conflicts of Interest: The authors declare no conflict of interest.

References

1. Santos-Ruiz, I.; López-Estrada, F.R.; Puig, V.; Valencia-Palomo, G.; Hernández, H.R. Pressure Sensor Placement for Leak Localization in Water Distribution Networks Using Information Theory. *Sensors* **2022**, *22*, 443. [CrossRef] [PubMed]
2. Alves, D.; Blesa, J.; Duviella, E.; Rajaoarisoa, L. Robust data-driven leak localization in water distribution networks using pressure measurements and topological information. *Sensors* **2021**, *21*, 7551. [CrossRef] [PubMed]
3. Navarro-Díaz, A.; Delgado-Aguiñaga, J.A.; Begovich, O.; Besançon, G. Two simultaneous leak diagnosis in pipelines based on input–output numerical differentiation. *Sensors* **2021**, *21*, 8035. [CrossRef]
4. Pérez, R.; Martínez-Torrents, A.; Martínez, M.; Grau, S.; Vinardell, L.; Tomàs, R.; Martínez-Lladó, X.; Jubany, I. Chlorine Concentration Modelling and Supervision in Water Distribution Systems. *Sensors* **2022**, *22*, 5578. [CrossRef] [PubMed]
5. Nejjari, F.; Khoury, B.; Puig, V.; Quevedo, J.; Pascual, J.; de Campos, S. Economic Linear Parameter Varying Model Predictive Control of the Aeration System of a Wastewater Treatment Plant †. *Sensors* **2022**, *22*, 6008. [CrossRef] [PubMed]
6. Palma-Heredia, D.; Verdaguer, M.; Puig-Cayuela, V.; Poch, M.; Cugueró-Escofet, M.À. Comparison of optimisation algorithms for centralised anaerobic co-digestion in a real river basin case study in Catalonia. *Sensors* **2022**, *22*, 1857. [CrossRef] [PubMed]
7. Pisa, I.; Morell, A.; Vilanova, R.; Vicario, J.L. Transfer learning in wastewater treatment plant control design: From conventional to long short-term memory-based controllers. *Sensors* **2021**, *21*, 6315. [CrossRef] [PubMed]
8. Zhou, M.; Zhang, Y.; Wang, J.; Shi, Y.; Puig, V. Water Quality Indicator Interval Prediction in Wastewater Treatment Process Based on the Improved BES-LSSVM Algorithm. *Sensors* **2022**, *22*, 422. [CrossRef] [PubMed]
9. Fil, P.P.; Yurova, A.Y.; Dobrokhotov, A.; Kozlov, D. Estimation of infiltration volumes and rates in seasonally water-filled topographic depressions based on remote-sensing time series. *Sensors* **2021**, *21*, 7403. [CrossRef] [PubMed]
10. Lloret, J.; Sendra, S.; Garcia, L.; Jimenez, J.M. A wireless sensor network deployment for soil moisture monitoring in precision agriculture. *Sensors* **2021**, *21*, 7243. [CrossRef] [PubMed]
11. Yang, L.; Driscol, J.; Sarigai, S.; Wu, Q.; Lippitt, C.D.; Morgan, M. Towards Synoptic Water Monitoring Systems: A Review of AI Methods for Automating Water Body Detection and Water Quality Monitoring Using Remote Sensing. *Sensors* **2022**, *22*, 2416. [CrossRef] [PubMed]

sensors

MDPI

Article

Pressure Sensor Placement for Leak Localization in Water Distribution Networks Using Information Theory

Ildeberto Santos-Ruiz [1], Francisco-Ronay López-Estrada [1,*], Vicenç Puig [2], Guillermo Valencia-Palomo [3] and Héctor-Ricardo Hernández [1]

[1] TURIX-Dynamics Diagnosis and Control Group, Tecnológico Nacional de México, I.T. Tuxtla Gutiérrez, Carretera Panamericana km 1080 S/N, Tuxtla Gutierrez 29050, Mexico; ildeberto.dr@tuxtla.tecnm.mx (I.S.-R.); hector.hl@tuxtla.tecnm.mx (H.-R.H.)
[2] Institut de Robòtica i Informàtica Industrial, CSIC-UPC, Universitat Politècnica de Catalunya, C/. Llorens i Artigas 4-6, 08028 Barcelona, Spain; vicenc.puig@upc.edu
[3] Tecnológico Nacional de México, I.T. Hermosillo, Av. Tecnológico y Periférico Poniente S/N, Hermosillo 83170, Mexico; gvalencia@hermosillo.tecnm.mx
* Correspondence: frlopez@tuxtla.tecnm.mx; Tel.: +52-961-615-0461

Abstract: This paper presents a method for optimal pressure sensor placement in water distribution networks using information theory. The criterion for selecting the network nodes where to place the pressure sensors was that they provide the most useful information for locating leaks in the network. Considering that the node pressures measured by the sensors can be correlated (mutual information), a subset of sensor nodes in the network was chosen. The relevance of information was maximized, and information redundancy was minimized simultaneously. The selection of the nodes where to place the sensors was performed on datasets of pressure changes caused by multiple leak scenarios, which were synthetically generated by simulation using the EPANET software application. In order to select the optimal subset of nodes, the candidate nodes were ranked using a heuristic algorithm with quadratic computational cost, which made it time-efficient compared to other sensor placement algorithms. The sensor placement algorithm was implemented in MATLAB and tested on the Hanoi network. It was verified by exhaustive analysis that the selected nodes were the best combination to place the sensors and detect leaks.

Keywords: sensor placement; pressure monitoring; information theory; leak localization; water distribution network

Citation: Santos-Ruiz, I.; López-Estrada, F.-R.; Puig, V.; Valencia-Palomo, G.; Hernández, H.-R. Pressure Sensor Placement for Leak Localization in Water Distribution Networks Using Information Theory. *Sensors* **2022**, *22*, 443. https://doi.org/10.3390/s22020443

Academic Editor: Hossam A. Gabbar

Received: 12 December 2021
Accepted: 5 January 2022
Published: 7 January 2022

1. Introduction

Finding a suitable sensor placement is a fundamental problem for monitoring water distribution networks (WDNs) because it is impossible to install sensors at each point of the geographic area covered by the distribution system. A WDN comprises hundreds of nodes; however, only a few sensors can be installed in certain carefully selected nodes. Then, the main question is how to select the optimal sensor placement. Finding an answer to this problem is not trivial because the selected nodes must capture the most relevant information to estimate hydraulic variables at non-measured points and provide essential information for different supervision algorithms, e.g., for leak localization [1,2]. Often there are pressure and flow instruments at the supplying nodes of a WDN and in some cases at critical points (e.g., at the minimum pressure node). However, these measurements are not sufficient for an accurate leak localization, so additional sensors must be installed at other sites [3]. A practical solution is to install more pressure sensors, because they are cheaper and easier to install and maintain than flow sensors. In addition, node pressures are more sensitive to leaks than flow rates, which is why many localization algorithms are based primarily on pressure measurements. The problem of sensor placement is closely related to other WDN management problems, such as the state estimation of the network [4–6],

model calibration [7,8], water quality monitoring such as detection of contaminants and cyberattacks [9–15], among others. Nevertheless, the present work focuses on the context of leak detection and localization as discussed in [16,17]. Regarding techniques for optimal sensor placement for leak/burst detection and localization in water distribution systems, a comprehensive review can be found at [18].

In a mathematical/computational context, the placement of pressure sensors is a mixed-integer programming problem. In this problem, for a network with N nodes, a sensor placement consists of a selection $[s_1, s_2, \ldots, s_N]$ where s_i are binary decision variables such that $s_i = 1$ indicates that a sensor will be placed on the i-th node, whereas $s_i = 0$ indicates that no sensor will be placed on that node.

Combinatorial analysis shows that there are $2^N - 1$ possible sensor placements when non-empty subsets with any number of sensors are considered. If the number of sensors is previously set to a fixed number S, then the number of possible sensor placements is reduced to $\binom{N}{S}$, which is still a very large number. Therefore, in medium-sized and large networks, it is not feasible to check all possible combinations. For example, in a network containing 500 nodes the number of different placements for 10 sensors is $\binom{500}{10} \approx 2.5 \times 10^{20}$. That is why it is important to find an optimal placement method without analyzing all the possible combinations.

Usually, sensor placement focused on leak localization is addressed with an optimization approach from synthetic pressure data obtained by simulation. Some authors have focused on minimizing the number of undetectable leaks [19,20], whereas others reduce the error in the leak location [16,21]. In [22], a min-max optimization algorithm that considers the isolation of the leaks from their signatures obtained through simulation is proposed. In [23], a multi-objective approach to mitigate errors both in the detection and localization of leaks, considering minimum night flow conditions, is presented. Regarding the optimization of the objective function, two approaches are usually used: deterministic methods (e.g., branch and bound [24]) and metaheuristic methods, (e.g., genetic algorithms [25–27] and particle swarm optimization [28]). Deterministic approaches guarantee an optimal solution, but the computation time increases exponentially with the number of nodes and possible leak scenarios. On the other hand, metaheuristic methods search for a near-optimal solution that only guarantees optimality when the number of candidate solutions evaluated (named "population size") tends to infinity. Furthermore, optimization-based sensor placement methods are linked to a specific leak localization method because the objective function is expressed in terms of a localization error or isolation index for that method [16,28,29]. Based on this, a sensor placement method may be optimal for one specific leak localization method but not as good for others. Furthermore, the method should be independent of the leak localization method since it is not feasible to change it for every method. Thus, an improved leak localization method could be proposed based on an ensemble of different machine learning algorithms using the information provided by the sensors.

The huge computing time in networks with hundreds and thousands of nodes using optimization-based methods and the high dependence on the selected leak localization method has motivated the present work. In this new proposal, it is not considered how specific leak localization methods will use the information provided by the sensors, but rather that the sensor placement method only focuses on the sensors capturing as much information related to the leaks as possible. The proposed method consists of a heuristic algorithm to select the subset of nodes where to place the sensors, seeking to maximize the relevance of the information captured by the sensors while minimizing the redundancy between the pressures in the selected nodes. Both metrics, relevance and redundancy, are defined in terms of information theory.

An important contribution of this work is the reduction in computing time for sensor placement, compared to methods based on metaheuristic optimization. Another relevant contribution is the nondependence of the sensor placement on the leak localization method used, which allows the use of the same sensor placement with different localization methods. Some aspects not yet covered in this work are the possible heterogeneity of the sensors

(e.g., different errors and measurement ranges) and the influence of the measurement noise in the optimal placement, but they are considered as future work.

The rest of the document is organized as follows: in Section 2, the concepts of redundancy and relevance is presented in terms of mutual information, and the information quotient used as the basis of the method is also defined. In Section 3, the proposed method is formally described and some guidelines for its implementation are given. In Section 4, the results of the proposed method applied to a simplified version of the Hanoi network (case study) are presented. Finally, in Section 5, the conclusions are presented and future related works are proposed.

2. Information Theory Fundamentals

In Shannon's information theory (IT), the self-information of a random variable is defined according to the unexpectedness of its values [30]. Thus, the information contained in a constant random variable is zero. Mathematically, if an event E has probability P, its information content is defined by:

$$I(E) \stackrel{\text{def}}{=} -\log_b(P), \tag{1}$$

where the unit of measure of I is defined by the base of the logarithm, b, which is called "bit" if $b = 2$. In a discrete random variable X with probability function $p(x) = \Pr(X = x)$, the self-information for obtaining x as a result when measuring X is given by:

$$I(x) = -\log_b(p(x)) = \log_b(1/p(x)). \tag{2}$$

To quantify the average information that a random variable contains, considering all its possible values, the *entropy* is used:

$$H(X) \stackrel{\text{def}}{=} E(I(x)) = \sum_x -p(x)\log_b(p(x)), \tag{3}$$

which is the expected value of the information contained in the measurements of X, that is, the sum of the self-information of each of its possible values weighted by its probability of occurrence.

The mutual information of two random variables, sometimes called "information gain", measures the amount of information obtained from one of the random variables by observing the other one. For example, in a practical application of WDN monitoring, the mutual information between two node pressures would indicate how much information about the pressure at one node is gained by knowing the pressure at the other one. In probabilistic terms, the mutual information determines how different the joint distribution of (X, Y) is from the product of the marginal distributions of X and Y.

For two discrete variables X and Y, defined over the space $\mathcal{X} \times \mathcal{Y}$, the mutual information is computed as the double sum:

$$I(X,Y) = \sum_{y\in\mathcal{Y}} \sum_{x\in\mathcal{X}} p(x,y) \log \frac{p(x,y)}{p(x)p(y)}, \tag{4}$$

where $p(x, y) = \Pr(X = x, Y = y)$ is the joint probability function of X and Y, whereas $p(x)$ and $p(y)$ are the marginal probability functions of X and Y, respectively. The mutual information (4) is derived from the entropy and the conditional probability by the following equivalences:

$$I(X,Y) \equiv H(X) - H(X \mid Y) \equiv H(Y) - H(Y \mid X). \tag{5}$$

Furthermore, $I(X, X) = H(X)$, $I(X, Y) = I(Y, X)$ and $I(X, Y) \geq 0$, where $I(X, Y) = 0$ iff X and Y are independent.

For continuous random variables, the summations in (4) are replaced by integrals and the probability functions by probability densities:

$$I(X,Y) = \int_{\mathcal{Y}} \int_{\mathcal{X}} p(x,y) \log \frac{p(x,y)}{p(x)p(y)} \, \mathrm{d}x \, \mathrm{d}y. \tag{6}$$

Due to the difficulty in modeling the probability densities and subsequently evaluating the double integrals in (6), a simplification to calculate the mutual information in continuous variables is to discretize the variables with n bits, so that the domain of each variable is reduced to 2^n bins. For example, to compute the mutual information of two node pressures in a hydraulic network, the span of the pressure variables $[P_{\min}, P_{\max}]$ must be divided into a discrete 8-bit grid (256 different values) and then (4) is applied.

3. Sensor Placement Method

The proposed sensor placement method is based on a dataset of node pressures that collects typical variations due to leaks of different sizes in all network nodes. The pressure dataset is obtained from simulations with the hydraulic model of the network in [31]. Each pressure data point is labeled with a "leak class" (the node where the leak occurs) so that the proposed method can be classified as supervised.

In the context of machine learning, the placement of pressure sensors is a *feature selection* stage. To select the features (the subset of nodes where the sensors will be placed), an algorithm is proposed that seeks to maximize the relevance of the selected features (node pressures) for the response variable (leaky node), while each of them avoids capturing information already contributed by the others, that is, minimizing redundancy.

The following definitions of relevance and redundancy, proposed in [32], are used as a basis for defining the methodology:

Definition 1 (Relevance)**.** *A metric of the relevance of the subset of node pressures $\mathcal{S}$ for the response variable y (leak node), is given by*

$$\mathrm{Rel}(\mathcal{S}) \stackrel{def}{=} \frac{1}{S} \sum_{x \in \mathcal{S}} I(x,y), \tag{7}$$

where x is any feature in $\mathcal{S}$, and $S = |\mathcal{S}|$ is the number of features in $\mathcal{S}$ (the cardinality).

Definition 2 (Redundancy)**.** *A metric for information redundancy in a feature subset $\mathcal{S}$ is given by:*

$$\mathrm{Red}(\mathcal{S}) \stackrel{def}{=} \frac{1}{S^2} \sum_{x,x' \in \mathcal{S}} I(x,x'), \tag{8}$$

where x and x' are any features in $\mathcal{S}$.

To apply the above definitions to compute a pressure sensor placement, first, a dataset of node pressures is built covering different scenarios that consider leaks of different magnitude in all nodes of the network. Through simulation with the hydraulic model of the network, a series of samples of the node pressures is obtained, one sample for each different leakage scenarios. In this way, if M different leakage scenarios are simulated in a network containing N nodes, the result of the simulation is a collection of N M-dimensional vectors, x and x' in (7) and (8), corresponding to the N candidate nodes (initially, it is assumed that all nodes are potential sensing nodes). In addition, an output vector, y in (7), is generated containing integer labels to indicate the leaky node corresponding to each simulated scenario.

The exhaustive search for the optimal subset of sensors, $\mathcal{S}$, requires testing the $2^N - 1$ different combinations, which would require an impractical computation time in networks with many nodes. Therefore, the use of the method proposed in [32] was considered to rank the node pressures through an iterative forward scheme that only requires $O(NS)$

computations. In fact, with this proposal, it is possible to rank all the node pressures in order of importance with a computational cost of $O(N^2)$.

Next, a heuristic algorithm is proposed, which orders the node pressures according to their importance to explain the different leak classes (leaky nodes). The first node pressures in the output list correspond to the nodes with the highest importance for explaining the leak positions according to the information contained in the dataset. The sequential selection of nodes starts from an empty subset and, at each iteration, adds the best-ranked node among those that are still available to be selected. At each iteration, the relevance of each available feature (node pressure) with respect to the output (leaky node) and its redundancy with respect to the variables that have been previously selected is evaluated using the following equations, adapted from (7) and (8):

$$\mathrm{Rel}_y(x) = I(x, y), \tag{9}$$

$$\mathrm{Red}_{\mathcal{S}}(x) = \frac{1}{S} \sum_{x' \in \mathcal{S}} I(x, x'). \tag{10}$$

Since maximizing relevance and simultaneously minimizing redundancy represents a multiobjective problem, a combined relevance/redundancy index (RRI) is defined that increases with increasing relevance and also with decreasing redundancy, so the problem is expressed as a single objective to be maximized:

$$\mathrm{RRI} = \mathrm{Rel}_y(x) / \mathrm{Red}_{\mathcal{S}}(x). \tag{11}$$

The complete node ranking process is formally expressed in Algorithm 1. When the process finishes, the nodes where to place the sensors are taken from the first positions in the list $\mathcal{S}$. If it is not necessary to obtain the complete ranking of the nodes, but only to know the best-ranked positions, the process may stop prematurely when the subset $\mathcal{S}$ already contains the number of sensors to be placed.

Algorithm 1: Node ranking based on information theory.

Data: Set with all node pressures, $\mathcal{A}$. The nodes in $\mathcal{A}$ will be placed in the ordered list $\mathcal{S}$ according to their importance (relevance/redundancy). During the process, $\widetilde{\mathcal{S}}$ denotes the elements of $\mathcal{A}$ not yet added in $\mathcal{S}$.
Result: Set with ordered node pressures, $\mathcal{S}$.
Initialization:
$\mathcal{S} \leftarrow \left[\underset{x \in \mathcal{A}}{\arg\max}\ \mathrm{Rel}_y(x) \right]$
repeat
  if $\exists x \in \widetilde{\mathcal{S}}, \mathrm{Rel}_y(x) \neq 0, \mathrm{Red}_{\mathcal{S}}(x) = 0$ **then**
    $\mathcal{S} \leftarrow \left[\mathcal{S}, \underset{x \in \widetilde{\mathcal{S}}, \mathrm{Red}_{\mathcal{S}}(x)=0}{\arg\max}\ \mathrm{Rel}_y(x) \right]$
  else
    break
  end
until $\forall x \in \widetilde{\mathcal{S}}, \mathrm{Red}_{\mathcal{S}}(x) \neq 0$
repeat
  $\mathcal{S} \leftarrow \left[\mathcal{S}, \underset{x \in \widetilde{\mathcal{S}}, \mathrm{Rel}_y(x) \neq 0}{\arg\max}\ \mathrm{Rel}_y(x) / \mathrm{Red}_{\mathcal{S}}(x) \right]$
until $\forall x \in \widetilde{\mathcal{S}}, \mathrm{Rel}_y(x) = 0$
$\mathcal{S} \leftarrow \left[\mathcal{S}, \widetilde{\mathcal{S}} \right]$

The number of sensors to place for leak localization purposes is determined by the equipment available in most cases. The minimum number of sensors for a successful leak localization method will depend on how that method uses the available information,

the measurement noise, as well as the quality, resolution and calibration of the sensors. If there are enough resources to intensively instrument the network, it must be taken into account that increasing the number of sensors does not always lead to better performance in locating leaks. To determine how many sensors should be placed, it is suggested to start from the ranking obtained by Algorithm 1, and run a marginal analysis with the leak localization method to be used. Starting from one sensor (the best ranked), the number of sensors is progressively increased and the leak localization performance is evaluated for each new set of sensors until adding a new sensor no longer represents a significant benefit for locating leaks.

It should be noted that Algorithm 1 does not take into account the geographical distribution of the nodes, since relevance and redundancy depend only on the mutual information between node pressures. This means that the network topology is what determines the amount of mutual information rather than the distance between sensors (i.e., two sensors can be geographically very close but have little mutual information).

4. Results and Discussion

Algorithm 1 was implemented in MATLAB and tested on the Hanoi network [33]. The model of the Hanoi network is composed of one reservoir, 31 consumer nodes, and 34 pipes, as shown in Figure 1. Due to its reduced topology, this network has been used as a standarized benchmark in different works [21,27,34].

In order to build the pressure dataset, leaks of different magnitude were simulated at each junction node using the EPANET 2 simulation program [35] through the EPANET/MATLAB Toolkit [36]. The procedure to generate the dataset using EPANET, the training and the predictive use of classifiers in locating leaks have been described in [37]. The dataset generated by simulation for this work considered leaks at all junction nodes with flow rates from 50 L/s. In order to simulate leaks at a node, the demand assigned to that node in the EPANET hydraulic model was modified by increasing this demand by an amount equal to the flow of the simulated leak. Because the Hanoi network contains few nodes, the optimality of the sensor placement calculated by Algorithm 1 was exhaustively verified.

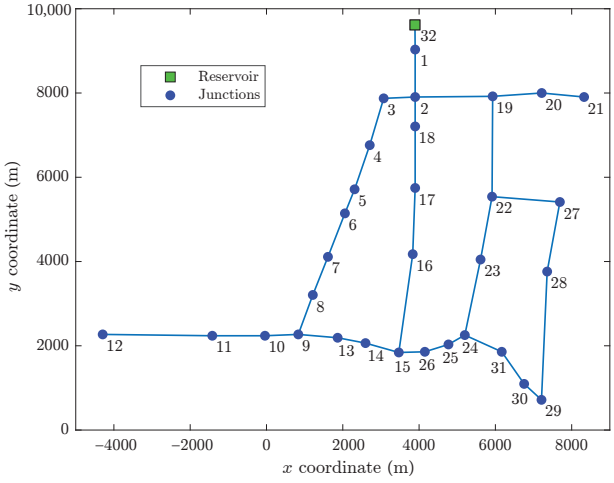

Figure 1. The Hanoi network.

To assess the optimality of the sensor placement obtained from Algorithm 1, leak localization tests were carried out using two machine learning methods that used the pressures in the selected nodes as features (input variables). The methods used were the *k*-nearest neighbors (*k*-NN) and quadratic discriminant analysis (QDA). These leak

localization methods are based on classifiers that recognize directional patterns in pressure residuals using supervised learning techniques, as described in [38].

Through the marginal analysis, suggested at the end of Section 3, it was determined that $S = 3$ is an adequate number of sensors in the Hanoi network, because the addition of the fourth sensor does not produce a statistically significant improvement (with 0.95 confidence level) in leak location (considering that measurement noise may possibly increase the minimum number of sensors, but this discussion has been considered as future work). Because the Hanoi network contains few nodes, it was possible to comprehensively analyze all 4495 possible combinations of three sensor nodes. For each triplet of nodes (three-sensor placement), 50 leak localization tests were carried out with flow rates $q_{\text{leak}} = 1, 2, \ldots, 50$ L/s at each node of the network. Finally, the overall performance of both methods was evaluated for each candidate triplet using the classification accuracy (Acc) and the average topological distance (ATD) as performance metrics, as defined in [39]. The Acc is the fraction of exactly located leaks considering all leak scenarios in the test dataset, where Acc $= 1$ means that all leaks were correctly located, whereas Acc $= 0$ means that no leaks were correctly located. The ATD is a measure of how far from the true leaky node the classifier locates the leak, counting the number of separation links between the true leaky node and the estimated leaky node, averaged across all scenarios in the test dataset. Therefore, the best sensor placements are the ones that lead to the highest Acc values and the lowest ATD values.

The results in Table 1 show that the node triplet $\{12, 21, 28\}$ computed by Algorithm 1 is among the best ranked, since it presents the highest accuracy and the lowest average topological distance.

Table 1. Better positions to place three sensors in the Hanoi network, obtained by exhaustive analysis. The shaded selection is the one obtained by Algorithm 1.

Rank	Nodes	Location Method	
		***k*-NN**	**QDA**
1	{12, 21, 28}	0.9974	0.9948
1	{12, 21, 27}	0.9974	0.9948
1	{12, 21, 31}	0.9974	0.9948
2	{7, 12, 21}	0.9961	0.9936
2	{12, 17, 21}	0.9961	0.9936
3	{3, 12, 21}	0.9961	0.9923
3	{4, 12, 21}	0.9961	0.9923
3	{6, 12, 21}	0.9961	0.9923
3	{5, 12, 21}	0.9961	0.9923

(a) Metric: classification accuracy

Rank	Nodes	Location Method	
		***k*-NN**	**QDA**
1	{12,21,28}	0.0026	0.0052
1	{12, 21, 27}	0.0026	0.0052
1	{12, 21, 31}	0.0026	0.0052
2	{12, 13, 21}	0.0065	0.0065
3	{7, 12, 21}	0.0065	0.0090
3	{12, 17, 21}	0.0065	0.0090
4	{3, 12, 21}	0.0039	0.0129
4	{4, 12, 21}	0.0039	0.0129
5	{6, 12, 21}	0.0065	0.0129

(b) Metric: average topological distance

Figure 2 shows the geographic location of the three-sensor placement obtained considering the three nodes best ranked by Algorithm 1. Figure 3 shows the complete ranking considering the 31 nodes of the network.

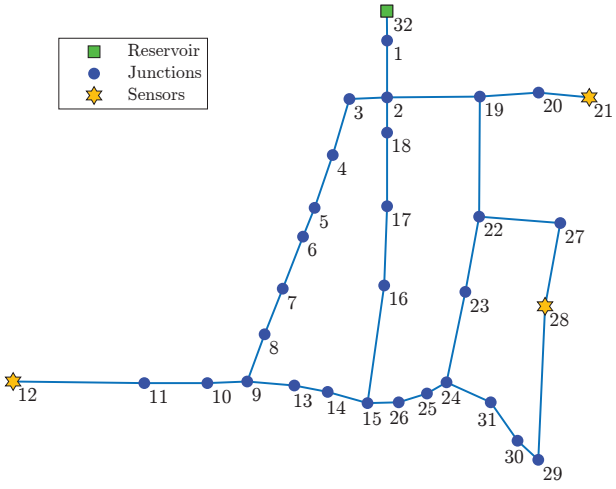

Figure 2. Computed three-sensor placement in the Hanoi network.

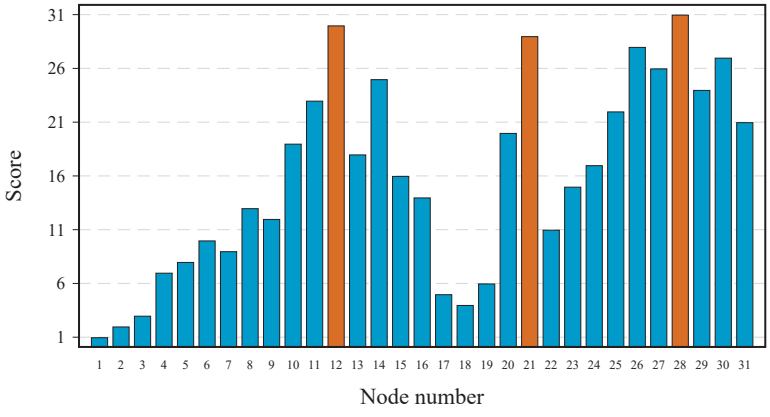

Figure 3. Node ranking in the Hanoi network.

Table 2 shows the sensor placements obtained for two, three and four sensors in the Hanoi network, and they are compared with the results obtained by metaheuristic methods reported in the literature [28]. The nodes selected by these methods are quite similar and produce very close results in terms of accuracy in locating leaks based on the pressures of the selected nodes. However, there is an important difference in the computation time of the IT-based method (Algorithm 1) compared with the metaheuristic methods. On a personal computer with an Intel 64-bit processor and 8 GB of RAM, the computation time for the IT-based method was around one second with the synthetic data from the Hanoi network, whereas it was 24 min for the genetic algorithm (it may be larger, depending on the initial population size) and about one hour for the exhaustive analysis.

Table 2. Optimal three-sensor placement in the Hanoi network using different methods.

S	IT [a]	GA [b]	PSO [c]	SE [d]
2	{12, 28}	{12, 21}	{12, 21}	{12, 21}
3	{12, 21, 28}	{12, 21, 27}	{12, 14, 21}	{12, 21, 29}
4	{12, 21, 26, 28}	{1, 12, 21, 29}	{1, 12, 21, 24}	{1, 12, 21, 29}

[a] Algorithm 1. [b] Genetic algorithm, reported in [28]. [c] Particle swarm optimization, reported in [28]. [d] Semi-exhaustive search, reported in [28].

Further tests were made on larger networks, e.g., in some midsize sectors of the Madrid network. Figure 4 shows a 10-sensor placement obtained using Algorithm 1 in a sector of the Madrid network containing one reservoir, 312 junction nodes and around 14 km of pipes. In this case, optimality was not exhaustively tested due to the vast number of possible placements to compare. However, it was found that the average accuracy in leak localization with sensor placements obtained by Algorithm 1 was at least better than that obtained with an existing placement (previously obtained by a genetic algorithm) for different leak scenarios.

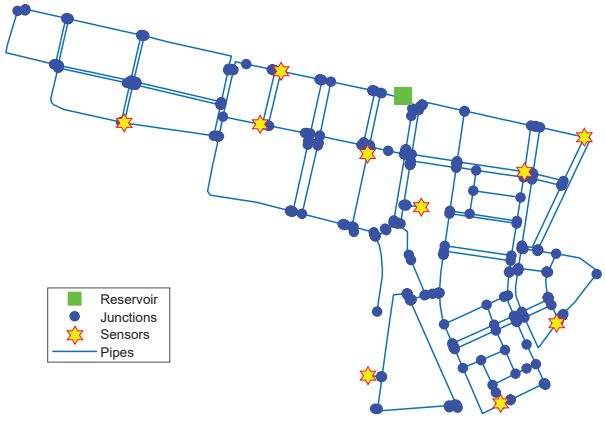

Figure 4. The optimal 10-sensor placement in a sector of the Madrid network.

Figures 2 and 4 show that the computed sensor placements do not show geometric regularity (i.e., the sensors do not appear equally spaced), since geometric or spatial criteria are not used to distribute the sensors in the network. However, regardless of geometric irregularity, leak location tests with these placements demonstrated that pressure measurements at these nodes provided the most useful information for discerning between different leak scenarios. In fact, when the placement of sensors obtained by Algorithm 1 is compared with the results reported by other authors using metaheuristics, sometimes very close performances can be found even though the sensors are distributed in different nodes, because the proposed algorithm does not optimize the position of each sensor individually but the entire set of sensors. This can be explained with an informal analogy: two soccer teams can achieve similar performances using different players.

Although, as noted above, there may be different sensor placements that lead to a good performance in locating leaks, the one obtained by Algorithm 1 has the advantage of being calculated in less time than the methods based on metaheuristics and that it is not linked to a specific leak location method, so changing the leak location method does not imply changing the location of the sensors, which would be impractical.

5. Conclusions

This paper has presented a technique for finding optimal sensor placements from information theory using a sequential forward selection, maximizing the relevance and

minimizing the redundancy of the selected node subset. The proposed technique is computationally less expensive than other methods reported in the literature because the proposed technique operates directly on the values of node pressures without performing calculations for leak localization in the implementation of the algorithm. The optimality of the sensor placement obtained with the proposed method was extensively tested by simulation with the Hanoi network. It was found that the selection of nodes where to place sensors using information theory produced the best combination of pressure variables to locate leaks using different machine learning methods.

An implicit assumption in the proposed algorithms is that all network nodes have the same availability to place the sensors. However, in practice, some specific nodes may have placement priority over others; for example, critical nodes (points of minimum pressure) and nodes that supply essential services (e.g., hospitals) could be monitored as a priority. It may also occur that some nodes already have a sensor installed and that previous partial placement must be held, or that the conditions in a node are physically adverse and instrumentation is avoided. These circumstances warrant adjustments to the proposed sensor placement algorithm that may lead to future work. Another possible working line is the combination of heterogeneous sensors where different sensing specifications are included (e.g., different precision) or where the sensors measure different physical magnitudes (e.g., sensor placements combining pressure and flow sensors).

Author Contributions: Conceptualization, I.S.-R., F.-R.L.-E. and V.P.; methodology, I.S.-R.; software, I.S.-R.; validation, F.-R.L.-E., V.P. and G.V.-P.; formal analysis, G.V.-P. and H.-R.H.; data curation, I.S.-R. and H.-R.H.; writing—original draft preparation, I.S.-R.; writing—review and editing, F.-R.L.-E., V.P. and G.V.-P.; supervision, F.-R.L.-E. and V.P.; project administration, F.-R.L.-E. All authors have read and agreed to the published version of the manuscript.

Funding: This work was cofinanced by the European Regional Development Fund of the European Union in the framework of the ERDF Operational Program of Catalonia 2014–2020, under the research project 001-P-001643 Agrupació Looming Factory. Tecnológico Nacional de México (TecNM) also cofinanced this work by granting the research project 11080.21-P.

Conflicts of Interest: The authors declare no conflict of interest. The funders had no role in the design of the study; in the collection, analyses, or interpretation of data; in the writing of the manuscript, or in the decision to publish the results.

References

1. Sela, L.; Amin, S. Robust sensor placement for pipeline monitoring: Mixed integer and greedy optimization. *Adv. Eng. Inform.* **2018**, *36*, 55–63. [CrossRef]
2. Puig, V.; Ocampo-Martínez, C.; Pérez, R.; Cembrano, G.; Quevedo, J.; Escobet, T. (Eds.) *Real-Time Monitoring and Operational Control of Drinking-Water Systems*; Springer International Publishing: Berlin/Heidelberg, Germany, 2017. [CrossRef]
3. Pérez, R.; Sanz, G.; Puig, V.; Quevedo, J.; Cugueró, M.À.; Nejjari, F.; Meseguer, J.; Cembrano, G.; Mirats, J.M.; Sarrate, R. Leak localization in water networks: A model-based methodology using pressure sensors applied to a real network in Barcelona [applications of control]. *IEEE Control Syst. Mag.* **2014**, *34*, 24–36.
4. Kang, D.; Lansey, K. Optimal Meter Placement for Water Distribution System State Estimation. *J. Water Resour. Plan. Manag.* **2010**, *136*, 337–347. [CrossRef]
5. Santos-Ruiz, I.; López-Estrada, F.R.; Puig, V.; Blesa, J. Estimation of Node Pressures in Water Distribution Networks by Gaussian Process Regression. In Proceedings of the 4th Conference on Control and Fault Tolerant Systems (SysTol'19), Casablanca, Morocco, 18–20 September 2019; pp. 50–55. [CrossRef]
6. Mankad, J.; Natarajan, B.; Srinivasan, B. Integrated approach for optimal sensor placement and state estimation: A case study on water distribution networks. *ISA Trans.* 2021, *in press*. [CrossRef]
7. Simone, A.; Giustolisi, O.; Laucelli, D.B. A proposal of optimal sampling design using a modularity strategy. *Water Resour. Res.* **2016**, *52*, 6171–6185. [CrossRef]
8. Wéber, R.; Hős, C. Efficient Technique for Pipe Roughness Calibration and Sensor Placement for Water Distribution Systems. *J. Water Resour. Plan. Manag.* **2020**, *146*, 04019070. [CrossRef]
9. Kessler, A.; Ostfeld, A.; Sinai, G. Detecting Accidental Contaminations in Municipal Water Networks. *J. Water Resour. Plan. Manag.* **1998**, *124*, 192–198. [CrossRef]
10. Eliades, D.G.; Polycarpou, M.M.; Charalambous, B. A Security-Oriented Manual Quality Sampling Methodology for Water Systems. *Water Resour. Manag.* **2011**, *25*, 1219–1228. [CrossRef]

11. Vaidya, U.; Fardad, M. On optimal sensor placement for mitigation of vulnerabilities to cyber attacks in large-scale networks. In Proceedings of the 2013 European Control Conference (ECC), Zurich, Switzerland, 17–19 July 2013; pp. 3548–3553. [CrossRef]
12. Rathi, S.; Gupta, R.; Kamble, S.; Sargaonkar, A. Risk Based Analysis for Contamination Event Selection and Optimal Sensor Placement for Intermittent Water Distribution Network Security. *Water Resour. Manag.* **2016**, *30*, 2671–2685. [CrossRef]
13. Zeng, D.; Gu, L.; Lian, L.; Guo, S.; Yao, H.; Hu, J. On cost-efficient sensor placement for contaminant detection in water distribution systems. *IEEE Trans. Ind. Inform.* **2016**, *12*, 2177–2185. [CrossRef]
14. Hu, C.; Dai, L.; Yan, X.; Gong, W.; Liu, X.; Wang, L. Modified NSGA-III for sensor placement in water distribution system. *Inf. Sci.* **2020**, *509*, 488–500. [CrossRef]
15. Hooshmand, F.; Amerehi, F.; MirHassani, S.A. Risk-Based Models for Optimal Sensor Location Problems in Water Networks. *J. Water Resour. Plan. Manag.* **2020**, *146*, 04020086. [CrossRef]
16. Cugueró-Escofet, M.À.; Puig, V.; Quevedo, J. Optimal pressure sensor placement and assessment for leak location using a relaxed isolation index: Application to the Barcelona water network. *Control Eng. Pract.* **2017**, *63*, 1–12. [CrossRef]
17. Soldevila, A.; Blesa, J.; Fernandez-Canti, R.M.; Tornil-Sin, S.; Puig, V. Data-Driven Approach for Leak Localization in Water Distribution Networks Using Pressure Sensors and Spatial Interpolation. *Water* **2019**, *11*, 1500. [CrossRef]
18. Romano, M. Review of Techniques for Optimal Placement of Pressure and Flow Sensors for Leak/Burst Detection and Localisation in Water Distribution Systems. In *ICT for Smart Water Systems: Measurements and Data Science*; Scozzari, A., Mounce, S., Han, D., Soldovieri, F., Solomatine, D., Eds.; Springer International Publishing: Cham, Switzerland, 2021; pp. 27–63. [CrossRef]
19. Forconi, E.; Kapelan, Z.; Ferrante, M.; Mahmoud, H.; Capponi, C. Risk-based sensor placement methods for burst/leak detection in water distribution systems. *Water Sci. Technol. Water Supply* **2017**, *17*, 1663–1672. [CrossRef]
20. Venkateswaran, P.; Han, Q.; Eguchi, R.T.; Venkatasubramanian, N. Impact driven sensor placement for leak detection in community water networks. In Proceedings of the 2018 ACM/IEEE 9th International Conference on Cyber-Physical Systems (ICCPS), Porto, Portugal, 11–13 April 2018; pp. 77–87.
21. Casillas, M.; Puig, V.; Garza-Castañón, L.; Rosich, A. Optimal sensor placement for leak location in water distribution networks using genetic algorithms. *Sensors* **2013**, *13*, 14984–15005. [CrossRef]
22. Pérez, R.; Puig, V.; Pascual, J.; Quevedo, J.; Landeros, E.; Peralta, A. Methodology for leakage isolation using pressure sensitivity analysis in water distribution networks. *Control Eng. Pract.* **2011**, *19*, 1157–1167. [CrossRef]
23. Quiñones-Grueiro, M.; Verde, C.; Llanes-Santiago, O. Multi-objective sensor placement for leakage detection and localization in water distribution networks. In Proceedings of the 4th Conference on Control and Fault Tolerant Systems (SysToL'19), Casablanca, Morocco, 18–20 September 2019; pp. 129–134. [CrossRef]
24. Sarrate, R.; Blesa, J.; Nejjari, F.; Quevedo, J. Sensor placement for leak detection and location in water distribution networks. *Water Sci. Technol. Water Supply* **2014**, *14*, 795–803. [CrossRef]
25. Zhao, M.; Zhang, C.; Liu, H.; Fu, G.; Wang, Y. Optimal sensor placement for pipe burst detection in water distribution systems using cost–benefit analysis. *J. Hydroinform.* **2020**, *22*, 606–618. [CrossRef]
26. Cheng, W.; Chen, Y.; Xu, G. Optimizing Sensor Placement and Quantity for Pipe Burst Detection in a Water Distribution Network. *J. Water Resour. Plan. Manag.* **2020**, *146*, 04020088. [CrossRef]
27. Ponti, A.; Candelieri, A.; Archetti, F. A New Evolutionary Approach to Optimal Sensor Placement in Water Distribution Networks. *Water* **2021**, *13*, 1625. [CrossRef]
28. Casillas, M.V.; Garza-Castañón, L.E.; Puig, V. Optimal sensor placement for leak location in water distribution networks using evolutionary algorithms. *Water* **2015**, *7*, 6496–6515. [CrossRef]
29. Blesa, J.; Nejjari, F.; Sarrate, R. Robust sensor placement for leak location: Analysis and design. *J. Hydroinform.* **2016**, *18*, 136–148. [CrossRef]
30. Thomas M.; Cover, J.A.T. *Elements of Information Theory*, 2nd ed.; Wiley Series in Telecommunications and Signal Processing; Wiley-Interscience: Hoboken, NJ, USA, 2006.
31. Cooper, J.P.; Robinson, L. *Computer Modeling of Water Distribution Systems*, 4th ed.; Manual of Water Supply Practices—M32; American Water Works Association, AWWA: Denver, CO, USA, 2017.
32. Ding, C.; Peng, H. Minimum redundancy feature selection from microarray gene expression data. *J. Bioinform. Comput. Biol.* **2005**, *3*, 185–205. [CrossRef] [PubMed]
33. Fujiwara, O.; Khang, D.B. A two-phase decomposition method for optimal design of looped water distribution networks. *Water Resour. Res.* **1990**, *26*, 539–549. [CrossRef]
34. Alves, D.; Blesa, J.; Duviella, E.; Rajaoarisoa, L. Robust Data-Driven Leak Localization in Water Distribution Networks Using Pressure Measurements and Topological Information. *Sensors* **2021**, *21*, 7551. [CrossRef]
35. Rossman, L.A.; Woo, H.; Tryby, M.; Shang, F.; Janke, R.; Haxton, T. *EPANET 2.2 User Manual*; Technical Report EPA/600/R-20/133; U.S. Environmental Protection Agency: Washington, DC, USA, 2020.
36. Eliades, D.G.; Kyriakou, M.; Vrachimis, S.; Polycarpou, M.M. EPANET-MATLAB Toolkit: An Open-Source Software for Interfacing EPANET with MATLAB. In Proceedings of the 14th International Conference on Computing and Control for the Water Industry (CCWI), Amsterdam, The Netherlands, 7–9 November 2016; p. 8. [CrossRef]
37. Ferrandez-Gamot, L.; Busson, P.; Blesa, J.; Tornil-Sin, S.; Puig, V.; Duviella, E.; Soldevila, A. Leak localization in water distribution networks using pressure residuals and classifiers. *IFAC-PapersOnLine* **2015**, *48*, 220–225. [CrossRef]

38. Santos-Ruiz, I.; Blesa, J.; Puig, V.; López-Estrada, F. Leak localization in water distribution networks using classifiers with cosenoidal features. *IFAC-PapersOnLine* **2020**, *53*, 16697–16702. [CrossRef]
39. Soldevila, A.; Blesa, J.; Tornil-Sin, S.; Fernandez-Canti, R.M.; Puig, V. Sensor placement for classifier-based leak localization in water distribution networks using hybrid feature selection. *Comput. Chem. Eng.* **2018**, *108*, 152–162. [CrossRef]

sensors

MDPI

Article

Robust Data-Driven Leak Localization in Water Distribution Networks Using Pressure Measurements and Topological Information

Débora Alves [1,2,*], Joaquim Blesa [1,3,4,*], Eric Duviella [2] and Lala Rajaoarisoa [2]

[1] Supervision, Safety and Automatic Control Research Center (CS2AC), Universitat Politècnica de Catalunya, Gaia Building, Rambla Sant Nebridi, 22, 08222 Terrassa , Spain
[2] IMT Nord Europe, Université de Lille, CERI Digital Systems, F-59000 Lille, France; eric.duviella@imt-lille-douai.fr (E.D.); lala.rajaoarisoa@imt-lille-douai.fr (L.R.)
[3] Institut de Robòtica i Informàtica Industrial (CSIC-UPC), Carrer Llorens Artigas, 4-6, 08028 Barcelona, Spain
[4] Serra Húnter Fellow Automatic Control Department (ESAII), Universitat Politècnica de Catalunya (UPC), Pau Gargallo, 5, 08028 Barcelona, Spain
* Correspondence: debora.costa.da.silva@upc.edu (D.A.); joaquim.blesa@upc.edu (J.B.)

Abstract: This article presents a new data-driven method for locating leaks in water distribution networks (WDNs). It is triggered after a leak has been detected in the WDN. The proposed approach is based on the use of inlet pressure and flow measurements, other pressure measurements available at some selected inner nodes of the WDN, and the topological information of the network. A reduced-order model structure is used to calculate non-leak pressure estimations at sensed inner nodes. Residuals are generated using the comparison between these estimations and leak pressure measurements. In a leak scenario, it is possible to determine the relative incidence of a leak in a node by using the network topology and what it means to correlate the probable leaking nodes with the available residual information. Topological information and residual information can be integrated into a likelihood index used to determine the most probable leak node in the WDN at a given instant k or, through applying the Bayes' rule, in a time horizon. The likelihood index is based on a new incidence factor that considers the most probable path of water from reservoirs to pressure sensors and potential leak nodes. In addition, a pressure sensor validation method based on pressure residuals that allows the detection of sensor faults is proposed.

Keywords: water distribution networks; leak localization; data-driven

Citation: Alves, D.; Blesa, J.; Duviella, E.; Rajaoarisoa, L. Robust Data-Driven Leak Localization in Water Distribution Networks Using Pressure Measurements and Topological Information. *Sensors* **2021**, *21*, 7551. https://doi.org/10.3390/s21227551

Academic Editor: Jason K. Levy

Received: 8 September 2021
Accepted: 6 November 2021
Published: 13 November 2021

1. Introduction

Water distribution networks are complex systems that are difficult to manage and monitor with extreme importance nowadays. The detection and location of leaks have become crucial for water distribution because when there are bursts or leaks, this can generate not only economic losses but also an environmental issue and represents a potential risk to public health with contaminated water [1]. Another concern is the scarcity of water that can occur in 2025, which may affect half the world's population that will not have access to safe and accessible water for their basic needs [2]. However, with all these risks, currently, this infrastructure does not perform satisfactorily in practice. According to [3], a global volume of water loss called Non-Revenue Water (NRW) has been calculated at 346 million cubic meters per day or 126 billion cubic meters per year.

The infrastructure in a medium-sized city can have pipes that span hundreds of kilometers connected to hundreds of nodes (pipe junctions or customers that connect to the network). Therefore, several factors can generate water loss during transport between the treatment plants and the reservoir for consumers, usually attributed to several causes, including leaks, measurement errors, and theft. Water loss can be divided into two terms,

"real losses" and "apparent losses". Apparent losses are constituted by badly read measurements, data handling errors, and illegal water tapping. In contrast, the real losses comprise leakage from all system parts and overflow at storage tanks. Real losses are divided into "background leakage" made up of small undetectable and into detectable leaks relevant for detection as they represent significant losses for the water distribution company.

Effective leak management is vital for all of the factors mentioned above to save financial resources and water. The methods of leak localization can be classified into two categories: Hardware-based system and Software-based.

The Hardware-based utilizes hardware sensors to detect a leak directly and help the localization of the leak. As there are various types of sensors and instruments available, they can be further subclassified as: acoustic [4,5] and non-acoustic detection methods [6].

Software-based methods generally rely on an algorithm or model for detecting leaks. Unlike hardware-based methods, these methods do not seek to locate the leak point accurately but minimize possible leakage areas. Since these methods are based on information, such as the pressure of the pipe network, flow data, and so forth, they work well on any type of pipe. These methods can be divided into physical modeling methods and data-driven methods. The physical modeling methods or model-based methods identify the leak using a numerical model and compare the results with the field data, for example, Ref. [7] which uses pressure sensitivity analysis, Ref. [8] uses leak signature space, Ref. [9] analyzes the sensitivity matrix and residuals, and [10] uses pressure and flow measurements to perform leakage detection through model-invalidation. On the other hand, data-driven methods analyze the monitoring data, combining tools such as artificial intelligence (e.g., classifiers [11–14] or artificial neural networks [15,16]). Thus, it is possible to identify potential areas of the leak based on certain rules or principles without resorting to the simulation of the physical model results [17]. However, these methods need, in general, an important number of non-leak and leak data scenarios in the training process to obtain reasonable results. As an exhaustive amount of leak scenarios are not available in general, a hydraulic simulator can be used to generate leak data. This work deals with the problem of leak localization and it is assumed that it is available a leak detection method that determines if a leak is present or not in the WDN. In particular, a non-numerical localization method, focused on a data-driven approach, is proposed.

Like other recent works [18,19], it requires only topological information of the network and historical data without leakage of the available measurements. In this work, the topological information provides the most probable paths for extra flows produced by leaks. A new incidence factor from every combination of nodes and sensors is computed with this information. Every incidence factor determines how a leak in a particular node affects a specific pressure sensor. On the other hand, historical data are used to calculate non-leak pressure estimations at sensed inner nodes. Residuals are generated using the comparison between these estimations and leak pressure measurements. Incidence factors are integrated with residuals in likelihood indexes to give the most probable leak node in a leak scenario. In addition, pressure residuals are used to detect sensor faults by means of a novel sensor validation algorithm.

The remainder of this paper is organized as follows: Section 2 presents the theory of graphs applied to WDN and explains the structure of the reduced-order model used in this work. The developed leak localization has been elaborated in Section 3. In Section 4 a sensor validation method that allows the detection of pressure sensor faults is presented. Section 5 introduces the case studies of Hanoi and Modena's WDNs. Section 6 presents the conclusions and future scope of the research work.

2. Water Distribution Networks

2.1. Preliminaries

A water distribution network is composed of m pipes, n internal consumer nodes and can be described by a directed graph $\mathcal{G} = \{\mathcal{V}, \mathcal{E}\}$, [20], with $\mathcal{V} = \{v_1, \ldots, v_n\}$ is the set of vertices that represent connections between the components of the network, additionally

the last $\{v_{n-n_I+1}, \ldots, v_n\}$, represent the vertices of the system's input, n_I being the number of the inlets, with $n_I \geq 1$. The elements of the set $\mathcal{E} = \{e_1, \ldots, e_m\}$ are the edges, which represent the m pipes in the network.

The graph $\mathcal{G}$ can be represented by the incidence matrix $\mathbf{H} = [h_{ij}]$, in which the elements h_{ij} are defined as:

$$h_{ij} = \begin{cases} -1 & \text{if the } j\text{th edge is entering } i\text{th vertex.} \\ 0 & \text{if the } j\text{th edge is not connected to the } i\text{th vertex.} \\ 1 & \text{if the } j\text{th edge is leaving } i\text{th vertex.} \end{cases}$$

The direction of the edge represents a reference direction for the flow in the corresponding pipe. The incidence matrix is composed of $H \in \{-1, 0, 1\}^{n \times m}$ with each row corresponding to a node and column corresponding to a pipe.

The WDN must fulfill mass conservation law, which expresses the conservation of mass in each vertex, described by:

$$\mathbf{H} \cdot \mathbf{q} = \mathbf{d}, \tag{1}$$

where $\mathbf{d} \in \mathbb{R}^n$ is the vector of nodal demands, with $\mathbf{d}_i > 0$ when the flow is into the node i, and $\mathbf{q} \in \mathbb{R}^m$ is the vector of flows in the edges. By virtue of the mass conservation, it is possible to have only $n - 1$ independent nodal demand, $\sum_{i=1}^{n} d_i = 0$, therefore the supply flow must equal the end-user demands as there is no storage in the network.

Let $\mathbf{p}$ be the vector of absolute pressures at the nodes and $\Delta\mathbf{p}$ be the vector of differential pressures across the pipes, both in meters of water column [mwc], then the energy law for water networks gives:

$$\Delta\mathbf{p} = \mathbf{H}^T\mathbf{p} = f(\mathbf{q}) - \mathbf{H}^T\mathbf{h}, \tag{2}$$

where $\mathbf{p} \in \mathbb{R}^n$, and $f : \mathbb{R}^m \to \mathbb{R}^m$, $f(\mathbf{q}) = (f_1(q_1), \ldots, f_m(q_m))$. The function $f_j(\cdot)$ describes the flow dependent pressure drop due to the hydraulic resistance in the jth edge. The relationship between pipe flow and energy loss caused by friction in individual pipes can be computed using the Hazen–Williams formula [21] for expression $f_j(\cdot)$:

$$f_j(q_j) = \frac{10.7 \cdot L_j}{\rho_j^{1.852} \cdot D_j^{4.87}} \cdot q_j^{1.852}, \tag{3}$$

where L_j is the length of the pipe and D_j is the diameter of the pipe, both in meters [m], q_j is the pipe flow in m^3/s and ρ_j is the pipe roughness coefficient.

The term $\mathbf{H}^T\mathbf{h}$ is the pressure drop across the pipes due to the difference in geodesic level (i.e., elevation) in meters [m] between the ends of the pipes with $\mathbf{h} \in \mathbb{R}^n$ the vector of geodesic levels at each vertex.

2.2. Structure of the Reduced Order Model

The reduced-order network model is used in this paper to calculate the nominal pressure at the measured internal nodes. The model uses the pressure dependence of the network's internal nodes with the pressure and flow measurements of the inlets. The details of the model derivation can be found in [22,23].

A network can be divided into nodes connected with reservoirs (the inlets nodes) and internal nodes that compose the system. To facilitate the explanation in this work, the information regarding inlet nodes will be represented by (r) superscript and those of the internal nodes, which will be expressed by the (i_n) superscript. In particular, vector $\mathbf{p}^{(in)}$ will contain pressure node values $p_1, \ldots, p_{n-n_I}$ and $\mathbf{p}^{(r)}$ inlet pressure values $p_{n+1-n_I}, \ldots, p_n$.

The network needs to fulfill some conditions for using the reduced model proposed:

Condition 1: corresponds to the demands of the internal nodes of the system, where Equation (1) can be defined as:

$$\mathbf{d}(k) = -\mathbf{v}(k)\sigma(k), \tag{4}$$

where $\sigma(k)$ denotes the total inlet flow into the network at time instant k, the vector $\mathbf{v}(k)$ defines the distribution of the total demand in the internal nodes at every time k, with the property $\sum_i^n v_i(k) = 1$. Notice that if all consumers are residential, all nodes demand have the same consumption profile, in consequence, the $\mathbf{v}(k)$ will be constant $\mathbf{v}(k) = \mathbf{v}$.

Condition 2: is a particularly case when the vector $\mathbf{p}^{(r)}$ of control inputs fulfill the following case,

$$\mathbf{p}^{(r)}(k) + \mathbf{h}^{(r)} = \kappa(k)\mathbb{1}, \tag{5}$$

for some $\kappa \in \mathbb{R}$, which is the total head at the inlets in [mwc] and where $\mathbb{1}$ denote the vector consisting of ones. In [23], there is a discussion on this definition's feasibility where the controllers should satisfy this premise at least in networks with the low total consumption.

If these two conditions are fulfilled, the pressure at the ith internal node can be expressed by:

$$p_i^{(i_n)}(k) = \alpha_i \sigma^2(k) + \sum_{j=1}^{n_I} \beta_{ij}(k) p_j^{(r)}(k), \tag{6}$$

where α_i is parameter dependent on the network topology and the distribution of demands in the network, and β_{ij} is dependent on the network topology with $j = 1, \ldots, n_I$. The total inlet flow σ is typically well-known since inlet flows are measured. α_i is a parameter dependent on the network topology and the distribution of demands in the network, and β_{ij} is dependent on the network topology with $j = 1, \ldots, n_I$. The total inlet flow σ is typically well-known since inlet flows are measured.

Some methods of identifying parameters can be used to identify parameters α_i and β_{ij} since model (6) of $p_i^{(i_n)}$ is linear [24], using the measures of σ, $\mathbf{p}^{(r)}$ and $p_i^{(i_n)}$ with nodes that contain pressure sensors that will be denoted as p_{s_i} $\forall i = 1, \ldots, n_s$ in the following, where n_s is the number of sensors installed in the inner nodes.

Once inner pressure model (6) has been calibrated, the accuracy of the model can be assessed by applying the computation of the model error or pressure residual defined by:

$$r_{s_i} = \hat{p}_{s_i}(c) - p_{s_i}(c), \quad \forall i = 1, \ldots, n_s, \tag{7}$$

where c denotes the boundary conditions (heads and inflows in inlets) necessary to compute pressure estimation by means of (6). For example, minimum and maximum residual bounds $\underline{\sigma_i}$ and $\bar{\sigma_i}$, considering the available data, can be computed for every sensor $i = 1, \ldots, n_s$ to obtain an idea of the accuracy of model (6). Sensor noises and error models can produce residual errors. If big values of residual bounds are obtained, improvements in model (6) should be considered. For example, the assumption that all the nodes have the same consumption profile can lead to a big error in some networks. In this case, the error could be decreased if model (6) is calibrated only using data from the same hour but on different days. It would be assumed that different users can have different profiles at a given hour, but a particular user will have the same profile at a particular hour for all the different days. This possible improvement will imply the calibration of 24 different models (6) (one for each hour) and will require more historical data to obtain good accuracy. Another method to obtain an estimation of the pressure in inner nodes $\hat{p}_{s_i}(c)$ is to use historical data directly as a lookup table, as was proposed in [18]. That is, given particular operating conditions, c provides the inner pressures from historical data that had the closest operating conditions $\hat{c}$ to c. Residuals (7) considering leak pressure measurements will be used in the leak localization, as will be explained in detail in the next section.

3. Leak Localization

The location of the leak on the WDN is typically divided into two steps: leak detection and leak localization [25]. The focus in this work is the leak localization assuming that the detection has already been effectuated. In addition, it is assumed that the leaks can only happen in the nodes of the network (as considered in [7,26], or [8]), making the number of nodes equal to the number of potential leaks. The nodes correspond to water users, pipe junctions, and other structures such as hydrants. However, if the number of nodes will not provide a representative discretization of the network, some artificial nodes could be considered.

In this Section, two leak localization methods will be proposed. The first one will only use available measurements, and its diagnosis will point to one of the inner pressure sensors installed in the WDN. Therefore, the detected leak should be in an area around this sensor (cluster). The second method will combine the information of the first method with the topological information: characteristics of the pipes and connections between the nodes of the WDN, in a likelihood index that will allow the leak localization at the node level.

3.1. Leak Localization at Cluster Level

As stated before, the proposed leak localization is applied after the leak detection. In addition to inlet pressure and flow sensors, it is assumed that n_s pressure sensors are installed at different inner nodes. Consider a leak l_j acting on the node j of the network, and the used measurements are assumed to be captured under a leaky situation. Additionally, admitting leak-free historical data of all the sensors are available. The residual pressure in internal nodes that contain a sensor, defined in (7), can be computed as:

$$r_{s_i} = \hat{p}_{s_i}(c) - p_{s_i}(c^{l_j}), \quad \forall i = 1, \ldots, n_s, \tag{8}$$

where $\hat{p}_{s_i}(c)$ is the pressure estimation considering boundary conditions c in a leak-free scenario. On the other hand, $p_{s_i}(c^{l_j})$ is the pressure value measured by the inner pressure sensor i under boundary conditions c^{l_j} (the same heads and inflows in inlets as in c but with a leak in node j).

Following the ideas in [18], positive residuals can be obtained from the following transformation:

$$\bar{r}_{s_i} = r_{s_i} - \min(r_{s_1}, \ldots, r_{s_{ns}}) \quad \forall i = 1, \ldots, n_s. \tag{9}$$

Then, as the leak localization can be achieved by determining the residual pressure component with maximum size (see [22,27]), leak localization can be formulated as:

$$\hat{\jmath} = \underset{i \in \{1,\ldots,n_s\}}{\arg\max} \{\bar{r}_{s_i}\}. \tag{10}$$

Notice that the result of the leak localization method (10) is one of the n_s pressure sensor locations.

Then, the leak localization results in $\hat{\jmath}$ point not only to sensor location s_j but also to the nodes that produce a higher incidence for this sensor than the other sensors (cluster j).

3.2. Leak Localization at Node Level

Considering the Hazen–Willians Equation (3) for every pipe (edge e_z) a resistance R_z can be defined:

$$R_z = \frac{10.7 \cdot L_z}{\rho_z^{1.852} \cdot D_z^{4.87}}. \tag{11}$$

Among the multiple pipe paths that can connect every pair of nodes ij, a path $\mathcal{P}_{ij}^{min}$ with a minimum total resistance R_{ij} can be computed by means of :

$$\mathcal{P}_{ij}^{min} = \underset{\mathcal{P}_{ij}^{(k)} \in \mathcal{P}_{ij}}{\arg\min} \sum_{e_z \in \mathcal{P}_{ij}^{(k)}} R_z, \tag{12}$$

where $\mathcal{P}_{ij} = \{\mathcal{P}_{ij}^{(r)}, \ldots, \mathcal{P}_{ij}^{(e)}\}$ denotes the set of paths connecting nodes i and j.

On the other hand, the minimum path from the n_I inlets to a node j , $\mathcal{I}_j^{min}$, can be obtained by applying the computation of the minimum paths from the n_I inlets to node j by means of (12) and determine which is the one with the minimum resistance among the n_I paths.

When a leak is produced in node j, $\mathcal{I}_j^{min}$ is the most probable path for the extra flow produced by the leak. So the effect of a leak in node j to sensor s_i depends on the intersection of the paths from inlets to node j and the node where the sensor is located s_i: $\mathcal{I}_j^{min}$ and $\mathcal{I}_{s_i}^{min}$. To quantify the degree of incidence of the leak to the sensor, an incidence factor g_{j,s_i} is defined as:

$$g_{j,s_i} = R_{j,s_i}^c \bar{g}_{j,s_i}, \tag{13}$$

where R_{j,s_i}^c is the resistance of the path defined by $\mathcal{I}_j^{min} \cap \mathcal{I}_{s_i}^{min}$, the superscript c refers to the common path between node and sensors, and $\bar{g}_{j,s_i}$ is a normalization factor that takes into account the inverse of the resistance from the node j to the different sensors:

$$\bar{g}_{j,s_i} = \begin{cases} \frac{\frac{1}{R_{j,s_i}}}{\sum_{l=1}^{n_s} \frac{1}{R_{j,s_i}}} & \text{if } j \neq s_i \\ 1 & \text{if } j = s_i. \end{cases}$$

The n_s incidence factors associated to a leak in node j, g_{j,s_i} $i = 1, \ldots, n_s$ can be normalized:

$$\lambda_{j,s_i} = \frac{g_{j,s_i}}{\sum_{l=1}^{n_s} g_{j,s_l}}, \tag{14}$$

where coefficient λ_{j,s_i} determines the relative incidence of a leak in node j to sensor s_i regarding all the n_s sensors and the need to fulfill:

$$\sum_{i=1}^{n_s} \lambda_{j,s_i} = 1 \quad \forall j = 1, \ldots, n - n_I. \tag{15}$$

For every node $j = 1, \ldots, n - n_I$, the most sensitive sensor to a leak in this node can be computed as:

$$\hat{\jmath} = \underset{i \in \{1,\ldots,n_s\}}{\arg\max} \{\lambda_{j,s_i}\}. \tag{16}$$

The n_s clusters used in the leak localization defined in (10) can be computed using the set of nodes that provide the same value of $\hat{\jmath}$. The following equation is the definition of the cluster associated with the sensed node l:

$$C_l = \{v_j \in V | \underset{i \in 1,\ldots,n_s}{\arg\max} \{\lambda_{j,s_i}\} = l\}, \tag{17}$$

where $l = 1, \ldots, n_s$. The topological information of λ_{j,s_i} and the measurement information of residuals $\bar{r}_{s_i}$ can be integrated in a parameter θ_j defined as:

$$\theta_j = \frac{1}{\bar{\theta}} \sum_{i=1}^{n_s} \lambda_{j,s_i} \bar{r}_{s_i} \tag{18}$$

where $\bar{\theta}$ is a normalization factor. Then, θ_j can be interpreted as a likelihood index, and the leak localization at cluster level defined in (10) can be formulated at node level as:

$$\hat{\jmath} = \underset{j \in \{1,\ldots,n-n_I\}}{\arg\max} \{\theta_j\}. \tag{19}$$

In order to improve the performance of the leak localization method, the information of the residuals at different time instants k can be taken into account applying the Bayes' rule as:

$$P_j(k) = \frac{P_j(k-1)\theta_j(k)}{\sum_{l=1}^{n-n_I} P_l(k-1)\theta_l(k)}, \tag{20}$$

where $P_j(k-1)$ is the prior probability whose initial value $P_j(k-1)$ has to be determined (for example $P_j(0) = 1/(n-n_I)$). Then, the leak node localization can be estimated by using posterior leak probabilities by:

$$\hat{\jmath}(k) = \underset{j \in \{1,\ldots,n-n_I\}}{\arg\max} \{P_j(k)\}. \tag{21}$$

4. Sensor Validation

When a leak is not detected by the leak detection method, anomalous values of pressure residuals $r_{s_i}(k)$ $i = 1,\ldots,n_s$ defined in (7) can be used to detect sensor faults. In the same operating conditions, the historical data of inner pressure sensors (leak-free data or data for a particular leak scenario) can be used first to calibrate a pressure estimation model as described in Section 2.2. Secondly, to determine residual bounds $\underline{\sigma_i}$ and $\bar{\sigma}_i$ that allows the implementation of pressure sensor fault detection through checking:

$$\begin{cases} r_{s_i}(k) \in [\underline{\sigma_i}, \bar{\sigma}_i] \Rightarrow \text{ No Fault } (\phi_i(k) = 0) \\ r_{s_i}(k) \notin [\underline{\sigma_i}, \bar{\sigma}_i] \Rightarrow \text{Fault in sensor } s_i \ (\phi_i(k) = 1). \end{cases} \tag{22}$$

The accuracy of this fault detection method depends on the length of residual bounds $\underline{\sigma_i}$ and $\bar{\sigma}_i$ and, therefore, on the accuracy of pressure estimation (6). In order to increase the accuracy of the fault detection method, spatial residuals [28] between pressure residuals (7) can be computed

$$Sr_{s_i,s_j}(k) = r_{s_i}(k) - r_{s_j}(k) \quad \forall i = 1,\ldots,n_s-1 \quad \text{and} \quad j = i+1,\ldots,n_s. \tag{23}$$

In the same way as the pressure residuals, spatial residual bounds $\underline{\varepsilon}_{i,j}$ and $\bar{\varepsilon}_{i,j}$ can be computed using leak-free data, and the fault detection can be implemented as follows:

$$\begin{cases} Sr_{s_i,s_j}(k) \in \left[\underline{\varepsilon}_{i,j}, \bar{\varepsilon}_{i,j}\right] \Rightarrow \text{No Fault}(\Phi_{i,j}(k) = 0) \\ Sr_{s_i,s_j}(k) \notin \left[\underline{\varepsilon}_{i,j}, \bar{\varepsilon}_{i,j}\right] \Rightarrow \text{Fault}(\Phi_{i,j}(k) = 1). \end{cases} \tag{24}$$

As model errors will affect in a similar way as close pressure sensors, it is expected that some spatial residual bounds will be smaller than pressure residual bounds. Therefore, fault detection defined by (24) will be more sensitive to pressure sensor faults than the one defined by (22). The accuracy of the sensor fault detection can be increased by means of average computing residuals in a time window leading to smaller residual bounds.

Once a residual has been violated, that is, at least one of the sensor faulty signals $\phi_i(k)$ $i = 1,\ldots,n_s$ or spatial faulty signals $\Phi_{i,j}(k)$ $\quad i = 1,\ldots,n_s-1 \quad$ and $\quad j = i+1,\ldots,n_s \quad$ is equal to one, the sensor fault isolation can be implemented in two stages as described in Algorithm 1:

Algorithm 1 Sensor validation search for sensor fault

Stage 1: In the case of the activation of one or more sensor faulty signals $\phi_i(k)$ $i = 1, \ldots, n_s$, as these signals are uniquely related to sensors s_i $i = 1, \ldots, n_s$, the isolation is trivial and faulty sensors must be discarded for future leak localization, and the number of available healthy sensors n_s should be updated.

Stage 2: Only considers Spatial faulty signals $\Phi_{i,j}(k)$ of the n_s non-faulty sensors from *Stage*1. As these fault signals are potentially affected by two possible sensor faults s_i and s_j, the fault isolation can be implemented iteratively by the following steps:

1: **for** $i \leftarrow 1, n_s - 1$ **do**

2: **for** $j \leftarrow i + 1, n_s$ **do**

3: **if** $\Phi_{i,j}(k) == 1$ **then**

4:

$$\hat{\imath} = \underset{i \in \{1,\ldots,n_s\}}{\arg\max} \{ \sum_{j=i+1}^{n_s-1} \Phi_{i,j}(k) + \sum_{j=1}^{i-1} \Phi_{j,i}(k) \}. \tag{25}$$

5: Discard sensor $s_{\hat{\imath}}$, eliminate faulty signals related to this sensors, update n_s.

6: **end if**

7: **end for**

8: **end for**

In the case that two or more sensors obtain the same cost function in (25) and less than the maximum possible value $n_s - 1$, the computation of (25) should be performed in a time window until new Spatial faulty signals are activated.

5. Case Study

5.1. Hanoi WDN

The Network used for the case study is a reduced city's network model from Hanoi's WDN (Vietnam). It is composed of one inlet (reservoir), 34 pipes, and 31 nodes, represented by Figure 1.

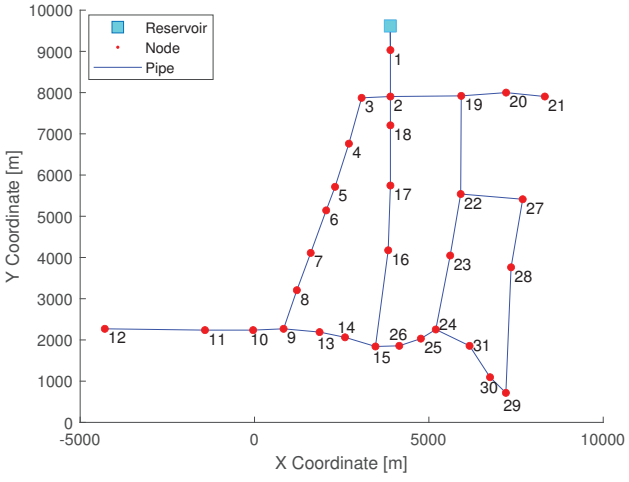

Figure 1. Simplified Hanoi topological WDN.

To analyze the performance of the proposed approach, data with different conditions have been generated artificially using the EPANET hydraulic simulator [29]. In order to consider realistic scenarios, some uncertainty has been added to the data [30]: the magnitude of the leak is random with a range of 25 to 75 [l/s], that is, between 1% and 2.5% of the average inlet flow of the WDN. Furthermore, white noise has been combined to emulate the noise present in real measurements, and uncertainty of 10% (uniform distribution) was added in the nominal demand value.

The daily water consumption pattern used for the calibration of Equation (6) is shown in Figure 2, having four days of operation.

The sample rate is 10 min, but average hourly measurements are calculated to reduce uncertainties on the diagnostic stage.

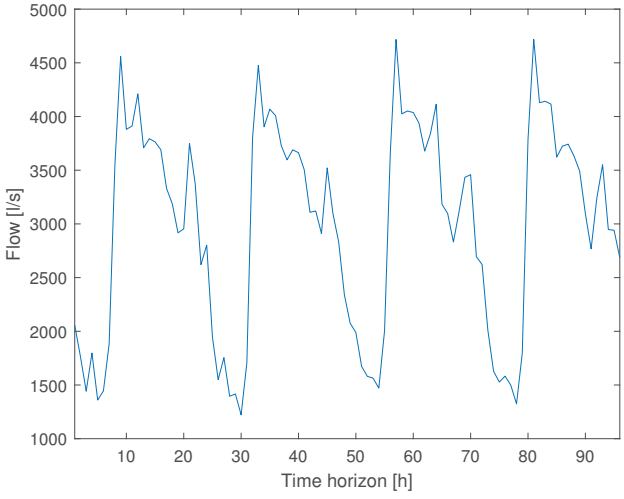

Figure 2. Flow consumption.

Results

The evaluation of the performance of the proposed leak localization method at node level defined in Equation (21) will be analyzed utilizing Average Topological Distance (ATD) [11]. The ATD represents the node's distance between the node predicted as leaking and the actual node with the leak. To calculate the ATD, it is first necessary to create a matrix containing the minimum topological distance (in nodes or meters), $A \in \mathbb{R}^{n-n_I \times n-n_I}$.

Finally, the confusion matrix $\Gamma_{i,j}(n - n_I \times n - n_I)$ defined in [18] and depicted in Table 1 is used to assess the performance of Equation (21). The rows of this matrix correspond to the leak scenario and the columns to where the leak is located ($\hat{l}$) by the leak localization method.

Table 1. Confusion matrix **Γ**.

	$\hat{l}_1$	$\cdots$	$\hat{l}_i$	$\cdots$	$\hat{l}_{n-n_I}$
l_1	$\Gamma_{1,1}$	$\cdots$	$\Gamma_{1,i}$	$\cdots$	$\Gamma_{1,n-n_I}$
$\vdots$	$\vdots$	$\vdots$	$\vdots$	$\vdots$	$\vdots$
l_i	$\Gamma_{i,1}$	$\cdots$	$\Gamma_{i,i}$	$\cdots$	$\Gamma_{i,n-n_I}$
$\vdots$	$\vdots$	$\vdots$	$\vdots$	$\vdots$	$\vdots$
l_{n-n_I}	$\Gamma_{n-n_I,1}$	$\cdots$	$\Gamma_{n-n_I,i}$	$\cdots$	$\Gamma_{n-n_I,n-n_I}$

Considering the confusion matrix Γ, the ATD can be computed as follows:

$$ATD = \frac{\sum_{i=1}^{n-n_I} \sum_{j=1}^{n-n_I} \Gamma_{i,j} A_{i,j}}{\sum_{i=1}^{n-n_I} \sum_{j=1}^{n-n_I} \Gamma_{i,j}}. \tag{26}$$

Four cases have been considered with different quantities of sensors in the network to analyze how this affects the final result. Table 2 presents the distribution of the selected nodes to contain a sensor. As seen in [31], the positioning of the sensors produces different results. As this work did not discuss the adequate sensors' arrangement, they were chosen to consider an improvement in the results regarding the number of sensors.

Table 2. Nodes with sensors.

Case	Nodes with Sensors
1	12, 17, 23, 29
2	6, 12, 17, 23, 29, 21
3	6, 12, 15, 17, 23, 21, 27, 30
4	6, 9, 12, 15, 17, 24, 21, 22, 28, 29, 31

Using the inlet flow data and non-leak historical pressure measurements of the selected sensors, the β_i and the α_i with $i = 1, \ldots, 31$ in (6) have been identified (notice that $n_I = 1$). With these parameters, the pressure estimations under a non-leak condition in the network can be calculated considering inlet measurements using Equation (6) and posteriorly applied to calculate the residuals (9) with measured pressures in leak scenarios. In addition, non-leak pressure measurements and estimations are used to generate fault-free pressure residuals $r_{s_i}(k)$ and bounds $\underline{\sigma_i}$, $\bar{\sigma}_i$ $i = 1, \ldots, n_s$, as well as spatial residuals $Sr_{s_i,s_j}(k)$ and bounds $\underline{\varepsilon}_{i,j}$, $\bar{\varepsilon}_{i,j}$ $\quad \forall i = 1, \ldots, n_s - 1 \quad$ and $\quad j = i + 1, \ldots, n_s$.

For every sensor configuration, normalized incidence factors (14) have been computed with topological information: node connections and pipe characteristics (length, diameter, and roughness). Figure 3 has the objective of comparing the information of the incidence of single leaks to pressure sensors obtained by a hydraulic model with the one obtained by means of topological information. The nodes selected to have sensors are the ones defined in the first case in Table 2. In particular, Figure 3c shows the clustering that groups the nodes that produce the highest effect in a specific pressure sensor. Nodes in yellow define the cluster of nodes where a leak produces a maximum pressure deviation from the non-leak scenario in the sensor installed in node 12, and the same is true for nodes in violet, red and green regarding pressure sensors in nodes 17, 23, and 29, respectively. Finally, nodes in black are nodes that produce a similar variation of pressure (difference of variation less than 0.1 [mwc]) in at least two different pressure sensors. In order to obtain this information, a hydraulic model to compute the difference of non-leak and leak pressures in all the nodes for the different leaks is required. On the other hand, Figure 3a shows the clustering that takes into account the shortest weighted pipe length (hydraulic distance), that is, the sum of $(L_z / D_z^{4.87})$ for all edge e_z in the path to the sensors, being the smallest one used to define the most resemblance to the sensor, used in Ref. [18]. Finally, the clustering depicted in Figure 3b is defined by Equation (17), which is based on the common resistance path explained in Section 3. These two last clusters that only require topological information could be used in the leak localization method at the cluster level defined in Equation (10). It is important to emphasize that the clustering based on the resistance common path, proposed in this paper and depicted in Figure 3b, resembles the clustering based on the actual leak effect in the network (given by the model) depicted in Figure 3c much more than the clustering based in the hydraulic distance depicted in Figure 3a. Therefore, the clustering proposed in this paper provides more accurate information for leak localization purposes than that based on the hydraulic distance. For

example, as shown in Figure 3c, when a leak is present in nodes 3, 4, 5, 6, 7, 8 or 9, the sensor most affected by the leak is the sensor in node 12. This information is the same as the one provided by the clustering depicted in Figure 3b and is computed only with topological information. However, using the clustering of Figure 3a based on the hydraulic distance between nodes and sensors, the closest sensor to these nodes is the sensor in node 17.

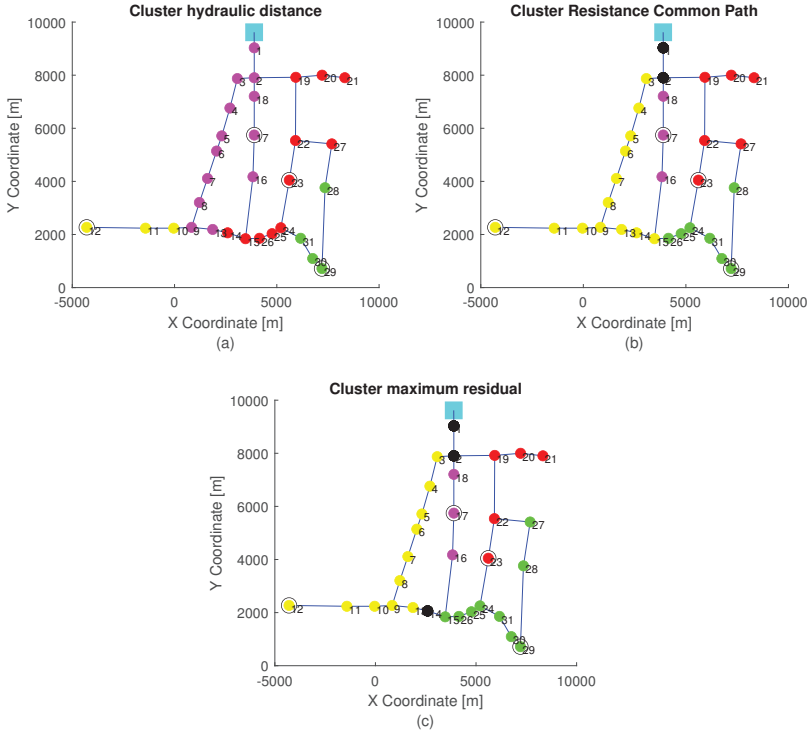

Figure 3. The n_s clustering generated with the aspects: (**a**) shortest weighted pipe length, (**b**) The resistance takes into account the common path R^c_{j,s_i}; (**c**) is the maximum residual. Nodes in yellow, violet, red and green define the cluster related to sensor installed in node 12, 17, 23, and 29, respectively.

Figure 4 shows the correlation analyses of the relative incidence index λ_{j,s_i} defined in Equation (14) for all the nodes $j = 1, \ldots, 31$ depicted in every subplot for every sensor s_i $i = 1, \ldots, 4$. As this index is normalized, its values are in the range [0,1). The nodes with the higher index (more brown color) are those that produce a higher effect in the pressure sensor s_i.

Figure 5a displays the evolution of the ATD (in nodes) obtained by the leak localization method based on the Kriging spatial interpolation methodology presented in [18] with the time horizon (in hours) used recursively by the Bayes' rule in (20). Four different sensor configurations are considered with 4, 6, 8, and 10 sensors placed optimally in order to maximize the performance of the leak localization proposed [18]. The performance can be compared with the one obtained by the new leak localization method proposed in this paper at node level defined in Equation (19) with the same dataset and the same sensor configurations as in [18], depicted in Figure 5b and with the sensor configurations shown in Table 2, depicted in Figure 5c.

Figure 5a shows that the leak detection performance of the Kriging method improves significantly from four to eight sensors and more moderately compared to ten sensors, still having a good result, even with noise data managing to reach an ATD equal to 2.5 node. When compared to the newly proposed leak localization method, as can be

seen in Figure 5b,c, the new leak localization method always outperforms the Krigring method, even in the case of using the sensor configurations proposed in [18] that were computed to optimize the performance of the Kriging method. Figure 5c shows that the sensor configurations proposed in [18] are not optimal for the proposed method but the performance can be improved by changing the sensor configurations, in this case manually.

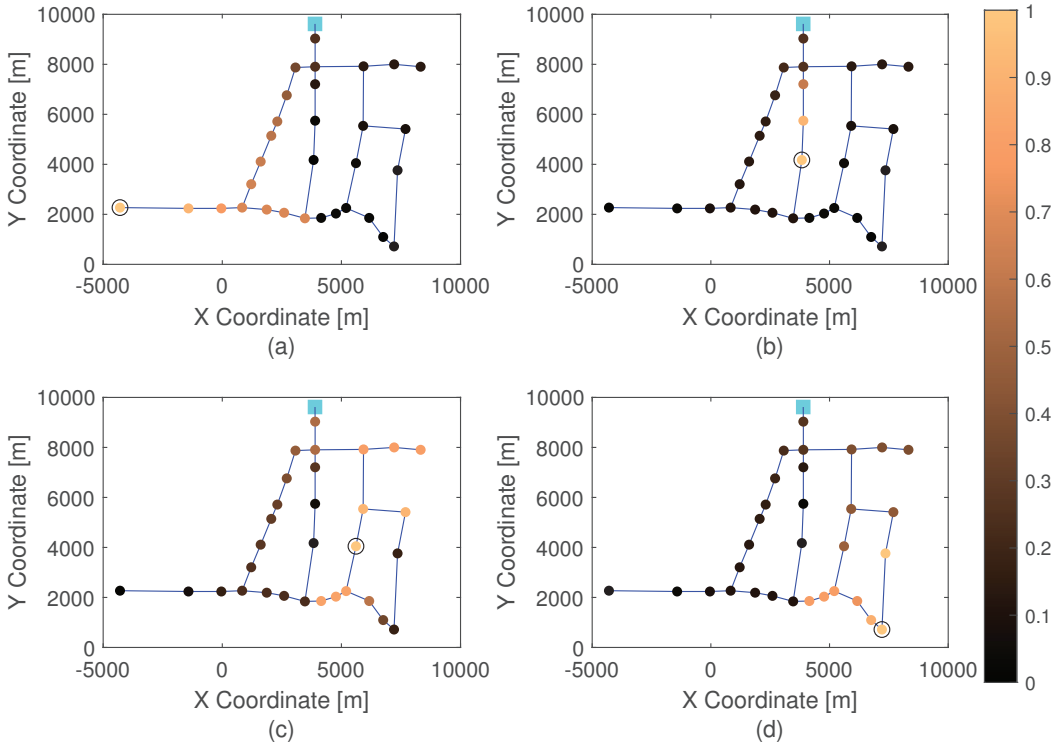

Figure 4. Relative incidence index λ_{j,s_i} for all the nodes ($j = 1, \ldots, 31$), corresponding to: (**a**) 1st sensor ($i = 1$), (**b**) 2nd senor ($i = 2$), (**c**) 3rd sensor ($i = 3$), and (**d**) 4th sensor ($i = 4$).

In order to illustrate the performance of the proposed sensor validation method, Case 1 (four sensors) will be considered. The four-sensor residuals computed by Equation (7) have been considered in a time window of 24 h using leak-free data leading to upper residual bounds equal to:

$$[\bar{\sigma}_1, \bar{\sigma}_2, \bar{\sigma}_3, \bar{\sigma}_4] = [0.11, 0.06, 0.09, 0.11]$$

and the lower residual bounds equal to:

$$[\underline{\sigma}_1, \underline{\sigma}_2, \underline{\sigma}_3, \underline{\sigma}_4] = [-0.14, -0.10, -0.10, -0.08].$$

In the same way, the six spatial residuals defined by (23) have been computed in the same conditions as sensor residuals leading to spatial residual bounds:

$$[\bar{\varepsilon}_{1,2}, \bar{\varepsilon}_{1,3}, \bar{\varepsilon}_{1,4}, \bar{\varepsilon}_{2,3}, \bar{\varepsilon}_{2,4}, \bar{\varepsilon}_{3,4}] = [0.06, 0.07, 0.08, 0.04, 0.05, 0.03]$$

and

$$[\underline{\varepsilon}_{1,2}, \underline{\varepsilon}_{1,3}, \underline{\varepsilon}_{1,4}, \underline{\varepsilon}_{2,3}, \underline{\varepsilon}_{2,4}, \underline{\varepsilon}_{3,4}] = [-0.04, -0.06, -0.08, -0.06, -0.09, -0.03].$$

Figures 6 and 7 depict the evolution of sensor and spatial residuals with their respective residual bounds in a fault scenario of sensor 1 that corresponds to the pressure sensor in node 12. The fault is a drift of 0.1 $[mcw]$ that starts on the 5th day. As shown in Figure 6, by applying (22) to sensor residuals it is impossible to detect the fault until the end of the day 9 (i.e., 4 days later) when residual sensor 1 violates the bounds. However, by applying (24) to spatial residuals it is possible to detect the fault in 10 h: Sr_{s_1,s_2} violates its bounds in 10 h, and Sr_{s_1,s_3}, Sr_{s_1,s_4} violate their bounds in 16 h and 22 h, respectively.

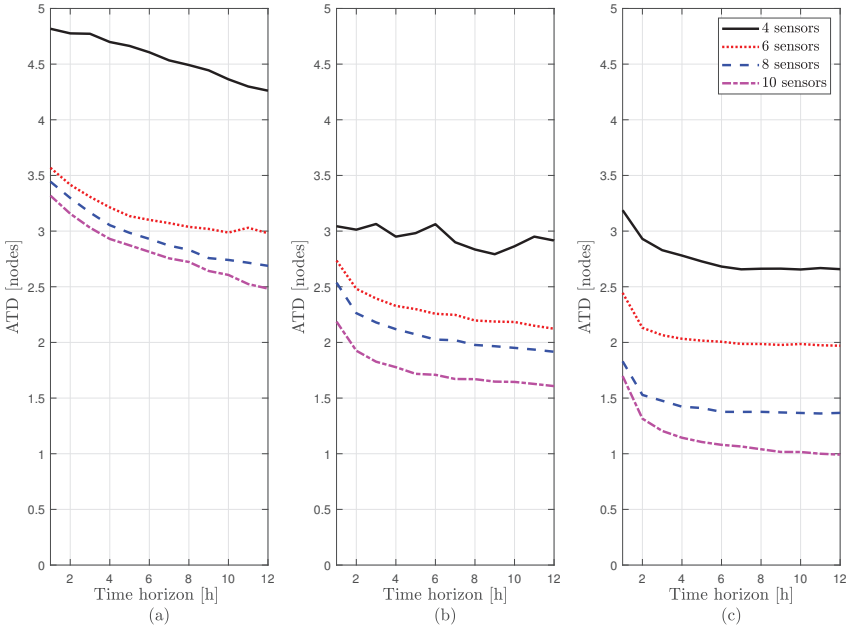

Figure 5. Evolution of the ATD between the methods: (**a**) using the Kriging interpolation method presented in [18], (**b**) using the new leak localization method with the same sensor configurations as in [18] and (**c**) using the new localization method with sensor configurations of Table 2.

5.2. Modena WDN

The second case study selected to test the performance is the reduced model of the real water distribution network of the Italian city Modena. This large-scale network is comprised of 268 junctions (nodes) connected through 317 pipes and served by four reservoirs. There are no pumps in the network since it is entirely gravity-fed [32,33].

The EPANET hydraulic simulator was used to generate artificial data to analyze the performance of the proposed method. The following simulation conditions were considered:

- The leak scenario consists of data samples collected every 10 min and filtered to hourly values to reduce the uncertainty in the data;
- The uncertainty of demand is considered by introducing the uncertainty of 10 [%] (normal distribution) of the nominal demand value. In addition, white noise is deemed to emulate the noise in the measurements;
- The leak size is randomly selected with a range of 3 to 6 [l/s], representing 1% to 2.5% of the network consumption.

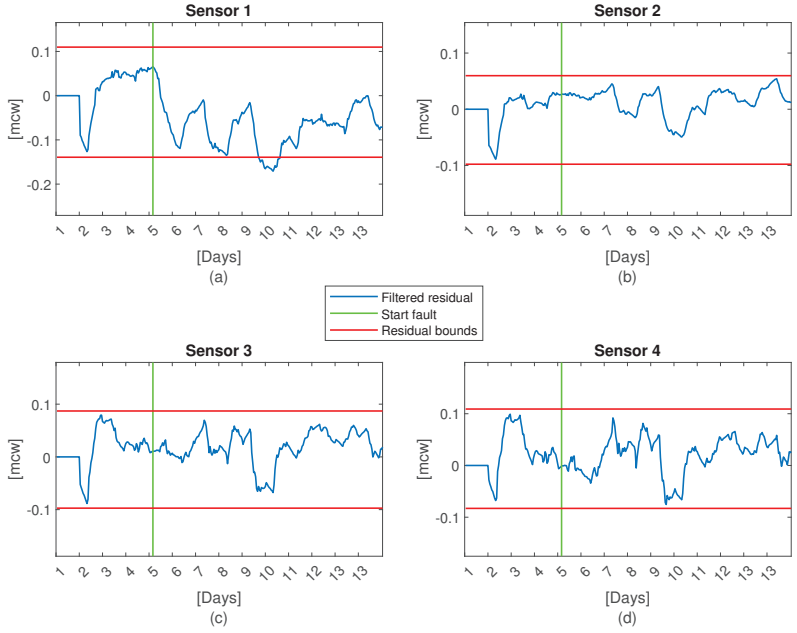

Figure 6. Graph of the filtered residual with a fault in sensor number 1 (**a**) 1st sensor, (**b**) 2nd senor, (**c**) 3rd sensor, and (**d**) 4th sensor.

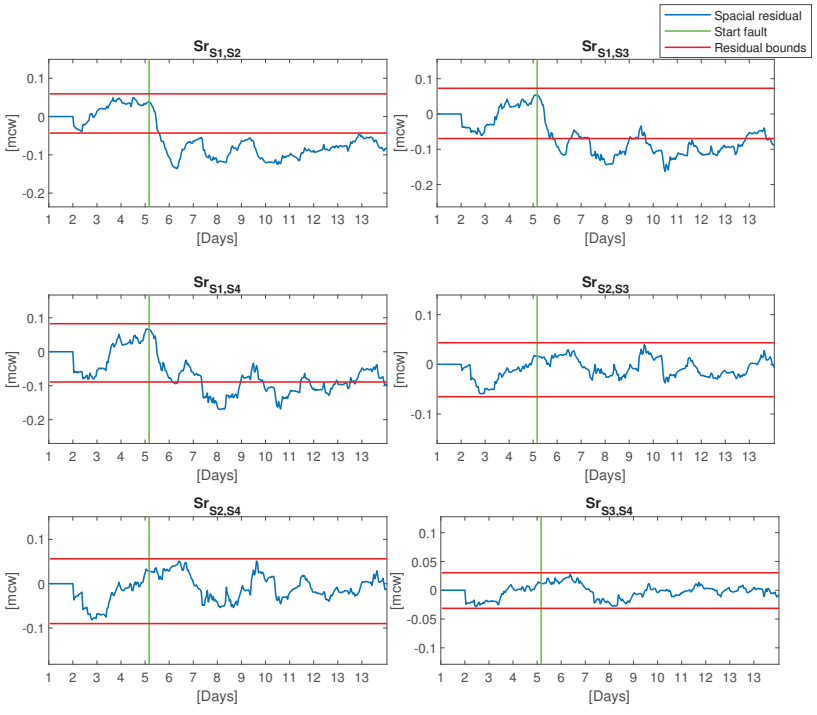

Figure 7. Graph of the spatial residual with a fault in sensor number 1.

The sensor bias, sensor drift, and abrupt sensor failure of sensor faults were proposed to analyze the sensor validation method. The sensor bias fault was simulated as a step change, and the drift fault was given as a time-varying ramp signal. In both cases, the fault magnitude was randomly chosen with a range of 0.1 to 0.2 [mwc]. The last fault was simulated by turning the sensor output to zero.

Results

As applied in the previous case study, the Average Topological Distance (ATD) was used to assess the performance of the proposed leak localization method at the node level defined in (19). Two scenarios have been considered with five and ten pressure sensors that are presented in Figure 8a,b respectively. As emphasized in the last section, performance in the leak localization task is highly dependent on the number of sensors installed in the network [34–36].

Figure 9 shows the result of ATD evolution as defined in (26) applied with Bayes' posterior time reasoning (20) to represent the leak location performance of the proposed method. This figure shows that the leak localization performance reached an ATD of 8 and 5.5 nodes with 5 and 10 inner pressure sensors installed in the network respectively. Considering that the proposed leak localization method only requires topological information and non-leak historical data in available measurements, the obtained performance is reasonably good.

On the other hand, a total of 6000 scenarios were simulated with 10 days each to evaluate the sensor validation method for the five sensor configurations depicted in Figure 8a. Thus, 1000 scenarios were generated for each sensor with sensor bias, sensor drift, and abrupt sensor failure applied randomly, and the remainder 1000 without faults.

To calculate the residual and spatial residuals bounds, a 6-month leak-free scenario was generated. The five sensor residuals computed by Equation (8) considering the time window of 24 h and increasing 24% observed bounds. Leading to upper residual bounds equal to:

$$[\bar{\sigma}_1, \bar{\sigma}_2, \bar{\sigma}_3, \bar{\sigma}_4, \bar{\sigma}_5] = [0.10, 0.06, 0.04, 0.01, 0.04]$$

and to lower residual bounds equal to:

$$[\underline{\sigma}_1, \underline{\sigma}_2, \underline{\sigma}_3, \underline{\sigma}_4, \underline{\sigma}_5] = [-0.08, -0.05, -0.03, -0.01, -0.06].$$

Following, the ten spatial residuals defined by (23) were computed in the same conditions as sensor residuals leading to spatial residual bounds:

$$\begin{aligned}[\bar{\varepsilon}_{1,2}, \quad \bar{\varepsilon}_{1,3}, \bar{\varepsilon}_{1,4}, \bar{\varepsilon}_{1,5}, \bar{\varepsilon}_{2,3}, \bar{\varepsilon}_{2,4}, \bar{\varepsilon}_{2,5}, \bar{\varepsilon}_{3,4}, \bar{\varepsilon}_{3,5}, \bar{\varepsilon}_{4,5}] = \\ [0.07, 0.08, 0.08, 0.10, 0.06, 0.05, 0.06, 0.03, 0.06, 0.05]\end{aligned}$$

and

$$\begin{aligned}[\underline{\varepsilon}_{1,2}, \quad \underline{\varepsilon}_{1,3}, \underline{\varepsilon}_{1,4}, \underline{\varepsilon}_{1,5}, \underline{\varepsilon}_{2,3}, \underline{\varepsilon}_{2,4}, \underline{\varepsilon}_{2,5}, \underline{\varepsilon}_{3,4}, \underline{\varepsilon}_{3,5}, \underline{\varepsilon}_{4,5}] = \\ [-0.07, -0.09, -0.08, -0.09, -0.05, -0.04, -0.06, -0.03, -0.04, -0.04].\end{aligned}$$

For this study, the evaluation metric applied was classification accuracy. To this purpose, the confusion matrix was used, which presents the classification accuracy and the misclassification error, and the horizontal axis of the confusion matrix describes the predicted labels of samples, while the longitudinal axis depicts the true labels of samples. The right side shows the percentages of correctly and incorrectly classified observations for each true class.

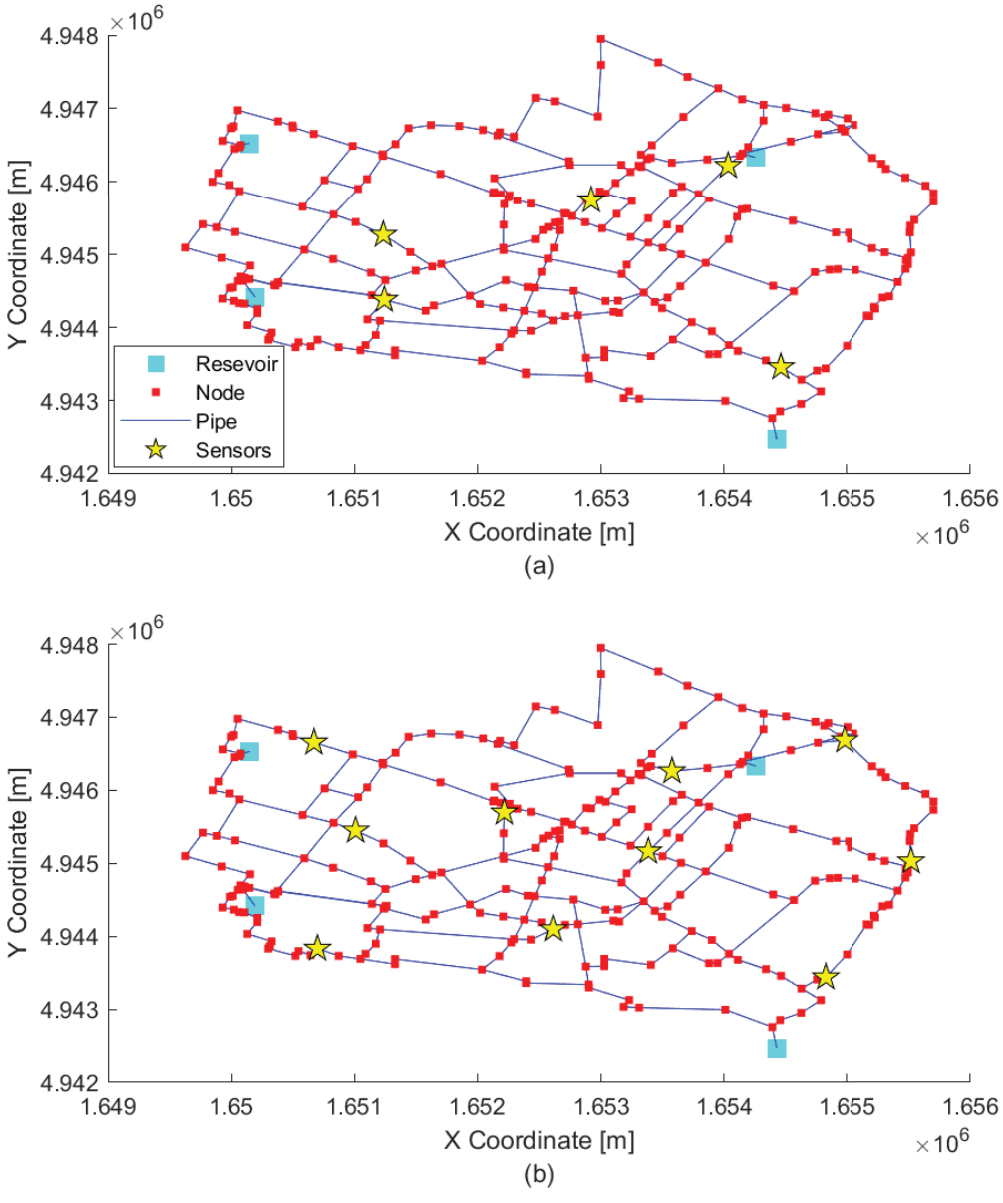

Figure 8. Configuration of pressure sensors in Modena WDN: (**a**) 5 sensors, (**b**) 10 sensors.

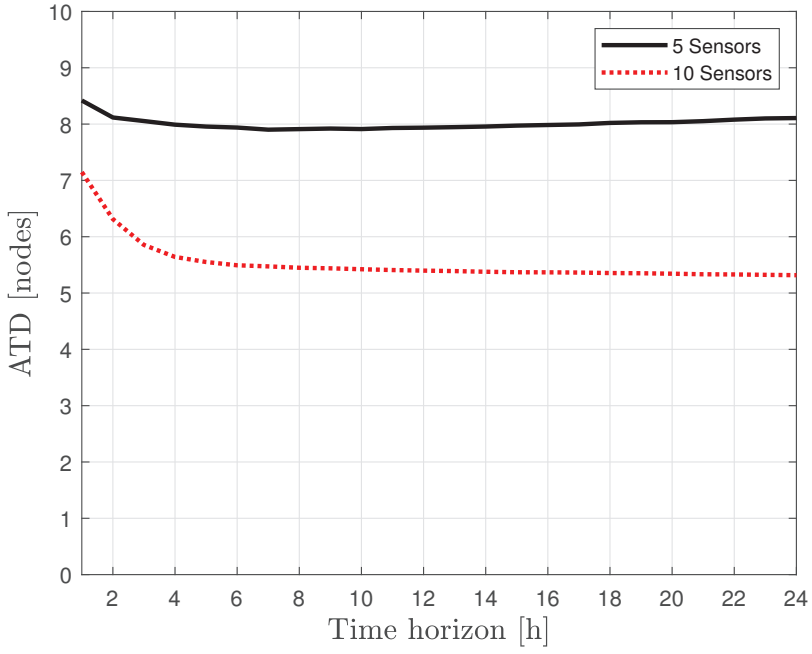

Figure 9. Evolution of the ATD.

Figure 10 illustrates the result for the confusion matrix for all scenarios generated, and depicts that the accuracy of detecting faults in the sensor is very high, where the lowest accuracy is presented in fault sensor number five with an accuracy of 95.4% and the highest in fault sensor number three with 100% accuracy. Regarding the accuracy of the scenario with no-fault, eight of the 1000 fault free scenarios presented one false alarm among the 240 samples of the scenario; therefore providing an average interval between false detections of 240,000/8 = 30,000 h.

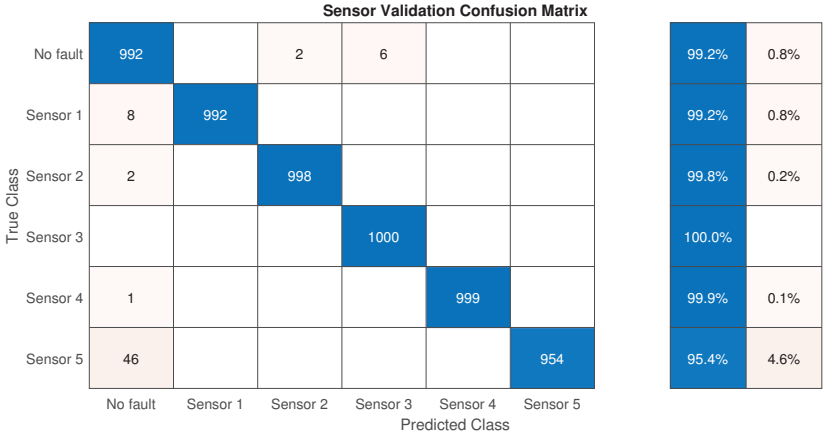

Figure 10. Confusion matrix for sensor validation method.

6. Conclusions

A new data-driven method for leak localization in WDN based on historical non-leak data and the topological information of the network is proposed. The proposed method is triggered when a leak is detected, and it is based on the evaluation of residuals generated by leak pressure measurements in some inner nodes and the estimation of leak-free pressures in these nodes utilizing a reduced-order model and historical data. Topological information is used to compute a new incidence factor that considers the most probable path of water from reservoirs to pressure sensors and potential leak nodes. The proposed incidence factor combined with residual information generates a likelihood index that allows leak localization at the node level. In addition, a sensor validation method based on the sensor pressure residuals, which is able to detect and isolate pressure sensor faults, is proposed.

The proposed method's general performance for leak location and sensor validation is evaluated in reduced models of the Hanoi and Modena water distribution networks. The results of the leak localization are compared to another technique published with satisfactory results. Future works can be developed to improve the leak localization and sensor validation performances, with a study of an algorithm to automatically determine the optimal sensors required to maximize the leak localization performance.

Author Contributions: Conceptualization, D.A., J.B., E.D. and L.R.; methodology, D.A., J.B., E.D. and L.R.; software, D.A.; validation, D.A. and J.B.; formal analysis, D.A., J.B., E.D. and L.R.; investigation, D.A., J.B., E.D. and L.R.; data curation, D.A.; writing—original draft preparation, D.A.; writing—review and editing, D.A., J.B., E.D. and L.R.; visualization, D.A. and J.B.; supervision, J.B., E.D. and L.R.; project administration, J.B., E.D. and L.R. All authors have read and agreed to the published version of the manuscript.

Funding: This work has been partially funded by SMART Project (ref.num. EFA153/16 Interreg Cooperation Program POCTEFA 2014-2020), L-BEST Project (PID2020-115905RB-C21) funded by MCIN/ AEI /10.13039/501100011033 and AGAUR ACCIO RIS3CAT UTILITIES 4.0–P1 ACTIV 4.0. ref.COMRDI-16-1-0054-03.

Institutional Review Board Statement: Not applicable.

Informed Consent Statement: Not applicable.

Data Availability Statement: The data can be found in https://github.com/adeboracris/Epanet_Leak_localization (accessed on 10 November 2021).

Conflicts of Interest: The authors declare no conflict of interest.

References

1. Puust, R.; Kapelan, Z.; Savic, D.; Koppel, T. A review of methods for leakage management in pipe networks. *Urban Water J.* **2010**, *7*, 25–45. [CrossRef]
2. Gosling, S.N.; Arnell, N.W. A global assessment of the impact of climate change on water scarcity. *Clim. Chang.* **2016**, *134*, 371–385. [CrossRef]
3. Liemberger, R.; Wyatt, A. Quantifying the global non-revenue water problem. *Water Supply* **2019**,*19*, 831–837. [CrossRef]
4. Muggleton, J.; Brennan, M.; Pinnington, R.; Gao, Y. A novel sensor for measuring the acoustic pressure in buried plastic water pipes. *J. Sound Vib.* **2006**, *295*, 1085–1098. [CrossRef]
5. Shimanskiy, S.; Iijima, T.; Naoi, Y. Development of microphone leak detection technology on Fugen NPP. *Prog. Nucl. Energy* **2003**, *43*, 357–364. [CrossRef]
6. Hunaidi, O.; Chu, W.; Wang, A.; Guan, W. Detecting leaks in plastic pipes. *J.-Am. Water Work. Assoc.* **2000**, *92*, 82–94. [CrossRef]
7. Pérez, R.; Puig, V.; Pascual, J.; Quevedo, J.; Landeros, E.; Peralta, A. Methodology for leakage isolation using pressure sensitivity analysis in water distribution networks. *Control Eng. Pract.* **2011**, *19*, 1157–1167. [CrossRef]
8. Casillas, M.V.; Garza-Castañón, L.E.; Puig, V.; Vargas-Martinez, A. Leak signature space: An original representation for robust leak location in water distribution networks. *Water* **2015**, *7*, 1129–1148. [CrossRef]
9. Pérez, R.; Cugueró, J.; Sanz, G.; Cugueró, M.A.; Blesa, J. Leak Monitoring. In *Real-Time Monitoring and Operational Control of Drinking-Water Systems*; Puig, V., Ocampo-Martínez, C., Pérez, R., Cembrano, G., Quevedo, J., Escobet, T., Eds.; Springer International Publishing: Cham, Switzerland, 2017; pp. 115–130.
10. Vrachimis, S.G.; Timotheou, S.; Eliades, D.G.; Polycarpou, M.M. Leakage detection and localization in water distribution systems: A model invalidation approach. *Control Eng. Pract.* **2021**, *110*, 104755. [CrossRef]

11. Soldevila, A.; Blesa, J.; Tornil-Sin, S.; Duviella, E.; Fernandez-Canti, R.M.; Puig, V. Leak localization in water distribution networks using a mixed model-based/data-driven approach. *Control Eng. Pract.* **2016**, *55*, 162 – 173. [CrossRef]
12. Quiñones-Grueiro, M.; Bernal-de Lázaro, J.M.; Verde, C.; Prieto-Moreno, A.; Llanes-Santiago, O. Comparison of Classifiers for Leak Location in Water Distribution Networks. *IFAC-PapersOnLine* **2018**, *51*, 407–413. [CrossRef]
13. Sun, C.; Parellada, B.; Puig, V.; Cembrano, G. Leak localization in water distribution networks using pressure and data-driven classifier approach. *Water* **2020**, *12*, 54. [CrossRef]
14. Santos-Ruiz, I.; Blesa, J.; Puig, V.; López-Estrada, F. Leak localization in water distribution networks using classifiers with cosenoidal features. *IFAC-PapersOnLine* **2020**, *53*, 16697–16702. [CrossRef]
15. Javadiha, M.; Blesa, J.; Soldevila, A.; Puig, V. Leak Localization in Water Distribution Networks using Deep Learning. In Proceedings of the 2019 6th International Conference on Control, Decision and Information Technologies (CoDIT), Paris, France, 23–26 April 2019; pp. 1426–1431. [CrossRef]
16. Pérez-Pérez, E.; López-Estrada, F.; Valencia-Palomo, G.; Torres, L.; Puig, V.; Mina-Antonio, J. Leak diagnosis in pipelines using a combined artificial neural network approach. *Control Eng. Pract.* **2021**, *107*, 104677. [CrossRef]
17. Wu, Y.; Liu, S. A review of data-driven approaches for burst detection in water distribution systems. *Urban Water J.* **2017**, *14*, 972–983. [CrossRef]
18. Soldevila, A.; Blesa, J.; Fernandez-Canti, R.M.; Tornil-Sin, S.; Puig, V. Data-driven approach for leak localization in water distribution networks using pressure sensors and spatial interpolation. *Water* **2019**, *11*, 1500. [CrossRef]
19. Soldevila, A.; Blesa, J.; Jensen, T.N.; Tornil-Sin, S.; Fernández-Cantí, R.M.; Puig, V. Leak Localization Method for Water-Distribution Networks Using a Data-Driven Model and Dempster–Shafer Reasoning. *IEEE Trans. Control Syst. Technol.* **2021**, *29*, 937–948. [CrossRef]
20. Deo, N. *Graph Theory with Applications to Engineering and Computer Science*, 1st ed.; Dover Books on Mathematics: Mineola, NY, USA, 2016; ISBN 13 978-0486807935.
21. Pérez, R.; Sanz, G. Modelling and simulation of drinking-water networks. In *Real-time Monitoring and Operational Control of Drinking-Water Systems*; Springer: Berlin/Heidelberg, Germany, 2017; pp. 37–52.
22. Jensen, T.N.; Kallesøe, C.S. Application of a novel leakage detection framework for municipal water supply on aau water supply lab. In Proceedings of the IEEE 2016 3rd Conference on Control and Fault-Tolerant Systems (SysTol), Barcelona, Spain, 7–9 September 2016; pp. 428–433.
23. Jense, T.N.; Kallesøe, C.S.; Bendtse, J.D.; Wisniewsk, R. Plug-and-play Commissionable Models for Water Networks with Multiple Inlets. In Proceedings of the IEEE 2018 European Control Conference (ECC), Limassol, Cyprus, 12–15 June 2018; pp. 1–6.
24. Simpkins, A. System identification: Theory for the user, (ljung, l.; 1999)[on the shelf]. *IEEE Robot. Autom. Mag.* **2012**, *19*, 95–96. [CrossRef]
25. Bort, C.G.; Righetti, M.; Bertola, P. Methodology for leakage isolation using pressure sensitivity and correlation analysis in water distribution systems. *Procedia Eng.* **2014**, *89*, 1561–1568. [CrossRef]
26. Soldevila, A.; Fernandez-Canti, R.M.; Blesa, J.; Tornil-Sin, S.; Puig, V. Leak localization in water distribution networks using Bayesian classifiers. *J. Process Control* **2017**, *55*, 1–9. [CrossRef]
27. Romano, M.; Woodward, K.; Kapelan, Z. Statistical Process Control Based System for Approximate Location of Pipe Bursts and Leaks in Water Distribution Systems. *Procedia Eng.* **2017**, *186*, 236–243. [CrossRef]
28. Blesa, J.; Jiménez, P.; Rotondo, D.; Nejjari, F.; Puig, V. An Interval NLPV Parity Equations Approach for Fault Detection and Isolation of a Wind Farm. *IEEE Trans. Ind. Electron.* **2015**, *62*, 3794–3805. [CrossRef]
29. Rossman, L.A. *EPANET 2 User's Manual*; U.S. EPA: Cincinnati, OH, USA, 2000.
30. Blesa, J.; Pérez, R. Modelling uncertainty for leak localization in Water Networks. *IFAC-PapersOnLine* **2018**, *51*, 730–735. [CrossRef]
31. Soldevila, A.; Blesa, J.; Tornil-Sin, S.; Fernandez-Canti, R.M.; Puig, V. Sensor placement for classifier-based leak localization in water distribution networks using hybrid feature selection. *Comput. Chem. Eng.* **2018**, *108*, 152–162. [CrossRef]
32. Wang, Q.; Guidolin, M.; Savic, D.; Kapelan, Z. Two-objective design of benchmark problems of a water distribution system via MOEAs: Towards the best-known approximation of the true Pareto front. *J. Water Resour. Plan. Manag.* **2015**, *141*, 04014060. [CrossRef]
33. Bragalli, C.; D'Ambrosio, C.; Lee, J.; Lodi, A.; Toth, P. *Water Network Design by MINLP*; Rep. No. RC24495; IBM Research: Yorktown Heights, NY, USA, 2008.
34. Quiñones-Grueiro, M.; Verde, C.; Llanes-Santiago, O. Multi-objective sensor placement for leakage detection and localization in water distribution networks. In Proceedings of the IEEE 2019 4th Conference on Control and Fault Tolerant Systems (SysTol), Casablanca, Morocco, 18–20 September 2019; pp. 129–134.
35. Ares-Milián, M.J.; Quiñones-Grueiro, M.; Verde, C.; Llanes-Santiago, O. A Leak Zone Location Approach in Water Distribution Networks Combining Data-Driven and Model-Based Methods. *Water* **2021**, *13*, 2924. [CrossRef]
36. Quiñones-Grueiro, M.; Milián, M.A.; Rivero, M.S.; Neto, A.J.S.; Llanes-Santiago, O. Robust leak localization in water distribution networks using computational intelligence. *Neurocomputing* **2021**, *438*, 195–208. [CrossRef]

sensors

MDPI

Article

Two Simultaneous Leak Diagnosis in Pipelines Based on Input–Output Numerical Differentiation

Adrián Navarro-Díaz [1], Jorge-Alejandro Delgado-Aguiñaga [2,*], Ofelia Begovich [3] and Gildas Besançon [4]

[1] Tecnologico de Monterrey, School of Engineering and Sciences, Av. General Ramón Corona 2514, Zapopan C.P. 45138, Mexico; adrian.navarro@tec.mx
[2] Centro de Investigación, Innovación y Desarrollo Tecnológico CIIDETEC-UVM, Universidad del Valle de México, Periférico Sur Manuel Gómez Morín 8077, Tlaquepaque C.P. 45601, Mexico
[3] CINVESTAV Guadalajara, Av. del Bosque 1145, Col. El Bajío, Zapopan C.P. 45019, Mexico; ofelia.begovich@cinvestav.mx
[4] GIPSA-Lab, Institute of Engineering, Université Grenoble Alpes, CNRS, Grenoble IPN, 38000 Grenoble, France; gildas.besancon@gipsa-lab.grenoble-inp.fr
* Correspondence: jorge.delgado@uvmnet.edu

Abstract: This paper addresses the two simultaneous leak diagnosis problem in pipelines based on a state vector reconstruction as a strategy to improve water shortages in large cities by only considering the availability of the flow rate and pressure head measurements at both ends of the pipeline. The proposed algorithm considers the parameters of both leaks as new state variables with constant dynamics, which results in an extended state representation. By applying a suitable persistent input, an invertible mapping in x can be obtained as a function of the input and output, including their time derivatives of the third-order. The state vector can then be reconstructed by means of an algebraic-like observer through the computation of time derivatives using a Numerical Differentiation with Annihilatorsconsidering its inherent noise rejection properties. Experimental results showed that leak parameters were reconstructed with accuracy using a test bed plant built at Cinvestav Guadalajara.

Keywords: fault diagnosis; pipelines; multiple leaks; numerical differentiation; experimental results

Citation: Navarro-Díaz, A.; Delgado-Aguiñaga, J.-A.; Begovich, O.; Besançon, G. Two Simultaneous Leak Diagnosis in Pipelines Based on Input–Output Numerical Differentiation. *Sensors* **2021**, *21*, 8035. https://doi.org/10.3390/s21238035

Academic Editors: Miquel À. Cugueró-Escofet and Vicenç Puig

Received: 3 November 2021
Accepted: 26 November 2021
Published: 1 December 2021

1. Introduction

In recent decades, climate change and the overuse of natural water resources have caused water scarcity in big cities. Furthermore, water distribution systems operators (WDSOs) are facing major water losses as high as 65% due to pipeline leaks caused by lack of maintenance, illegal intrusion, or accidents.

According to a study performed by the Organisation for Economic Co-operation (OECD), entitled Water Governance in Cities [1], aging water networks have a negative impact in terms of efficiency. One of the consequences is water loss from pipeline leaks. On average, water loss in the surveyed cities (in the referred report) was 21% in 2016. However, for Mexican cities, water loss was more than 40% (Chihuahua, Mexico City, San Luis Potosi) or even up to 65% (Tuxtla), see Figure 1.

On the other hand, to satisfy the current demand, government policies are focused on bringing more water from far away places instead of solving water losses due to leaks. This means that the amount of water lost is currently considered in the water budget. Interestingly, the amount of water needed to meet the demand in deficit is very similar to what is lost through leaks. In other words, it could be possible to satisfy the current water demand by minimizing the water losses due to leaks without the need for bringing more water from far away places.

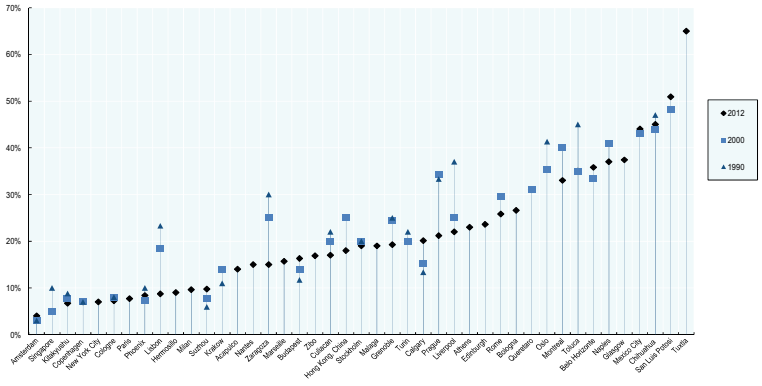

Figure 1. Proportion of water loss in surveyed cities (leakage rate).

The implementation of leak detection and isolation (*LDI*) systems has demonstrated a reduction in water losses in pipelines. *LDI* systems are algorithms that perform the following tasks: *detection* and *localization* of one or several leaks in a pipeline system. Thus, once a leak is identified, the repair technicians can fix the leak and avoid the water loss. Many works that address the *LDI* problem for one leak have been reported [2–6]. For instance, in [2], a leak isolation methodology using a fitting loss coefficient calibration is presented on the basis of two stages: in the first stage, the equivalent straight length (*ESL*) is fixed by a model-based observer designed as an extended Kalman filter (*EKF*); in the second stage, an algebraic observer is started with the *ESL* value fixed by the previous observer. Finally, the estimated leak position is recovered in original coordinates since the observer deals with *ESL* coordinates. Authors in [3] presented a methodology for leak detection and isolation in pipelines based on data fusion using two approaches: a steady-state estimation and an *EKF*. Authors concluded that the solution of the *LDI* problem improves significantly when a steady-state estimation is incorporated to the estimation provided by the *EKF*. In other words, the solution provided by the *EKF* is less accurate by itself. In [4], authors propose a bank of observers together with a Genetic Algorithm (*GA*), which is exploited to minimize the integration of the square observation error. The minimum integral observation error is reached in the observer where the estimated leak parameters match the real values. Experimental results evidence an accurate leak position estimation in a test bed pilot plant. In [5], a combined artificial neural network (*ANN*) for leak diagnosis in pipelines is presented. The *ANN* scheme estimates the location and friction factor based on measurement data. An average error of 0.629% was obtained for leak location in the experiments. More recently, in [6], a new approach for solving the *LDI* problem in pipelines is introduced on the basis of a Kalman filter for linear parameter varying (*LPV*) systems. The off-line computation of the filter gain allows the computational effort to be reduced and the authors claim that the *LPV* design outperforms the classical *EKF* design in terms of parameter-estimation accuracy.

On the other hand, the multi-leak case study has also been considered from two different perspectives: (i) for sequential leaks (non-concurrent case) [7–9] and (ii) for the simultaneous leak problem (concurrent case) [10].

In [7], a model adaptation strategy is proposed to isolate non-concurrent multiple leaks based on extended Kalman filters. Experimental results show the potential of this approach by allowing to monitor each new leak, no matter where it appears. Following this direction, a scheme is proposed in [8] for detecting and locating multiple sequential leaks based on a combination of an adaptive observer to identify the hydraulic gradient in real time and a leak location observer to estimate the leak position and its outflow. Experimental results of a pilot pipeline showed a satisfactory estimation in spite of operational changes and leaks. More recently, in [9], a pressure distribution analysis is proposed to diagnose

the location of leaks via an experimental study and computational fluid dynamics (*CFD*) simulation. Multiple flow rate testing is conducted to detect the locations of two leaks.

In the same way, a more complex case of the multi-leak problem is when two or more leaks occur at the same time, also known as the concurrent case. In [10], the orthogonal collocation method (*OCM*) is used to obtain an approximate solution of the water hammer equations (*WHE*). An estimator is then designed based on the spatially-discretized model to detect multiple leaks by identifying their positions and leak coefficients by applying a persistent input [11]. The results are presented via simulation.

Regarding the one leak problem, state observer-based techniques have been proposed and successfully evaluated since the observer convergence is guaranteed, even by applying constant inputs. This is because the structure of underlying state-space representation fulfills a uniform observability condition (which is independent of the input) [12]. Conversely, when two or more leaks occur simultaneously, such an observability condition is no longer satisfied and the observability depends on the input. Particularly in steady state, the output obtained by two or more leaks is equivalent to the one obtained by a single *virtual* leak, which is known as indistinguishability [11].

1.1. Problem Statement

- In a real pipeline system, several leaks can occur and usually they are not fixed as they appear; this means that the leak problem becomes a challenging multi-leak problem known as the simultaneous leak case. In addition, this situation worsens when water management companies frequently lack flow rate and pressure head records of the leak events.
- Therefore, a methodology to address the simultaneous leak case is proposed on the basis of an input–output numerical differentiation-based strategy by applying a persistent input in the sense of [11].

1.2. Methods

- By considering a state-space representation of a pipeline with two leaks in which the leak parameters are considered as new state variables with constant dynamics, the extended state can be reconstructed via its expression in terms of input, output, and the corresponding time derivatives.
- A persistent input is experimentally generated via a frequency variation of the pump driver that produces a sine-like pressure signal. This persistent input allows the parameters of each leak to be reconstructed. This approach could be extended to a more general case of simultaneous leaks if the applied input is regularly persistent, such that the observability condition is guaranteed [11]. However, this approach could also be limited to physical constraints since a persistent input might cause additional leaks due to the flow transient effect that it produces.

Hereinafter, the paper is organized as follows: In Section 2, a mathematical model is derived from the well-known water hammer equations and the two simultaneous leak problem is stated. State vector reconstruction based on injection of input–output time derivatives is presented in Section 3. Experimental results are presented in Section 4 by using databases from a pilot plant built at Cinvestav Guadalajara. Finally, several conclusions and future perspectives are given in Section 5.

2. Preliminaries

2.1. Pipeline Mathematical Model

2.1.1. Governing Equations

The transient fluid through a pipeline can be described by conservation mass and momentum equations known as water hammer equations, which are a couple of quasi-linear hyperbolic partial differential equations (*PDE*). Generally, *PDE* are derived considering the following assumptions: the fluid is slightly compressible, the duct wall is slightly

deformable, and the convective velocity changes are negligible. The cross section and the fluid density are assumed to be constant [13]:
Momentum Equation

$$\frac{\partial Q(z,t)}{\partial t} + gA\frac{\partial H(z,t)}{\partial z} + \mu Q(z,t)|Q(z,t)| = 0 \tag{1}$$

Continuity Equation

$$\frac{\partial H(z,t)}{\partial t} + \frac{b^2}{gA}\frac{\partial Q(z,t)}{\partial z} = 0 \tag{2}$$

Here, Q stands for the flow rate [m^3/s]; H is the pressure head [m]; z is the length coordinate [m]; t is the time coordinate [s]; g is the gravity acceleration [m/s^2]; A is the cross-section area [m^2]; b is the pressure wave speed in the fluid [m/s]; $\mu = \tau/2\phi A$, where ϕ is the inner diameter [m] and τ is the friction factor. The dynamics in Equations (1) and (2) are fully defined by related pairs of initial and boundary conditions.

2.1.2. Finite Difference Approximation

For the purpose of obtaining a finite dimensional model from (1) and (2), the partial differential equations are discretized with respect to the spatial variable z, as in [14,15], by using the following approximations:

$$\text{Section } i: \begin{cases} \frac{\partial H(z_i,t)}{\partial z} \backsimeq \frac{H_{i+1}-H_i}{\Delta z_i} & \forall i = 1, \cdots, n \\ \frac{\partial Q(z_{i-1},t)}{\partial z} \backsimeq \frac{Q_i - Q_{i-1}}{\Delta z_{i-1}} & \forall i = 2, \cdots, n \end{cases} \tag{3}$$

where index i stands for the variable discretized in (1) and (2) at section i. To solve the *LDI* problem for two simultaneous leaks, Equations (1) and (2) admit a simple spatial discretization as shown in Figure 2, where sections are defined according to the two leakage positions:

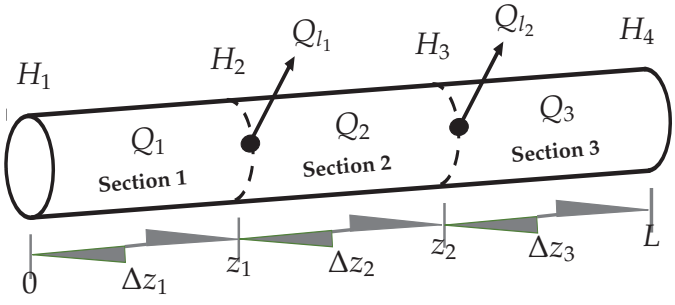

Figure 2. Discretization of the pipeline with two arbitrarily located leaks.

Here, $Q_{l_{1,2}}$ represent the leaking flows that can be modeled as:

$$Q_{l_{1,2}} = \lambda_{1,2}\sqrt{H_{2,3}} \tag{4}$$

where, $\lambda_{1,2}$ is a constant that depends on the orifice size and the discharge coefficient, and $H_{2,3}$ is the head pressure at the leak point.

Thus, assuming a lumped-parameter model for the flow equations and considering that the pressure head and flow rate measurements are available at both ends of the pipeline via sensors, a low order dynamical representation of the system with two leaks can be written using approximation (3) in Equations (1) and (2), as follows:

$$\begin{bmatrix} \dot{Q}_1 \\ \dot{H}_2 \\ \dot{Q}_2 \\ \dot{H}_3 \\ \dot{Q}_3 \end{bmatrix} = \begin{bmatrix} \frac{-gA}{\Delta z_1}(H_2 - H_1) - \frac{\tau}{2\phi A} Q_1 |Q_1| \\ \frac{-b_2^2}{gA\Delta z_1}(Q_2 - Q_1 + \lambda_1 \sqrt{H_2}) \\ \frac{-gA}{\Delta z_2}(H_3 - H_2) - \frac{\tau}{2\phi A} Q_2 |Q_2| \\ \frac{-b_2^2}{gA\Delta z_2}(Q_3 - Q_2 + \lambda_2 \sqrt{H_3}) \\ \frac{-gA}{\Delta z_3}(H_4 - H_3) - \frac{\tau}{2\phi A} Q_3 |Q_3| \end{bmatrix} \tag{5}$$

Notice that, due to mass conservation, $Q_{l_{1,2}}$ must satisfy the next relation:

$$Q_{l_{1,2}} = Q_{b_{1,2}} - Q_{a_{1,2}} \tag{6}$$

where $Q_{b_{1,2}}$ and $Q_{a_{1,2}}$ are the flows in an infinitesimal length before and after the leak, respectively.

2.1.3. Pipeline Equivalent Straight Length

It is worth pointing out that the mathematical model (5) assumes a straight pipe. This is not a loss of generality because even if the pipe is not straight, it is possible to obtain an equivalent straight length (*ESL*) of the pipe. The *ESL* is the straight length of a virtual pipe (with the same parameters as the original duct) that would give rise to the same pressure drop as the real pipeline. Such an equivalence is calculated by considering losses due to each "non-straight element" (i.e., fitting) in accordance with the Darcy–Weisbach formula [2,16,17]:

$$l_e = \frac{\phi}{\tau} K \tag{7}$$

where, l_e means the equivalent straight length of a specific fitting, K is the so-called loss coefficient parameter, which is normally provided by the pipe manufacturer, and τ is the friction coefficient. Thus, the total ESL of the pipe, L_e, can be calculated as follows:

$$L_e = L_r + \frac{\phi}{\tau} \sum_{i=0}^{n_f} K_i \tag{8}$$

where L_r stands for the sum of all pipeline straight length elements, K_i is the fitting loss coefficient for the i-th fitting, and n_f the number of the pipeline fittings.

2.1.4. Friction Model

The friction factor (τ in Equation (1)) represents the loss of pressure of a fluid due to the interactions between the fluid and the internal surface roughness of the pipe. Thus, such a friction factor is a function of the Reynolds number, Re, and the pipe's roughness, ϵ [18,19].

In many practical cases, τ is deemed to be a constant value, which is commonly taken from the Moody chart; nevertheless, in pipes with a relative roughness usually less than 1×10^{-3} m, the zone where the friction factor is almost constant (i.e., the complete turbulence zone), is difficult to reach. Consequently, when the *LDI* scheme is applied to a plastic pipe, it is preferable to obtain a more accurate friction value by using a formula or an algorithm to estimate such value. In this work, the authors propose the use of the well know Swamee–Jain equation to directly calculate the coefficient of friction:

$$\tau_i(Q_i) = \frac{0.25}{\left[\log_{10}\left(\frac{\epsilon}{3.7\phi} + \frac{5.74}{\mathrm{Re}_i^{0.9}}\right)\right]^2} \tag{9}$$

where subscript i denotes the section number of the pipeline (see Figure 2). The Reynolds number is, in turn, function of the flow rate, Q_i, as follows:

$$\mathrm{Re}_i = \frac{Q_i \phi}{\nu A} \tag{10}$$

where, ν is the kinematic viscosity of the water. Notice that, due to leak occurrence, the flow rate is different in each pipeline section (see Figure 2), causing a significant deviation of the friction factor value (since the working plastic pipe area is commonly in the transition zone). Therefore, it is important to introduce Equations (9) and (10) in the mathematical model to calculate, at any sampling time, the friction coefficient due to the flow variations in each i-th section.

2.2. Two Simultaneous Leak Problem Statement

In this work, the two simultaneous leak case is considered, i.e., a couple of leaks can appear in a pipeline at locations: $z_1 \in (0, L)$ and $z_2 \in (0, L)$, with $z_2 > z_1$. Thus, the problem is reduced to the size estimation of the pipe sections: Δz_1 ($\Delta z_1 = z_1$) and Δz_2 ($\Delta z_2 = z_2 - z_1$), see Figure 2.

Now, Equation (5) can be written in compact form as follows:

$$\begin{array}{rcl} \dot{\zeta} & = & \xi(\zeta) + \rho(\zeta)\gamma \\ \Psi & = & \vartheta(\zeta) \end{array} \tag{11}$$

where $\zeta = [\zeta_1\ \zeta_2\ \zeta_3\ \zeta_4\ \zeta_5]^T = [Q_1\ H_2\ Q_2\ H_3\ Q_3]^T \in \mathbb{R}^5$ is the state vector, $\gamma = [H_{in}\ H_{out}]^T \in \mathbb{R}^2$ is the input vector, and $\Psi = [Q_{in}\ Q_{out}]^T \in \mathbb{R}^2$ is the output vector for some functions ξ, ρ, and ϑ.

The leak diagnosis problem for two simultaneous leaks appearing in a pipeline can then amount to the estimation of parameters Δz_1, Δz_2, λ_1, and λ_2 in (5). Let us consider those parameters as new state variables with constant dynamics [11], that is: if $\theta = [z_1\ z_2\ \lambda_1\ \lambda_2]^T$ then $\dot{\theta} = 0$. This results in an extended state: $x = [\zeta\ \theta]^T = [Q_1\ H_2\ Q_2\ H_3\ Q_3\ \Delta z_1\ \Delta z_2\ \lambda_1\ \lambda_2]^T =: [x_1\ x_2\ x_3\ x_4\ x_5\ x_6\ x_7\ x_8\ x_9]^T \in \mathbb{R}^9$. Then, considering an unidirectional flow given by $Q_i|Q_i| = Q_i^2$, the extended state representation of (11) can take a form as follows:

$$\begin{array}{rcl} \dot{x} & = & f(x,u) \\ y & = & h(x) \end{array} \tag{12}$$

where $u \doteq [H_1\ H_4]^T \doteq [u_1\ u_2]^T$, and f, g are differentiable vector fields with the following structure:

$$f(x,u) = \begin{bmatrix} -\frac{gA}{x_6}(x_2 - u_1) - \mu_1(x_1)x_1^2 \\ -\frac{b^2}{Agx_6}(x_3 - x_1 + x_7\sqrt{x_2}) \\ -\frac{gA}{x_8}(x_4 - x_2) - \mu_2(x_3)x_3^2 \\ -\frac{b^2}{Agx_8}(x_5 - x_3 + x_9\sqrt{x_4}) \\ -\frac{gA}{L - x_6 - x_8}(u_2 - x_4) - \mu_3(x_5)x_5^2 \\ \mathbb{O}^{4\times 1} \end{bmatrix} \tag{13}$$

$$h(x) = \begin{bmatrix} y_1(x) \\ y_2(x) \end{bmatrix} = \begin{bmatrix} Q_1 \\ Q_3 \end{bmatrix} = \begin{bmatrix} x_1 \\ x_5 \end{bmatrix}$$

where $\mathbb{O}^{4\times 1}$ is the 4×1 zero matrix, $\mu_i = \frac{\tau_i}{2\phi A}$ is computed as in Equation (9), and $\tau_{1,2,3}$ are functions of x_1, x_3, and x_5, respectively.

3. State Vector Reconstruction Based on Input–Output Numerical Differentiation

3.1. Observability Discussion

For the one leak case, the so-called observability rank condition is satisfied, and such a property does not depend on the inputs [12]. However, in the case of two simultaneous leaks (or even more), this is no longer true, since the states are not distinguishable by applying constant inputs, and thus a persistent input is required [11].

In fact, to reconstruct the actual state vector x of (12), one can compute time derivatives of the output as functions of state variables as well as input and its time derivatives (using Equation (13)), such that an invertible map with respect to the full state vector x is obtained by applying an appropriate input. More precisely, by considering the two simultaneous leak case described by (12), we have two input variables and two output variables, from which input–output time derivative vectors can be generally defined up to orders p, p' for the input and q, q' for the output, as:

$$U_{(p,p')}(t) := \left[u_1\ \dot{u}_1\ \cdots\ u_1^{(p)}\ u_2\ \dot{u}_2\ \cdots\ u_2^{(p')}\right]^T \tag{14}$$

and

$$Y_{(q,q')}(t) := \left[y_1\ \dot{y}_1\ \cdots\ y_1^{(q)}\ y_2\ \dot{y}_2\ \cdots\ y_2^{(q')}\right]^T \tag{15}$$

Clearly, from (13), the output time derivatives depend on the state and input time derivatives, so that we can get:

$$Y_{(q,q')}(t) = \Gamma\left(x, U_{(p,p')}\right) \tag{16}$$

for some p, p', given q, q'.

On this basis, observability somehow means that this relationship is invertible and that it is possible to find elements among the components of Γ defining an invertible map with respect to x [20,21]. Specifically, if such an inverted map exists, and the input–output and the corresponding time derivatives are known, then, it is possible to compute each independent state in (16) as follows:

$$x = \Gamma^{-1}\left(U_{(p,p')}, Y_{(q,q')}\right) \tag{17}$$

Notice that, in general, it can be of interest to avoid or limit time derivatives of the input, but assuming that they are available or can be estimated in the same way as time derivatives of y is enough for our present application.

It should be noted that for this LDI problem, it is even enough to obtain an expression by only relating the input, output, and their time derivatives with leak parameters. We will propose this in Section 3.3, with a similar procedure as *elimination* (which, conversely to realization, consists of deriving an externally equivalent representation not containing the state [22]). We will even see how to recover the full state vector. However, let us first discuss the way to obtain input–output time derivatives.

3.2. Numerical Differentiation with Annihilators

The *LDI* scheme proposed in this work is based on Equation (17), that is, the injection of the inputs, outputs, and their time derivatives. Although there are multiple algorithms to numerically compute a time derivative, here we use a numerical differentiation with annihilators [23] due to its inherent noise rejection properties. Hereinafter, a brief explanation of such an algorithm is given, which is proposed for the first time in this paper, and it is described by Equation (25).

Let $\gamma^m(t)$ denote the m-th order derivative of a smooth signal $\gamma(t)$ defined on an interval $\mathcal{I} \subset \mathbb{R}^+$. The signal $\gamma(t)$ could represent a measurement variable corrupted by some noise, whose derivatives are not directly available.

Ignoring the noise for a moment, let $\gamma(t)$ be an analytical function on $\mathcal{I}$. So, without any loss of generality, it is possible to consider the truncated Taylor expansion at $t = 0$:

$$\gamma(t) = \sum_{i=0}^{m} a_i \frac{t^i}{i!} + \mathcal{O}(t^m) \tag{18}$$

where $a_i = \frac{d^i\gamma(t)}{dt^i}\Big|_{t=0}$. This implies that $\gamma(t)$ can be approximated by the polynomial $p_m(t) = \sum_{i=0}^{m} a_i \frac{t^i}{i!}$.

In this way, the i-th order time derivative estimation of $\gamma(t)$ can be tackled as a parameter estimation problem for $p_m(t)$. Using the method described in [23], it is possible to calculate each a_i $(i = 0, \ldots, m)$ independently, reducing in this manner the sensitivity to noise and numerical computation errors which often appear in simultaneous estimation methods. Moreover, the independent calculation allows the use of higher order polynomials without the calculation of all their coefficients. The algorithm is described as follows (a complete explanation is given in [23]):

- Let $p_m(t)$ be the m-th order polynomial approximation of $\gamma(t)$,

$$p_m = \frac{a_0}{0!} + \frac{a_1}{1!}t + \frac{a_2}{2!}t^2 + \ldots + \frac{a_m}{m!}t^m \tag{19}$$

- Transforming Equation (19) into Laplace domain yields:

$$P_m = \frac{a_0}{s} + \frac{a_1}{s^2} + \frac{a_2}{s^3}t^2 + \ldots + \frac{a_m}{s^{m+1}} \tag{20}$$

- In order to calculate the i-th time derivative approximation, a_i, it is necessary to first annihilate every a_x $(x > i)$ in (20), using the next operator:

$$\left[\prod_{l=0}^{m-i} \frac{d}{ds}\right] \cdot s^{m+1} \tag{21}$$

- Then, to annihilate every a_x $(x < i)$, the following operator is subsequently applied to Equation (20):

$$\left[\prod_{h=0}^{i} \frac{d}{ds}\right] \cdot s^{-1} \tag{22}$$

- Finally, the resulting equation (after applying Equations (20)–(22)) is:

$$\begin{aligned} &(-1)^i(m-i)!i!a_i s^{-(i+1)} = \\ &\sum_{h=0}^{i}\sum_{l=0}^{m-1+h} (-1)^{i-h}\binom{i}{h}\binom{m-i+h}{l}\frac{(i-h)!(m+1)!}{(i+1-h+l)!}s^l\frac{d^l P_m(s)}{ds^l} \end{aligned} \tag{23}$$

- Now, multiplying both sides of the above equation by $s^{-(m+1)}$ yields a polynomial taking the following form:

$$\frac{c_m}{s^{i+m+2}}a_i = \frac{1}{s}\frac{d^m P_m(s)}{ds^m} + \frac{c_{m-1}}{s^2}\frac{d^{m-1}P_m(s)}{ds^{m-1}} + \ldots + \frac{c_0}{s^{m+1}}P_m(s) \tag{24}$$

- Using the Cauchy rule for iterated integrals, the time domain expression for a_i in Equation (24) yields:

$$a_i = \frac{(m+i+1)!}{c_m T^{m+i+1}}\int_0^T \left[t^m + \frac{c_{m-1}}{1!}(T-t)t^{m-1} + \ldots + \frac{c_0}{m!}(T-t)^m\right]p(t)\cdot dt \tag{25}$$

It should be noted that each constant c_j, $j = \{0, 1, \ldots, m\}$, is obtained from Equation (23), and T represents a moving window of length T for the integrals. A short time window is sufficient to obtain accurate estimations. In addition, the iterated integrals work as low pass filters that provide a smoother form of highly fluctuating noises. Therefore, no previous knowledge on the statistical properties of the noise is required to filter it out.

3.3. Extended State Vector Reconstruction

The purpose of this section is to provide a synthesis of the proposed *LDI* scheme. In this sense, the method is based on the study of the structure of the input–output differential equation; thus, the problem is solved by exploiting the observability property of the system (13). First, a set of equations describing each state just as a function of the inputs, outputs, and the corresponding time derivatives is derived. Then, taking advantage of the filtering characteristic of the numerical differentiation exposed in Section 3.2, the input–output time derivatives are computed. Thus, the leak positions and magnitudes can be calculated by a pair of algebraic equations. In the next step, the algorithm used to derive this set of equations is described.

It is easy to check that the observability rank condition for the system (12) is satisfied (for the finite number of input–output time derivatives), only by applying a persistent input. More precisely, it is also easy to see that for an input of the form $A_p \sin(\omega t)$. This wave form is easy to achieve by a variable frequency drive, a commonly installed device in a pumping station.

The rank condition of (12) is fulfilled with $p = 3$, $p' = 2$, $q = 4$, and $q' = 3$ for Equations (14) and (15). Thus, the output derivatives as well as the inverse mapping can be computed as follows (perhaps the major difficulty of the algorithm is to obtain the inverse mapping due to the complexity of the resulting equation):

First, by construction of Equation (13), the state variables x_1 and x_5 are taken directly from the measurements:

$$x_1 = y_1 \tag{26}$$

$$x_5 = y_2 \tag{27}$$

Now, the following step is to take the time derivatives of Equations (26) and (27), by using (13) and replacing x_1, x_5 by outputs according to (26) and (27) solving the resulting equation for x_2 and x_4, respectively, yields expressions without x_1 and x_5:

$$x_2 = \Phi_1(x_6, u_1, y_1, \dot{y}_1) \tag{28}$$

$$x_4 = \Phi_2(x_6, x_8, u_2, y_2, \dot{y}_2) \tag{29}$$

In the same way, the third step is to compute the derivative of Equation (28), substitute x_1, x_5, x_2, and x_4 according to (26), (27), (28), and (29), respectively. Solving this equation for x_3, yields an expression without x_1, x_5, x_2, x_4:

$$x_3 = \Phi_3(x_6, x_7, u_1, \dot{u}_1, y_1, \ldots, y_1^{(2)}) \tag{30}$$

Following the same steps, now for (29) and (30), it is possible to find an expression for x_7 and x_9 free of x_1, x_2, x_3, x_4, and x_5:

$$x_7 = \Phi_4(x_6, x_8, u_1, \ldots, u_1^{(2)}, u_2, y_1, \ldots, y_1^{(3)}, y_2, \dot{y}_2,) \tag{31}$$

$$x_9 = \Phi_5(x_6, x_8, u_1, \ldots, u_1^{(2)}, u_2, \dot{u}_2, y_1, \ldots, y_1^{(3)}, y_2, \ldots, y_2^{(2)}) \tag{32}$$

The final step is to apply the same methodology for Equations (31) and (32), but now for solving for the states x_6 and x_8. In this way, it is feasible to obtain an expression of x_6 and x_8 just as a function depending on the input and output, and their time derivatives:

$$x_6 = \Phi_6(u_1, \ldots, u_1^{(3)}, u_2, \dot{u}_2, y_1, \ldots, y_1^{(4)}, y_2, \ldots, y_2^{(3)}) \tag{33}$$

$$x_8 = \Phi_7(u_1, \ldots, u_1^{(3)}, u_2, .., u_2^{(2)}, y_1, \ldots, y_1^{(4)}, y_2 \ldots, y_2^{(3)}) \tag{34}$$

At this point, we are able to recover the whole state with the acknowledgement of the input and output time derivatives calculated through Equation (25); this is achieved by first obtaining x_6 and x_8 (leak positions) from Equations (33) and (34). Once x_6 and x_8 are

obtained, leak magnitudes, x_7 and x_9, can be computed by using (31) and (32). The rest of the state can then be recovered going backwards through Equations (30)–(28) .

4. Experimental Results

In this section, experimental results are presented to evaluate the proposed *LDI* methodology. The experiments are performed using several databases from the pilot plant located at Cinvestav Guadalajara. A couple of different two simultaneous leak scenarios were emulated by opening different electrovalves located along the pilot plant. A general description of the pipeline prototype is presented below with a detailed description of each experiment.

4.1. Pilot Pipeline Description

The layout of the pilot pressurized water pipe of Cinvestav Guadalajara, which is 68.2 [m] long (between sensors) with an internal diameter of 6.271×10^{-2} [m], thickness 1.27×10^{-2} [m], friction coefficient 1.66×10^{-2}, pressure wave speed 358 [m/s], and gravity acceleration 9.81 [m/s^2], is shown in Figure 3. The line is instrumented with two water-flow (FT) and pressure-head (PT) sensors at the inlet and outlet of the pipe. To emulate the leak, three control valves at position 16.8, 33.3, and 49.8 [m] are installed together with a electronic-based actuator to practically set any opening of the valve.

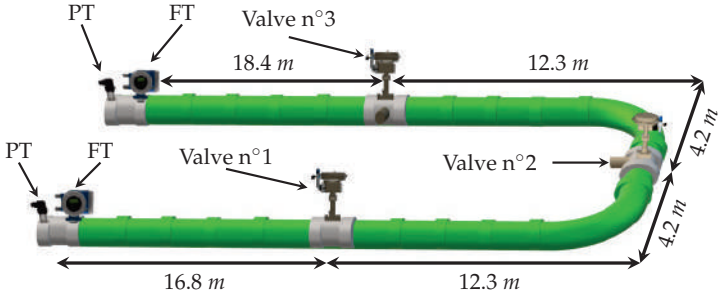

Figure 3. Schematic diagram of the pipeline's prototype.

The prototype is manufactured with a plastic material known as polypropylene copolymer random, for which technical characteristics can be found in [24]. It is integrated with a store tank of 7.5×10^{-1} [m^3], a hydraulic pump of 5 HP, and a variable-frequency driver (*VFD*) which controls the pressure in the system through the rotational speed of the pump motor (more details about the pipeline prototype can be found in [25]).

To ensure the application of a persistent input, experiments with operation point variations are carried out by the pump variation via the *VFD* (specifically, a change in the form of $A_p \sin(\omega t)$, where ω stands for the angular frequency induced via the *VFD*). Table 1 summarizes the pipeline's main parameters.

Table 1. Pipeline's main parameters.

Parameter	Symbol	Value	Units
Pipeline length	L_r	68.2	[m]
Upstream to valve $n^\circ 1$	z_1	16.8	[m]
Upstream to valve $n^\circ 2$	z_2	33.3	[m]
Upstream to valve $n^\circ 3$	z_3	49.8	[m]
Internal diameter	ϕ	6.271×10^{-2}	[m]
Pipe roughness	ϵ	7×10^{-6}	[m]
Friction factor	τ	1.66×10^{-2}	[dimensionless]
Pressure wave speed	b	358	[m/s]
Gravity acceleration	g	9.8	[m/s^2]

4.2. LDI Results

Hereinafter, two off-line examples of the *LDI* scheme are displayed. Both results were carried out by taking data from the pipeline prototype previously described. The experiment was performed as follows: Pump 1 is started in a steady state operation during the first 65 [s] approximately. After that, it begins to operate in some unsteady state, namely a sine-like pressure signal is introduced, just exactly like a persistent input in the sense of [11]. This sine signal was experimentally obtained by setting up the pump controller as follows:

$$\begin{array}{rcl} VFD(t) & = & 60[Hz], \forall t \leq 65[s] \\ VFD(t) & = & 50 + 5sin(2.7313t)[Hz], \forall t > 65[s] \end{array} \tag{35}$$

At $t \approx 60$ [s], two leaks were induced simultaneously at the opening of the control valves in the pilot plant.

The leak position estimations were undertaken by the injection of the inputs and outputs for which a low pass filter was previously applied (u_1, u_2, y_1, and y_2 in (13)), and the corresponding derivatives together with Equations (33) and (34), respectively.

Then, the leak magnitudes were also estimated by using Equations (31) and (32). It is possible to recover the whole state going backwards using Equations (30)–(28). As stated earlier, the time derivatives were computed using the methodology discussed in Section 3.2.

4.2.1. Experiment 1: Leaks Induced in Valves $n^\circ 1$ and $n^\circ 3$

The first experiment consists of simultaneously inducing two leaks in valve $n^\circ 1$ and valve $n^\circ 3$ (see Figure 3). The algorithm starts once the leak is detected. This initial detection is obtained when a deviation between the upstream and downstream flow is detected $|Q_{in} - Q_{out}| > \delta$, where δ is a constant threshold defined by the designer (normally related to the signal-noise ratio): here $\delta = 1 \times 10^{-4}$ [m^3/s]. Immediately afterwards, a sinusoidal wave form as (35) is applied to ensure enough observability of the model (13) via persistent inputs (see Section 3.1). Once the sinusoidal steady state has been reached, the *LDI* scheme starts. Figure 4 shows the time evolution of the pressure head at the inlet and outlet of the pipe (system input, $H_{in} = u_1$ and $H_{out} = u_2$). As it can be seen, the *LDI* algorithm begins close to 65 [s].

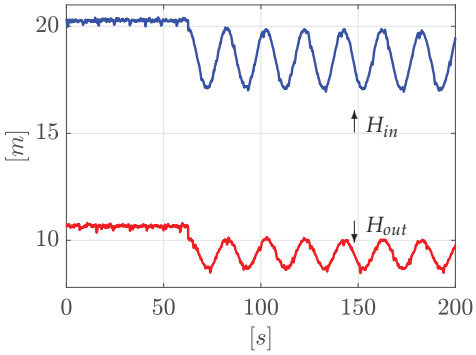

Figure 4. Pressure heads H_{in} and H_{out}.

Following with the same idea, Figure 5 shows the inlet and outlet flows (system output $Q_{in} = y_1$ and $Q_{out} = y_2$). It is clear that, due to the physical nature of the leak phenomena, the inlet flow is separated from the outlet flow:

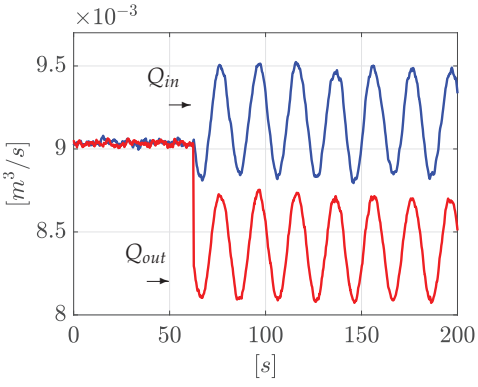

Figure 5. Flow rates Q_{in} and Q_{out}.

Now, once the input and output time derivatives have been computed with Equations (25), (33), and (34), then they are used to reconstruct the leak positions. For clarity, just one signal cycle ($T_{in} = 20$ s), as seen in Figure 6, is enough to correctly locate the two leaks, despite signal noise. To quantify the accuracy of the leak position estimation, a Mean Absolute Error index is applied. For the first leak, the estimation accuracy is 96.62% (with respect to the whole pipeline length), whereas the second leak localization accuracy is 96.33%. As Figure 6 shows, one cycle has demonstrated to be enough to isolate the leak well despite signal noise.

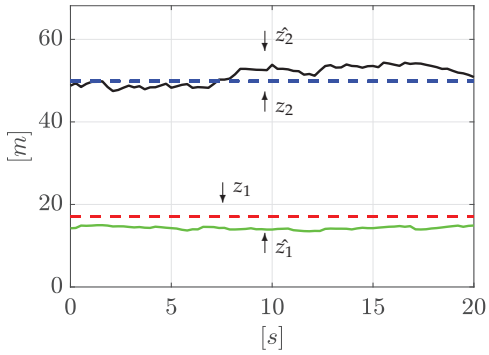

Figure 6. Estimation of leak positions.

Similarly, once the leak positions are obtained, it is possible to reconstruct the leak magnitudes using Equations (31) and (32). The corresponding results are shown in Figure 7, where estimated magnitudes are set around 1.3×10^{-4} [$m^{5/2}$/s] and 0.95×10^{-4} [$m^{5/2}$/s], respectively. The outflow computed by using Equation (4) for each leak is consistent with the total outflow.

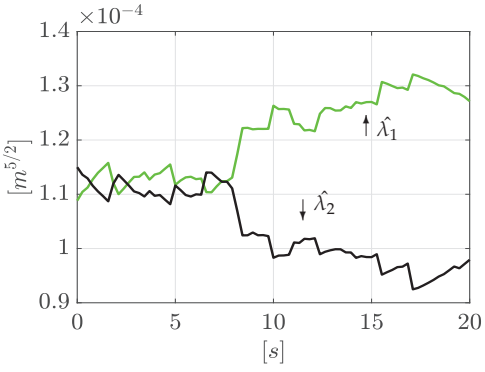

Figure 7. Estimation of leak magnitudes.

Notice that for the *LDI* problem, the estimation of the leak parameters of both leaks is enough, but, as mentioned before, it is also possible to recover the remaining states of (13), going backwards from Equations (30) and (28).

4.2.2. Experiment 2: Leaks Induced in Valve $n°1$ and $n°2$

To better illustrate the effectiveness of the method, a second experiment is exposed. The experiment setup was exactly the same as in Section 4.2.1 except that two leaks are now induced in valve $n°1$ and valve $n°2$ (see Figure 3). Figure 8 shows the time evolution of the pressure head at upstream and downstream, respectively. In the same way as before, the *LDI* algorithm starts when a flow deviation exceeds a predefined threshold, δ, ($|Q_{in} - Q_{out}| > \delta$).

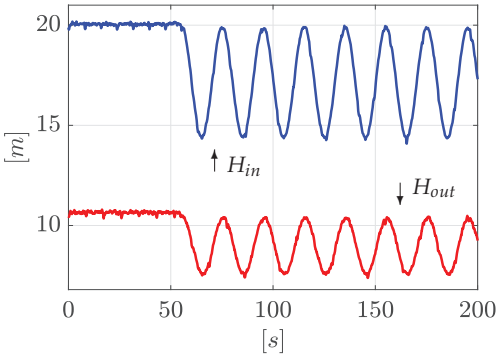

Figure 8. Pressure heads H_{in} and H_{out} (2nd experiment).

Figure 9 shows the corresponding flow rate evolution at upstream and downstream. As stated above, due to the physical nature of the leak phenomena, the inlet flow is separated from the outlet flow.

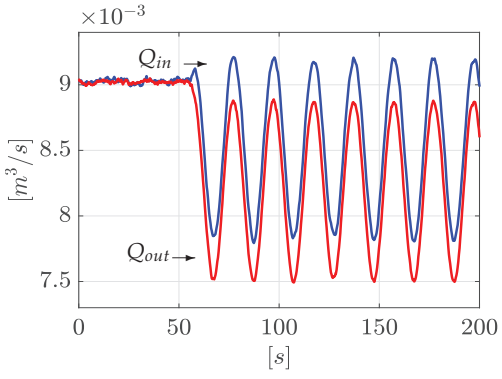

Figure 9. Flow rate Q_{in} and Q_{out} (2nd experiment).

As performed above, once the algorithm starts, the input and output time derivatives are computed following the algorithm explained in Section 3.2. Subsequently, Equations (33) and (34) are used to obtain the leak positions. The results are presented in Figure 10. As before, the leak positions are well estimated despite signal noise in just one signal cycle ($T_{in} = 20$ s). Here, the MAE yields an estimation accuracy for the first leak of 95.01%, while the second leak position presents an estimation accuracy of 97.94%.

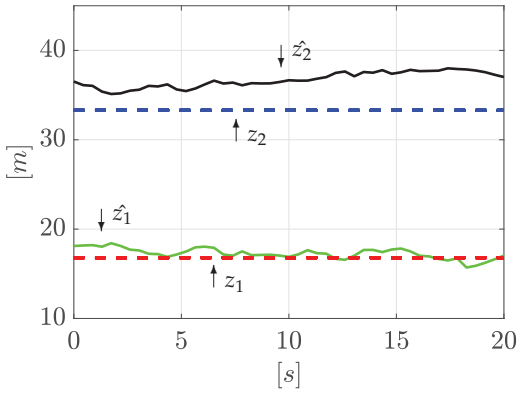

Figure 10. Estimation of leak positions (2nd experiment).

Continuing with the algorithm, the leak magnitudes are computed with Equations (31) and (32). These results are shown in Figure 11.

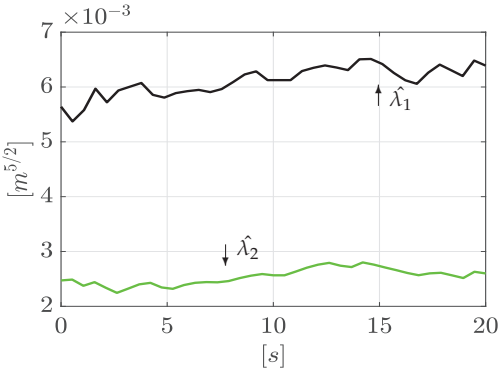

Figure 11. Estimation of leak magnitudes (2nd experiment).

5. Conclusions

The simultaneous leak detection and isolation problem is currently an open and challenging problem. Even though extensive research in the field is currently in progress, to the best of our knowledge, only simulation results have been reported until now. One of the reasons is that the distinguishability of two (or more) simultaneous leaks depends on the input.

In this work, an *LDI* methodology for the two simultaneous leak detection and isolation has been proposed based on an algebraic observer that uses the injection, the inputs and outputs of the system, and the corresponding time derivatives, by applying an appropriate input. The time derivatives are computed using *Numerical Differentiation with Annihilators* and the approach has been successfully applied to real data. This methodology could be extended to more general cases of simultaneous leaks in real operational conditions, such as the case of the *SIAPA* aqueduct in Guadalajara, Mexico.

Author Contributions: A.N.-D .: software, validation, data curation, writing—original draft preparation, methodology, formal analysis, and investigation; J.A.D.-A.: conceptualization, methodology, formal analysis, writing—review and editing, and investigation; O.B.: writing—review; G.B.: writing—review and editing. All authors have read and agreed to the published version of the manuscript.

Funding: This work was funded by the Tecnológico de Monterrey through the School of Engineering and Science.

Acknowledgments: Authors would like to thank Tecnológico de Monterrey for the financial support and the facilities granted for fulfillment of this research article. All databases were obtained by the second author during his PhD studies at Cinvestav Guadalajara.

Conflicts of Interest: The authors declare no conflict of interest.

References

1. OECD. *Water Governance in Cities*; OECD: Paris, France, 2016; p. 140. [CrossRef]
2. Navarro, A.; Begovich, O.; Sánchez, J.; Besancon, G. Real-Time Leak Isolation Based on State Estimation with Fitting Loss Coefficient Calibration in a Plastic Pipeline. *Asian J. Control* **2017**, *19*, 255–265. [CrossRef]
3. Santos-Ruíz, I.; Bermúdez, J.; López-Estrada, F.; Puig, V.; Torres, L.; Delgado-Aguiñaga, J. Online leak diagnosis in pipelines using an EKF-based and steady-state mixed approach. *Control Eng. Pract.* **2018**, *81*, 55–64. [CrossRef]
4. Navarro, A.; Delgado-Aguiñaga, J.A.; Sánchez-Torres, J.D.; Begovich, O.; Besançon, G. Evolutionary Observer Ensemble for Leak Diagnosis in Water Pipelines. *Processes* **2019**, *7*, 913. [CrossRef]
5. Pérez-Pérez, E.; López-Estrada, F.; Valencia-Palomo, G.; Torres, L.; Puig, V.; Mina-Antonio, J. Leak diagnosis in pipelines using a combined artificial neural network approach. *Control Eng. Pract.* **2021**, *107*, 104677. [CrossRef]
6. Delgado-Aguiñaga, J.; Puig, V.; Becerra-López, F. Leak diagnosis in pipelines based on a Kalman filter for Linear Parameter Varying systems. *Control Eng. Pract.* **2021**, *115*, 104888. [CrossRef]
7. Delgado-Aguiñaga, J.; Besançon, G.; Begovich, O.; Carvajal, J. Multi-leak diagnosis in pipelines based on Extended Kalman Filter. *Control Eng. Pract.* **2016**, *49*, 139–148. [CrossRef]
8. Rojas, J.; Verde, C. Adaptive estimation of the hydraulic gradient for the location of multiple leaks in pipelines. *Control Eng. Pract.* **2020**, *95*, 104226. [CrossRef]
9. Fu, H.; Wang, S.; Ling, K. Detection of two-point leakages in a pipeline based on lab investigation and numerical simulation. *J. Pet. Sci. Eng.* **2021**, *204*, 108747. [CrossRef]
10. Torres, L.; Besançon, G.; Georges, D. Multi-leak estimator for pipelines based on an orthogonal collocation model. In Proceedings of the 48h IEEE Conference on Decision and Control (CDC) held jointly with 2009 28th Chinese Control Conference, Shanghai, China, 15–18 December 2009; pp. 410–415. [CrossRef]
11. Besançon, G. *Nonlinear Observers and Applications*; Springer: Berlin/Heidelberg, Germany, 2007; Volume 363.
12. Torres, L.; Besançon, G.; Georges, D.; Navarro, A.; Begovich, O. Examples of pipeline monitoring with nonlinear observers and real-data validation. In Proceedings of the 8th International Multi-Conference on Systems, Signals and Devices, Sousse, Tunisia, 22–25 March 2011.
13. Roberson, J.A.; Cassidy, J.J.; Chaudhry, M.H. *Hydraulic Engineering*; John Wiley & Sons: Hoboken, NJ, USA, 1998.
14. Verde, C. Accommodation of multi-leak location in a pipeline. *Control Eng. Pract.* **2005**, *13*, 1071–1078. [CrossRef]
15. Besançon, G.; Georges, D.; Begovich, O.; Verde, C.; Aldana, C. Direct observer design for leak detection and estimation in pipelines. In Proceedings of the 2007 European Control Conference (ECC), Kos, Greece, 2–5 July 2007; pp. 5666–5670.
16. Mott, R.L.; Noor, F.M.; Aziz, A.A. *Applied Fluid Mechanics*; Pearson Prentice Hall: Singapore, 2006.
17. Navarro, A.; Begovich, O.; Besancon, G. Calibration of fitting loss coefficients for modelling purpose of a plastic pipeline. In Proceedings of the ETFA2011, Toulouse, France, 5–9 September 2011; pp. 1–6.
18. Takacs, G. *Sucker-Rod Pumping Handbook: Production Engineering Fundamentals and Long-Stroke Rod Pumping*; Gulf Professional Publishing: Houston, TX, USA, 2015.
19. E Shashi Menon, P. *Piping Calculations Manual*; McGraw-Hill Education: New York, NY, USA, 2005.
20. Diop, S.; Fliess, M. Nonlinear observability, identifiability, and persistent trajectories. In Proceedings of the 30th IEEE Conference on Decision and Control, Brighton, UK, 11–13 December 1991; pp. 714–719.
21. Isidori, A. *Nonlinear Control Systems*; Springer: Berlin/Heidelberg, Germany, 1995.
22. Diop, S. Elimination in control theory. *Math. Control. Signals Syst.* **1991**, *4*, 17–32. [CrossRef]
23. Mboup, M.; Join, C.; Fliess, M. Numerical differentiation with annihilators in noisy environment. *Numer. Algorithms* **2009**, *50*, 439–467. [CrossRef]
24. Rotoplas. *Tuboplus: Mejor Tubería, Mejor Agua*; Rotoplas: Mexico City, Mexico, 2018.
25. Begovich, O.; Pizano-Moreno, A.; Besançon, G. Online implementation of a leak isolation algorithm in a plastic pipeline prototype. *Lat. Am. Appl. Res.* **2012**, *42*, 131–140.

sensors

MDPI

Article

Chlorine Concentration Modelling and Supervision in Water Distribution Systems

Ramon Pérez [1,2], Albert Martínez-Torrents [2], Manuel Martínez [2,3], Sergi Grau [4,5], Laura Vinardell [2], Ricard Tomàs [4], Xavier Martínez-Lladó [2] and Irene Jubany [2,*]

[1] Research Center for Supervision, Safety and Automatic Control, Universitat Politècnica de Catalunya, Rambla Sant Nebridi 10, 08222 Terrassa, Spain; ramon.perez@upc.edu
[2] Sustainability Area, Eurecat, Centre Tecnològic de Catalunya, Plaça de la Ciència, 2, 08243 Manresa, Spain; albert.martinez@eurecat.org (A.M.-T.); manuel.martinez@eurecat.org (M.M.); laura.vinardell@eurecat.org (L.V.); xavier.martinez@eurecat.org (X.M.-L.)
[3] Department of Mechanical Engineering, Universitat Rovira i Virgili, Av. Països Catalans 26, 43007 Tarragona, Spain
[4] Aigües de Manresa S.A., Plana de l'Om 6, 3r-3a, 08240 Manresa, Spain; sgrau@aiguesmanresa.cat (S.G.); rtomas@aiguesmanresa.cat (R.T.)
[5] Department of Mining, Industrial and ICT Engineering, Universitat Politècnica de Catalunya, Av. de les Bases de Manresa, 61-73, 08242 Manresa, Spain
* Correspondence: irene.jubany@eurecat.org; Tel.: +34-93-877-73-73

Abstract: The quality of the drinking water distributed through the networks has become the main concern of most operators. This work focuses on one of the most important variables of the drinking water distribution networks (WDN) that use disinfection, chlorine. This powerful disinfectant must be dosed carefully in order to reduce disinfection byproducts (DBPs). The literature demonstrates researchers' interest in modelling chlorine decay and using several different approaches. Nevertheless, the full-scale application of these models is far from being a reality in the supervision of water distribution networks. This paper combines the use of validated chlorine prediction models with an intensive study of a large amount of data and its influence on the model's parameters. These parameters are estimated and validated using data coming from the Supervisory Control and Data Acquisition (SCADA) software, a full-scale water distribution system, and using off-line analytics. The result is a powerful methodology for calibrating a chlorine decay model on-line which coherently evolves over time along with the significant variables that influence it.

Keywords: chlorine; water distribution networks; modelling; supervision; decay model

Citation: Pérez, R.; Martínez-Torrents, A.; Martínez, M.; Grau, S.; Vinardell, L.; Tomàs, R.; Martínez-Lladó, X.; Jubany, I. Chlorine Concentration Modelling and Supervision in Water Distribution Systems. *Sensors* **2022**, *22*, 5578. https://doi.org/10.3390/s22155578

Academic Editors: Eduard Llobet and Angela Maria Stortini

Received: 9 May 2022
Accepted: 19 July 2022
Published: 26 July 2022

1. Introduction

Disinfection is one of the most important steps in water treatment, as it must ensure the microbiological safety of the water generated, not only after treatment, but also throughout the transport process to the consumption point. Many countries use chlorine-based chemicals (sodium hypochlorite, chlorine dioxide, chloramines, etc.) to achieve this objective, as they guarantee the degree of residual disinfection potential that is required by their laws [1]. If required, booster disinfection stations are installed at different points in the network. Their need and best location can be optimized using models and tools based on estimates of the chlorine concentration. Chlorine concentration is precisely one of the most relevant parameters to consider for the water distribution network (WDN) quality management. Although chlorine ensures the absence of pathogens, it is the main cause of the formation of disinfection byproducts (DBPs) [2]. Most of these compounds are toxic or carcinogenic for human health and need to be controlled to ensure drinking water safety [3]. Thus, European legislation limits the concentration of some DBPs in drinking water [4].

Nowadays, given the lack of reliable and applicable models for predicting chlorine behavior, disinfection management is not optimal in most WDNs, since it is based on

a point-specific control as opposed to the consideration of the whole network [5]. There are often dark points where the chlorine level may be too low, along with over-chlorination at other points (particularly in summer), with a subsequent increase in both operating costs and DBP concentrations.

The absence of robust models for predicting chlorine behavior in WDNs is fundamentally due to two aspects: (1) the complexity of modelling the hydraulics of the WDNs and (2) the need for on-line quality data. Although authors report good results in chlorine prediction in full-scale networks in some studies [6], the predictions become less accurate when the environmental conditions or the water composition change from those of the calibration. Such a situation is very common in WDNs fed with treated surface water.

Regarding the first aspect, WDNs are highly meshed and complex systems, the behavior of which is difficult to predict. The introduction of flow, level and pressure sensors, and automated metering readers (AMR) for consumption has recently increased the model accuracy [7,8]. Thus, the intense use of a large amount of hydraulic data together with hydraulic models and numerical simulators allow prediction of residence time, which is one of the main parameters needed for successful water quality prediction.

Regarding the second aspect, it is mandatory to obtain information on water quality in the effluent of the drinking water treatment plant and the relevant points in the WDNs in order to predict the behavior of chlorine. Several studies [6,9] base their decay models on parameters that are easily measured on-line, such as temperature, pH, redox potential, conductivity, turbidity, and chlorine concentration. Nevertheless, the calibration and maintenance of these models for their on-line use is seldom performed.

Common models for chlorine modelling in WDNs are first-order linear differential equations [10] such as:

$$\frac{dC}{dt} = K_b \cdot C^{\alpha} \quad (1)$$

where K_b is a constant that contains the different parameters and physicochemical phenomena that may affect chlorine decay, such as natural organic matter, inorganic compounds, or temperature [6]. More sophisticated models have also been studied, including second-order models [11].

Furthermore, knowing the effect of the parameters influencing chlorine decay is also important, as this will, in turn, allow the prediction of such decay and, in some cases, the application of corrective measures to reduce its effect.

Equations of different complexity have been used to model the effect of some of these parameters. One of the most influencing and studied parameters is temperature, which is usually based on Arrhenius's model [12] or other power models. Liu et al. [13] took pH and temperature into account in their models, thus differentiating the effect of HOCl and OCl species on pH. Similarly, Arevalo, in his doctoral dissertation [14], used a model that considered temperature and UV254 as an indication of organic matter. In this case, two decay constants were used, one related to chlorine decay on bulk water and one related to chlorine decay on water close to pipe wall.

Hassan et al. [15] studied the specific case of organic matter adsorbed onto goethite, which is the predominant iron oxide in pipe deposits, in order to see how effectively the presence of organic matter increased the decay rate. Their main conclusions were: (i) an increase in temperature causes an increase in the decay constant and therefore in the decay rate, (ii) the pH has not been seen to greatly affect decay, (iii) a higher initial chlorine concentration leads to a lower decay rate, (iv) a higher organic matter concentration, in general dissolved organic matter (DOC), causes an increase in the rate of decay, (v) an increase in the velocity of the water flow through the pipe causes an increase in the rate of decay, and (vi) the concentration of ammonium, nitrites, iron, and manganese seems to affect the rate of decay, causing its increase.

Chlorine decay first-order equations can also be used in software like EPANET, which has sufficient power to simulate and predict the concentration of chlorine in the network. EPANET is a public domain software for WDN modelling developed by the United States

Environmental Protection Agency (US EPA). This software can perform transient simulations of hydraulic behavior and water quality in pressurized pipe networks. In order to properly model water quality and its time evolution at consumer points, it is mandatory to have a reliable hydraulic model of the WDN. However, like any simulation software, EPANET depends on the availability and application of continuous data into robust models. The default built-in models have fixed calibration parameters that are not easily extrapolated in most real cases. The approach some authors take to overcome these barriers is to modify and recalibrate the default models included in the EPANET database based on the real system data to be modelled [16].

Another important aspect when modelling chemical reactions in pipes is the different behavior in wall and in bulk water. In the literature, bulk reactions are usually considered first-order and wall reactions are considered zero-order. Values for the bulk reaction coefficient are usually obtained using laboratory measurements [17]. Nevertheless, changing water characteristics in the network requires updating the model. There are a few approaches for the quality model calibration. This calibration requires a validated hydraulic model and water quality data. This is often carried out in a well-monitored part of the network and then generalized to the whole network [18,19].

This paper focuses on the chlorine decay process and variables that affect it, the models for concentration prediction, and their application within WDNs in a specific case-study. First, an on-line calibration procedure, with available data from the transport network, is adapted to the full-scale system and performed over a long period so that the evolution of the decay parameters can be studied. This model is used to predict the chlorine concentration in the distribution network and validated with discrete monitoring data. The dependence of chlorine decay on the relevant variables is also studied. Finally, this dependence is compared with the evolution of the parameters estimated using the on-line calibration method. The aim is to illustrate how the intense use of models and available data can provide a better understanding of the behavior of chlorine in a WDN and, thus, be used to support decision-making to improve water quality.

2. Materials and Methods

2.1. Case Study Network

The case study in this work is a WDN in Catalonia (Spain) (see location in Figure 1) managed by Aigües de Manresa, who provided the network configuration information and hydraulic and water quality data for a period of 14 months (2017–2018). The water supplied comes from the Llobregat River and goes through a prechlorination step with sodium hypochlorite (Apliclor Water Solutions S.L., Sant Martí Sesgueioles, Spain) or chlorine dioxide generated using sodium chlorite (Apliclor Water Solutions S.L., Sant Martí Sesgueioles, Spain) and hydrochloric acid (Apliclor Water Solutions S.L., Sant Martí Sesgueioles, Spain) (depending on the season), a sand filtration process, and a final disinfection step with sodium hypochlorite.

Two parts of the network were used in this study: the transport network and the district metered area (DMA). The transport network (Figure 2) consists of two water storage tanks (T_1 and T_2) equipped with sensors for chlorine concentration (input of T_1 (Cl_1) and output of T_2 (Cl_2)), flowmeters (outflows from the tanks, Q_1 and Q_2), and water level (H_1 and H_2). Water flows from T_1 to T_2 through a 6859 m main. T_2 is a boosting station with known sodium hypochlorite (Apliclor Water Solutions S.L., Sant Martí Sesgueioles, Spain) addition. The geometry of the tanks (volume) and pipes (length and diameter) are known. Water from T_2 is distributed to the rest of the network (through Q_2) of the DMA.

The DMA corresponds to a residential area. The hydraulic model includes 572 nodes and 610 pipes with a total length of 31 km, providing water to 300 consumers. Water flows by gravity. There are two quality-sampling points where the chlorine concentration is measured weekly. Figure 3 presents the model of this DMA visualized in EPANET. The input tank (corresponding to T_2 in Figure 2) and the two sampling points are highlighted (S_1 and S_2).

Figure 1. Study site location, a network in Catalonia supplied by the Llobregat River.

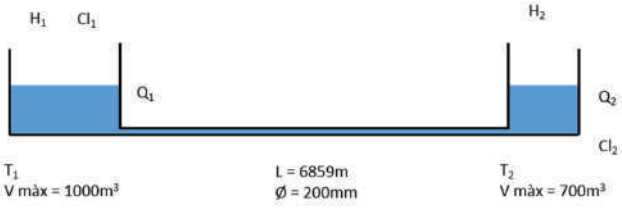

Figure 2. Outline of the network section used for the on-line calibration.

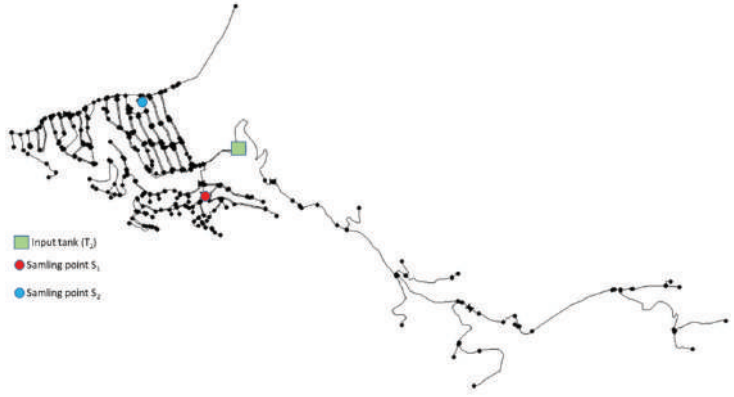

Figure 3. DMA network model in EPANET.

2.2. On-Line Calibration

A very well parametrized system in terms of hydraulics and chlorine concentration (at least at two points) is required to calibrate the chlorine decay constant of a WDN. As in this study, the transport network often fulfils this condition. Therefore, the network used for on-line calibration in this study was the transport network shown in Figure 2. The objective was to find the decay constants for the model that best explained the chlorine concentration measured at the output of T_2.

The chosen model was a first-order model. Higher-order models could be used with no fundamental changes in the methodology. Equation (2) shows that the chlorine

concentration (Cl_2) at the outflow of T_2 depends on the input chlorine concentration (Cl_1) and the residence time in the system (t). The solution of Equation (1) is as follows:

$$Cl_2 = Cl_1 \cdot e^{-K_b \cdot t} \tag{2}$$

where K_b is the decay constant and α is considered as 1.

This dependence is defined by the decay constant K_b, which was calibrated on-line using the measurements available so that it was adapted throughout the year to the different water characteristics and environmental conditions. Estimations were performed on a weekly basis, since some information was only available at this frequency (chlorine dosing in T_2).

The residence time (RT) in T_1 was calculated from the hydraulic information available using (3). The weekly mean residence time at tank T_1 and the pipe was calculated using the flowmeter data (Q_1) and the volume of this subsystem.

$$\overline{RT}_1 = \frac{\overline{V}_1 + V_{pipe}}{\overline{Q}_1} \tag{3}$$

In order to estimate the mean water volume in T_1, the level data of the tank (H_1) and the geometric information was used. The residence time in T_2 was calculated using the mean values of the volume obtained from the level data (H_2) and the mean values of the tank effluent (Q_2), as shown in (4):

$$\overline{RT}_2 = \frac{\overline{V}_2}{\overline{Q}_2} \tag{4}$$

The chlorine concentration increase due to rechlorination ($\overline{Cl}_{added}$) was calculated using the added volume of chlorine divided by the mean volume of water treated:

$$\overline{Cl}_{added} = \frac{\overline{\Delta V_{Cl}} \cdot 143}{\int Q_2} \tag{5}$$

where $\overline{\Delta V}_{Cl}$ is the volume in liters of the concentrated chlorine added weekly to the network and 143 is the concentration of the added chlorine in g/L (value obtained from the conversion of the 15% NaClO to reactive chlorine, see Section S1 in the Supplementary Material).

Finally, a decay K_b constant was calculated which explained the chlorine concentration $\overline{Cl}_2$ at the outflow of T_2 given the residence time calculated using (6)

$$\overline{Cl}_2 = \overline{Cl}_1 \cdot e^{-K_b(\overline{RT}_1 + R\overline{RT}_2)} + \overline{Cl}_{added} \cdot e^{-K_b \overline{RT}_{T_2}} \tag{6}$$

where $\overline{Cl}_2$ was considered equal to 0.6 ppm, which is the set point of the chlorine control system in the boosting station. The algorithm for K_b calibration is shown in the Supplementary Material (Section S2).

The first order decay model is the most used in the water industry. Its decay constant includes all the dependencies related to environmental and water characteristics. Thus, the continuous updating of this constant is the guarantee of its reliability. The limitation of this methodology is the information required. Hydraulic information, that allows the determination of the residence time, must be available. Multiple chlorine concentration measurements and the exact volume of added chlorine between these measurements are also mandatory data.

2.3. Chlorine Decay Calibration and Validation

The chlorine decay first-order model validation for the transport network was carried out using available the on-line data of the chlorine concentration in the output of T2 considering the residence time in this tank. The data used covered the period from February 2017 to April 2018. The chlorine decay model was also validated for its use in the distribution network in the section where chlorine concentration is monitored.

Applying the calibrated decay model directly to the distribution network produced poor results. This was expected, due to the difference between the transport network and the distribution network regarding pipe size, materials, age, etc. To adjust the model, the available data period was divided into two sets: one for training the new distribution quality model and the remaining data for validation. There were 35 samples available in S_1 and 11 samples in S_2. Thus, the first 21 samples in S_1 were used for the training and the remaining ones for the validation. The algorithm used for this calibration is shown in the Supplementary Material (Section S3).

2.4. Parametrised Chlorine Decay Model

The decay constant, determined from the available on-line data, evolved clearly throughout 2017. The question arose if this could be due to the effect of the available variables such as temperature, the initial chlorine concentration, the cumulative precipitation, and the turbidity at the drinking water treatment plant or not.

This suggested the idea of analyzing the variables that influence chlorine decay in order to generate an empirical model based on the available independent variables. The availability of considerable data (temporal and spatial) implies dealing with large amounts of data, multiple variables, and experimental noise, which hinders the direct extraction of valuable information.

Principal component analysis (PCA) is a multivariate statistical technique that allows the description of the data according to the variance [20]. This method transforms data in noncorrelated new variables by linear transformation, decreasing the data dimensions. New data description is more condensed and can describe patterns that are hard to identify in multivariable datasets. PCA has already been used to determine the physical and chemical parameters influencing chlorine decay [21]. Therefore, for being a powerful, reliable, and globally accepted tool when dealing with big data, PCA was selected to extract the main trends, patterns, and correlations among the variables (dimensions) [11].

Based on the PCA results, the chlorine decay constant was modelled using the available variables and a potential multiparametric model (7).

$$K_b = K \cdot Parameter1^a \cdot Parameter2^b \cdot Parameter3^c \cdot \ldots \quad (7)$$

Specifically, a power model (8) and an Arrhenius model (9) [12] where calibrated using experimental data (temperature in 2017) and K_b obtained from the on-line calibration using the least square error fitting method implemented in the "Solver" function in Excel.

$$K_b = K_{power} \cdot T^a \quad (8)$$

$$K_b = A \cdot exp(-E_a/RT) \quad (9)$$

where, K_{power}, a, and A are constants, E_a is the activation energy (Jmol^{-1}), R is the universal gas constant, and T is the temperature. Finally, the parametrized chlorine decay model was compared with that obtained in the on-line calibration to assess its coherence throughout the year.

3. Results and Discussion

3.1. On-Line Calibration

The decay constants K_b obtained are presented in Figure 4. In the upper graphic, the weekly evolution between February 2017 and April 2018, can be observed. A different icon was used for the data of each trimester to clearly identify the season of the year. In the lower graphic obtained, K_b are grouped by month to observe how this parameter evolves throughout the year (some months include estimations of both years). It seems clear that there may be a seasonal variation related to temperature.

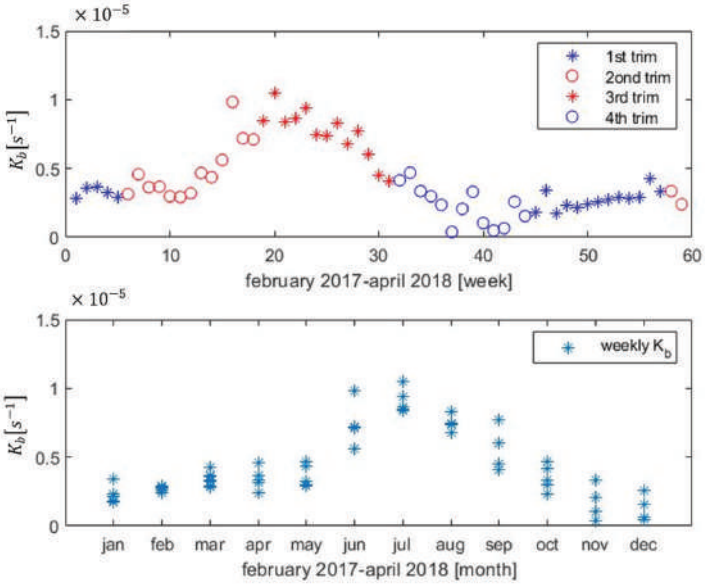

Figure 4. Up: Mean K_b calculated weekly indicating the season of the year (by trimester). Down: Data of mean K_b grouped by month.

3.2. Chlorine Decay Validation

The calibrated model was applied to the peak episodes observed at the output of T_2 due to the rechlorination and mixing effect. The dataset used in this validation was not used for the estimation. The dataset for calibration consisted of the mean values corresponding to the stationary state. Figure 5 shows the chlorine concentration data and the model prediction. It can be observed how this high-frequency dynamic is adjusted with the model obtained with the mean values. For this prediction, K_b evolves weekly.

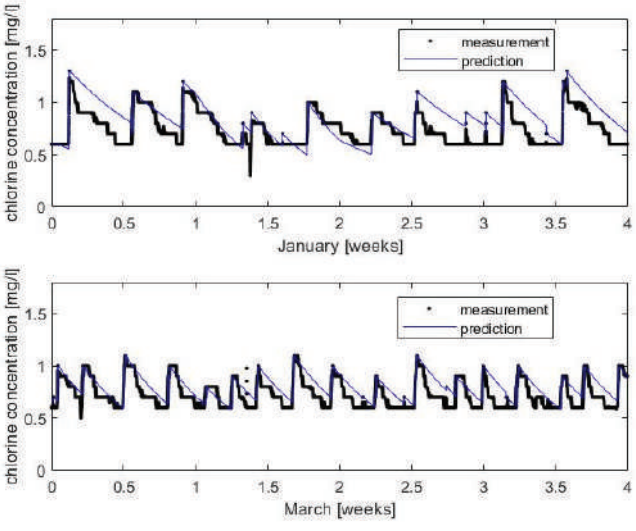

Figure 5. Chlorine decay model validation at the output of T_2. Up: data from January 2017. Down: data from March 2017. Due to high frequency of sampling measurement, data appears like a thick line.

For the distribution network simulation, a relation between the transport K_b, estimated by on-line calibration, with the distribution K_b^* was obtained by adjusting the concentration in the training set of chlorine sampling. This relation was applied to the entire period and the predicted concentration was compared with the measurements for the validation set of samples. A total of 40 days were simulated. The decay constant for both the bulk and wall were fitted using the first 21 samples of the chlorine concentration in S1. These are the first samples of upper graphic in Figure 6.

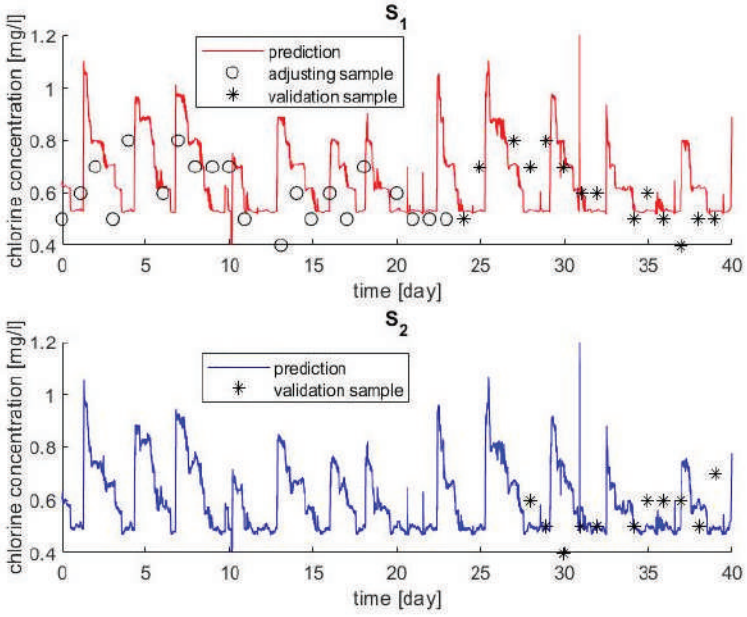

Figure 6. Simulation results for the two sampling points (**S_1** and **S_2**) compared with experimental samplings.

The result was that both decay constants minimize the error when the original K_b obtained in the transport system was divided by 2, as if the calibrated effect was distributed in the two phenomena ($K^*_{b,bulk} = K^*_{b,wall} = K_b/2$). The results obtained are compared with the available experimental data in Figure 6. The mean absolute percentage error was 16% for S_1 (including calibration and validation samples) while it was 17% using only validation samples. Therefore, not significantly different deviations were obtained for the calibration and the validation steps. Graphically, the fit may seem poor; however, the concentration is lower in S_2 than in S_1 both in prediction and measurements, and the mean values in both sampling points are coherent between the prediction and measurements. One aspect that may justify part of the mismatching is that the exact hour of the day of the manual measurements was not available and, therefore, each experimental data may not be in its exact position. This difficulty could be overcome with on-line chlorine sensors instead of manual analysis. Figure 7 presents the measured chlorine concentration at the source (T_2) and the chlorine prediction in the two sampling points (S_1 and S_2). The chlorine concentration decreases with the residence time, since the concentration in S_2 is lower than in S_1, and both are lower than in T_2.

Finally, Figure 8 shows the network nodes colored by their chlorine concentration: green, black, or red, depending on whether their concentration is too low, acceptable, or too high, respectively. In fact, no red points exist in this area and period. Such a representation is very useful in order for the network operator to make decisions. Nodes in this figure correspond to those in Figure 3 and are presented with north at the top.

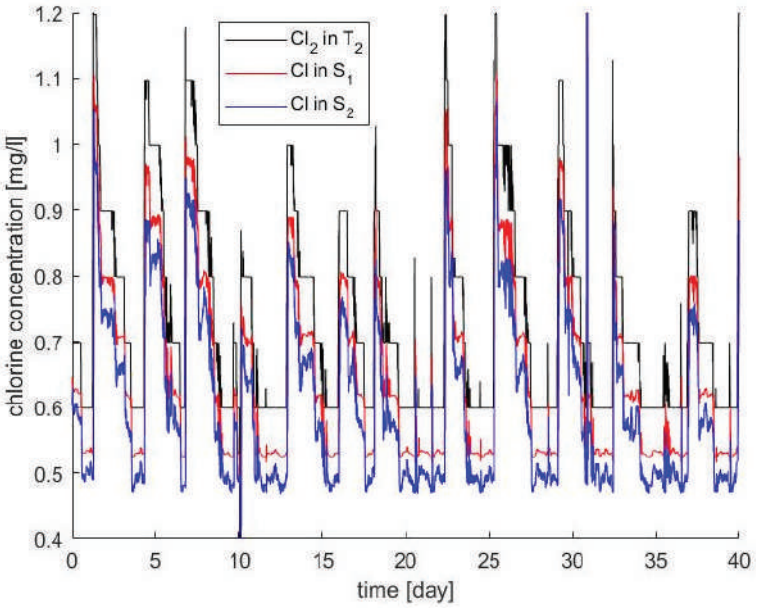

Figure 7. Measured chlorine concentration at the source (T_2) and prediction at the two sampling points (S_1 and S_2).

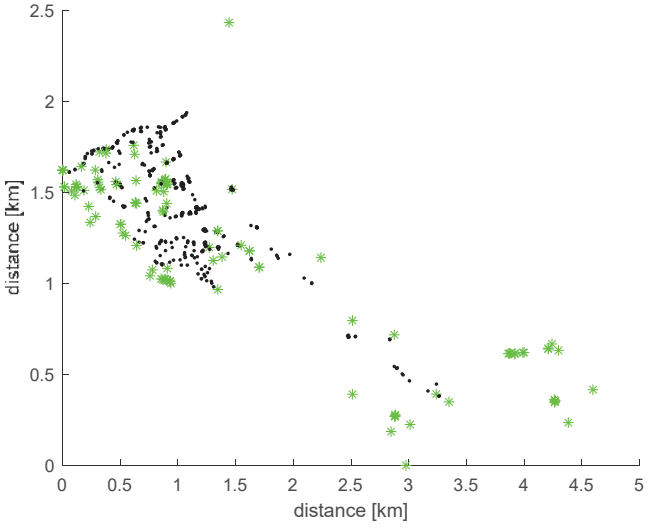

Figure 8. Distribution of network nodes with low concentration (<0.4 ppm, green), acceptable concentration (0.4 ppm > chlorine < 1 ppm, black), and excessive concentration (>1 ppm, red).

Results from the PCA applied to the decay constant (K_Cl_decay) determined in the distribution network and other data available (temperature as Tavg_C, initial chlorine concentration as Initial_Cl, cumulative precipitation as Cumulative_Prec, and turbidity at the drinking water treatment plant) are shown in Figure 9.

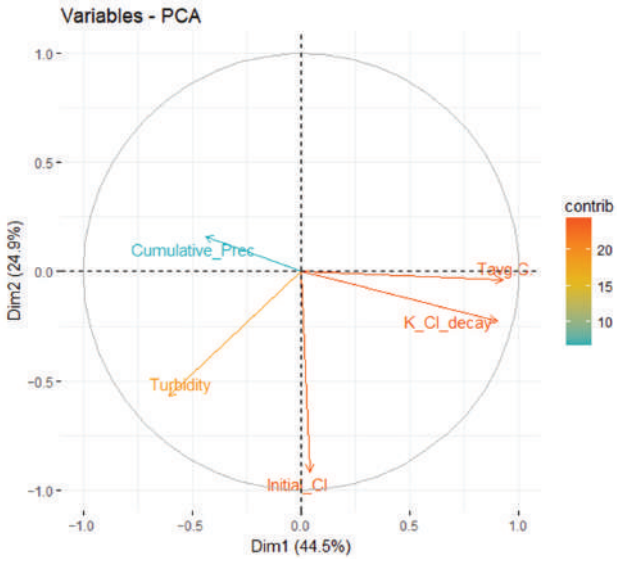

Figure 9. Variables for the two main dimensions of the PCA.

In this case, dimension one was related to the temperature, and dimension two was related to the initial chlorine concentration. Therefore, the decay constant was closely related to the temperature. Figure 10 shows the variables that had the most influence on dimension five, which were again the temperature and the chlorine decay, demonstrating the clear strong relation of the temperature on the decay constant.

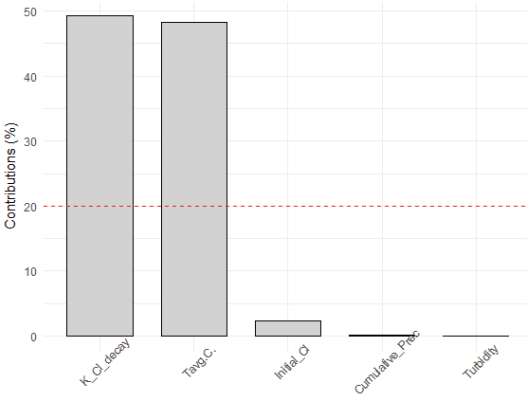

Figure 10. Contribution of variables to dimension 5. Variables with contributions below the dotted line are considered not significant for that dimension.

Thus, it was concluded that the variable that had a higher effect on the decay constant was temperature. It was observed that the variables turbidity, precipitation, and initial chlorine did not excessively improve the fit between the decay constants of the model and the decay constants obtained. Therefore, only the temperature was used, since the effort required to obtain values for the rest of the parameters did not compensate the improvement of the model adjustment.

Experimental data from 2017 and K_b obtained with the on-line calibration were used to calibrate the parameters of the two equations, an Arrhenius model (8) and

a power model (9), to predict the temperature effect on the decay constant. The following Equations (10) and (11) show the results obtained.

$$K_b = 5.477 \cdot 10^{-8} \cdot T^{1.524} \left(\mathrm{s}^{-1}\right) \quad (10)$$

$$K_b = 3950 \cdot exp(-49873/RT) \left(\mathrm{s}^{-1}\right) \quad (11)$$

The fit obtained using the Arrhenius model and the power model were similar, although the Arrhenius one was slightly better. The Arrhenius model also determines the activation energy (J/mol), which is the minimum energy that the system needs for the reaction to take place. The ratio Ea/R obtained in this study was 5999 K, which is in accordance with other authors. For example, Courtis et al. [22] estimated 5388 K and 6701 K for two different water distribution systems, Powell et al. [23] obtained a range between 7500 and 9600 K, and Hua et al. [12] obtained a range between 8203 and 8727 K, depending on the type of water. The variability of the values for this ratio suggests that this is a water-specific parameter that might depend significantly on the natural organic matter composition [24].

Figure 11 shows the fit of the two models to data from 2017, and Figure 12 their forecast for the first days of 2018. In these figures, K Chlorine is the chlorine decay constant determined previously, K power the constant determined following the potential model, and K Arrhenius the constant obtained from the Arrhenius model. As it can be seen, the Arrhenius model provides good predictions while using only the temperature as an input parameter.

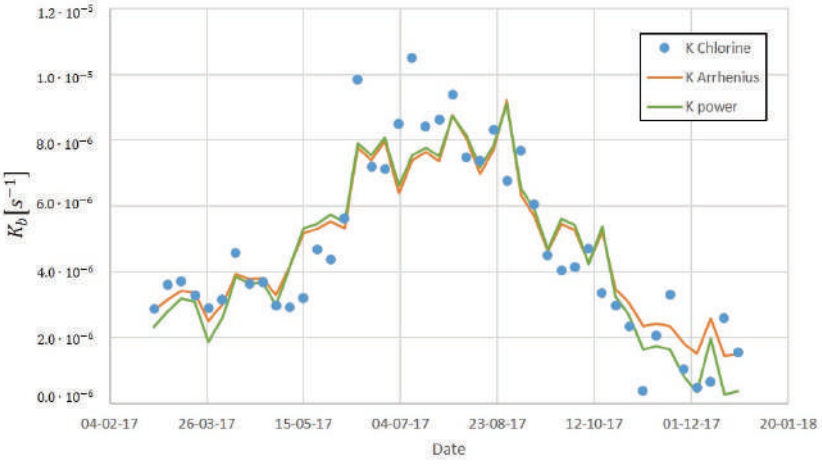

Figure 11. Chlorine decay constant fitting to temperature dependent models using data from 2017.

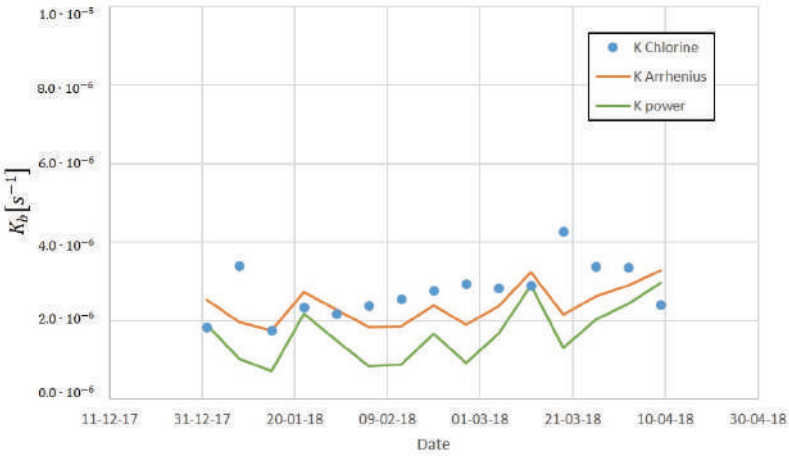

Figure 12. Chlorine decay constant forecast for the first days of 2018.

4. Conclusions

The literature review shows that only the simplest models of chlorine decay are applied to water distribution networks where the hydraulic behavior is complex enough. Even so, these models are seldom used due to the lack of proper calibration. In this paper, the performance of a decay model was evaluated when the parameters were calibrated using state-of-the-art techniques.

The calibration was first carried out in the transport network, where the on-line data allowed an on-line calibration. The relation between the decay constant in the transport and distribution networks used analytical data and, thus, it could not be done on-line.

The prediction error in the validation data was 17% and quite similar to the error obtained for the training set (16%), which meant that there was no overfitting. The decay constant obtained changed during the year following the assumed dependence of the chlorine decay on the temperature. This result suggested the possibility of using available data for predicting this decay constant.

The principal component analysis determined that the temperature was the parameter with higher effect on the decay of chlorine. The chlorine decay constant was obtained using temperature as an independent variable. The obtained constants were compared with the data-driven model obtained in the on-line calibration, showing a high correlation. While the dominant dependence on the temperature is not a novelty, it is important to ensure this unique dependency, as it guarantees that other characteristics of the water source will not be relevant. This has been studied throughout one year, and the results obtained by both models are coherent.

This procedure could also be applied to other quality parameters, such as disinfection byproduct concentrations, which are currently under investigation by the authors. The variables analyzed for chlorine decay estimation are being studied for the trihalomethanes formation prediction.

The final aim of this study is to increase knowledge within the network in order to enable decision-making processes regarding chlorine dosing (quantity and frequency) both in the disinfection process and the boosting stations, in addition to identifying whether other control systems are required to ensure the continuous good quality of supplied water to the final user at a minimum cost.

Supplementary Materials: The following supporting information can be downloaded at: https://www.mdpi.com/article/10.3390/s22155578/s1, Table S1: Pseudocode to estimate the decay chlorine constant; Table S2: Pseudocode to estimate the chlorine decay constant in the distribution network.

Author Contributions: Conceptualization, R.P., R.T. and X.M.-L.; Data curation, R.P., A.M.-T., M.M. and S.G.; Formal analysis, R.P., A.M.-T. and M.M.; Funding acquisition, R.T., X.M.-L. and I.J.; Investigation, A.M.-T., M.M. and L.V.; Methodology, R.P., A.M.-T. and M.M.; Project administration, X.M.-L. and I.J.; Resources, S.G. and R.T.; Software, R.P., A.M.-T. and M.M.; Supervision, R.P., X.M.-L. and I.J.; Validation, R.P. and X.M.-L.; Visualization, R.P., A.M.-T. and L.V.; Writing—original draft, R.P., A.M.-T. and L.V.; Writing—review and editing, R.P., L.V. and I.J. All authors have read and agreed to the published version of the manuscript.

Funding: This research received no external funding.

Data Availability Statement: The data presented in this study are available on request from the corresponding author. The data is not publicly available because the owners want to keep track of its use, as it is sensitive information from a full-scale system (hydraulic models). Nevertheless, software for data treatment and chlorine decay model estimation and validation including nonsensitive data (model_estimation.m and model_validation.m) are available at https://cs2ac.upc.edu/en (18 July 2022) in Matlab format.

Conflicts of Interest: The authors declare no conflict of interest.

References

1. Tsitsifli, S.; Kanakoudis, V. Disinfection Impacts to Drinking Water Safety–A Review. *EWaS3* **2018**, *2*, 603. [CrossRef]
2. Mazhar, M.A.; Khan, N.A.; Ahmed, S.; Khan, A.H.; Hussain, A.; Rahisuddin; Changani, F.; Yousefi, M.; Ahmadi, S.; Vambol, V. Chlorination disinfection by-products in municipal drinking water–A review. *J. Clean. Prod.* **2020**, *273*, 123159. [CrossRef]
3. Richardson, S.D.; Plewa, M.J.; Wagner, E.D.; Schoeny, R.; DeMarini, D.M. Occurrence, genotoxicity, and carcinogenicity of regulated and emerging disinfection by-products in drinking water: A review and roadmap for research. *Mutat. Res. Rev. Mutat. Res.* **2007**, *636*, 178–242. [CrossRef] [PubMed]
4. European Commission. Directive (EU) 2020/2184 of the European Parlliament and of the Council of 16 December 2020 on the quality of water intended for human consumption. *Off. J. Eur. Union* **2020**, *2019*, 1–61.
5. Wang, Y. Optimization of booster chlorination for water distribution system under dual uncertainties. *Urban Water J.* **2022**, *19*, 363–373. [CrossRef]
6. Tiruneh, A.T.; Debessai, T.Y.; Bwembya, G.C.; Nkambule, S.J. A Mathematical Model for Variable Chlorine Decay Rates in Water Distribution Systems. *Model. Simul. Eng.* **2019**, *2019*, 5863905. [CrossRef]
7. Walski, M.T.; Chase, V.D.; Savic, A.D.; Grayman, W.; Beckwith, S.; Koelle, E. Methods. In *Advanced Water Distribution Modeling and Management*, 1st ed.; Bentley Institute Press: Exton, PA, USA, 2007.
8. Puig, V.; Ocampo-Martínez, C.; Pérez, R.; Cembrano, G.; Quevedo, J.; Escobet, T. *Real-Time Monitoring and Operational Control of DrinkingWater Systems*; Springer Nature: Berlin/Heidelberg, Germany, 2017.
9. Shahamat, Y.D.; Godini, K.; Khademi, S.M.R.S.; Rahmani, K.; Rahmani, A. Investigation of chlorine decay of water resource in khanbebein city, Golestan, Iran. *Int. J. Environ. Health Eng.* **2013**, *2*, 11. [CrossRef]
10. Kowalska, B.; Kowalski, D.; Musz, A. Chlorine decay in water distribution systems. *Env. Prot. Eng.* **2006**, *32*, 5–16.
11. Clark, R.M.; Sivaganesan, M. Predicting Chlorine Residuals in Drinking Water: Second Order Model. *J. Water Resour. Plan. Manag.* **2002**, *128*, 152–161. [CrossRef]
12. Hua, P.; Vasyukova, E.; Uhl, W. A variable reaction rate model for chlorine decay in drinking water due to the reaction with dissolved organic matter. *Water Res.* **2015**, *75*, 109–122. [CrossRef] [PubMed]
13. Liu, B.; Reckhow, D.A.; Li, Y. A two-site chlorine decay model for the combined effects of pH, water distribution temperature and in-home heating profiles using differential evolution. *Water Res.* **2014**, *53*, 47–57. [CrossRef] [PubMed]
14. Arevalo, J. *Modeling Free Chlorine and Chloramine Decay in a Pilot Distribution System*; University of Central Florida: Orlando, FL, USA, 2007.
15. Hassan, K.Z.A.; Bower, K.C.; Miller, C.M. Iron Oxide Enhanced Chlorine Decay and Disinfection By-Product Formation. *J. Environ. Eng.* **2006**, *132*, 1609–1616. [CrossRef]
16. Seyoum, A.G.; Tanyimboh, T.T. Integration of Hydraulic and Water Quality Modelling in Distribution Networks: EPANET-PMX. *Water Resour. Manag.* **2017**, *31*, 4485–4503. [CrossRef]
17. Fisher, I.; Kastl, G.; Sathasivan, A. Evaluation of suitable chlorine bulk-decay models for water distribution systems. *Water Res.* **2011**, *45*, 4896–4908. [CrossRef] [PubMed]
18. Xie, X.; Zeng, B.; Nachabe, M. Sampling design for water distribution network chlorine decay calibration. *Urban Water J.* **2015**, *12*, 190–199. [CrossRef]

19. Nejjari, F.; Puig, V.; Pérez, R.; Quevedo, J.; Cugueró, M.; Sanz, G.; Mirats, J. Chlorine Decay Model Calibration and Comparison: Application to a Real Water Network. *Procedia Eng.* **2014**, *70*, 1221–1230. [CrossRef]
20. Anderson, T.W. *An Introduction to Multivariate Statistical Analysis*; John Wiley & Sons: Hoboken, New Jersey, USA, 2003.
21. Chowdhury, S.; Champagne, P.; McLellan, P.J. Factors Influencing Formation of Trihalomethanes in Drinking Water: Results from Multivariate Statistical Investigation of the Ontario Drinking Water Surveillance Program Database. *Water Qual. Res. J.* **2008**, *43*, 189–199. [CrossRef]
22. Courtis, B.J.; West, J.R.; Bridgeman, J. Temporal and Spatial Variations in Bulk Chlorine Decay within a Water Supply System. *J. Env. Eng.* **2009**, *135*, 147–152. [CrossRef]
23. Powell, J.C.; Hallam, N.B.; West, J.R.; Forster, C.F.; Simms, J. Factors which control bulk chlorine decay rates. *Water Res.* **2000**, *34*, 117–126. [CrossRef]
24. Monteiro, L.; Viegas, R.; Covas, D.I.C.; Menaia, J. Modelling chlorine residual decay as influenced by temperature. *Water Environ. J.* **2015**, *29*, 331–337. [CrossRef]

sensors

MDPI

Article

Economic Linear Parameter Varying Model Predictive Control of the Aeration System of a Wastewater Treatment Plant †

Fatiha Nejjari [1], Boutrous Khoury [1], Vicenç Puig [1,2,*], Joseba Quevedo [1], Josep Pascual [1] and Sergi de Campos [3]

[1] Advanced Control Systems Group, Automatic Control Department, Edifici Gaia Campus de Terrassa, Universitat Politècnica de Catalunya, Rambla Sant Nebridi, 22, 08222 Terrassa, Spain
[2] Institut de Robòtica i Informàtica Industrial (CSIC-UPC), Llorens i Artigas, 4-6, 08028 Barcelona, Spain
[3] ADASA Sistemas, S.A.U. C/Ignasi Iglesias, 217, 08820 El Prat de Llobregat, Spain
* Correspondence: vicenc.puig@upc.edu
† This paper is an extended version of our paper published in Proceedings of the 27th European Symposium on Computer Aided Process Engineering (ESCAPE 27), Barcelona, Spain, 1–5 October 2017.

Abstract: This work proposes an economic model predictive control (EMPC) strategy in the linear parameter varying (LPV) framework for the control of dissolved oxygen concentrations in the aerated reactors of a wastewater treatment plant (WWTP). A reduced model of the complex nonlinear plant is represented in a quasi-linear parameter varying (qLPV) form to reduce computational burden, enabling the real-time operation. To facilitate the formulation of the time-varying parameters which are functions of system states, as well as for feedback control purposes, a moving horizon estimator (MHE) that uses the qLPV WWTP model is proposed. The control strategy is investigated and evaluated based on the ASM1 simulation benchmark for performance assessment. The obtained results applying the EMPC strategy for the control of the aeration system in the WWTP of Girona (Spain) show its effectiveness.

Keywords: economic model predictive control; linear parameter varying modelling; wastewater treatment process

Citation: Nejjari, F.; Khoury, B.; Puig, V.; Quevedo, J.; Pascual, J.; de Campos, S. Economic Linear Parameter Varying Model Predictive Control of the Aeration System of a Wastewater Treatment Plant. *Sensors* **2022**, 22, 6008. https://doi.org/10.3390/s22166008

Academic Editor: Assefa M. Melesse

Received: 10 May 2022
Accepted: 9 August 2022
Published: 11 August 2022

1. Introduction

Biological wastewater treatment plants (WWTPs) are complex nonlinear systems with large variations in their flow rates and feed concentrations. These plants have to be operated continuously taking care of strict environmental regulations. Thus, the use of advanced control strategies becomes necessary to make them more efficient.

The most widely used biological wastewater treatment is the activated sludge process (ASP). In the ASP, microorganisms are mixed with wastewater. The pollutants of the wastewater constitute the nutrient of the microorganisms. As the organisms feed on the organic pollutants in the wastewater, the pollutants are converted to more organisms, biomass, and some by-products. Following an adequate amount of treatment time, the mixture of microorganisms and wastewater, the mixed liquor flows from the aeration tank to a clarifier or settler where the sludge is separated from the treated water. Some of the settled sludge is continuously recirculated from the clarifier to the aeration tank to ensure the maintenance of adequate amounts of microorganisms in this tank. The microorganisms are again mixed with incoming wastewater where they are reactivated to consume organic nutrients. There are five major groups of microorganisms generally found in the aeration basin of the activated sludge process: (i) aerobic bacteria responsible for removing the organic nutrients, (ii) protozoa to remove and digest dispersed bacteria and suspended particles, (iii) metazoa to dominate longer age systems and clarify effluent, (iv) filamentous bacteria or bulking sludge, which are present when operating conditions change, (v) algae and fungi, which are photosynthetic organisms that are present with pH changes and older sludge.

The majority of the culture is mixed and reused with inlet wastewater to keep high reaction rates and sludge age characteristics. In particular, nitrogen is eliminated as follows: First, ammonium is oxidized producing nitrate under nitrification in the aerobic step. The nitrate that is produced is then converted into nitrogen gas by means of denitrification in the anoxic step. Thus, the control of aeration is very important because a low amount of dissolved oxygen can cause the biomass death. On the other hand, an excess of dissolved oxygen could cause the sludge to settle insufficiently. Moreover, because 60% to 80% of the global energy consumption is due to aeration and the operating costs of a WWTP [1], an excessive aeration is not desirable regarding economic efficiency.

The models that are usually considered for characterizing the WWTP processes are the ones developed by the International Association on Water Quality (IAWQ) known as Activated Sludge Models (ASMs) [2].

In this paper, optimal economic operation of the aeration system is considered to improve the efficiency and reliability of an ASP with intermittent aeration, which is used for the removal of nitrogen from domestic wastewater. The objective of the control is to design an aeration strategy (air-on and air-off periods) which minimizes the energy dissipated by the aeration system, with adherence to the limits of the effluent requirements and the operating constraints. The implementation of optimal operation strategies is therefore interesting because WWTPs face the challenge of treating water properly albeit ensuring the minimization of operational costs. This has been the driving force for the active research in the development of advanced control techniques and hierarchical control schemes to improve the operation of the WWTPs, see for example [3,4].

Model predictive control (MPC) has been the most successful advanced control approach applied to control WWTPs. This is due to the fact that MPC controllers allow in a straightforward manner the different operational requirements, the multivariate nature of the control problem (that could even include delay) and directly handling constraints on the control inputs, system outputs and/or internal states [5]. It can also include disturbance prediction, allowing to anticipate the appropriate control actions (feedforward) to achieve optimal performance according to defined criteria in the cost function, which can include different quality criteria and operational costs. Adjusting the MPC control strategy is carried out by suitable manipulating prioritization of different objectives of the performance index that could also include the use of soft constraints. In this way, MPC has become an attractive control strategy for a considerable number of WWTP applications in the last few years. Some examples of MPC control of WWTP can be found in [6,7]. In [6], a benchmarking of different hierarchical control structures for WWTPs that combines static and dynamic real-time optimization (RTO) and nonlinear model predictive control (NMPC) is presented. In [8], a procedure to find the best controlled variables in an economic sense for the activated sludge process in a wastewater treatment plant, despite the large load disturbances, is introduced.

Classical MPC formulation considers pre-established set points, and the objective functions related with error and energy effort have quadratic forms [5]. However, the determination of optimal and reachable reference set points in real time is not an easy task because of the existence of disturbances, set-point changes, time-varying parameters and model uncertainties, among others. This constitutes one of the main limitations of classical MPC. To remedy this issue, real-time optimizers (RTO) or steady-state target optimizers (SSTO) are used to pre-compute the reference set- points at a supervisory layer in the control hierarchy. Then, these pre-computed set points are sent to the lower layer, where a classical MPC behaves as a regulatory controller, forcing the process to follow the desired set points. However, in spite of the use of an RTO, not reachable trajectories might be generated because of the appearance of unexpected disturbances or set points variations, among others. Moreover, there is a delay between the different layers, because the lower layer receives the reference set points determined from the upper layer before its execution. These problems can be avoided by using economic MPC (EMPC) that optimizes process performance directly (e.g., by means of economic objective functions), eliminating the need

of generating reachable reference set points [9]. The first results of the application of EMPC to DO concentration control in WWTPs have been presented in a previous work from the authors [10] considering the nonlinear model of the plant. However, this leads to a nonlinear optimization problem.

Alternatively, this paper proposes an EMPC strategy using the linear parameter-varying (LPV) framework to optimize the effluent quality and minimize the operational cost of a WWTP under operating and physical constraints. The objective is to minimize the energy used by the aeration system with the control of the dissolved oxygen (DO) concentrations in the aerated reactors and maintain the effluent concentration under the required limits. The proposed approach is based on real-time dynamic optimization methods. Optimization in MPC with nonlinear models presents a non-convex problem which is computationally demanding, especially when dealing with large-scale plants with complex dynamics such as the WWTP. Thus, the LPV framework allows the embedding of these nonlinearities in scheduling variables, which are functions of system states (i.e., qLPV). This allows obtaining a pseudo-linear model which is linear in state space but nonlinear in the parameter space and deriving a less demanding convex MPC optimization problem, since convex quadratic optimization tools can be applied. The stability and recursive feasibility of MPC with LPV models has been studied (see [11] for a review of the recent results). The application of dynamic optimization methods requires a sufficiently accurate mathematical model describing the wastewater treatment process. The present work uses the Activated Sludge Model No. 2 (ASM2) [12]. To illustrate the proposed approach a WWTP located in Girona (Spain) is considered as a case study.

In Section 2, the WWTP is described and modeled using a reduced ASM2 model, which is then represented in a qLPV form. The proposed EMPC strategy is introduced and described in Section 3, while the proposed MHE approach is presented in Section 4. The results are presented in Section 5, with simulation scenarios obtained from the application of the EMPC strategy on the Girona WWTP. Finally, some conclusions are given in Section 6.

2. WWTP Description and Modeling

2.1. WWTP Description

The Girona WWTP is a biological treatment plant designed to treat the wastewater generated by 200,000 inhabitant equivalents with a medium daily inflow of 35,000 m^3/d. The processes of the plant can be divided into two main treatment lines: water and sludge (see Figure 1). The water line is separated into three phases: pre-treatment, primary treatment and secondary treatment. The secondary treatment is designed to convert biodegradable, organic wastewater constituents and certain inorganic fractions into new cell mass and by-products. The plant uses an activated sludge system and has three lines composed of three main reactors that are divided into various compartments and three clarifiers. Each line is made of two anoxic reactors located at the beginning, three aerated tanks and an anoxic tank followed by an aerated one. With this configuration, the plant can nitrify and denitrify with great efficiency. The anoxic and aerobic tanks have volumes of 1335, 4554, 1929, and 1929 m^3 for anoxic and 1929, 1276, and 1409 m^3 for aerobic, respectively. Oxygen is supplied to aerated tanks by the aeration system, which delivers air to each of the aeration tanks. The wastewater and activated sludge are separated into three parallel secondary settlers. The volume of each secondary settler is approximately 5024 m^3. The activated sludge is internally recirculated from the last aerobic zone to the anoxic tank (210% of influent waste). Additionally, the wastewater is recirculated from the secondary settlers to the anoxic tank (45 to 100% of influent waste).

Figure 2 shows a standard WWTP technological layout. The wastewater flow enters into the biological part after the mechanical treatment. The nutrient removal takes place in the activated sludge reactor through the biological treatment. The first zone in this treatment is anaerobic, where phosphorus is released. The mixed liquor internal recirculation originates from the anoxic zone. The denitrification occurs in the second zone.

The activated sludge returned from the clarifiers bottom, and the internal recirculation from the aerobic zones end is directed toward the anoxic zone.

2.2. WWTP Modeling

The Benchmark Simulation Model (BSM1), developed within the framework of COST Actions 624 and 682 [2], has been adapted to represent the Girona WWTP (see Figure 1).

Figure 1. Girona Wastewater Treatment Plant.

The Activated Sludge Model No. 1 (ASM1) describes the biological phenomena that takes place in the biological reactors, and it is supposed that no biological reactions take place in the settlers. Due to the complexity of the nonlinear model describing the different complex processes in the plant, various reduced models have been proposed in the literature [13–15] to aid in the online implementation of certain modern control schemes (e.g., MPC), which would have otherwise presented ill-conditioned or stiff numerical problems due to slow and fast dynamic interactions. In [15,16], one can see some successful implementations using reduced WWTP models in various areas of control applied to WWTPs. The reduced model as suggested in [14], which primarily involves certain simplification criteria for a reduced order of the rigorous high dimensional WWTP model, has been adapted to conditions representing the Girona WWTP. This basically involves the derivation of the reactor model based on mass balances of the wastewater species, which are generally expressed as follows:

$$Accumulation = Inflow - Outflow + Reaction$$

Validation of the reduced model considering data from the ASM1 and the reduced model has been undertaken in [14]. In simplifying the complex model, a systematic reduction process of the high-dimensional model considers some assumptions, with the principal conditions given as follows:

- The soluble (S_S) and particulate (X_S) organic compounds are aggregated as a single variable X_{COD}, the chemical oxigen demand (COD).
- Through reduction by time scale from the theory of singular pertubation, the slow dynamics of the variables X_I, X_{BH} and X_{BA} together with the soluble inert organic compounds (S_I) are excluded.
- Finally, simplification of complicated kinetic process, assumption of no alkalinity and separation of aerobic and anoxic conditions are considered.

Under these conditions, the resultant state variables of the reduced model are therefore the chemical oxygen demand (X_{COD}), the dissolved oxygen concentration, (S_O), het-

erotrophic biomass, X_{BH}, ammonia concentration (S_{NH}), nitrate concentration (S_{NO}) and autotrophic biomass (X_{BA}). The control of oxygen concentration (S_0) in the aerobic tanks is via the manipulation of the control input, the oxygen transfer coefficient $K_{La}(t)$.

The states and input vectors are thus given as:

$$x(t) = \Big[X_{COD}(t), S_O(t), X_{BH}(t), S_{NH}(t), S_{NO}(t), X_{BA}(t)\Big]^T$$

$$u(t) = K_{La}(t)$$

The WWTP process is therefore described by the following dynamic equations of the reduced model:

$$\dot{X}_{COD}(t) = \frac{1}{Y_h}\Big[\theta_1(t) + \theta_2(t)\Big] + \Big(1 - f_p\Big)\Big(\theta_4(t) + \theta_5(t)\Big) + \vartheta_1(t), \tag{1}$$

$$\dot{S}_O(t) = \frac{Y_h - 1}{Y_h}\theta_1(t) + \frac{Y_a - 4.57}{Y_a}\theta_3(t) + \vartheta_2(t), \tag{2}$$

$$\dot{S}_{NH}(t) = -i_{xb}\Big[\theta_1(t) + \theta_2(t)\Big] - \Big[i_{xb} + \frac{1}{Y_a}\Big]\theta_3(t) + \Big(i_{xb} - f_p i_{xp}\Big)\Big[\theta_4(t) + \theta_5(t)\Big] + \vartheta_3(t), \tag{3}$$

$$\dot{S}_{NO}(t) = \frac{Y_h - 1}{2.86Y_h}\theta_2(t) + \frac{1}{Y_a}\theta_3(t) + \vartheta_4(t), \tag{4}$$

$$\dot{X}_{BH}(t) = \theta_1(t) + \theta_2(t) - \theta_4(t) + \vartheta_5(t), \tag{5}$$

$$\dot{X}_{BA}(t) = \theta_3(t) - \theta_5(t) + \vartheta_6(t). \tag{6}$$

where

$$\theta_1(t) = \mu_h \frac{X_{COD}(t)}{K_{COD} + X_{COD}(t)} \frac{S_O(t)}{K_{OH} + S_O(t)} X_{BH}(t)$$

$$\theta_2(t) = \mu_h \eta_{NO_g} \frac{X_{COD}(t)}{K_{COD} + X_{COD}(t)} \frac{S_{NO}(t)}{K_{NO} + S_{NO}(t)} \frac{K_{OH}}{K_{OH} + S_O(t)} X_{BH}(t)$$

$$\theta_3(t) = \mu_a \frac{S_{NH}(t)}{K_{NH,A} + S_{NH}(t)} \frac{S_O(t)}{K_{O,A} + S_O(t)} X_{BA}(t)$$

$$\theta_4(t) = b_H X_{BH}(t)$$

$$\theta_5(t) = b_A X_{BA}(t)$$

With the flow rate given as $Q_{in}(t)$, V_o as the volume of the aerobic tank and considering that $S_{0_{in}}(t), S_{NO_{in}}(t), X_{BA_{in}}(t)$ are equal to zero. $\vartheta_1(t), \vartheta_2(t), \cdots, \vartheta_6(t)$ are given as follows:

$$\vartheta_1(t) = \frac{Q_{in}(t)}{V_o}\Big[X_{COD_{in}}(t) - X_{COD}(t)\Big]$$

$$\vartheta_2(t) = \frac{Q_{in}(t)}{V_o}\Big[-S_O(t)\Big] + K_{La}(t)\Big[S_{O_{sat}} - S_O(t)\Big]$$

$$\vartheta_3(t) = \frac{Q_{in}(t)}{V_o}\Big[S_{NH_{in}}(t) - S_{NH}(t)\Big]$$

$$\vartheta_4(t) = \frac{Q_{in}(t)}{V_o}\Big[-S_{NO}(t)\Big]$$

$$\vartheta_5(t) = \frac{Q_{in}(t)}{V_o}\Big[X_{BH_{in}}(t) - \frac{f_w(1+f_r)}{f_r + f_w}X_{BH}(t)\Big]$$

$$\vartheta_6(t) = \frac{Q_{in}(t)}{V_o}\Big[X_{BA}(t) - \frac{f_w(1+f_r)}{f_r + f_w}X_{BA}(t)\Big]$$

where Y_H, Y_A, f_r, f_w, b_h, b_A, i_{xb}, and f_p are the stoichiometric parameters and μ_h, K_{COD}, K_{OH}, μ_a, $K_{NH,A}$, and $K_{O,A}$ are the kinetic parameters.

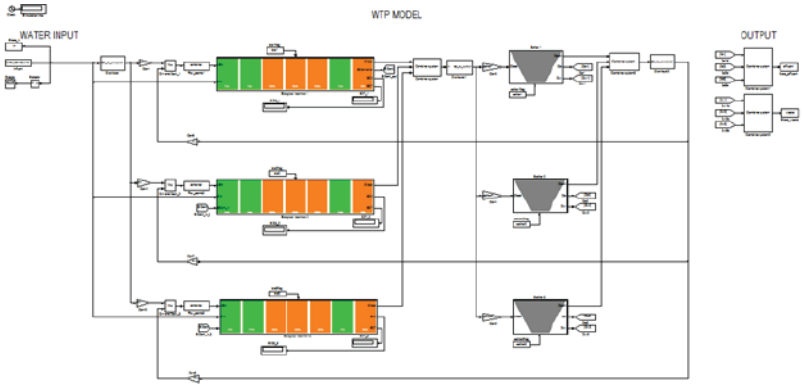

Figure 2. Layout of Girona WWTP.

2.3. LPV Representation of the WWTP

For ease of computational burden, the nonlinear reduced model is represented in a LPV form which involves the embedding of nonlinearities in varying parameters, resulting in a linear representation in state space. This procedure offers benefits when applied to MPC over its nonlinear MPC [15] and linear MPC [17] counterparts as applied on the WWTP by providing a faster run time and the avoidance of numerical problems with respect to the former and the ability to operate in a wide range of operating points with regard to the latter. The nonlinear model in this case is defined by linear systems at each time instance based on some time-varying parameters $\sigma(t) \in \mathbb{R}^{n_\sigma}$, with an assumption that the parameters $\sigma(t)$ are not known a priori but can be measured or estimated online [18]. The dynamic behavior of the LPV model is therefore described as:

$$\dot{x}(t) = A(\sigma(t))x(t) + B(\sigma(t))u(t) \tag{7}$$

$$y(t) = C(\sigma(t))x(t) + D(\sigma(t))u(t) \tag{8}$$

where $x(t) \in \mathbb{R}^{n_x}$ and $u(t) \in \mathbb{R}^{n_u}$ are the states and inputs, respectively, with $y(t) \in \mathbb{R}^{n_y}$ as the measured signals. $A(\sigma(t))$, $B(\sigma(t))$, $C(\sigma(t))$ and $D(\sigma(t))$ are time-varying matrices of appropriate dimensions that are affine in $\sigma(t) \in \mathbb{R}^{n_\sigma}$. In the quasi LPV case, the scheduling parameters are dependent on measured signals, $y_s(t) \in \mathbb{R}^k \subset y(t) \in \mathbb{R}^{n_y}$, such that

$$\sigma(t) = f(y_s(t))$$

where $f : \mathbb{R}^k \mapsto \mathbb{R}^{n_\sigma}$ is a continuous mapping [19]. With observed states and exogenous inputs ($w(t)$), nonlinearities involving the system states can be "hidden" in the varying parameters, $\sigma(t, y_s(t), w(t))$.

Therefore, from the generic nonlinear form

$$\begin{aligned} \dot{x}(t) &= f(x(t), u(t), w(t)) \\ y(t) &= g(x(t), u(t)) \end{aligned} \tag{9}$$

a linear quadruple $(A(\sigma(t, y_s(t), w(t))),\ B(\sigma(t, y_s(t), w(t))),\ C(\sigma(t, y_s(t), w(t))), and\ D(\sigma(t, y_s(t), w(t)))$ estimate is formulated and incorporated into the EMPC for a convex optimization problem. In the following, the function $\sigma(t, y_s(t), w(t)))$ will simply be represented as $\sigma(t)$. The choice of scheduling parameters considering the origin of nonlinearities in the reduced model (1) are

$$\sigma_1(t) = Q_{in}(t), \qquad \sigma_2(t) = \frac{X_{COD}(t)}{K_{COD} + X_{COD}(t)} \frac{X_{BH}(t)}{K_{OH} + S_O(t)},$$
$$\sigma_3(t) = \frac{X_{COD}(t)}{K_{COD} + X_{COD}(t)} \frac{S_{NO}(t)}{K_{NO} + S_{NO}(t)} \frac{K_{OH}}{K_{OH} + S_O(t)},$$
$$\sigma_4(t) = \frac{1}{K_{OA} + S_O(t)} \frac{S_{NH}(t)}{K_{NH} + S_{NH}(t)} X_{BH}(t), \qquad \sigma_5(t) = S_O(t).$$

The dynamic LPV model is thus given as:

$$\dot{x} = A(\sigma(t))x(t) + B(\sigma(t))u(t) + Ew(t). \tag{10}$$

with the time-varying matrices, $A(\sigma(t))$, $B(\sigma(t))$, and time-invariant disturbance matrix E as:

$$A(\sigma(t)) = \begin{bmatrix} a_{11}(t) & 0 & 0 & 0 & a_{15}(t) & a_{16} \\ 0 & a_{22}(t) & 0 & 0 & a_{25}(t) & 0 \\ 0 & a_{32}(t) & 0 & 0 & a_{35}(t) & a_{36} \\ 0 & a_{42}(t) & 0 & 0 & a_{45}(t) & 0 \\ 0 & 0 & 0 & 0 & a_{55}(t) & 0 \\ 0 & a_{62}(t) & 0 & 0 & 0 & a_{66}(t) \end{bmatrix},$$
$$B(\sigma(t)) = \begin{bmatrix} 0 \\ b_{12}(t) \\ 0 \\ 0 \\ 0 \\ 0 \end{bmatrix} \text{ and } E = \frac{1}{V_O} \begin{bmatrix} 1 & 0 & 0 \\ 0 & 0 & 0 \\ 0 & 1 & 0 \\ 0 & 0 & 0 \\ 0 & 0 & 1 \\ 0 & 0 & 0 \end{bmatrix}.$$

where

$$a_{11}(t) = \frac{\sigma_1(t)}{V_o}, \qquad a_{15}(t) = -\frac{\mu_h}{Y_h}\sigma_2(t) + (1 - f_p)b_h - \frac{\mu_h \eta_{NO_g}}{Y_h}\sigma_3(t), \qquad a_{16} = (1 - f_p)b_a,$$
$$a_{22}(t) = -\frac{\sigma_1(t)}{V_O} - \frac{4.57 - Y_a}{Y_a}\mu_a\sigma_4(t), \qquad a_{25}(t) = \frac{Y_h - 1}{Y_h}\mu_h\sigma_2(t)$$
$$a_{32}(t) = -\left(i_{xb} + \frac{1}{Y_a}\right)\mu_a\sigma_4(t), \qquad a_{35}(t) = (i_{xb} - f_p i_{xp})b_h - i_{xb}\mu_h\sigma_2(t) - (i_{xb}\mu_h\sigma_3(t)),$$
$$a_{36} = (i_{xb} - f_p i_{xb})b_a, \qquad a_{42}(t) = \frac{1}{Y_a}\mu_a\sigma_4(t), \qquad a_{45}(t) = \frac{Y_h - 1}{2.86Y_h}\mu_h\eta_{NO_g}\sigma_3(t),$$
$$a_{55}(t) = \mu_h\sigma_2(t) - b_h - \left(\frac{\sigma_1(t)}{V_O} - \frac{f_w(1 + f_r)}{f_r + f_w}\right) - b_a, \qquad a_{62}(t) = \mu_a\sigma_4(t),$$
$$a_{66}(t) = \frac{\sigma_1(t)}{V_O}\left(-\frac{f_w(1 + f_r)}{f_r + f_w} - 1 - b_a\right), \qquad b_{12}(t) = S_{sat} - \sigma_5(t).$$

The input concentrations are

$$w(t) = \begin{bmatrix} Q_{in}(t)X_{COD_{in}}(t) & Q_{in}(t)S_{NH_{in}}(t) & Q_{in}(t)X_{BH_{in}}(t) \end{bmatrix}^T.$$

Remark 1. *In this work, it is assumed that all the concentrations are measured online, but it must be noted that in practice, not all the concentrations, such as, e.g., $X_{COD_{in}}$ can be measured.*

3. EMPC of a WWTP

3.1. Operational Goals

The immediate control goal of a WWTP is to meet water quality levels established by regulators while operating efficiently by reducing operational cost. As discussed in the introduction, predictive control techniques may be used to compute strategies which achieve this goal while at the same time optimizing the system performance in terms of different operational indices. To achieve this objective, the control of dissolved oxygen concentration

as well as nitrates within certain limits is necessary. The MPC presents the advantage of being a non-conservative control strategy, such that in periods of low influents, with a minimal level of pollutants, the effluent quality can be achieved by regulating the levels of S_0 and S_{NO} below the stipulated reference point to avoid waste of energy. Subsequently, during periods of high influents levels, it is then important to meet the predefined set points to reduce pollutants, avoiding the violation of the standard effluent quality set by authorities [15]. In this work, a PI-EMPC control strategy is employed: PI designed by authors of the BSM1 for the regulation of S_{NO} and a designed EMPC for the control of S_O in the aeration tank. In the proposed LPV EMPC, the following objectives are then considered:

- **Economic costs.** The main economic costs associated with WWTP are primarily due to treatment and electricity costs. Water through the WWTP involves important electricity costs in pumping stations in charge of internal and external water recirculations as well as aeration in the aerobic tanks. In our case, only the aeration energy is considered with an objective of minimizing the cost associated with supply of oxygen for controlled culture growth. The performance index is described as follows

$$J_{eco}(k) = \frac{S_{o_{sat}}}{1800} V_o K_{La}(k) \Big[\frac{\text{kwh}}{\text{day}}\Big]. \tag{11}$$

- **DO concentration control.** In order to control the S_o within some bounds in the EMPC during the aeration process, slack variables are introduced in the optimization problem, which seek to penalize the dissolved oxygen states, such that they are maintained in a range to maintain effluent quality. Selecting slack variables, ($\lambda^+ > 0$ and $\lambda^- > 0$), additional terms of soft constraints (see (16c) and (16d)) and a quadratic objective index are introduced with x_{sp} as the selected DO concentration value. The introduction of the slack variables ensures that the DO concentration varies within a boundary around x_{sp} aided by the appropriate selection of weights in the objective function. The performance index is thus given as

$$J_\lambda(k) = \|\lambda(k)\|_2^2, \tag{12}$$

  where $\lambda(k) = \Big[\lambda^-(k), \lambda^+(k))\Big]^T$.

- **Smooth set points for equipment conservation.** The operation of WWTP and main valves and pumps usually requires smooth flow set-point variations. To obtain such a smoothing effect, the proposed MPC controller includes a third term in the objective function to penalize the control signal variation between consecutive time intervals. This term is expressed as

$$J_{smo}(k) = \Delta u(k)^T W_u \Delta u(k). \tag{13}$$

  Therefore, the performance function J considering the aforementioned control objectives has the form

$$J = w_1 \sum_{k=0}^{H_p-1} J_{eco}(k) + w_2 \sum_{k=0}^{H_p-1} J_{smo}(k) + w_3 \sum_{k=1}^{H_p} J_\lambda(k). \tag{14}$$

3.2. Control Strategy Computation

The control strategy is determined by the computation of an optimal sequence of control actions for a prediction horizon, H_p.

$$\tilde{u}_k = (u(k|j))_{j=0}^{H_{p-1}} = \big(u(k|0), u(k|1), \cdots, u(k|H_{p-1})\big). \tag{15}$$

We solve at each time instance k, the following optimal control problem with initial state obtained from measurements (or state estimation) of the dynamics WWTP model and prediction in the MPC loop with the qLPV plant model (10),

$$\min_{\tilde{u}_k} J(\tilde{u}_k, k) \tag{16a}$$

subject to

$$x(i+1|k) = A(\sigma(k))x(i|k) + B(\sigma(k))u(i|k) + Ew(i|k) \quad i = 0, \cdots, H_p - 1, \tag{16b}$$
$$x_{s_o}(i|k) >= x_{sp} + \lambda^+(i|k), \quad i = 1, \cdots, H_p, \tag{16c}$$
$$x_{s_o}(i|k) <= x_{sp} - \lambda^-(i|k), \quad i = 1, \cdots, H_p, \tag{16d}$$
$$u(i|k) \in \mathcal{U} \quad i = 0, \cdots, H_p - 1, \tag{16e}$$
$$x(i|k) \in \mathcal{X} \quad i = 1, \cdots, H_p, \tag{16f}$$
$$y(i|k) \in \mathcal{Y} \quad j = 0, \cdots, H_p, \tag{16g}$$
$$\lambda^+(i|k), \lambda^-(i|k) >= 0 \tag{16h}$$

where x_{s_o} is the dynamic state representing the soluble oxygen. (16c–f) are described by the box constraints:

$$\begin{array}{l} \mathcal{U} = \left\{ u \in \mathbb{R}^{n_u} | u^{\min} \leq u \leq u^{\max} \right\}, \\ \mathcal{X} = \left\{ x \in \mathbb{R}^{n_x} | x^{\min} \leq x \leq x^{\max} \right\}, \\ \mathcal{Y} = \left\{ y \in \mathbb{R}^{n_y} | y^{\min} \leq y \leq y^{\max} \right\}. \end{array} \tag{17}$$

which are determined from the maximum residual concentrations imposed in order to cope with the European Union effluent standards on chemical oxygen demand COD, suspended solids S_S and total nitrogen T_N:

$$COD \leqslant COD_{max} = 125\,\mathrm{g m^{-3}},$$
$$S_S \leqslant S_{Smax} = 35\,\mathrm{g m^{-3}},$$
$$T_N \leqslant T_{Nmax} = 10\,\mathrm{g m^{-3}}.$$

The first control action of the sequence $u(k|0)$ is applied to the WWTP plant to obtain the system measurements and/or MHE estimated states, which are then used in the succeeding optimization problem, resulting in a recursive procedure. Not all the state variables are measured as stated earlier; the moving horizon estimator (MHE), which is the dual of the MPC controller, estimates the unmeasurable states.

4. Moving Horizon Estimation

Since some states cannot be measured online in the operation of the WWTP, a design of an estimator, in our case the MHE, is necessary for the prediction of system outputs, bearing in mind that apart from purposes of feedback control, the quasi-LPV formulation relies on information of the system states for the model construction. By solving a constrained optimization problem, the MHE utilizes a limited N-prediction horizon of past measurements through an error minimization scheme aided by information of the system model in a prediction window to estimate the system states. The optimization problem is therefore set up with the discretized plant model as:

$$\begin{array}{ll} \min\limits_{\{\hat{x}(i|k)\}_{i=-N}^{0}} & \left(\hat{x}(-N|k) - x_o\right)^T P_o \left(\hat{x}(-N|k) - x_o\right) + \sum\limits_{i=-N}^{k} \left(\epsilon(i|)^T Q \epsilon(i|k) + s(i|k)^T R s(i|k)\right) \\ \text{s.t.} & \hat{x}(i+1|k) = A(\sigma(i|k))\hat{x}(i|k) + B(\sigma(i|k))u(i|k) + Ew(i|k) + \epsilon(i|k) \quad i = -N, \cdots, -1, \\ & y(i|k) = Cx(i|k) + s(i|k), \\ & \hat{x}_k \in \mathcal{X}. \end{array} \tag{18}$$

where $R = R^T \in \mathbb{R}^{n_y \times n_y} > 0$, $Q = Q^T \in \mathbb{R}^{n_x \times n_x} \geq 0$ and $P_o = P_o^T \in \mathbb{R}^{n_x \times n_x} \geq 0$ are the weighting matrices that are defined according to uncertainty levels induced respectively by the noise, disturbance and unknown initial conditions (x_o). $\mathcal{X}$ bounds the estimated states. At every iteration, N sets of control inputs, $\{u(i|k)\}_{i=-N}^{-1} \in \mathbb{R}^{n_u \times N}$, measurements $\{y(i|k)\}_{i=-N}^{-1} \in \mathbb{R}^{n_y \times N}$ and N sets of LPV matrices $\{A_i\}_{i=-N}^{-1} \in \mathbb{R}^{(n_x \times n_x)N}$, $\{B_i\}_{i=-N}^{-1} \in \mathbb{R}^{(n_x \times n_u)N}$ are taken as inputs into the optimization problem to predict the state sequence $\{\hat{x}(i|k)\}_{i=-N}^{0} \in \mathbb{R}^{n_x \times (N+1)}$ by solving the dynamical optimization problem (18). The last element of the sequence $\{\hat{x}(i|k)\}_{i=-N}^{0}$ is subsequently chosen as the estimated states, the measurements and inputs are then discarded, and the procedure is repeated. The ammonia concentration (S_{NH}), nitrate concentration (S_{NO}) and the soluble oxygen (S_o) are supposedly measurable; therefore, the MHE is designed for the estimation of $[X_{COD}, X_{BH}, X_{BA}]^T$ as shown in Figures 3–5 .

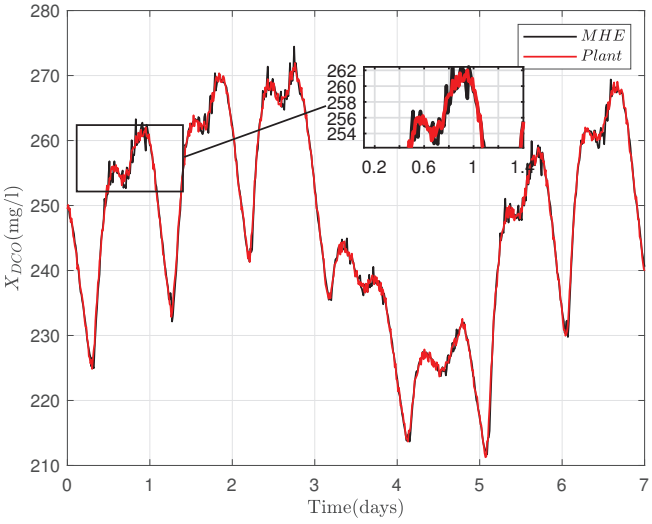

Figure 3. MHE estimate of oxygen demand concentration (X_{COD}) for 7 days.

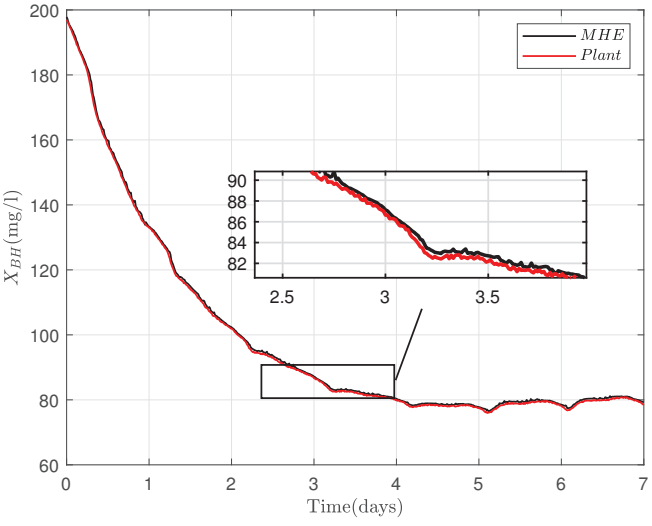

Figure 4. MHE estimate of heterotrophic biomass (X_{BH}) for 7 days.

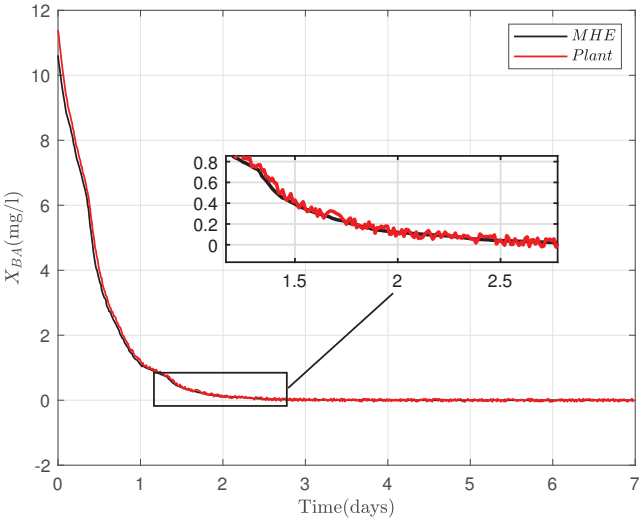

Figure 5. MHE estimate of autotrophic biomass (X_{BA}) for 7 days.

5. Simulation Results

5.1. LPV EMPC Implementation Details

To illustrate LPV EMPC approach presented in this paper, the Girona WWTP case study presented in Section 2 is used. The constituents of the influent wastewater of Girona WWTP varies during the day between the following bounds :

- Qin (between 10,000–35,000 m^3/d);
- COD (between 400–650 mg/L);
- DBO (175–225 mg/L); and
- Nitrogen (between 40–65 mg/L).

The inflow of Girona WWTP is shown in Figure 6.

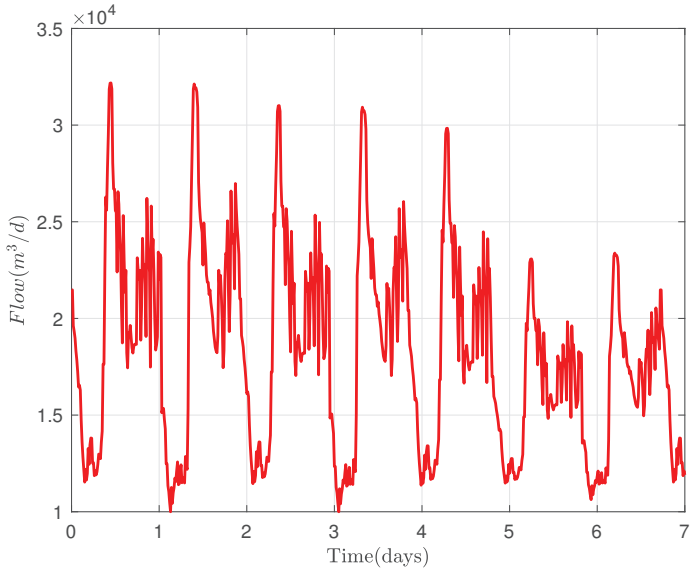

Figure 6. WWTP inflow.

With a quasi-linear approximation of the nonlinear WWTP via the LPV representation, the constrained optimization problem (16) is solved using quadratic programming formulation using the CPLEX® solver in MATLAB® on an Intel Core i7, 8 GB of RAM PC. A sampling time of 15 min and a prediction horizon of 6 h is chosen for simulation. The process is simulated for 7 days in a Simulink environment representing the dynamics of the Girona WWTP, as shown in Figure 1.

Using the weights w_i associated with the multiobjective EMPC cost function, (14) is tuned using the procedure as performed in [20,21] with the aim of maintaining the quality of the exit water at some levels within the current regulations regardless of the entry at a minimum cost.

Some control scenarios are selected to show different behaviors of the proposed scheme by altering X_{sp} and manipulating weights w_i, ideally to illustrate the different actions of aeration corresponding to different dissolved oxygen requirements for a quality effluent.

5.2. First Scenario

The first scenario consists of controlling the dissolved oxygen concentration in the exit of the biological treatment plant between the bounds $(1.5, 2.5)$. Figure 7 shows the dynamics of the DO concentration (above) and its corresponding aeration energy (below). The operation of the aeration, as stated in the preceding section, corresponds to the variation of the influents during the day; therefore, the DO concentration varies between the defined bounds in relation to the amount of pollutants at each time instance in the influents, which can be inferred from Figure 6.

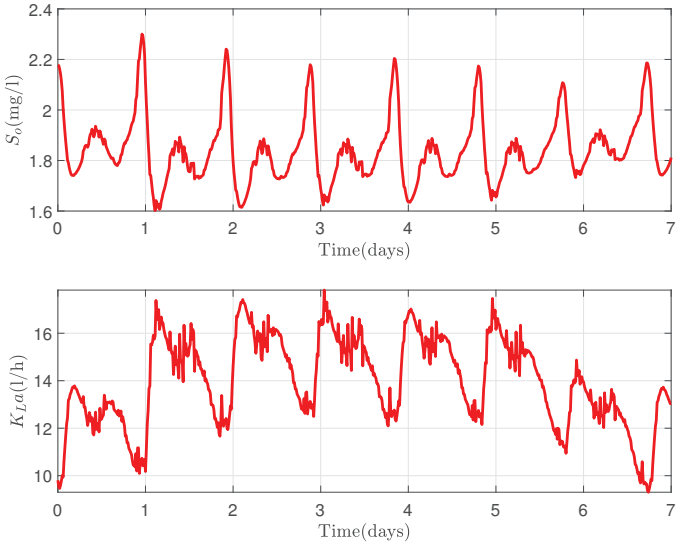

Figure 7. (**Above**): DO concentraton variation. (**Below**): Aeration flow for Scenario 1.

5.3. Second Scenario

The second scenario also consists of controlling the DO concentration between the ranges of 0.5 to 1.2 mg/L with minimum aeration energy consumption.

From Figure 8, a similar behavior of oxygen in the tanks as in the first scenario is realized with an expected less aeration energy, as less DO is required for treatment. The nitrates in the exit of the WWTP (Figure 9) range approximately between 5 and 7 mg/L.

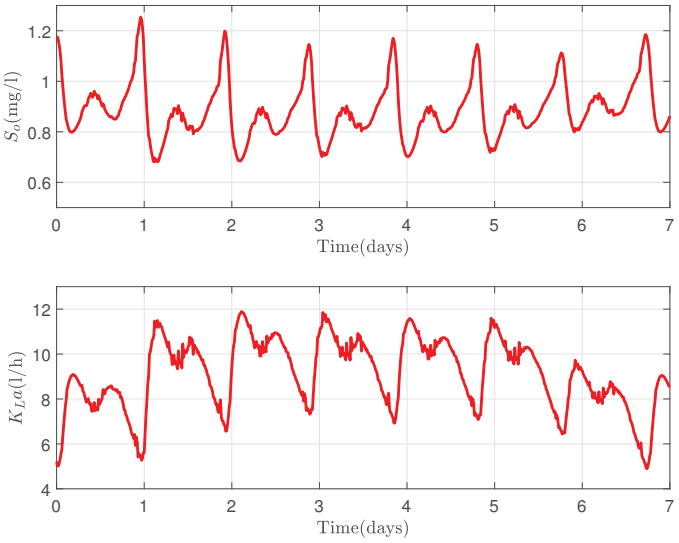

Figure 8. (**Above**): DO concentration variation and (**Below**): Aeration flow for Scenario 2.

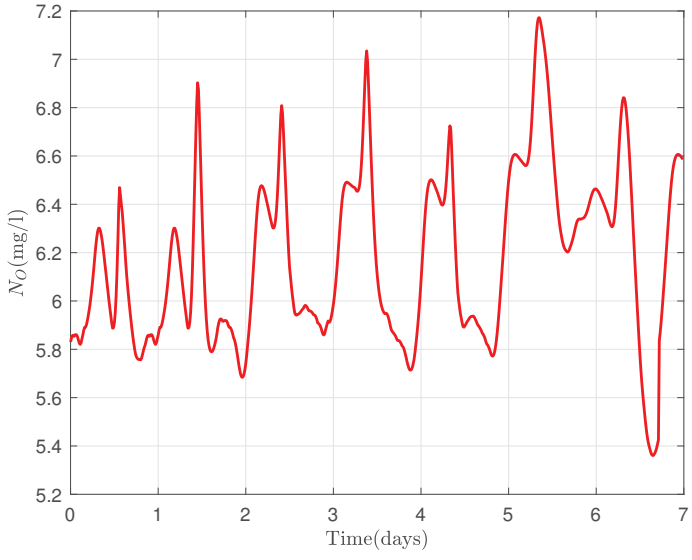

Figure 9. Nitrate concentration variation.

6. Conclusions

In this paper, an LPV EMPC strategy for the control of dissolved oxygen concentration in the aerated reactors of a WWTP is proposed and applied to the Girona (Spain) case study. The proposed approach combines two improvements with respect to the existing approaches in the literature: First, differently from standard tracking MPC, the proposed EMPC strategy optimizes the economic performance of the plant instead of following some pre-established set points. Second, a reduced model of the WWTP is represented in a quasi-LPV form allowing the real-time implementation of the controller thanks to the use of quadratic programming optimization tools. If otherwise, the nonlinear model plant was used, nonlinear programming algorithms are required that usually prevent the real-

time implementation because of the large computational time. Moreover, an LPV moving horizon state estimation scheme has also been proposed that allows the implementation of the LPV EMPC with the available sensors in the WWTP. The effectiveness of the proposed scheme has been illustrated in the considered case study with two scenarios aiming at keeping the DO within some bounds.

As future work, real testing in the WWTP plant will be conducted to further validate the performance of the proposed solution. Another issue to take into consideration is the application of the proposed methodology for aerobic conditions maintenance in sewer networks [22].

Author Contributions: Conceptualization, F.N., B.K. and V.P.; methodology, F.N., B.K. and V.P.; software, B.K. and J.P.; writing—original draft preparation, F.N.; writing—review and editing, F.N., B.K, V.P., J.P., J.Q. and S.d.C.; supervision, F.N., B.K and V.P. All authors have read and agreed to the published version of the manuscript.

Funding: This work has been co-financed by the Spanish State Research Agency (AEI) and the European Regional Development Fund (ERFD) through the project SaCoAV (ref. MINECO PID2020-114244RB-I00), by the European Regional Development Fund of the European Union in the framework of the ERDF Operational Program of Catalonia 2014–2020 (ref. 001-P-001643 Looming Factory), and by the DGR of Generalitat de Catalunya (SAC group ref. 2017/SGR/482).

Institutional Review Board Statement: Not applicable.

Informed Consent Statement: Not applicable.

Data Availability Statement: All the required data are included in the paper.

Conflicts of Interest: The authors declare no conflict of interest.

Abbreviations

The following abbreviations are used in this manuscript:

ASM	Active Sludge Model
ASP	Active Sludge Process
BSM	Benchmark Simulation Model
COD	Chemical Oxygen Demand
DO	Dissolved Oxygen
EMPC	Economic Model Predictive Control
qLPV	Quasi-Linear Parameter Varying
LPV	Linear Parameter Varying
MHE	Moving Horizon Estimator
MPC	Model Predictive Control
NEMPC	Nonlinear Economic Model Predictive Control
NMPC	Nonlinear Model Predictive Control
RTO	Real-Time Optimization
SSTO	Steady-State Target Optimizator
WWTP	Wastewater Treatment Plant

References

1. Chachuat, B.; Roche, N.; Lati, M. Long-term optimal aeration strategies for small-size alternating activated sludge treatment plants. *Chem. Eng. Process.* **2005**, *44*, 593–606. [CrossRef]
2. Jeppsson, U.; Pons, M.N. The cost benchmark simulation model current state and future perspective. *Control Eng. Pract.* **2004**, *12*, 299–304. [CrossRef]
3. Holenda, B.; Domokos, E.; Redey, A.; Fazakas, J. Dissolved oxygen control of the activated sludge wastewater treatment process using model predictive control . *Comput. Chem. Eng.* **2008**, *32*, 1270–1278. [CrossRef]
4. Santin, I.; Pedret, C.; Vilanova, R. Fuzzy control and model predictive control configurations for effluent violations removal in wastewater treatment plants. *Control Eng. Pract.* **2015**, *54*, 2763–2775. [CrossRef]
5. Maciejowski, J.M. *Predictive Control: With Constraints*; Pearson Education: London, UK, 2002.

6. Vega, P.; Revollar, S.; Francisco, M.; Martin, J. Integration of set point optimization techniques into nonlinear MPC for improving the operation of WWTPs. *Comput. Chem. Eng.* **2014**, *68*, 2763–2775. [CrossRef]
7. Ostace, G.S.; Cristea, V.M.; Agachi, P. Cost reduction of the wastewater treatment plant operation by MPC based on modified ASM1 with two-step nitrification/denitrification model. *Comput. Chem. Eng.* **2011**, *35*, 2469–2479. [CrossRef]
8. Francisco, M.; Skogestad, S.; Vega, P. Model predictive control for the self-optimized operation in wastewater treatment plants: Analysis of dynamic issues. *Comput. Chem. Eng.* **2015**, *82*, 259–272. [CrossRef]
9. Rawlings, J.; Angeli, D.; Bates, C. Fundamentals of economic model predictive control. In Proceedings of the 51st IEEE Conference on Decision and Control, Maui, HI, USA, 10–13 December 2012; pp. 3851–3861.
10. Nejjari, F.; Puig, V.; Quevedo, J.; Pascual, J.; de Campos, S. Economic Model Predictive Control of Aeration Systems in a Full Scale Biological Wastewater Treatment Plant. In *Computer Aided Chemical Engineering (Proceedings of the 27th European Symposium on Computer Aided Process Engineering)*; Elsevier: Amsterdam, The Netherlands, 2017; Volume 40, pp. 1579–1584.
11. Morato, M.M.; Normey-Rico, J.E.; Sename, O. Model predictive control design for linear parameter varying systems: A survey. *Annu. Rev. Control* **2020**, *49*, 64–80. [CrossRef]
12. Olsson, G.; Newell, B. *Wastewater Treatment Systems: Modeling, Diagnosis and Control*; IWA Publishing: London, UK, 1999.
13. Jeppsson, U.; Olsson, G. Reduced Order Models for On-Line Parameter Identification of the Activated Sludge Process. *Water Sci. Technol.* **1993**, *28*, 173–183. [CrossRef]
14. Chachuat, B.; Roche, N.; Latifi, A. Réduction du modèle ASM 1 pour la commande optimale des petites stations d'épuration à boues activées. *Rev. Des Sci. de l'eau* **2003**, *16*, 5. [CrossRef]
15. Revollar, S.; Vega, P.; Vilanova, R.; Francisco, M. Optimal Control of Wastewater Treatment Plants Using Economic-Oriented Model Predictive Dynamic Strategies. *Appl. Sci.* **2017**, *7*, 813. [CrossRef]
16. Boulkroune, B.; Darouach, M.; Zasadzinski, M.; Gillé, S.; Fiorelli, D. A nonlinear observer for an activated sludge wastewater treatment process. *J. Process Control* **2009**, *19*, 1558–1565. [CrossRef]
17. Harja, G.; Vlad, G.; Nascu, I. MPC advanced control of dissolved oxygen in an activated sludge wastewater treatment plant. In Proceedings of the 2016 IEEE International Conference on Automation, Quality and Testing, Robotics (AQTR), Cluj-Napoca, Romania, 19–21 May 2016; pp. 1–6. [CrossRef]
18. Shamma, J.; Cloutiert, J. Gain-Scheduled Missile Autopilot Design using Linear Parameter Varying Transformation. *J. Guid. Control Dyn.* **1993**, *16*, 256–263. [CrossRef]
19. Kwiatkowski, A.; Werner, H. Parameter reduction for LPV systems via principle components analysis. *IFAC Proc. Vol.* **2005**, *38*, 596–601. [CrossRef]
20. Toro, R.; Ocampo-Martinez, C.; Logist, F.; Impe, J.V.; Puig, V. Tuning of Predictive Controllers for Drinking Water Networked Systems. *IFAC Proc. Vol.* **2011**, *44*, 14507–14512. [CrossRef]
21. Ocampo-Martinez, C.; Toro, R.; Puig, V.; Van Impe, J.; Logist, F. Multi-Objective-Based Tuning of Economic Model Predictive Control of Drinking Water Transport Networks. *Water* **2022**, *14*, 1222. [CrossRef]
22. Freire Diogo, A.; Oliveira, M.A. A preliminary numerical approach for the study of compressed air injection in inverted siphons. *J. Hydraul. Eng.* **2013**, *139*, 772–784. [CrossRef]

sensors

MDPI

Article

Comparison of Optimisation Algorithms for Centralised Anaerobic Co-Digestion in a Real River Basin Case Study in Catalonia

David Palma-Heredia [1,*], Marta Verdaguer [1], Vicenç Puig [2,3], Manuel Poch [1] and Miquel Àngel Cugueró-Escofet [2]

[1] Laboratory of Chemical and Environmental Engineering (LEQUIA), Institute of the Environment, Universitat de Girona, Mª Aurelia Capmany, 69, 17003 Girona, Spain; marta.verdaguer@udg.edu (M.V.); manuel.poch@udg.edu (M.P.)
[2] Advanced Control Systems (SAC) Research Group, Polytechnic University of Catalonia (UPC-BarcelonaTech), Terrassa Campus, Gaia Research Bldg, Rambla Sant Nebridi, 22, 08222 Terrassa, Spain; vicenc.puig@upc.edu (V.P.); miquel.angel.cuguero@upc.edu (M.À.C.-E.)
[3] Institut de Robòtica i Informàtica Industrial (CSIC-UPC), 46 Llorens i Artigas Street, 08028 Barcelona, Spain
* Correspondence: david.palma@udg.edu; Tel.: +34-972-41-98-59

Abstract: Anaerobic digestion (AnD) is a process that allows the conversion of organic waste into a source of energy such as biogas, introducing sustainability and circular economy in waste treatment. AnD is an intricate process because of multiple parameters involved, and its complexity increases when the wastes are from different types of generators. In this case, a key point to achieve good performance is optimisation methods. Currently, many tools have been developed to optimise a single AnD plant. However, the study of a network of AnD plants and multiple waste generators, all in different locations, remains unexplored. This novel approach requires the use of optimisation methodologies with the capacity to deal with a highly complex combinatorial problem. This paper proposes and compares the use of three evolutionary algorithms: ant colony optimisation (ACO), genetic algorithm (GA) and particle swarm optimisation (PSO), which are especially suited for this type of application. The algorithms successfully solve the problem, using an objective function that includes terms related to quality and logistics. Their application to a real case study in Catalonia (Spain) shows their usefulness (ACO and GA to achieve maximum biogas production and PSO for safer operation conditions) for AnD facilities.

Keywords: anaerobic co-digestion; ant colony optimisation; particle swarm optimisation; genetic algorithms; waste management; circular economy

Citation: Palma-Heredia, D.; Verdaguer, M.; Puig, V.; Poch, M.; Cugueró-Escofet, M.À. Comparison of Optimisation Algorithms for Centralised Anaerobic Co-Digestion in a Real River Basin Case Study in Catalonia. *Sensors* **2022**, *22*, 1857. https://doi.org/10.3390/s22051857

Academic Editor: Ernest W. Tollner

Received: 27 January 2022
Accepted: 24 February 2022
Published: 26 February 2022

1. Introduction

In the context of global climate change with rising and more extreme events—such as droughts and floods—which will likely provide growing uncertainty to water demand and jeopardise the availability of specific resources, there is a growing interest in the adaptation and use of technologies related to the circular economy that promote environmental sustainability. In this framework, resource recovery is a key issue for industrial and environmental processes and shows a wide spectrum of study possibilities. In water sanitation, wastewater treatment plants (WWTPs) offer a wide range of possibilities for resource recovery, mainly related to sludge treatment processes [1–7] as biogas generation via the substrate co-digestion process, which can be an alternative source for thermal and electrical energy production [8–14]. This potential for biogas generation could be translated as well to a source of renewable natural gas, which has specific composition requirements that demand high-tech sensors to assure its quality no matter its origin, as those developed in [15,16]. Due to their potential for resource recovery and the further implications in the water–food–energy nexus, WWTPs have been a research focus from different areas of

expertise: from modelling and engineering design [17–24] to process dynamics, simulation and integration [25–28].

Anaerobic digestion (AnD), a complex process involved in biogas production, has a delicate balance of substrate composition. The optimal performance requires avoiding process inhibition and maximising biogas generation. The optimal balance may be achieved with the correct mixture of available substrates, but this task is challenging and difficult to achieve manually due to the high combinatorial possibilities and changing availability of substrates of heterogeneous nature. The complexity increases when the process is co-digestion, with the addition of residual substrates produced by agro-food and similar industries, each with its own dynamics of substrate generation and composition [29–32]. Additionally, not all WWTPs have an anaerobic digester. Therefore, optimisation also requires logistical challenges to process a maximum volume of the available substrates in a certain geographical area and its travel logistics (of sludge and co-substrates) from its origin to the destination digester.

Hence, dealing with such complexity is a former step to tackle optimal co-digestion in a complex network composed of many substrate sources—including WWTPs without AnD processes and industrial producers—and several co-substrate receptors. These will be located in different geographical places. As a result, the logistics of substrates will be affected by the geographical distance between actors involved and the restrictions related to the receptors.

Optimisation of the individual digester feed requires optimal blending of different co-substrates in order to fulfil the volumetric and compositional requirements of the anaerobic procedure. This problem can be understood as a multidimensional knapsack problem (MKP) [33–35]. The MKP is an NP-hard problem [36] and has been widely studied in the literature. To solve this type of problem, the use of combinatorial optimisation metaheuristics is proposed in [37,38], mainly when a high number of restrictions are presented [39].

Many tools have been developed to this end, either focused on modelling, control of the optimum co-substrate blending, or system operation, as shown in [37,39–43]. In [37,40], identification and modelling of critical parameters are performed; in [39] control schemes based on the composition qualities are developed; and in [42,43], optimised control strategies are implemented according to blend composition. In [41], logistics are also included to optimise the performance of a single anaerobic digester with co-digestion strategies.

However, in real-world installations, most of these systems are managed and supervised not in a single fashion but in a network fashion. Thus, proper system management requires simultaneous consideration of the entire AnD network to select which combination is the best for each digester to maximise the potential of the overall infrastructure. Besides, literature on this matter is relatively scarce due to its ad-hoc nature. There is literature related to optimised placement of new AnD plants, such as in [44], but it lacks optimisation of the operational part involved in the feeding of the anaerobic digesters. Very specific works can be found about optimisation of supply chain networks in the field of waste valorisation, such as in [45], where an integrated geographical information system (GIS)-based optimisation is performed, but it requires highly detailed and tailored data, so its implementation becomes time-consuming and highly dependent on data availability; furthermore, it does not tackle process optimisation regarding waste processing facilities. Regarding logistics, other works can be found for path planning optimisation such as in [46], where truck routes are traced based on GIS-oriented algorithms, or in [47], where a smart waste bin prototype is developed for sensor-based waste classification. As it can be seen, there is a gap in the literature regarding network optimisation of existing waste management facilities (such as AnD plants) that would include both logistics (i.e., minimising route impact and length) and quality (i.e., improving process performance) optimisation. This is a necessary gap to fulfil, since, as stated before, AnD networks are currently managed in an ad-hoc, manual fashion by the practitioners, which is dramatically time-consuming and needs highly qualified personnel. Although there are currently different approaches

that could help overcoming specific parts of this challenge (i.e., those observed in [44–47]), none of them can currently successfully accomplish the overall task.

The approach presented in this study continues the work introduced in [48] where the optimisation problem of blending in anaerobic co-digestion (AnCD) is handled by an ant colony optimisation (ACO) algorithm in a synthetic case study with realistic conditions, simulating a centralised AnD single-stage reactor that received feed once a day. In [41], the work is extended while considering the quality, social and travel logistics of the co-substrates, analysing its importance to the overall optimisation. In addition, ACO has been implemented in real-world waste sector case studies, e.g., [48,49]. Here, the work is extended to a similar real-world case study considering multiple receptors in the geographical area of the Besòs River basin (Catalonia, Spain). The data used correspond to the real operation conditions of this area. For these conditions, the authors have also evaluated the results obtained using different optimisation approaches such as ACO, genetic algorithms (GA) and particle swarm optimisation (PSO).

ACO, GA and PSO algorithms were selected as convenient approaches to tackle a problem of the nature stated here after reviewing applications of similar nature in the literature. In [50], a review of nature-inspired algorithms is performed, including GA, ACO and PSO—among others—for AnD modelling and optimisation, showing how in the field of AnD, PSO obtains better performance in substrate feed optimisation for agricultural biogas plants than other evolutionary methods. For example, in [51] genetic algorithms are used to minimize the environmental impact caused by mine water. The main drawback for PSO pointed out in [50] is premature convergence, since particles may become trapped in local optima or suffer stagnation, but this may be solved by a partial restart of the process introducing new particles in the search space. In [52], ACO and GA are applied to optimise the route of waste collection vehicles for municipal waste collection and transportation—the highest cost of the entire waste management system—with similar performance attained by both algorithms; however, only the problem of travel logistics is considered, not the blending of municipal waste. Ref. [53] proposes a nonlinear model predictive control strategy using the MATLAB BioOptim toolbox, developed by the same authors, for optimal control of substrate feed to AnD operation of an agricultural biogas plant, with a graphical user interface (GUI) integrating a fitness function including different operating constraints and parameters such as pH, solids or methane concentration, and using evolutionary optimisers such as PSO, covariance matrix adaptation evolution strategy (CMAES). Alternatively, they propose differential evolution (DE), which achieved better performance with PSO but without considering the substrate travel logistics in the optimisation. Ref. [54] presents a prediction and optimisation method using a multi-layer perceptron artificial neural network (ANN) and PSO for the maximisation of biogas generation in a real wastewater treatment facility. A similar approach is presented in [55], where modelling and optimisation of biogas production with mixed substrates are obtained with a combination of ANN and GA methods.

Additionally, ref. [55] and references therein point out how stochastic global optimisation algorithms (SGOAs), such as PSO, the ACO, and GA, among others, are considered efficient alternatives in the design of optimal production media and optimal process operating conditions in fermentation research and can significantly reduce the process development time. Regarding the comparison of the optimisation algorithms selected here solving combinatorial optimisation (CO) problems, in [56], ACO and GA are compared, both achieving good performance but with GA exhibiting slightly better performance than ACO. In the latter reference, it is also mentioned how trimming of specific parameters for both optimisers—e.g., number of iterations, evaporation coefficient and number of ants for ACO, or chromosome population, crossover and mutation probabilities for GA—is required to achieve good performance in both cases. In [57], relationships between GA and ACO-type algorithms are detailed, presenting their similitudes and showing how they use similar principles to succeed in CO problems with globally convex structure of its solution space. Overall, SGOAs such as ACO, GA or PSO have shown good performance

in the type of applications presented and hence demonstrated suitability for non-convex nonlinear multidimensional optimisation problems, as presented here. Optimal blending for AnCD is considered, e.g., in [40,55], but to the knowledge of the authors, the optimisation of such blending combined with the travel logistics of co-substrates in a centralised multi-receptor co-digestion strategy has not yet been studied. Additionally, a comparison between different suitable optimisation algorithms for such applications, i.e., ACO, GA and PSO, is presented.

The application of optimisation strategies in AnD allows a significant enhancement of co-digestion strategies [30] maximising biogas production and minimising associated risks to each AnD operation (e.g., overdosing or acidification). In this work, the performance of each optimisation approach considered is evaluated on a real case study in the area of the Besòs River basin in Catalonia, including a network of substrate generators and three anaerobic digesters. Hence, the objective of this study is to develop a tool that is able to optimise the centralised digestion process of an AnD network with multiple waste sources and waste receptors by means of three evolutionary optimisation algorithms—namely, ACO, GA and PSO. Such a tool is tested in a real case study to further analyse and compare the performance of each algorithm in the overall AnD network optimisation.

2. Material and Methods

2.1. Optimisation Algorithms Considered

The optimisation algorithms presented here fall within the set of SGOA, concretely in the subset of evolutionary algorithms (EA) for GA—which use mechanisms inspired by biological evolution, e.g., mutation or recombination to achieve the goal of optimisation—and in the subset of swarm intelligence methods for ACO and PSO based on the collective behaviour of self-organised decentralised systems, respectively. SGOA algorithms have been widely used to solve NP-hard combinatorial optimisation problems, such as that presented in this study, which deterministic optimisation methods fail to handle due to their complexity.

Regarding each proposal, ACO is a metaheuristic approach that has been shown to be effective in solving a variety of NP-hard problems [58]. The algorithm is based on simulation of the behaviour of real ants in their search for food. When ants find food, they leave a pheromone trail on their path. Then, new ants follow that trail. In this way, an increasing number of ants are concentrated in places where there is food. In a similar way, the virtual ants construct a solution moving through the graph that represents the search space of solutions. Their paths are guided by a probabilistic state transition rule, which is based on pheromone trails and specific heuristic information. The algorithmic procedure is iterative. At each iteration, the pheromone trails are updated by applying an evaporation coefficient (when the value selected is not part of a feasible solution). To avoid rapid stagnation of the solution, the ACO algorithms can use several strategies [59], such as that related to the limitation of the pheromone trails between maximum and minimum values. Max–Min Ant System [60] uses this procedure.

The GA is a metaheuristic approach also used in combinatorial optimisation problems. It is based on the mechanics of natural selection and natural genetics. GA applications cover a range of combinatorial optimisations, e.g., hydraulic model calibration [61], performance of photovoltaic systems under variable atmospheric conditions [62], and sensor placement for leak detection in water distribution networks [39,63]. The GA is based on three main parameters: selection, crossover and mutation. The population matrix is randomly generated and consists of the design variables, and the best variables are selected according to their fitness value. From these solutions, new solutions are produced via the crossover operator [64]. The mutation operator is finally employed to avoid the algorithm converging to local optima (i.e., to maintain the genetic diversity).

The GA cycle is repeated through a number of generations until a stopping criterion is met. It is worth noting that elitism is not generally considered an operator in the canonical GA. However, it is deemed a robust and effective operator because it leads the optimisation

procedure towards the optimal solution. Accordingly, this operator stops the best solutions from being mutated. In this way, the best solutions of each generation would pass to the next, unaltered. Over the course of the algorithm and through a sufficient number of generations, the traits of these solutions would transfer to their offspring, increasing the chance of producing new solutions whose fitness function values might be better than their parents [64]. Some drawbacks of GAs are noted in [61], e.g., achieving a global optimum for large and complex systems is not guaranteed, which is also a drawback for ACO. In [57], the relation between GAs and ACO is noted.

PSO is a recently developed EA that includes features such as easy implementation for solving practical problems, high accuracy and fast convergence of the solution as some of its main advantages [65,66]. While similarities exist in the iterative nature of PSO and GAs, conversely, in PSO, there are no, e.g., "crossover" or "mutation" operations. Instead, PSO is based on a population of candidate solutions, defined as particles. The set of particles composes a swarm, where each individual flows through the parameter space. The flow of such particles is defined by trajectories, which are driven by the best performance of the particle and the neighbouring particles in the parameter space. The initialization of particle swarm is random. The initial solution of each particle represents an alternative solution; that is, each particle has its own initial position and speed and is randomly distributed in each position of the feasible solution space to be searched. Therefore, the initialization of the particle swarm represents the preparation of the particle swarm search. Its size is determined by its speed and position, and the particle update is based on the comparison of the fitness values between each search particle and its neighbouring search particles to determine the necessity of updating a particle. The updated particle adjusts its speed and position according to the particle's new flight path model, which is based on the best results achieved by its neighbouring particles. These conditions yield different optimal experiences for different particle subgroups, which dynamically evolve according to the current position of particles, the particle current velocities, the distance between each particle of the subgroup and its best position and the distance between each particle of the subgroup and the best position of the whole subgroup.

The PSO algorithm does not need cross-mutation or other genetically inspired operations, so the algorithm has fewer parameters and is still high efficiency [65]. These properties are suitable for both engineering applications and scientific research, and a significant number of research results have been produced in recent years [67]. For example, in [68], PSO is applied for function optimisation regarding eco-economics modelling and assessment; in [69], it is used as part of fuzzy systems developed to optimise fuel consumption of hybrid vehicles; and in [70], PSO is used to train neural network models and perform real-time optimisation.

2.2. Centralised Co-Digestion as an Optimisation Problem

Mathematical optimisation involves the selection of one solution amongst a set, according to some criterion and constraints (that is, the optimisation problem). This optimisation problem can be stated as:

$$\min_{x \in X} f(x) \text{ subject to } g(x), \tag{1}$$

where $f(x)$ is the objective or cost function, X is a feasible region and $g(x)$ are the constraints that have to hold to find a minimiser x^* of $f(x)$ such that $f(x^*) = \min_{x \in X} f(x)$. ACO, GA and PSO introduced in Section 2.1 are algorithms aimed at finding the optimal solution of the optimisation problem posed in (1)—i.e., minimise the objective function $f(\cdot)$ subject to the set of constraints $g(x)$ that apply—which here consists of the selection of the best substrates and volumes according to a set of restrictions related to the operation of the anaerobic digester. In addition, the cost function allows quantifying each alternative potential solution according to (1), involving the calculation of a value or "cost" associated with each alternative considered to find the optimal solution.

The problem statement is similar to that presented in [41], although the number of waste receptors increases from one to three, thus making necessary a reformulation of

the optimisation problem involved. Specifically, it is required to increase the dimensions of all data vectors that define each generator-receptor interaction and their subsequent calculations. In addition, matrix operations are repeated per new dimension (i.e., waste receptor) added.

This optimisation problem, which can be understood as a MKP and is of combinatorial nature, can be represented as a matching problem. It is defined with a graph $G = (N, E)$ that summarises all the possible combinations. The graph consists of N vertices (or nodes) and E edges or pairs of vertices. Specifically, for the case of AnD optimisation, a bipartite graph can be used to represent the posed optimisation problem to differentiate between the set of waste generators (N_1), containing W nodes, and the set of waste receptors (N_2), containing R nodes. For the specific optimisation problem, all W nodes are connected to each R node, thus resulting in a total of $W{\cdot}R = E$ edges. Figure 1 shows a generic representation of the defined matching problem applied to AnD co-digestion optimisation.

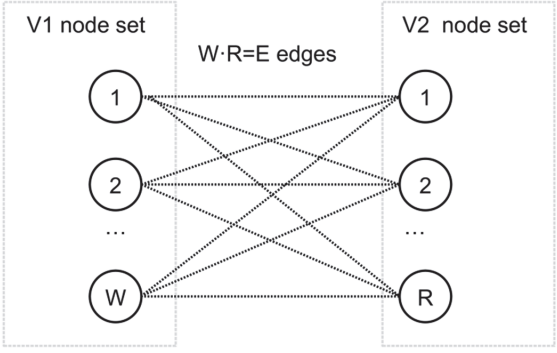

Figure 1. Generic representation of the posed matching problem.

A set of substrate generators $w \in \{1, \ldots, N\}$ is considered. The volume of each substrate V_w can be selected as a contribution to any of the AnD systems. The binary decision variable y_w^s allows generating array volumetric possibilities (V_w^s, with $s \in \{0 \ldots, l_w\}$ that are determined as a multiple of a number (e.g., 1000 by default) such that $1000 l_w = V_w$. The selection of each volumetric possibility is determined by the corresponding value of the binary decision variable, y_w^s, where $y \in \{0, 1\}$, with $y_w^s = 0$ when the corresponding volumetric configuration is not selected, and $y_w^s = 1$ when it is selected. Note that for each waste generator w, there are l_w different volumetric configurations in y_w^s, but only one is selected at a time, i.e., $\sum_{s=1}^{l_w} y_w^s = 1 \; \forall w \in \{1 \ldots, N\}$.

To normalise the objective function, selected volumes V_w^s are divided by the maximum volume from their corresponding waste generator (V_w). This approach provides values of the cost function between 0 and 1, where the closest to 1 the better the solution. However, note that the ACO algorithm looks for a maximum of the objective function, while GA and PSO look for a minimum. This behaviour is considered using the constant $K \in \{-1, 1\}$, which depends on the algorithm considered: for the ACO algorithm $K = 1$ and for the GA and PSO algorithms $K = -1$. Hence, cost index B would take positive values between 0 and 1 for ACO and negative values between 0 and -1 for GA and PSO. Instead, the absolute value is taken for all three algorithms.

F_w^c ($c = 1, \ldots, 3$) and T_w are the set of dimensionless coefficients corresponding to the substrate characterisation and the quality term $\left(\sum_{c=1}^{3} F_w^c\right)\rho_q$, already used and explained previously in [41,46] and defined as shown in Figure 2.

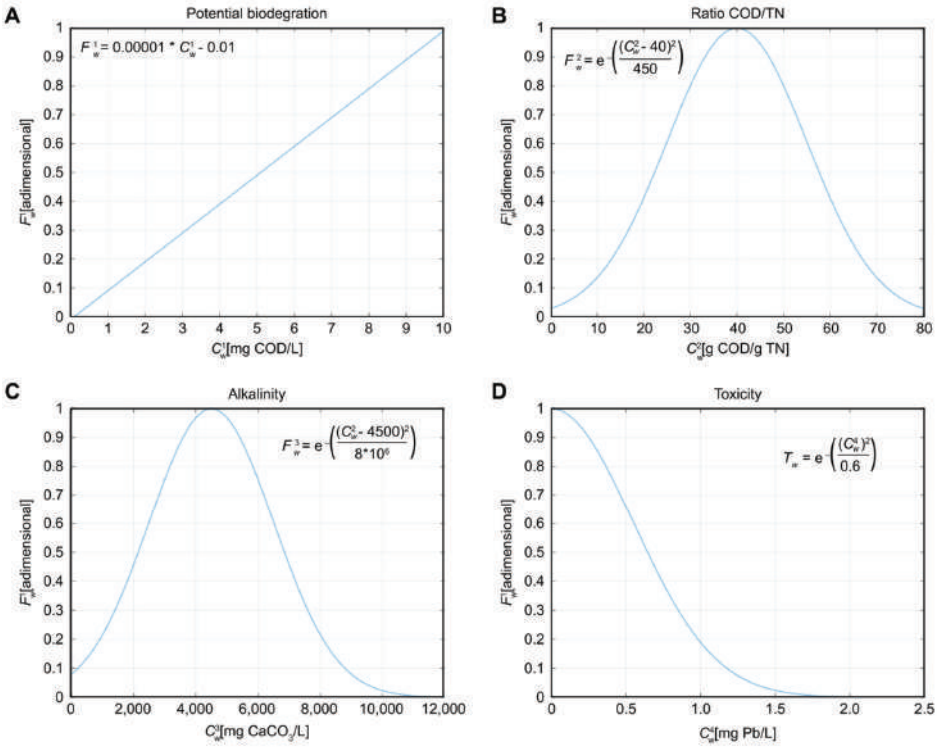

Figure 2. (**A**) F_w^1, (**B**) F_w^2, (**C**) F_w^3 and (**D**) T_w equations used for dimensionless coefficient calculation.

F_w^1 is a coefficient related to the potential biogas production, measured as a function of the Chemical Oxygen Demand (*COD*) content. F_w^2 indicates the ratio of *COD*/*TN* (where *TN* refers to Total Nitrogen), a useful measure to prevent situations of acidification and other undesired reactions of the AnD process, as long as it is maintained around the range of 20–60. F_w^3 is linked to the alkalinity (Alk) concentration, and it is associated with a restriction ranging from 2500 to 6000 mg $CaCO_3$/L integrated within all optimisation algorithms. T_w is a coefficient of the utmost importance since it describes the toxicity level of all waste fluxes, which should be kept at the lowest level possible (specifically below 2.1 mg Pb/L).

The N different substrate generators are located at different distances (d_w) from each anaerobic digester. The conveyance of the selected volumes implies a travel distance d_w (in km) with an economic cost x_w (in €/km) and a social impact $I_w = 1, \ldots, 3$ (dimensionless). The higher the value of I_w, the higher the social impact of the related route (e.g., proximity to sensitive areas due to pollution, traffic density, or pedestrian presence). Since each route is different for each generator, different values are assigned to approach the logistic impact of the corresponding waste generator, so a value for I_w is assigned for each sludge/substrate generator depending on its route to the ST.

The coefficient weight ρ_q (dimensionless) is related to the quality term $\left(\sum_{c=1}^{3} F_w^c\right)\rho_q$, and the coefficient ρ_x (dimensionless) is the coefficient that weights the logistics term $\frac{\rho_x}{X_w d_w I_w}$. Each weight is given a value of 0.5 to provide a balance between the quality and logistics terms in the optimisation. Selected volumes of each substrate to each receptor contribute to the input to the AnD network, and the aforementioned parameters constitute the objective or cost function $f(x)$.

Additionally, the optimisation problem presented considers a set of restrictions $g(x)$ related to each of the total inputs to each of the receptor systems, based on those presented

in [41,48]. The first restriction is the sum of accepted substrates $\sum_{w=1}^{N}\sum_{s=0}^{l_w} y_w^s V_w^s$ must not exceed the maximum acceptable volume V for each AnD system. Moreover, the COD/TN ratio, related to the dimensionless coefficient F_w^2, must be kept within the range $\left[C_{min}^2, C_{max}^2\right]$. The alkalinity concentration, related to the dimensionless coefficient F_w^3, must also be kept within the range $\left[C_{min}^3, C_{max}^3\right]$. The toxicity level, related to T_w, does not require restriction since the corresponding coefficient T_w is considered to be restrictive enough, as shown in Figure 2.

In addition, an estimation of the produced biogas is made assuming a conversion factor of 0.268 m^3 biogas/kg COD. Finally, note that the cost function presented in this work is adapted from [41,48], where the ACO algorithm was used for waste management optimisation in a similar fashion but limited to one AnD receptor.

The objective function $f(x)$ for the presented optimisation problem is as follows in (2). However, note that the performance comparison of the ACO, GA and PSO algorithms is not conducted directly on the value of the optimised objective function, B', but on its absolute value, B, as shown in (3).

$$B' = K\left\{\sum_{w=1}^{N}\sum_{s=0}^{l_w} y_w^s \frac{V_w^s}{V_w} T_w \left[\left(\sum_{c=1}^{3} F_w^c\right)\rho_q + \frac{\rho_x}{X_w d_w I_w}\right]\right\} \tag{2}$$

$$B = \left|B'\right| \tag{3}$$

3. Results

3.1. Case Study

The case study includes a network of 19 organic waste generators and three organic waste receptors. These 22 locations (i.e., 19 generators and 3 receptors) are part of the wastewater treatment system managed by Consorci Besòs Tordera (CBT), a public local water administration composed of 64 municipalities in four different regions of Catalonia (Spain) with a population of approximately 470,000 inhabitants. This case study and its anaerobic network system were also considered in [41]. Figure 3 shows the corresponding bipartite graph of the case study.

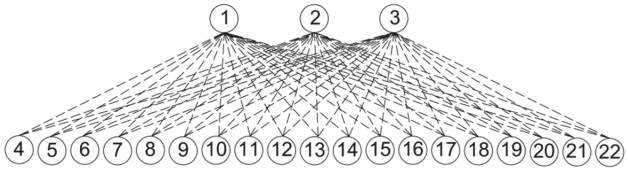

Figure 3. Bipartite graph of the case study.

The three organic waste receptors (R1–R3, or nodes 1–3 of Figure 3) refer to three separate WWTPs that produce their own sewage sludge, but that also have available AnD technology. Due to oversized design, which is a usual practice in WWTP design [71], these AnD systems in R1–R3 have available capacity. This free excess capacity can be used to accept wastes from external sources, such as the undigested sewage sludge of W1–W12 or the industrial substrates from C1–C7.

The 19 waste generators consist of 12 WWTPs that produce undigested sewage sludge (W1–W12, or nodes 4–15 of Figure 3) and seven industrial substrate generators (C1–C7, or nodes 16–22 of Figure 3), which were considered suitable sources of organic waste for the AnD network under study. Each of these locations is a separate and independent system that must manage its own waste produced as best as possible. Additionally, seven industrial substrate generators have been previously verified as feasible substrates for AnD by CBT technical services.

3.2. Simulation Methodology

The algorithms used in this work have been implemented in the MATLAB environment. Simulations were performed with a Lenovo ThinkPad (Lenovo Group, Ltd., Girona, Spain) L14 Gen1-20U10016SP ×64 using the OS Microsoft Windows 10 Pro and an Intel(R) Core(TM) i7-10510U CPU processor (1.80 GHz, 2304 MHz) consisting of four main processors and eight logic processors.

The main optimisation parameters of both GA and PSO algorithms were trimmed in an attempt to select the most suitable array to provide reliable results. Accordingly, the same procedure was already performed for the ACO algorithm to determine the values of its corresponding optimisation parameters in [48], where the same optimisation parameters are used in this work.

For the ACO algorithm, an initial population of 100 individuals (or ants) and 500 iterations per repetition is set, and the values used for the algorithm optimisation parameters are $\alpha = 1$, $\beta = 2$ and $\rho = 0.98$, each corresponding to the importance assigned to the pheromone trail, the importance assigned to the heuristic information and the persistence degree or pheromone evaporation, as explained in [38,58,60]. For GA, the initial population is set to 100, the total number of iterations (or generations) is set to 500, the crossover fraction is set to 0.8 and the fraction of elite children is set to 5% of the corresponding total children. For PSO, the initial population was set to 100, the total number of iterations was set to 500, cognitive attraction was set to 0.8 and the social attraction factor is set to 1.25. Tables 1 and 2 summarise trimming tests for GA and PSO, respectively, where the best results are obtained for higher values of objective index *B*.

Table 1. Summary of trimming tests for the GA.

Tested Parameters		Best Index (*B*)	Time(s)
Crossover Fraction	0.2	0.0274	525.73
	0.5	0.0295	574.46
	0.8	**0.0304**	**537.98**
Elite Count	**0.05**	**0.0309**	**541.48**
	0.15	0.0300	536.15
	0.3	0.0291	554.83

Table 2. Summary of trimming tests for PSO.

Tested Parameters		Best Index (*B*)	Time(s)
Cognitive Attraction	0.2	0.0293	82.86
	0.5	0.0304	62.93
	0.8	**0.0322**	**57.26**
Social Attraction	1.05	0.0301	55.78
	1.25	**0.0329**	**74.98**
	1.95	0.0308	63.45

For the sake of performance comparison, some parameters were fixed for the three algorithms. The fixed parameters are the number of independent simulations (set to 10, the best result is selected), the population (set to 100 individuals), and the maximum number of iterations (set to 500). With these constraints on algorithm trimming, a performance comparison of ACO, GA and PSO was conducted.

The comparison of ACO, GA and PSO performances is based on the value of the fitness function, execution time and an array of technical variables related to the total expected performance of the optimised AnD network: total daily biogas production (in Nm^3), average organic load (in kg of COD per m^3 of volume of the digestion system and day), average carbon to nitrogen ratio (C/N), and average alkalinity (in mg of $CaCO_3$). All algorithms are tested with data from a real case study as the main simulation scenario.

However, other synthetic scenarios are tested to further compare the performance of each algorithm under different scenario conditions.

In the approach presented here, simulated scenarios are based on the waste generator data in Table 3, alongside route distance and receptor system characterisation. For all the 19 waste generators (i.e., the 12 WWTPs without AnD and the seven substrate generators), the addition to the AnD network is optimised. For each of the three AnD systems (i.e., receptors R1, R2 and R3), different volume constraints have been determined, according to operational data and assuming a limit to the hydraulic retention time of 20 days (below that retention time, AnD efficiency is expected to greatly decrease).

Table 3. Waste generator dataset, including distance between waste generators and receptors and characterisation of each receptor of the case study (Baseline Scenario or Scenario 0).

Waste Generator ID	Vw (L by Day)	COD (mg/L)	C/N	Alk (mg/L)	Tw (mg/L)	R1 Distance to R1 (km)	R2 Distance to R2 (km)	R3 Distance to R3 (km)
W1	27,600	19,900	17.8	4300	1.55	5.3	20.5	9.5
W2	47,000	16,900	20.6	3200	1.36	35.9	33.9	45.7
W3	46,300	18,600	19.4	10,100	1.42	21.8	16.6	28.9
W4	20,200	23,400	15.6	3400	1.38	30.4	43.2	19.7
W5	38,400	21,100	17.9	4500	1.35	19.7	24.7	12.4
W6	34,400	18,800	14.0	3800	1.61	14.8	19.9	15.9
W7	13,800	22,600	15.3	2700	1.57	32.1	44.9	18.4
W8	4400	22,100	15.2	1800	2.30	26.5	31.6	27.7
W9	10,800	21,700	15.1	5300	0.93	20.3	33.1	8.8
W10	9500	20,400	15.5	2500	1.28	30	24.8	37.1
W11	17,000	23,300	14.8	7800	0.98	36.9	31.7	44
W12	6500	20,100	16.5	3100	1.40	20.5	33.3	8.7
C1	9000	667,400	42.5	250	0.01	15.9	11.1	23
C2	9000	497,400	461.8	330	0.01	7	12	17.9
C3	9000	155,900	3118.1	60	0.02	27.9	40.7	17.2
C4	9000	459,100	274.1	660	0.10	16.2	11.1	22.9
C5	9000	657,200	2330.6	630	0.01	52.8	65.6	43.8
C6	9000	266,200	2832.4	20	0.01	56.1	33	21
C7	9000	262,100	32,768.4	110	0.01	36.7	24.1	66.4
Maximum Volume (L/day)						122,000	146,000	111,000
COD (mg/L)						18,600	19,100	18,200
C/N						19.1	20.3	18.4
Alk (mg/L)						3100	2900	3400
Tw (mg/L)						1.41	1.68	1.53

Each simulation for ACO, GA and PSO is repeated 10 times since these algorithms have probabilistic, iterative-based search methods. The best solution among these runs is selected for further analysis, although the average fitness function is also registered for discussion.

The data obtained for ACO, GA and PSO (each comprising 10 repetitions of the corresponding algorithm) are compared for every simulated scenario. The baseline scenario (i.e., Scenario 0) corresponds to the real case study, as described in Table 3. Additional synthetic Scenarios 1–4 are simulated, and their corresponding data are created from alterations of the baseline scenario, as described in Table 4.

Table 4. Synthetic scenarios created from original Scenario 0 in Table 3. Description of data alteration procedure.

ID	Description
Baseline (Scenario 0) scenario	Scenario based on data form real case study (see Table 3)
Scenario 1	High COD (×10 COD concentration)
Scenario 2a	Linear modification of distances: ×10 distances
Scenario 2b	Nonlinear modification of distances: square root of original distance
Scenario 3	High volumes (×3 volumes)
Scenario 4	C/N variations (increase of W1–W12 C/N ratio to the 50–60 range)

While for Scenarios 1 and 2 any modification is viable, for Scenario 3, an increase in volume involves a significant increase in execution time. This is because the optimisation problem works around combinations of fixed volumes, and an increase in volume would involve a higher number of possible combinations for the algorithms to consider (i.e., an increase in the search space), hence the expected increase in execution time. Thus, volume modification for Scenario 3 was limited to a triple increase in the baseline scenario volume. Alternatively, for Scenario 4, the C/N ratios were modified while being kept below 60 to facilitate the algorithms in finding a viable solution. This measure was adopted because the C/N ratio was the most limiting optimisation parameter in previous applications of a similar optimisation problem in [41]. Scenario 2 was designed with both linear and nonlinear distance modifications (Scenarios 2a and 2b, respectively) to discuss the effect of distance distribution, as pointed out in [41]. Note that trimming tests were carried out only for GA and PSO using the baseline scenario, assuming that trimmed parameters would suffice for simulation of other synthetic scenarios similar to the baseline scenario.

The optimisation results are presented as a sequence of contributions from all the generators to each anaerobic digester. This optimised contribution sequence can be considered a suggested logistic plan for the co-substrate distribution as follows: once enough substrate has been produced and stocked on a waste generator, a truck of 20 metric tonnes capacity would be fully loaded with substrate from the corresponding waste generator, disregarding the truck waiting time before starting each route; once fully loaded, the truck is assumed to travel to the waste receptor without further stops (assuming it always follows the same route). As long as the cycle of supply routes of all involved waste generators is completed within the AnD retention time of 20 days, the properties of the resulting blending should not vary significantly, especially considering that every waste receptor would have a receiving system for these external organic substrates, where they would be stored and blended before being added to the AnD system. The specific start and finish time for each route along the day have not been considered; this does not affect the optimisation, although it has been noted that it has considerable impact on real-world implementation.

3.3. Algorithm Performance Comparison and Scenario Analysis

The simulation results for each scenario are shown in Table 5. For every scenario and for ACO, GA and PSO, this table shows the best cost index (B) achieved, elapsed optimisation time, and additional parameters related to the performance of the AnD systems: total biogas production, average organic load, average carbon/nitrogen ratio and average alkalinity.

In the baseline scenario, ACO and GA show higher biogas production than PSO (23% and 30% higher, respectively). However, they show a slightly lower *B* index achieved (4% and 11% lower). This result indicates that although one of the main goals of AnD optimisation involves maximising biogas production, it is not all that matters because there are other parameters also subjected to optimisation. PSO appears to find a solution with lower biogas production but better optimises other quality parameters, such as the C/N ratio and alkalinity. However, it is remarkable that out of the three algorithms, ACO

and GA find a "similar solution" (prioritising high biogas production), and PSO fins a significantly different solution (prioritising other quality-related parameters).

Table 5. Summary of algorithm performance. The best value *B* is highlighted. Scenario 2a feasible results (*) are associated with a poor solution, so no direct comparison is conducted.

Scenario	**Baseline Scenario**			**Scenario 1**		
Optimisation Method	**ACO**	**GA**	**PSO**	**ACO**	**GA**	**PSO**
Best Index (B)	0.0336	0.0313	**0.0349**	**0.0330**	0.0328	0.0211
Time (seconds)	595.46	325.37	**90.20**	1825.34	1035.53	**221.74**
Total Biogas Production (Nm^3/d)	25,657	**27,133**	20,852	114,870	**198,284**	102,927
Avg Organic Load ($kg\ COD/m^3 \cdot d$)	2.32	**2.59**	2.09	9.67	**17.46**	9.73
Avg C/N ratio (limited below 60)	50.5	56.1	**46.4**	24.1	54	**32.4**
Avg Alkalinity ($g\ CaCO_3/m^3$)	3079	3141	**3245**	3183	3193	**3282**
Scenario	**Scenario 2a**			**Scenario 2b**		
Optimisation Method	**ACO**	**GA**	**PSO**	**ACO**	**GA**	**PSO**
Best Index (B)	-	0.0001 *	0.0001 *	0.0287	**0.0333**	0.0319
Time (seconds)	-	62	60	669.56	193	**63.61**
Total Biogas Production (Nm^3/d)	-	14,278	12,325	17,468	**25,404**	19,237
Avg Organic Load ($kg\ COD/m^3 \cdot d$)	-	1.6	1.4	1.69	**2.5**	2.24
Avg C/N ratio (limited below 60)	-	45.9	32.8	23.4	55.2	**32.4**
Avg Alkalinity ($g\ CaCO_3/m^3$)	-	3298	3319	**3338**	3174	3221
Scenario	**Scenario 3**			**Scenario 4**		
Optimisation Method	**ACO**	**GA**	**PSO**	**ACO**	**GA**	**PSO**
Best Index (B)	0.0077	**0.0324**	0.0300	0.0339	0.0319	**0.0354**
Time (seconds)	671.03	548.46	**68.10**	1824.94	350.89	**86.47**
Total Biogas Production (Nm^3/d)	17,224	33,657	**35,395**	20,770	**23,326**	19,524
Avg Organic Load ($kg\ COD/m^3 \cdot d$)	1.70	2.79	**2.92**	2.02	**2.23**	1.90
Avg C/N ratio (limited below 60)	19.1	26.3	**32.9**	35.9	56.4	**37.8**
Avg Alkalinity ($g\ CaCO_3/m^3$) (limited above 2500)	2985	3020	**3233**	3217	3199	**3272**

In Scenario 1, the COD concentration was increased tenfold. This was done to compare the efficiency of algorithms to optimise substrates with high organic loads, which is especially meaningful for maximisation of biogas production. For this scenario, ACO and GA have better performance, according to the best index *B* achieved. As a natural consequence of substantial COD increases, biogas production also dramatically increases. However, PSO is unable to achieve a competitive solution in relation to both ACO and GA within this scenario and the baseline scenario, respectively.

In Scenario 2a, a tenfold lineal increase in the geographical distances between facilities was conducted. This scenario allows comparing how well each algorithm can handle situations where most substrates have long distances. For this scenario, ACO is unable to find a feasible solution. On the other hand, GA and PSO find a solution, but the corresponding biogas production is far lower than that obtained in the baseline scenario (48% and 41% lower biogas production for GA and PSO, respectively).

Alternatively, Scenario 2b shows the optimisation results when nonlinearly modifying geographical distances between facilities by the square root of the original distances. This modification allows understanding which algorithm would be more favoured by a more equally distributed geographic location of plants. All the algorithms tested are able to find a feasible solution, showing that GA has the best performance (both in terms of best *B* and biogas production). On the other hand, ACO shows the worst best index *B* achieved.

Scenario 3 was modified by a threefold increase in available volume from all sources. The presented modification allows studying the performance of each algorithm when the total number of possible solutions is much greater. ACO shows noticeably poor performance, below the best index *B* achieved by ACO in former scenarios. Although GA shows better performance than PSO in terms of the best index *B* achieved, biogas production appears similar to that in other scenarios.

In Scenario 4, an increase in the C/N ratio for waste generators W1–W12 was conducted. This modification would test the ability of each algorithm when one of the restrictions (i.e., C/N ratio) requires more adjustments. In this case, PSO shows the best index *B* achieved, although it presents the lowest biogas production. Similar to the baseline scenario, ACO shows slightly better performance than GA in terms of the best *B* achieved, but GA still has slightly better biogas production.

Geographical distance modification was performed with two alternative scenarios. Scenario 2a includes a lineal modification of the distance matrix (tenfold), and Scenario 2b considers a distance modified by the square root of the original distance. The relative locations of all involved waste generators and receptors in the case study are shown in Figure 4. For the baseline scenario, waste generators are homogeneously geographically distributed, but receptors are located in a relatively small area—i.e., the geographical distance difference of each receptor from the emitters might be negligible by the optimisation—which may be interpreted as a single receptor with higher volume capacity, caused by the geographical overlapping of waste receptors, or the "big dot" effect. The linear modification of geographical distances in Scenario 2a does not alter this relative distribution, but the nonlinear modification in Scenario 2b does so, avoiding this "big dot" effect by dispersing Receptors A, B, and C in the geographical space. It is important to note that for Scenario 2a, ACO was unable to find a viable solution, and both GA and PSO achieved a relatively poor solution compared to the corresponding solutions for the baseline scenario.

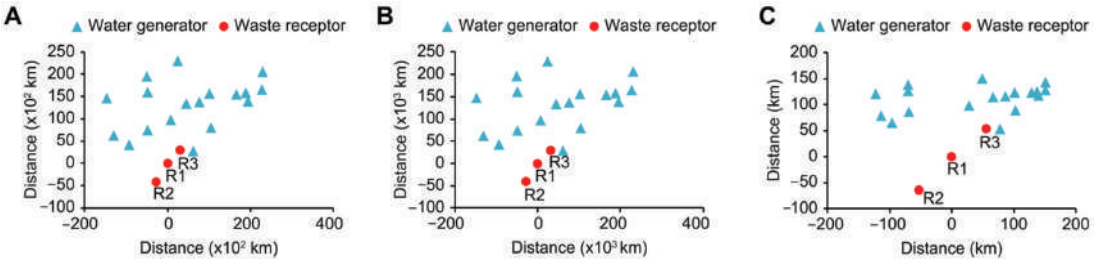

Figure 4. Map of waste generators and waste receptors R1–R3 for Baseline Scenario (**A**), Scenario 2a (**B**) and Scenario 2b (**C**). Distance is expressed as longitudinal distance (X-axis) and latitudinal distance (*Y*-axis) with respect to the R1 plant.

Figure 5 shows the resulting blending profile for the baseline scenario and Scenario 2b. For the baseline scenario, PSO tends to balance the blending of substrates with a low organic load content—i.e., from W1–W12—and selects noticeably lower amounts of high organic load substrates—i.e., from C1–C7— than ACO or GA. This observed behaviour is similar between the three waste receptors A, B and C. On the other hand, ACO and GA tend towards selective blending, showing similar preferences for both receptors B and C. For receptor A, the GA algorithm tends towards slightly more homogeneous blending. In any case, both ACO and GA include more substrates of high organic load—i.e., from C1–C7—except for receptor C.

For Scenario 2b, the ACO blending profiles are similar to those obtained in the baseline scenario—showing a certain tendency to include particular waste generators, —although varying the substrates that the algorithm selects. The GA blending profiles obtained in Scenario 2b are the most affected by geographical distance distortion. GA appears to balance the blending of substrates from all waste generators, much like PSO for both

scenarios 2a and 2b. Additionally, the GA blending profile for Scenario 2b accounts for more industrial, high organic load wastes—i.e., from C1–C7—than the PSO blending profile, which remains relatively similar between the baseline scenario and Scenario 2b.

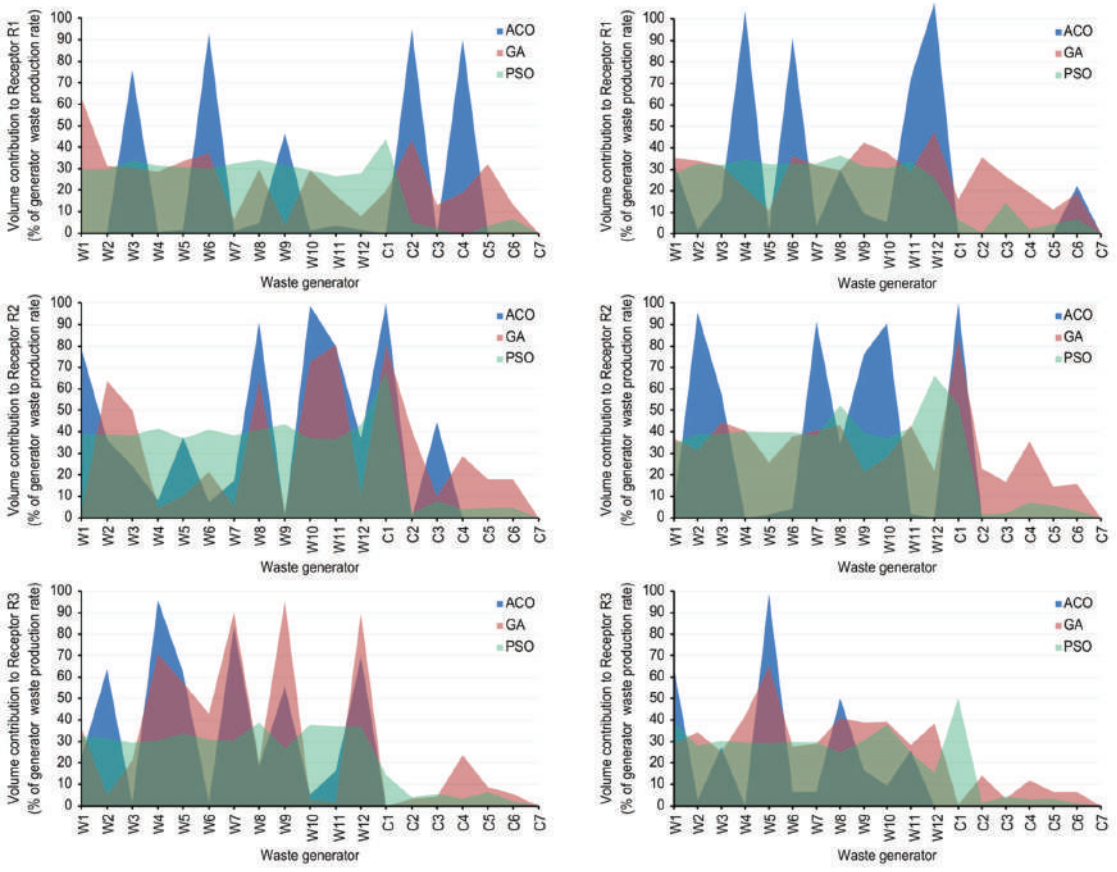

Figure 5. Blending profiles for every waste receptor and ACO, GA and PSO algorithms for the baseline scenario (**left**) and Scenario 2b (**right**).

4. Discussion

Simulations with the optimisation algorithms ACO, GA and PSO were performed, showing successful optimisation results in almost all scenarios. Data from a real case study were used to carry simulations of centralised anaerobic co-digestion blending. As detailed in Section 3, these datasets are composed of 19 organic waste generators and three organic waste receptors within the context of a sanitation network in an area of high industrial activity in Catalonia. This case study composes the baseline scenario. In that previous work, the potential impacts of optimising AnD with wastes from external sources were already demonstrated, bearing up to 77% cost savings regarding waste management. Different modifications were made to this dataset to compare the performance of the ACO, GA, and PSO algorithms under different conditions to assess the performance of each optimisation algorithm in relevant situations. Regarding the optimisation problem, the C/N ratio is the dominant restriction, as was previously seen in [41]. This is the reason why this parameter is included in the discussion of the results, together with biogas production.

For the baseline scenario as seen in Table 5, PSO shows the best index *B* achieved but also the lowest biogas production. However, PSO also shows the lowest C/N ratio,

which might play a role in achieving the best solution, compensating for the lack of biogas produced. If biogas production is increased by the design of a particular setup, this could be trimmed by the corresponding weight in the objective function *B* as a trade-off among the different parameters involved. The results obtained have been considered convenient for the installation under study and improved dramatically performance obtained in the baseline scenario [41]. However, both ACO and GA generally show higher amounts of biogas production, but their best index *B* values achieved are below that of PSO, and their C/N ratios are above 50.

As shown in Figure 5, ACO and GA show similar behaviours for the baseline scenario, prioritising specific substrates. A first hypothesis suggests that prioritised substrates would be those with higher COD since they would allow higher biogas production. On the other hand, PSO shows a different strategy blending more available substrates and tends to exclude industrial substrates. This trend may point to PSO performing a conservative strategy where it is avoided in all cost situations where the operation of the AnD would be put at risk. Therefore, the general trend is that ACO and GA solve the presented optimisation problem by maximising biogas production and pushing restrictions to the limit, while PSO tends to balance biogas maximisation and the C/N ratio trade-off. In addition, note that PSO has the shortest execution times and ACO the largest, which is observed for all scenarios, indicating PSO to be more computationally efficient, where even here, the execution time is not a drawback for real implementation with the values obtained.

The similarities between ACO and GA and the differences between those and PSO could be partially explained by the nature of these algorithms. Both ACO and GA tend to explore the search space of solutions around the borders, thus increasing the number of non-feasible solutions but also increasing the chances of finding a "rare" solution with a higher best index [72,73]. Thus, these algorithms appear to be based on relatively independent behaviour between particles so that each one can explore separate areas of the border search space and be able to find different non-redundant solutions. On the other hand, PSO algorithm exploration of the search space is based on dependent behaviour between neighbouring particles, which does not encourage particles to explore the limits of the search space. Instead, it promotes the exploration of other mid-term areas between the centre and the borders of the search space. This could help explain why the PSO algorithm attains solutions within shorter execution times but also with generally lower biogas production. Hence, PSO would tend to be a conservative strategy where instead of selecting the most promising solution, single ant or particle, it would prioritise a consensus between the best neighbourhoods.

As detailed in Section 3, Scenario 1 is modified by increasing the organic load of all substrates tenfold. Thus, the dominant condition, in this case, is that organic waste valorisation is fostered, leading to higher biogas production. As observed in Table 5, ACO and GA show better performance than PSO in this scenario, but GA is more efficient since its attained biogas production is noticeably higher than that achieved with ACO.

Additionally, as detailed in Section 3, Scenarios 2a and 2b include a geographical location modification of the involved facilities. As observed in Figure 4, the relative distances between waste generators and receptors (R1, R2, R3) are not modified by lineal modification of the distance when the map plot of the baseline scenario is compared to that of Scenario 2a. However, nonlinear modification of geographical distances in Scenario 2b leads to a different map plot, where waste receptors are more dispersed between them in relation to waste generators (Figure 4). The effect of this distortion of distances is that waste receptors are more separated, thus avoiding geographical overlapping of waste receptors, or the "big dot" effect, i.e., assimilating closer plants as a single centralised plant from a geographical perspective.

Hence, Scenario 2a is modified by tenfold increasing the geographical distances between waste generators and receptors, making geographical distance a dominant condition for optimisation. In this case, ACO is unable to find a solution, and both GA and PSO show extremely poor performance when compared with the baseline scenario, as shown in

Table 5. The linear modification of distances of Scenario 2a shows the performance of each algorithm under the pressure of cases with high geographical distances. This pressure case of Scenario 2a was especially relevant to test because it can significantly impact the logistics processes. On the other hand, Scenario 2b presents a different trend due to the nonlinear modification of distances. As detailed in Table 5, GA shows the best performance, and PSO shows better performance than ACO even in terms of biogas production.

As observed in Figure 5, ACO and PSO maintain similar blending profiles, while GA and PSO also exhibit similar blending profiles, but including GA results in a greater volume of industrial substrates. This shared behaviour between GA and PSO is exclusive to Scenario 2b, but it might indicate that GA behaves similarly to PSO in this case. However, from the operational point of view, GA solutions involve major risks since they tend to include more industrial substrate than PSO solutions.

In Scenario 3, a threefold increase in the volume of all waste generated was performed. First, this result implies that the search space—i.e., the total number of combinations and possible solutions—drastically increases. In this case, Table 5 confirms a similar trend observed for previous scenarios, where GA obtained the best performance and ACO the worst. Again, this finding is consistent with the observation that the ACO algorithm attains weaker performance than GA and PSO for this particular case and that GA and PSO attain similar performance in this study, although GA appears to generally provide better performance than PSO.

Finally, Scenario 4 was composed of increasing the C/N ratio of W1–W12 substrates. These substrates originally conformed to sewage sludge with a low nitrogen load, but in Scenario 4, the drastic increase in the C/N content of sewage sludge was the dominant condition to be tested. Table 5 also presents a summary of the results for Scenario 4, where PSO shows the best performance and GA the worst. The main observation is that the PSO algorithm is more able than the GA to manage situations with high nitrogen loads or major restrictions, while the GA has more potential to maximise biogas production. However, it is more sensitive to high nitrogen loads because it reduces available space to acquire industrial wastes with both high organic loads and high nitrogen loads.

The developed algorithms have successfully optimised the AnD network of the case study, and their performances have been tested under different conditions (i.e., Scenarios 1–4). Simultaneous logistics and quality optimisation of a network of existing waste management facilities is a gap in the current state of the art due to its ad-hoc nature and its interdisciplinarity: there are specialized works for logistics optimisation such as in [45,46], but they do not include process optimisation. The present study implements this logistic optimisation by minimising a cost function designed to this end. The reason for choosing this approach is also based on the need for professionals who manage the AnD network considered here to have a decision support tool capable of integrating logistics and process performance optimisation. And, in addition, to have the ability to handle changing operation conditions and scenarios, as it actually happens in real facilities.

It is also worth noting that it exists a variety of sensors for the determination of physical-chemical parameters that could complement the sensor network considered in this case study, such as a variation of the ones presented in [47]. These sensors could provide additional insight, especially if combined with GIS and process optimisation, and also facilitate the real-time implementation of the presented approach. Additionally, they could also be used as control mechanisms for those cases where ACO and GA optimisation is applied, since attained optimised outcomes pushed quality restrictions of the AnD process close to their thresholds. However, there is a trade-off between information (i.e., data gathered from new sensors) and resources (e.g., implementation, maintenance) which has to be taken into account when considering new sensors.

Overall, this study presents a step forward towards the integrated optimisation of AnD networks, making an innovative attempt to couple logistics and quality optimisation of the centralised digestion process of a real AnD network.

5. Conclusions

In this study, three approaches were developed for the simultaneous optimisation of multiple AnD systems based on ACO, GA and PSO. These methods were applied to a case study based on real data from an AnD network in the area of the Besòs River basin in Catalonia. The performance of each optimisation approach was evaluated. All the approaches successfully optimised biogas production for simulated scenarios while preserving some practical restrictions in optimisation.

For the baseline scenario, ACO and GA allowed maximum biogas production by placing restrictions on the limits of safe operations. On the other hand, PSO solved the optimisation problem with a more conservative strategy where biogas production is lower than that in ACO or GA solutions, in favour of the best AnD operation conditions (i.e., by adjusting the C/N ratio and alkalinity).

In those cases with high opportunities for biogas production (i.e., Scenario 1), GA and ACO would perform the best due to their capabilities of maximising biogas production over that of PSO. GA would perform as the best optimisation algorithm both for cases where distances are significantly different amongst them (i.e., Scenario 2b) and for cases where higher volumes should be handled (i.e., Scenario 3), presumably due to GA's computational potential. Finally, for those cases where other quality-related parameters are restrictions (i.e., Scenario 4), PSO would be the best performing algorithm.

The present study shows an innovative contribution to optimize the performance of centralized AnD systems, combining logistical and quality parameters. To the authors' knowledge, this optimization has not yet been addressed in the literature for an AnD network. In addition, the framework has proven its effectiveness in minimizing the total distance travelled to transport the waste and maximizing biogas production. At the same time, the physical-chemical parameters of the process have been kept within their operational limits.

Further work may include methodologies to improve social impact factor quantification in the optimisation, which might allow better characterisation of the logistic impact of each substrate generator. Additionally, the development of logistic route simulations would be required to enhance real-world distribution planning considering daytime, travel frequency, dynamic waste production-consumption coupled with stocking problems and other time-related issues key to logistic planning.

Author Contributions: Conceptualization, D.P.-H., M.V. and M.À.C.-E.; methodology, D.P.-H., M.V. and M.À.C.-E.; software, D.P.-H.; validation, M.V., M.À.C.-E. and V.P.; formal analysis, M.V., M.P., M.À.C.-E. and V.P.; investigation, D.P.-H., M. Verdaguer; resources, M.P. and M.À.C.-E.; data curation, D.P.-H., M.V., V.P. and M. À. Cugueró-Escofe; writing—original draft preparation, D.P.-H., M.V. and M.À.C.-E.; writing—review and editing, D.P.-H., M.V., V.P. and M.À.C.-E.; supervision, V.P., M.P. and M.À.C.-E.; project administration, M.P. and M.À.C.-E.; funding acquisition, M.P. and M.À.C.-E.. All authors have read and agreed to the published version of the manuscript.

Funding: This research received no external funding.

Institutional Review Board Statement: Not applicable.

Informed Consent Statement: Not applicable.

Data Availability Statement: No new data were created or analyzed in this study. Data sharing is not applicable to this article.

Acknowledgments: The authors would like to acknowledge the support received from Consorci Besòs Tordera. LEQUIA-UdG and SAC-UPC have been recognized as consolidated research groups by the Catalan Government (2017-SGR-1552 and 2017-SGR-482, respectively).

Conflicts of Interest: The authors declare no conflict of interest.

Abbreviations

WWTPs	wastewater treatment plants
AnD	anaerobic digestion
MKP	multidimensional knapsack problem
AnCD	anaerobic co-digestion
ACO	Ant colony optimisation
GA	Genetic algorithm
PSO	Particle swarm optimisation
GUI	graphical user interface
CMAES	covariance matrix adaptation evolution strategy
DE	differential evolution
ANN	perceptron artificial neural network
SGOAs	how stochastic global optimisation algorithms
CO	combinatorial optimisation
EA	evolutionary algorithms
COD	Chemical Oxygen Demand
TN	Total Nitrogen
C/N	Carbon to Nitrogen ratio
CBT	Consorci Besòs Tordera
GIS	geographical information system

References

1. Batstone, D.J.; Virdis, B. The role of anaerobic digestion in the emerging energy economy. *Curr. Opin. Biotechnol.* **2014**, *27*, 142–149. [CrossRef]
2. Bolzonella, D.; Pavan, P.; Battistoni, P.; Cecchi, F. Anaerobic co-digestion of sludge with other organic wastes and phosphorus reclamation in wastewater treatment plants for biological nutrients removal. *Water Sci. Technol.* **2006**, *53*, 177–186. [CrossRef] [PubMed]
3. Melián, J.A.H. Sustainable Wastewater Treatment Systems (2018–2019). *Sustainability* **2020**, *12*, 1940. [CrossRef]
4. Lorick, D.; Macura, B.; Ahlström, M.; Grimvall, A.; Harder, R. Effectiveness of struvite precipitation and ammonia stripping for recovery of phosphorus and nitrogen from anaerobic digestate: A systematic review. *Environ. Evid.* **2020**, *9*, 27. [CrossRef]
5. Namuli, R.; Laflamme, C.B.; Pillay, P. A Computer Program for Modeling the Conversion of Organic Waste to Energy. *Energies* **2011**, *4*, 1973–2001. [CrossRef]
6. Scarlat, N.; Dallemand, J.-F.; Fahl, F. Biogas: Developments and perspectives in Europe. *Renew. Energy* **2018**, *129*, 457–472. [CrossRef]
7. Fouladi, J.; Al-Ansari, T. Conceptualising multi-scale thermodynamics within the energy-water-food nexus: Progress towards resource and waste management. *Comput. Chem. Eng.* **2021**, *152*, 107375. [CrossRef]
8. Baldi, F.; Pecorini, I.; Iannelli, R. Comparison of single-stage and two-stage anaerobic co-digestion of food waste and activated sludge for hydrogen and methane production. *Renew. Energy* **2019**, *143*, 1755–1765. [CrossRef]
9. Mattioli, A.; Gatti, G.; Mattuzzi, G.; Cecchi, F.; Bolzonella, D. Co-digestion of the organic fraction of municipal solid waste and sludge improves the energy balance of wastewater treatment plants: Rovereto case study. *Renew. Energy* **2017**, *113*, 980–988. [CrossRef]
10. Siddique, N.I.; Wahid, Z.A. Achievements and perspectives of anaerobic co-digestion: A review. *J. Clean. Prod.* **2018**, *194*, 359–371. [CrossRef]
11. Villamil, J.; Mohedano, A.F.; Martínez, J.A.V.; Rodriguez, J.; DE LA Rubia, M.A. Anaerobic co-digestion of the process water from waste activated sludge hydrothermally treated with primary sewage sludge. A new approach for sewage sludge management. *Renew. Energy* **2019**, *146*, 435–443. [CrossRef]
12. Díaz-Trujillo, L.A.; Fuentes-Cortés, L.F.; Nápoles-Rivera, F. Economic and environmental optimization for a biogas supply Chain: A CVaR approach applied to uncertainty of biomass and biogas demand. *Comput. Chem. Eng.* **2020**, *141*, 107018. [CrossRef]
13. Mpofu, A.; Kaira, W.; Oyekola, O.; Welz, P. Anaerobic co-digestion of tannery effluents: Process optimisation for resource recovery, recycling and reuse in a circular bioeconomy. *Process Saf. Environ. Prot.* **2021**, *158*, 547–559. [CrossRef]
14. Yağlı, H.; Koç, Y.; Köse, Ö.; Koç, A.; Yumrutaş, R. Optimisation of simple and regenerative organic Rankine cycles using jacket water of an internal combustion engine fuelled with biogas produced from agricultural waste. *Process Saf. Environ. Prot.* **2021**, *155*, 17–31. [CrossRef]
15. Sweelssen, J.; Blokland, H.; Rajamäki, T.; Boersma, A. Capacitive and Infrared Gas Sensors for the Assessment of the Methane Number of LNG Fuels. *Sensors* **2020**, *20*, 3345. [CrossRef] [PubMed]
16. Furst, L.; Feliciano, M.; Frare, L.; Igrejas, G. A Portable Device for Methane Measurement Using a Low-Cost Semiconductor Sensor: Development, Calibration and Environmental Applications. *Sensors* **2021**, *21*, 7456. [CrossRef] [PubMed]

17. Al, R.; Behera, C.R.; Gernaey, K.V.; Sin, G. Stochastic simulation-based superstructure optimization framework for process synthesis and design under uncertainty. *Comput. Chem. Eng.* **2020**, *143*, 107118. [CrossRef]
18. Fouladi, J.; AlNouss, A.; Al-Ansari, T. Sustainable energy-water-food nexus integration and optimisation in eco-industrial parks. *Comput. Chem. Eng.* **2021**, *146*, 107229. [CrossRef]
19. Padrón-Páez, J.I.; Almaraz, S.D.-L.; Román-Martínez, A. Sustainable wastewater treatment plants design through multiobjective optimization. *Comput. Chem. Eng.* **2020**, *140*, 106850. [CrossRef]
20. Dewasme, L.; Sbarciog, M.; Rocha-Cózatl, E.; Haugen, F.; Wouwer, A.V. State and unknown input estimation of an anaerobic digestion reactor with experimental validation. *Control Eng. Pract.* **2019**, *85*, 280–289. [CrossRef]
21. Han, H.-G.; Zhang, H.-J.; Liu, Z.; Qiao, J.-F. Data-driven decision-making for wastewater treatment process. *Control Eng. Pract.* **2020**, *96*, 104305. [CrossRef]
22. Li, Z.; Yan, X. Ensemble model of wastewater treatment plant based on rich diversity of principal component determining by genetic algorithm for status monitoring. *Control Eng. Pract.* **2019**, *88*, 38–51. [CrossRef]
23. Szeląg, B.; Drewnowski, J.; Łagód, G.; Majerek, D.; Dacewicz, E.; Fatone, F. Soft Sensor Application in Identification of the Activated Sludge Bulking Considering the Technological and Economical Aspects of Smart Systems Functioning. *Sensors* **2020**, *20*, 1941. [CrossRef]
24. Ma, Y.; Rose, F.; Wong, L.; Vien, B.; Kuen, T.; Rajic, N.; Kodikara, J.; Chiu, W. Detection of Defects in Geomembranes Using Quasi-Active Infrared Thermography. *Sensors* **2021**, *21*, 5365. [CrossRef] [PubMed]
25. Sánchez, J.B.; Vuono, M.; Dionisi, D. Model-based comparison of sequencing batch reactors and continuous-flow activated sludge processes for biological wastewater treatment. *Comput. Chem. Eng.* **2020**, *144*, 107127. [CrossRef]
26. Naqvi, S.R.; Tariq, R.; Shahbaz, M.; Naqvi, M.; Aslam, M.; Khan, Z.; Mackey, H.; Mckay, G.; Al-Ansari, T. Recent developments on sewage sludge pyrolysis and its kinetics: Resources recovery, thermogravimetric platforms, and innovative prospects. *Comput. Chem. Eng.* **2021**, *150*, 107325. [CrossRef]
27. Babaee, A.; Shayegan, J. Effect of Organic Loading Rates (OLR) on Production of Methane from Anaerobic Digestion of Vegetables Waste. In Proceedings of the World Renewable Energy Congress-Sweden, Linköping, Sweden, 8–13 May 2011; pp. 411–417. [CrossRef]
28. Avilés, A.B.L.; Velázquez, F.D.C.; Del Riquelme, M.L.P. Methodology for Energy Optimization in Wastewater Treatment Plants. Phase III: Implementation of an Integral Control System for the Aeration Stage in the Biological Process of Activated Sludge and the Membrane Biological Reactor. *Sensors* **2020**, *20*, 4342. [CrossRef]
29. Okolie, J.A.; Epelle, E.I.; Tabat, M.E.; Orivri, U.; Amenaghawon, A.N.; Okoye, P.U.; Gunes, B. Waste biomass valorization for the production of biofuels and value-added products: A comprehensive review of thermochemical, biological and integrated processes. *Process Saf. Environ. Prot.* **2021**, *159*, 323–344. [CrossRef]
30. El Ibrahimi, M.; Khay, I.; El Maakoul, A.; Bakhouya, M. Food waste treatment through anaerobic co-digestion: Effects of mixing intensity on the thermohydraulic performance and methane production of a liquid recirculation digester. *Process Saf. Environ. Prot.* **2021**, *147*, 1171–1184. [CrossRef]
31. Fan, Y.; Lv, M.; Niu, X.; Ma, J.; Zhang, D. The key step of gaseous phosphorus release in anaerobic digestion. *Process Saf. Environ. Prot.* **2020**, *137*, 238–245. [CrossRef]
32. Horf, M.; Gebbers, R.; Vogel, S.; Ostermann, M.; Piepel, M.-F.; Olfs, H.-W. Determination of Nutrients in Liquid Manures and Biogas Digestates by Portable Energy-Dispersive X-ray Fluorescence Spectrometry. *Sensors* **2021**, *21*, 3892. [CrossRef]
33. Fréville, A. The multidimensional 0–1 knapsack problem: An overview. *Eur. J. Oper. Res.* **2004**, *155*, 1–21. [CrossRef]
34. Grandón, J.; Derpich, I. A Heuristic for the Multi-knapsack Problem. *WSEAS Trans. Math.* **2011**, *10*, 95–104.
35. Kellerer, H.; Pferschy, U.; Pisinger, D. Multidimensional Knapsack Problems. In *Knapsack Problems*; Springer: Berlin/Heidelberg, Germany, 2004; pp. 235–283. [CrossRef]
36. Glaser, C.; Pavan, A.; Travers, S. The fault tolerance of NP-hard problems. *Inf. Comput.* **2011**, *209*, 443–455. [CrossRef]
37. Somani, D.; Srivastava, H.; Sabumon, P.C.; Anjali, G. A short review of anaerobic co-digestion and feasibility of anaerobic co-digestion of sewage and food waste for sustainable waste management. *Int. J. Earth Sci. Eng.* **2016**, *9*, 55–70.
38. Verdaguer, M.; Clara, N.; Monclús, H.; Poch, M. A step forward in the management of multiple wastewater streams by using an ant colony optimization-based method with bounded pheromone. *Process Saf. Environ. Prot.* **2016**, *102*, 799–809. [CrossRef]
39. Cugueró-Escofet, M.; Puig, V.; Quevedo, J. Optimal pressure sensor placement and assessment for leak location using a relaxed isolation index: Application to the Barcelona water network. *Control Eng. Pract.* **2017**, *63*, 1–12. [CrossRef]
40. García-Gen, S.; Rodríguez, J.; Lema, J. Optimisation of substrate blends in anaerobic co-digestion using adaptive linear programming. *Bioresour. Technol.* **2014**, *173*, 159–167. [CrossRef]
41. Palma-Heredia, D.; Verdaguer, M.; Molinos-Senante, M.; Poch, M.; Cugueró-Escofet, M. Optimised blending for anaerobic co-digestion using ant colony approach: Besòs river basin case study. *Renew. Energy* **2020**, *168*, 141–150. [CrossRef]
42. Rodriguez-Verde, I.; Regueiro, L.; Lema, J.; Carballa, M. Blending based optimisation and pretreatment strategies to enhance anaerobic digestion of poultry manure. *Waste Manag.* **2018**, *71*, 521–531. [CrossRef]
43. Santos, A.T.; Carballa, M.; Morales, N.; Vázquez-Padín, J.R.; Gutierrez, R.; Lema, J. An optimised control system to steer the transition from anaerobic mono- to co-digestion in full-scale plants. *Environ. Sci. Water Res. Technol.* **2019**, *5*, 1004–1011. [CrossRef]
44. Thiriet, P.; Bioteau, T.; Tremier, A. Optimization method to construct micro-anaerobic digesters networks for decentralized biowaste treatment in urban and peri-urban areas. *J. Clean. Prod.* **2019**, *243*, 118478. [CrossRef]

45. Rentizelas, A.; Shpakova, A.; Mašek, O. Designing an optimised supply network for sustainable conversion of waste agricultural plastics into higher value products. *J. Clean. Prod.* **2018**, *189*, 683–700. [CrossRef]
46. Bueno-Delgado, M.-V.; Romero-Gázquez, J.-L.; Jiménez, P.; Pavón-Mariño, P. Optimal Path Planning for Selective Waste Collection in Smart Cities. *Sensors* **2019**, *19*, 1973. [CrossRef] [PubMed]
47. Longo, E.; Sahin, F.A.; Redondi, A.E.C.; Bolzan, P.; Bianchini, M.; Maffei, S. A 5G-Enabled Smart Waste Management System for University Campus. *Sensors* **2021**, *21*, 8278. [CrossRef] [PubMed]
48. Verdaguer, M.; Molinos-Senante, M.; Poch, M. Optimal management of substrates in anaerobic co-digestion: An ant colony algorithm approach. *Waste Manag.* **2016**, *50*, 49–54. [CrossRef]
49. Verdaguer, M.; Clara, N.; Gutierrez, O.; Poch, M. Application of Ant-Colony-Optimization algorithm for improved management of first flush effects in urban wastewater systems. *Sci. Total Environ.* **2014**, *485-486*, 143–152. [CrossRef] [PubMed]
50. Ramachandran, A.; Rustum, R.; Adeloye, A.J. Review of Anaerobic Digestion Modeling and Optimization Using Nature-Inspired Techniques. *Processes* **2019**, *7*, 953. [CrossRef]
51. Zhang, Z.; Liu, Y.; Bo, L.; Yue, Y.; Wang, Y. Economic Optimal Allocation of Mine Water Based on Two-Stage Adaptive Genetic Algorithm and Particle Swarm Optimization. *Sensors* **2022**, *22*, 883. [CrossRef] [PubMed]
52. Marković, D.; Stanković, A.; Petrović, G.; Trajanović, M.; Ćojbašić, Ž. Genetic and Ant Colony Optimization Based Communal Waste Collection Vehicle Routing. *Conf. Inf. Soc. Technol.* **2019**, 209–212.
53. Gaida, D.; Sousa Brito, A.L.; Wolf, C.; Bäck, T.; Bongards, M.; McLoone, S. Optimal Control of Biogas Plants Using Nonlinear MPC. IET Irish Signals Syst. Conf. 2011. Available online: https://www.researchgate.net/publication/224863615_Optimal_Control_of_Biogas_Plants_using_Nonlinear_Model_Predictive_Control (accessed on 26 January 2022).
54. Akbaş, H.; Bilgen, B.; Turhan, A.M. An integrated prediction and optimization model of biogas production system at a wastewater treatment facility. *Bioresour. Technol.* **2015**, *196*, 566–576. [CrossRef]
55. Kana, E.G.; Oloke, J.; Lateef, A.; Adesiyan, M. Modeling and optimization of biogas production on saw dust and other co-substrates using Artificial Neural network and Genetic Algorithm. *Renew. Energy* **2012**, *46*, 276–281. [CrossRef]
56. Alhanjouri, M.; Alfarra, B. Ant Colony versus Genetic Algorithm based on Travelling Salesman Problem. *Int. J. Comput. Technol. Appl.* **2011**, *2*, 570–578.
57. Dorigo, M.; Birattari, M.; Stutzle, T. Ant colony optimization. *IEEE Comput. Intell. Mag.* **2006**, *1*, 28–39. [CrossRef]
58. Dorigo, M.; Stützle, T. The Ant Colony Optimization Metaheuristic: Algorithms, Applications, and Advances. In *Handbook of Metaheuristics. International Series in Operations Research & Management Science*; Glover, F., Kochenberger, G.A., Eds.; Springer: Boston, MA, USA, 2003; Volume 57. [CrossRef]
59. Dorigo, M.; Stützle, T. *Ant Colony Optimization*; MIT Press: Cambridge, MA, USA, 2004.
60. Stützle, T.; Hoos, H. MAX–MIN Ant System. *Futur. Gener. Comput. Syst.* **2000**, *16*, 889–914. [CrossRef]
61. Walters, G.; Savic, D.; Morley, M.; de Schaetzen, W.; Atkinson, R. Calibration of water distribution network models using genetic algorithms. *Trans. Ecol. Environ.* **1998**, *19*, 131–140.
62. Aldosary, A.; Ali, Z.M.; Alhaider, M.M.; Ghahremani, M.; Dadfar, S.; Suzuki, K. A modified shuffled frog algorithm to improve MPPT controller in PV System with storage batteries under variable atmospheric conditions. *Control Eng. Pract.* **2021**, *112*, 104831. [CrossRef]
63. Galuppini, G.; Creaco, E.; Magni, L. Sum-of-delay models for pressure control in Water Distribution Networks. *Control Eng. Pract.* **2021**, *113*, 104844. [CrossRef]
64. Haupt, R.L.; Haupt, S.E. *Practical Genetic Algorithms*; Wiley: Hoboken, NJ, USA, 2004.
65. Gandomi, A.H.; Yang, X.S.; Talatahari, S.; Alavi, A.H. *Metaheuristic Applications in Structures and Infrastructures*; Elsevier Inc.: Amsterdam, The Netherlands, 2013. [CrossRef]
66. Xia, L.; de Jager, B.; Donkers, T.; Willems, F. Robust constrained optimization for RCCI engines using nested penalized particle swarm. *Control Eng. Pract.* **2020**, *99*, 104411. [CrossRef]
67. Aminbakhsh, S.; Sonmez, R. Discrete particle swarm optimization method for the large-scale discrete time–cost trade-off problem. *Expert Syst. Appl.* **2016**, *51*, 177–185. [CrossRef]
68. Ye, C.; Chen, L.; Ni, S.; Zhou, J. Evaluation model of forest eco economic benefits based on discrete particle swarm optimization. *Environ. Technol. Innov.* **2021**, *22*, 101426. [CrossRef]
69. Li, P.; Jiao, X.; Li, Y. Adaptive real-time energy management control strategy based on fuzzy inference system for plug-in hybrid electric vehicles. *Control Eng. Pract.* **2020**, *107*, 104703. [CrossRef]
70. Tuttle, J.F.; Tuttle, J.F.; Vesel, R.; Vesel, R.; Alagarsamy, S.; Alagarsamy, S.; Blackburn, L.D.; Blackburn, L.D.; Powell, K.; Powell, K. Sustainable NOx emission reduction at a coal-fired power station through the use of online neural network modeling and particle swarm optimization. *Control Eng. Pract.* **2019**, *93*, 104167. [CrossRef]
71. Nghiem, L.; Koch, K.; Bolzonella, D.; Drewes, J.E. Full scale co-digestion of wastewater sludge and food waste: Bottlenecks and possibilities. *Renew. Sustain. Energy Rev.* **2017**, *72*, 354–362. [CrossRef]
72. Hibler, D. The GA-ACO Method Applied to Engineering Design. *Procedia Comput. Sci.* **2012**, *12*, 152–157. [CrossRef]
73. Valdez, F.; Moreno, F.; Melin, P. *A Comparison of ACO, GA and SA for Solving the TSP Problem BT—Hybrid Intelligent Systems in Control, Pattern Recognition and Medicine*; Castillo, O., Melin, P., Eds.; Springer International Publishing: Berlin/Heidelberg, Germany, 2020; pp. 181–189. [CrossRef]

sensors

MDPI

Article

Transfer Learning in Wastewater Treatment Plant Control Design: From Conventional to Long Short-Term Memory-Based Controllers

Ivan Pisa [1,2,*], Antoni Morell [1], Ramón Vilanova [2] and Jose Lopez Vicario [1]

[1] Wireless Information Networking (WIN) Group, Escola d'Enginyeria, Universitat Autònoma de Barcelona, 08193 Bellaterra, Spain; antoni.morell@uab.cat (A.M.); jose.vicario@uab.cat (J.L.V.)
[2] Advanced Systems for Automation and Control (ASAC) Group, Escola d'Enginyeria, Universitat Autònoma de Barcelona, 08193 Bellaterra, Spain; ramon.vilanova@uab.cat
* Correspondence: ivan.pisa@uab.cat

Abstract: In the last decade, industrial environments have been experiencing a change in their control processes. It is more frequent that control strategies adopt Artificial Neural Networks (ANNs) to support control operations, or even as the main control structure. Thus, control structures can be directly obtained from input and output measurements without requiring a huge knowledge of the processes under control. However, ANNs have to be designed, implemented, and trained, which can become complex and time-demanding processes. This can be alleviated by means of Transfer Learning (TL) methodologies, where the knowledge obtained from a unique ANN is transferred to the remaining nets reducing the ANN design time. From the control viewpoint, the first ANN can be easily obtained and then transferred to the remaining control loops. In this manuscript, the application of TL methodologies to design and implement the control loops of a Wastewater Treatment Plant (WWTP) is analysed. Results show that the adoption of this TL-based methodology allows the development of new control loops without requiring a huge knowledge of the processes under control. Besides, a wide improvement in terms of the control performance with respect to conventional control structures is also obtained. For instance, results have shown that less oscillations in the tracking of desired set-points are produced by achieving improvements in the Integrated Absolute Error and Integrated Square Error which go from 40.17% to 94.29% and from 34.27% to 99.71%, respectively.

Keywords: control design; industrial control; transfer learning; WWTP

Citation: Pisa, I.; Morell, A.; Vilanova, R.; Vicario, J.L. Transfer Learning in Wastewater Treatment Plant Control Design: From Conventional to Long Short-Term Memory-Based Controllers. *Sensors* **2021**, *21*, 6315. https://doi.org/10.3390/s21186315

Academic Editors: Miquel À. Cugueró-Escofet and Vicenç Puig

Received: 13 July 2021
Accepted: 18 September 2021
Published: 21 September 2021

1. Introduction

Industrial environments are characterised by running complex and repetitive processes which are sometimes maintained over time. In that sense, control systems are adopted in order to ensure that these processes perform correctly [1]. Most of the times, the development of control strategies can become a complex and time-demanding task since a deep knowledge of the process under control is required. However, the incursion of the Industry 4.0 paradigm and Artificial Neural Network (ANNs) applications are changing the way we control and manage industrial environments. Their main aim is to provide the industries with solutions mainly based on measurements obtained from their systems [2]. Some of these solutions go from basic forecasting systems to more complex solutions, like predictive maintenance ([3], Chapter 9). However, one of the sectors where Industry 4.0 and ANNs are making the point corresponds to the industrial control ([3], Chapter 5). There, ANNs have been adopted for a wide range of tasks, such as the design of soft-sensors or the detection of malfunctions [4–6]. Not only this, but the industrial control domain is experiencing a change in its tendency: ANNs are used more and more as the main control structures than conventional controllers.

One of the industrial sectors where this tendency is observed corresponds to the Wastewater Treatment Plants (WWTPs), which are characterised by running very complex processes where individual operations and actions can change the whole operation of the plant [7]. For that reason, a huge number of control loops are required in order to ensure that each individual operation is correctly performed. Proportional Integral (PI) controllers have mostly been considered as the default and basic controller strategy able to ensure correct WWTP behaviour [8]. However, a complete reduction of the pollutants present in the residual waters cannot be ensured. For that reason, more complex structures have been proposed in order to improve the control performance. Fuzzy and Model Predictive Controllers (MPCs) have been adopted in [9] as the main control strategy to avoid the effluent violations of a WWTP plant, whereas in [10], a hierarchical structure with fuzzy and MPC controllers has also been proposed to determine the control actuation, taking into account the weather and a variable set-point. In this case, the set-point adopted by the MPC controllers is determined by the fuzzy controller whose objective is to maintain the ammonium in the fifth reactor tank of a WWTP at a desired value (please observe Figure 1 to see the distribution of the tanks of a general-purpose WWTP). The problem observed with this kind of structure lies in the fact that they require a model which replicates the relationships between input and output measurements. Besides, most of the time, these relationships consist of non-linear relations which are difficult and tedious to model. This is where ANNs come in, since they are algorithms offering good performance when dealing with these kinds of relationships ([11], Chapter 6). The first approach consists of the adoption of ANNs as elements whose predictions are adopted by conventional control structures. For instance, the solution proposed in [10] has been improved in [12], where Long Short-Term Memory (LSTM) cells have been adopted to predict the WWTP effluent concentrations and determine when and which controller has to actuate. In other cases, neural networks have been considered to directly determine the optimal set-point values adopted by conventional controllers [13] or to implement a Reinforcement Learning (RL) module performing the same task [14]. Moreover, in the last few years, ANNs have been directly considered as the control strategy. In [15], neural networks have been considered to implement an Internal Model Controller (IMC) devoted to managing certain concentrations required in the pollutant reduction tasks performed in the WWTP. This also entails that the control actuation can be decoupled from the physical specifications of the environment [16,17].

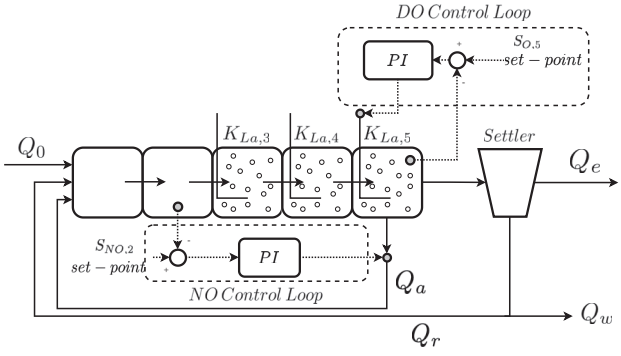

Figure 1. Benchmark Simulation Model No. 1 layout. Q_o, Q_a, Q_r, Q_e, and Q_w are the influent, internal recycle, the external recycle, the effluent, and the wastage flow rates, respectively. Dotted lines correspond to control signals (measured concentrations, desired set-points and actuation signals), while solid lines correspond to process media.

The incursion of ANNs in the industrial control domain presents its own drawbacks that have to be taken into account [18]. The most important one consists in the fact that ANNs have to be designed and trained with amounts of data. This training process is

devoted to determining the different hyperparameters of the ANNs, such as the numbers of hidden layers, neurons, learning rates, or even the topology of networks. This has to be performed for each ANN considered, either to complement a conventional controller (PI, MPC, Fuzzy), or to act as the controller as such. Besides, this training process can last hours or even days with regard to the network structure, the hyperparameters, and the amount of data, accordingly [19]. For that reason, transfer learning (TL) methods have been considered to alleviate these tasks.

TL was adopted from image classification tasks, where they were considered to obtain a good image classifier from predesigned and pretrained structures in a source domain [20]. Then, these pretrained structures were retrained with images of the target domain in what is called a fine-tuning process ([21], Chapter 6). In terms of industrial environments, TL was adopted in the design process of soft-sensors, where they are firstly designed and trained in a source domain where a huge number of measurements are available. TL techniques have been adopted mainly to design and implement soft-sensors in those harsh environments, showing a lack of measurements. In [22], TL techniques were considered to design a soft-sensor which would be deployed over a sulphur recovery unit. The problem there is that this environment shows a severe problem of data scarcity; therefore, a traditional ANN training process cannot be performed. To alleviate this, the authors proposed the adoption of TL to design and implement the soft-sensor in an environment without data scarcity problems (the source domain). Then, the obtained soft-sensor was transferred into the environment with the scarcity problem (the target domain) and fine-tuned to adapt its behaviour to this environment [22]. In our case, we propose the adoption of the Transfer Learning-based Control design approach to implement and design the complete control strategy of a general-purpose WWTP. The main idea is to substitute all the PI controllers by LSTM-based PI controllers, where only one is implemented while the others are obtained from transferred versions. The main point here is that instead of training and designing as many LSTM-based PIs as PI controllers, we will implement only a unique LSTM-based structure which will then be transferred into the remaining control loops. In that way, the design of the control loops can be eased at the same time its complexity is reduced. Now, efforts will be focused on designing a unique controller, which will be based on data instead of designing and tuning as many controllers as control loops. In this work, only two control loops have been designed and implemented following this approach. Thus, the benefit of this control approach is not as widely explored as it could be in a scenario where there exists multiple control loops, like in the petrochemical industry [4,23]. However, it has to be taken into account that this approach is mainly based on the adoption of ANNs, which are trained with amounts of data coming from the control loops. Therefore, data have to be accessible in order to adopt this approach; otherwise, the ANNs will not be properly trained, and consequently, the control loops will not act as they should.

This approach has firstly been conducted in [24], where a LSTM-based PI structure has been trained with data from a unique control loop and then transferred into the remaining control loop of a WWTP environment. Notwithstanding this, the structure proposed in [24] considers a unique LSTM cell which requires a total amount of 4 h of WWTP measurements in order to achieve a good control approach. Besides, neither the design of the LSTM-based PI, nor its fine-tuning process is carried out. Therefore, the control performance of the LSTM-based PI can be improved if it is fine-tuned with measurements coming from the target domain, that is, the control loop where the LSTM-based PI is transferred. For that reason, in this manuscript we will continue the work started in [24]. Here, we propose the fine-tuning process and we also analyse the benefits and losses of implementing the LSTM-based PI with data coming from different control loops. Moreover, a new LSTM-based PI structure able to manage the WWTP control loops without requiring 4 h of measurements will be proposed at the same time the control performance will be improved by means of the fine-tuning of this LSTM-based PI controller. Results will show that among all the LSTM-based PI, there exists one able to perform well in the different control loops. Thereby, the fine-tuning process of this LSTM-based controller and its control performance will also

be analysed in this work. Besides, the speed-up of the design and implementation process will be explored and analysed in this manuscript as a function of the amount of time required to train the LSTM-based structures. The application where it is tested is specific, but the proposed design approach can be adopted in any kind of industrial environment where measurements are available. In summary, a TL-based design approach is proposed to implement the complete control strategy of a WWTP. The main contributions of this work can be summed up as:

- Conventional PI controllers will be substituted by LSTM-based structures able to improve the conventional controller performance.
- The required knowledge of the process under control will be reduced, since the LSTM-based structures only require input and output measurements of the conventional controllers. Besides, these measurements are easily obtained from a well-known WWTP digital framework: the Benchmark Simulation Model No. 1 [25].
- The design and implementation process of the LSTM-based structures will be sped up, since only a LSTM-based structure will be implemented from scratch. The remaining ones will be obtained through TL approaches.
- A fine-tuning process will be carried out to ensure that the control performance of the control loop is improved with respect to the conventional WWTP controller.

The structure of the manuscript is as follows. The work presented here is introduced in Section 1. The materials and methods adopted in this work are presented in Section 2, especially the Benchmark Simulation Model No. 1 (BSM1), a digital framework which models a general-purpose WWTP. In addition, the LSTM cells, as well as the TL principles are explained in this section. Then, the main contribution of this work, that is, the adoption of TL methods to design and implement the controllers of WWTP control loops are defined and explained in Section 3. The results of the exploratory analyses carried out are reflected in Section 4, while Section 5 concludes the paper.

2. Materials and Methods

2.1. Benchmark Simulation Model No. 1

The Transfer Learning-based Control Design approach proposed here is tested over the Benchmark Simulation Model No. 1 (BSM1). The BSM1 plant is a fictitious WWTP designed by using the engineering principles of an activated sludge process. It characterizes a medium-scale and general-purpose WWTP plant whose main objective is to reduce the nitrogen-derived pollutant products present in residual urban waters [25]. Besides, one of the major aims of BSM1 is to implement a digital framework where different control strategies can be designed and tested before being applied in the real environment. Thus, BSM1 is able to offer generality, easy comparison, and replicability of results in terms of the different control strategies devoted to maintaining certain pollutant components under certain levels or limits [8].

In such a context, BSM1 implements the Activated Sludge Model No. 1 (ASM1) which corresponds to a set of mathematical expressions describing the non-linear and highly complex biological and biochemical processes carried out inside the WWTP plant [26]. These processes mainly consist of the denitrification and nitrification processes where the nitrate and ammonia components are transformed into nitrogen and its derivate products [27]. Notwithstanding this, there are other Activated Sludge Models whose main aim is not only to model the processes carried out to reduce the nitrogen-derived pollutants, but also the phosphorus-derived ones. This is the case for the Activated Sludge Models No. 2, 2d, and 3 [28], which require some updates in the BSM1 framework in order to either consider the phosphorus removal processes like in the phosphorus removal BSM1 framework (BSM1-P), or the sludge treatment, like in the Benchmark Simulation Model No. 2 (BSM2) [29,30]. Nevertheless, the study of these behaviours, as well as the layout of these benchmarks is out of the scope of this work.

2.1.1. BSM1 Layout

The BSM1 layout consists of a set of five reactor tanks and a settler placed just before spilling the clean water into the receiving waters (see Figure 1). The five reactor tanks, where the biological and biochemical processes described in the ASM1 model are carried out, are characterised by their aerated conditions: the first two are anoxic tanks (working with a lack of oxygen), whereas the last three work under aerated conditions [8]. They have a total volume of 6000 m^3 , 1000 m^3 for each anoxic tank and 1333 m^3 for each aerated tank. The settler has a total volume of 6000 m^3. Thus, the total volume of BSM1 equals to 12,000 m^3. Besides, the BSM1 framework has been designed to process an average influent flow rate equal to 18,446 m^3/d and an average biodegradable chemical oxygen demand (COD) of 300 g/m^3. This entails that the BSM1 retention time is equivalent to 14.4 h on average [8,31].

The influent data for municipal WWTP consists of time-series data of the flow and concentrations of the water quality parameters. These influent flow rates depend on many factors: the size of the catchment, the type of the sewer system, and the number of person equivalents, among others. For instance, influent profiles for a WWTP of 100,000 PE are available in [32]. They include dry, rainy, and stormy weather conditions. Besides, these are the usual ones considered when working with BSM1, and therefore the ones considered in the presented work. More information about the BSM1 influent flow and concentrations can be obtained in the BSM1 specifications [8]. Among these 15 variables, the ones of interest in this work are the ones related to the BSM1 default control strategies:

- Nitrate and nitrite nitrogen (NO) control loop: control loop in charge of controlling the nitrate and nitrite nitrogen concentration present in the second reactor tank ($S_{NO,2}$).
- Dissolved oxygen (DO) control loop: control loop in charge of managing the dissolved oxygen present in the fifth reactor tank ($S_{O,5}$).

In the case of the NO control loop, a proportional integral (PI) controller is proposed to manage the internal recycle flow rate (Q_a) in order to ensure that the $S_{NO,2}$ concentration is maintained at the default set-point (1 mg/L). The DO control loop considers another PI structure whose main aim is to maintain the $S_{O,5}$ concentration at the default set-point of 2 mg/L. This is performed by means of varying the oxygen transfer coefficient of the fifth reactor tank ($K_{La}5$) accordingly to the measured $S_{O,5}$. In that sense, it is worth noting that the two default PI controllers provided in the BSM1 framework have already been tuned, that is, the proportional gain and the integral time parameters are predefined by the BSM1 designers. The control performance of these PI configurations is provided as a start and a baseline with which a new control structure can be compared. Moreover, we have considered the default control strategies, that is, their parameters have been left as the initial configuration proposed by the BSM1 designers.

2.1.2. BSM1 Simulation and Evaluation Protocols

As previously stated, BSM1 has been widely considered as a general-purpose WWTP digital framework offering generality, easy replication, and comparison between different control strategies. In order to ensure a fair comparison in the control performance, BSM1 considers two kind of simulations: (i) a simulation where no variations are produced in the influent, and (ii) a simulation where daily influent and weather variations are produced. In that sense, four influent profiles considering 14 days of influent measurements are provided [25]:

- Constant influent: Influent profile showing constant influent concentrations and flow rates during 14 days.
- Dry influent: Influent profile showing daily variations of the influent concentrations and without any perturbation induced by weather changes.
- Rainy influent: Influent profile showing daily variations of the influent concentrations. Two large rainy perturbations are considered during days 9 and 10.

- Stormy influent: Influent profile showing daily variations of the influent concentrations. Two short but intense stormy perturbations are produced at days 8 and 11.

Thus, the kind of simulation is set accordingly to the influent profile considered in the simulation. However, the BSM1 model has to be previously initialised before performing the simulations. The initialisation process mainly consists in the stabilization of the BSM1 reactor tanks by means of simulating a total amount of 100 days of constant influent ([8], Section 3). Once the model is stabilised, one can perform the desired simulation. From the 14 days simulated, only the last seven days of the simulation, that is, day 7 to day 14 are considered in the performance computation ([8], Section 6). It is also worth noting that only dry, rainy, and stormy influent profiles are considered in this work.

BSM1 also considers its own performance metrics which ease the comparison process among control strategies. They can be divided into two main categories: the environmental metrics and the control ones. The environmental metrics are those showing the improvements achieved in terms of the pollutant reduction when a control strategy is considered instead of another one. Among the different metrics, the two most widely adopted ones are the Overall Cost Index (OCI) and the Effluent Quality Index (EQI). OCI is related to the costs generated in the pollutant reduction process, while the EQI can be understood as a metric telling how clean the water is [8,30]. Nevertheless, we will focus on the control metrics which do not have either an environmental nor a pollutant flavour. In our case, we are going to consider the Integrated Absolute (*IAE*) and Integrated Squared Errors (*ISE*) between the measured variables and their corresponding set-points:

$$IAE = \int_{t=7^{th}\,day}^{t=14^{th}\,day} |r(t) - y(t)|\, dt \tag{1}$$

$$ISE = \int_{t=7^{th}\,day}^{t=14^{th}\,day} (r(t) - y(t))^2\, dt, \tag{2}$$

where $r(t)$ corresponds to the desired set-point, and $y(t)$ to the measured concentration. In this case, $y(t) = \{S_{NO,2}(t), S_{O,5}(t)\}$. Notice that only the control metrics are considered due to the fact that this work is mainly focused on the adoption of transfer learning approaches and ANNs to ease and speed up the design and implementation of the control strategies.

2.2. Long Short-Term Memory Cells

The ANN-based PI controller adopted in this work is mainly based on Long Short-Term Memory (LSTM) cells. They correspond to a type of gated networks which are characterised by their good performance when dealing with time-series signals ([11], Chapter 10). This is possible thanks to the gates that each LSTM cell implements: (i) three sigmoid activation layers, the input gate ($\mathbf{i}(t)$), the forget gate ($\mathbf{f}(t)$), and the output gate ($\mathbf{o}(t)$), and (ii) one hyperbolic tangent layer, the state gate ($\tilde{\mathbf{c}}(t)$) (see Figure 2).

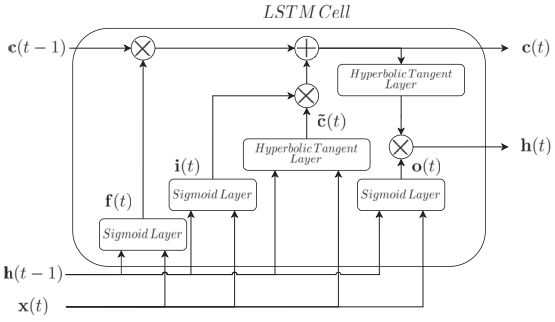

Figure 2. LSTM cell internal structure.

In terms of data, the LSTM cell considers the input data ($\mathbf{x}(t)$) and the output data ($\mathbf{h}(t)$) vectors. Accordingly to them, the forget gate determines the amount of the cell state information that has to be deleted:

$$\mathbf{f}(t) = \sigma(\mathbf{W}_f \cdot \mathbf{x}(t) + \mathbf{U}_f \cdot \mathbf{h}(t-1) + \mathbf{b}_f(t)). \tag{3}$$

Then, the input and state gates determine the new information to be stored in the cell state:

$$\mathbf{i}(t) = \sigma(\mathbf{W}_i \cdot \mathbf{x}(t) + \mathbf{U}_i \cdot \mathbf{h}(t-1) + \mathbf{b}_i(t)) \tag{4}$$

$$\tilde{\mathbf{c}}(t) = tanh(\mathbf{W}_c \cdot \mathbf{x}(t) + \mathbf{U}_c \cdot \mathbf{h}(t-1) + \mathbf{b}_c(t)) \tag{5}$$

$$\mathbf{c}(t) = \mathbf{f}(t) \circ \mathbf{c}(t-1) + \mathbf{i}(t) \circ \tilde{\mathbf{c}}(t). \tag{6}$$

Finally, the output data of the LSTM cell is computed as a function of the input and previous output, as well as the outcome of the output gate:

$$\mathbf{o}(t) = \sigma(\mathbf{W}_o \cdot \mathbf{x}(t) + \mathbf{U}_o \cdot \mathbf{h}(t-1) + \mathbf{b}_o(t)) \tag{7}$$

$$\mathbf{h}(t) = \mathbf{o}(t) \circ tanh(\mathbf{c}(t)). \tag{8}$$

Notice that $\mathbf{W}_x$ and $\mathbf{U}_x$ are the weights of the different gates modifying the input and output data vectors, respectively. $\mathbf{b}_x$ are the biases of the different gates. Finally, $\circ$ is the Hadamard product between two matrices. σ and *tanh* are the sigmoid and hyperbolic tangent activation functions, respectively. If more information about LSTM cells and their behaviour is required, readers are referred to ([11], Section 10.10).

2.3. Transfer Learning

The main contributions of this work are mainly focused on the adoption of Transfer Learning (TL) techniques to ease and speed up the control design in industrial environments, especially in the WWTPs. In that sense, TL consists of transferring the knowledge obtained in the training process of an ANN structure into another one. For instance, TL techniques have been widely adopted in the design and implementation of image classifiers among others [20]. One clear example is shown in ([21], Chapter 6), where the Inception model, a general-purpose image classifier, is adopted to develop a dog breed classifier. This new classifier is implemented with the Inception classifier without the last layer plus three new convolutional layers connected to the output of the penultimate Inception layer. Therefore, the dog breed classification performance will be derived from the Inception classification one and a new retraining process where a new set of dog breed pictures is considered ([21], Chapter 6). This shows that TL techniques can be considered as techniques which not only obtain ANN models performing well from a source model, but also speed up their designing process since the knowledge of the source model is shared with the new ones ([21], Chapter 4).

In that sense, TL techniques can be categorised into three classes as a function of the data availability in the source and target domains or scenarios ([21] Chapter 4, [22]):

- Inductive Transfer Learning: In inductive transfer learning, the source and target domains do not show data scarcity problems. Therefore, the transfer model can be designed and firstly trained in the source domain and then fine-tuned in the target domain in order to adapt its behaviour to its final application.
- Transductive Transfer Learning: Transductive transfer learning is characterised by the necessity of retraining the transferred model every time a new set of labelled data is available in the target domain. This is motivated by the fact that at the first moment, the target domain has no labelled data.
- Unsupervised Transfer Learning: Unsupervised transfer learning is characterised by the fact that there is no available data neither in the source domain, nor in the target one. Thus, this technique is mainly focused on solving unsupervised tasks like dimensionality reduction.

In our case, we are faced with an Inductive Transfer Learning task, since the source and target domains do not show a data scarcity problem. Here, the source domain consists in the $S_{O,5}$ control loop (DO control loop) or the $S_{NO,2}$ control loop (NO control loop) depending on the base ANN-based controller being implemented. In that sense, if the DO control loop is considered as the source domain, the NO control loop will be considered as the target domain and vice versa.

2.4. Modelling

Three different tools have been considered in this work to implement and test the proposed Transfer Learning-based Control Design approach. They correspond to Simulink and Python. Simulink was adopted due to the fact that the BSM1 model is completely deployed over this simulator. Simulink version 10.1 running over Matlab R2020b was considered. Moreover, all the ANNs involved in the proposed approach are also deployed over the BSM1 model in order to test their behaviour. Thus, they are also implemented in Simulink. In that sense, the ANNs, and especially the LSTM cells have been designed and trained by adopting Python 3.6 with three open-source libraries and a NVIDIA GeForce RTX 2080 Titan GPU memory, which is considered to speed up the LSTM training process:

- NumPy (1.18.1) [33]: library providing a huge amount of tools and operations involving vectors and matrices.
- Scikit-Learn (0.22.1) [34]: library providing most of the functions considered in data preprocessing, cross-validation, and evaluation processes.
- Tensorflow (1.14.0) [35]: library providing lots of ANN structures and techniques. It also implements the Keras API, which offers predefined ANN structures, optimizers, cost functions, or training algorithms. Therefore, nearly any ANN structure can be designed by means of concatenating different predefined Keras structures.

3. TL-Based Control Design

As it has been stated, one of the problems in industrial control is related to the conception and design of the control loop. Most of the times, the design of the controllers can become a tedious and time-consuming process since one has to determine the topology of the controller to be used, as well as the plant or process it is going to manage. In that sense, ANNs have arisen as a possible solution able to alleviate this. They only require pairs of input and output data of the process to be controlled [15]. However, this has its own drawbacks: ANNs have to be correctly trained and designed if a good control performance is required. This can become a time-demanding and computationally expensive process if there are a lot of control loops to design.

For that reason and to alleviate this issue, we propose in this work the TL-based Control Design approach, which is focused on designing and implementing the control strategies of a general purpose WWTP. In this case, the TL-based Control Design approach consists in two stages: (i) the LSTM-based controller, where the design and training of an ANN-based controller is carried out, and (ii) the Control Knowledge Transfer approach, where the transfer of the controller knowledge into the different industrial control loops is performed. The first stage is mainly based on designing an ANN able to manage the signals considered in the control of the industrial process. To achieve this, the proposed ANN-based controller predicts the corresponding actuation signal accordingly to its input measurements, that is, the measured value and its set-point. In our case, the signals involved in the control loops correspond to either the $S_{O,5}$ or the $S_{NO,2}$ concentrations, and their respective actuation signals, the $K_{La,5}$ or Q_a. Besides, the ANN-based controller will be implemented with LSTM cells due to their good performance when dealing with time-series signals, such as the ones obtained from the BSM1 framework. ([11] Section 10.10, [8]). The second stage is mainly focused on transferring the knowledge of the proposed LSTM-based controller into the other control loops. In this case, the LSTM-based controller is considered as the baseline strategy to be transferred (see Figure 3). Thus, the objective is to design only a LSTM-based controller instead of as many LSTM-based structures

as control loops present in the WWTP. Then, its knowledge will be transferred into the remaining loops.

It is also important to notice that this transfer approach can be adopted in any industrial scenario. However, there is a requirement that has to be fulfilled; the TL-based Control Design can only be applied among control loops sharing the same control objective. This is motivated by the fact that the ANN-based structure trained in the source control loop will learn how to generate an actuation signal from the controlled ones with the objective of performing certain tasks, for instance, the tracking of a given set-point. Then, the knowledge of this ANN-based structure will be transferred into the target one, which should have the same objective. Otherwise, the target structure would generate actuation signals which do not fulfil the control objective. In the case of this work, the control objective is clear, where both the DO and the NO control loops are designed to track the given set-points regardless of the fact that the involved signals show different values and dynamics [8,25].

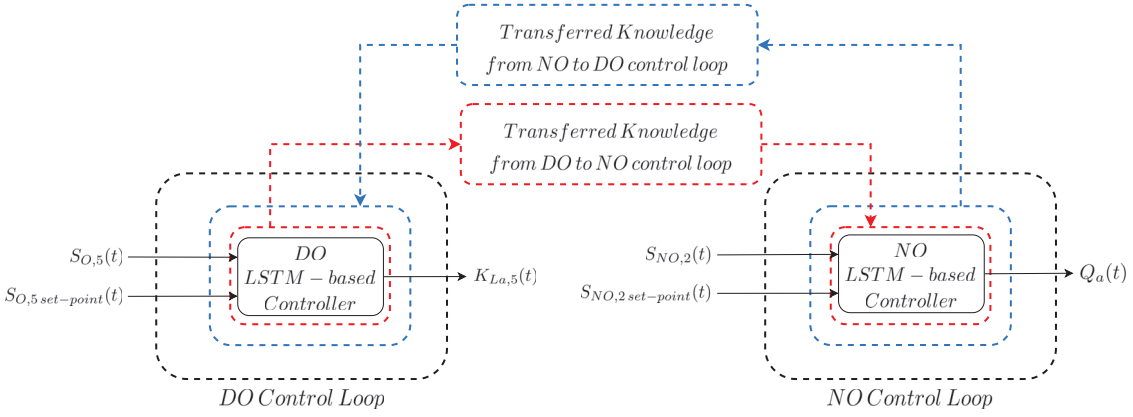

Figure 3. Graphical description of the TL-based Control Design approach. Notice that DO refers to the Dissolved Oxygen ($S_{O,5}$) control loop, whilst NO refers to the nitrate and nitrite ($S_{NO,2}$) control loop.

Once the knowledge of the LSTM-based control structure is transferred, the control performance of the LSTM-based controller can be adjusted through a fine-tuning process which consists in a retraining of the LSTM-based structure. However, this fine-tuning process is different from the usual fine-tuning processes performed in the usual applications of transfer learning, that is, the development of image classifiers. There, the data considered to carry out the fine-tuning process consist in a set of new images where the labels are intrinsically obtained from the same images. Taking up the dog breed classifier, the TL fine-tuning process is performed to the Inception structure with images of different dog breeds where the labels are obviously clear. When talking about industrial processes, the situation completely changes. The new measurements have to be obtained from the control loop where the LSTM-based controller is going to be transferred. In addition, the knowledge about how to control this loop has to also be obtained. For that reason, the data required to perform the fine-tuning processes have to be obtained by means of simulating the behaviour of the industrial process when an existing and conventional controller is applied. If not, the LSTM-based controller will not be able to offer a good control performance.

In this manuscript, two LSTM-based controllers will replicate the behaviour of the default WWTP PIs since they are the ones present in the BSM1 digital framework [8]. This is motivated by the fact that the LSTM-based PI controller can be obtained with data from the DO control loop (DO LSTM-based PI) and then transferred into the NO control loop, or it can be designed considering measurements from the NO control loop (NO LSTM-based

PI) and then transferred into the DO loop. From these two controllers, the one offering the best control performance in both control loops will be fine-tuned.

3.1. LSTM-Based PI

As it has been previously stated, the controller proposed in the TL-based Control Design approach consists in a LSTM-based controller which will act as a PI controller managing either the $S_{O,5}$, or the $S_{NO,2}$ concentrations. Hence, two LSTM-based PI candidates are proposed since there exists two control loops, the DO and the NO control loop. For that reason, we will analyse the control performance of each one in order to determine which LSTM-based PI will be transferred and fine-tuned. The first LSTM-based PI controller corresponds to the DO LSTM-based PI, which is derived from the PI managing the $S_{O,5}$ concentration, while the second one corresponds to the NO LSTM-based PI. It is derived from measurements of the default PI managing the $S_{NO,2}$. Before designing and training the two LSTM-based PIs, one can guess which one will offer the best control performance. If the control performance of the default PI controllers is taken into account (see Figure 4), one can observe that the best PI corresponds to the one managing the $S_{O,5}$, since it is able to maintain the S_O concentration at the desired value (2 mg/L). On the other hand, the PI managing the $S_{NO,2}$ is not able to maintain the desired set-point. Thereby, the control performance of the LSTM-based ones will be similar to the default PI controller from which the data were obtained. In other words, the better the conventional controller performance, the better the LSTM-based one.

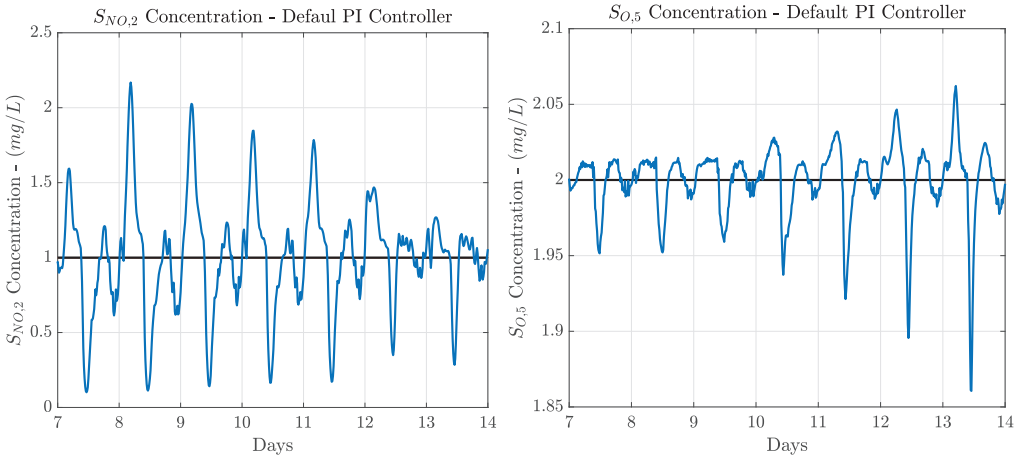

(**a**) $S_{NO,2}$ Default PI control (**b**) $S_{O,5}$ Default PI control

Figure 4. Control performance when the default PI controllers are adopted. Notice that the worst performance is offered by the $S_{NO,2}$ default PI controller.

The DO LSTM-based PI and the NO LSTM-based PI structures are obtained by means of a grid search method where different LSTM-based structures are trained with the same set of measurements. The efforts of the grid search are focused on determining the number of LSTM cells, feedforward layers, and hidden neurons per layer of the LSTM-based structure. Then, the LSTM structure offering the best prediction performance without committing overfitting is the one considered as the main structure in which the LSTM-based PI is based on. In that sense, the grid search is performed instead of finding the parameters characterising the PI controller, that is, the integral time and the proportional gain [36]. This means that a deep knowledge of the process under control is not required. Only pairs of input and output measurements of the existing default PI controllers are needed. To obtain them, a complete year of randomly distributed weather profiles has

been simulated in order to achieve a good control performance regardless of the weather conditions. From all the available measurements, the input and output measurements of the LSTM-based PI controller will be determined accordingly to the control loop they will manage:

- DO Control loop: the measurements involved in the DO control loop are the dissolved oxygen ($S_{O,5}$), its desired set-point ($S_{O,5_{set-point}}$), and the oxygen transfer coefficient of the fifth reactor tank of the WWTP ($K_{La,5}$).
- NO Control loop: the measurements involved in the NO control loop are the nitrate and nitrite nitrogen ($S_{NO,2}$), its desired set-point ($S_{NO,2_{set-point}}$) and the internal recirculation flow of the WWTP (Q_a).

These measurements are the ones considered to carry out the grid search method devoted to determining the LSTM-based PI structures. Each one of these measurements is split into three different sets: 70% of the measurements to train the different LSTM-based net configurations, 15% to validate them, and the remaining 15% to test the structures. The grid search process has been carried out adopting the Adam optimizer ([11], Sections 6.5 and 8.5.3) and a total amount of 500 epochs. The initial learning rate value has been set to 1×10^{-3}, however, it is reduced along the process. In addition, LSTM nets are also known to suffer overfitting problems, where they memorise the input and output measurements instead of deriving a model from them ([11], Chapter 7). To avoid this problem, the L2 parameter regularisation technique and early stopping method are considered. The L2 parameter regularisation consists in the addition of extra penalty to the weights of the corresponding layer ([11], Section 7.1.1). This extra penalty is known as the weight decay parameter, which in this case has been set to 5×10^{-4}. On the other hand, early stopping acts as a technique which stops the training process when the validation performance changes its tendency with respect to the training one ([11], Section 7.8). Here, the important point corresponds to the early patience, which determines the amount of epochs that this change of tendency is allowed. In this work, we consider an early patience of five epochs, understanding an epoch as a complete pass over the training dataset ([37], Chapter 2). Both LSTM-based controllers consider the same LSTM-based structure (see Figure 5) which mainly consists in two LSTM cells devoted to extracting and obtaining information from the time correlation between measurements and two feedforward layers which will transform this information into the desired output. Moreover, each structure considers Normalisation and Denormalisation stages in charge of normalising the input measurements towards zero mean and unity variance, and to take them into its natural range, respectively. These two stages are needed since the range of the measurements involved in the control loops are quite different: the mean of the measurements involved in the DO control loop equal to 1.9752 and 144.68 for the $S_{O,5}$ and the $K_{La,5}$, respectively. In the case of the NO loop, the mean values of the variables involved in the control are equal to 0.9937 and 2.1802×10^4 for the $S_{NO,2}$ and Q_a measurements. As a summary, the DO LSTM-based and NO LSTM-based structures are as follows:

- DO LSTM-based PI
  - Input measurements: the dissolved oxygen in the fifth reactor tank ($S_{O,5}(t)$) and its desired set-point ($S_{O,5_{set-point}}(t)$). Besides, the DO LSTM-based net considers the Nonlinear Autoregressive Exogenous principle (NARX) where the output predicted by the net will be considered as an extra input. This extra input provides the LSTM-based structure with information about its performance in the prediction process [38], thus it will be able to correct its predictions as a function of this extra input. In this case, the extra input corresponds to the previously computed actuator signal ($K_{La,5}(t-1)$).
  - Normalisation Stage: stage devoted to normalising the input measurements towards zero mean and unity variance.

- LSTM-based Net: main part of the LSTM-based Controller. It consists of two LSTM cells with 100 and 50 hidden neurons and two feed forward layers with 50 and 25 hidden neurons, respectively.
- Denormalisation Stage: stage devoted to denormalising the actuation signal (DO LSTM-based Net output) towards its real range of values.
- Output: the actuation signal which corresponds to the oxygen transfer coefficient of the fifth reactor tank ($K_{La,5}(t)$).

• NO LSTM-based PI

- Input measurements: the nitrate and nitrite nitrogen in the second reactor tank ($S_{NO,2}(t)$) and its desired set-point ($S_{NO,2_{set-point}}(t)$). As it happens with the DO LSTM-based PI, the NO LSTM-based controller also considers the NARX principle. In this case, the extra input corresponds to the previously computed actuator signal ($Q_a(t-1)$).
- Normalisation Stage: stage devoted to normalising the input measurements towards zero mean and unity variance.
- LSTM-based Net: main part of the LSTM-based Controller. It consists of two LSTM cells with 100 and 50 hidden neurons and two feed forward layers with 50 and 25 hidden neurons, respectively.
- Denormalisation Stage: stage devoted to denormalising the actuation signal (DO LSTM-based Net output) towards its real range of values.
- Output: the actuation signal which corresponds to the WWTP internal recirculation flow rate ($Q_a(t)$).

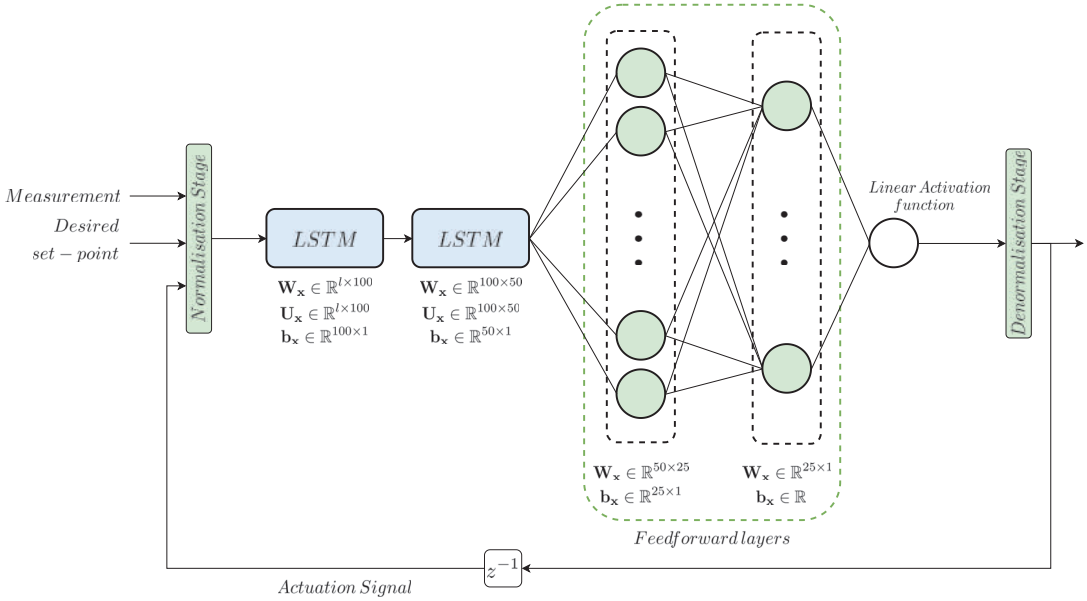

Figure 5. LSTM-based net considered in the LSTM-based Controller. l corresponds to the number of inputs, which in this case is set to three measurements: the measured concentration of interest, $S_{O,5}(t)$ or $S_{NO,2}$, its set-point, $S_{O,5_{set-point}}(t)$ or $S_{NO,2_{set-point}}(t)$, and the actuation variable, $K_{La,5}(t-1)$ or $Q_a(t-1)$.

The prediction performance of both structures has been computed in terms of the difference between the predicted actuation variables and the expected ones (remember that the DO LSTM-based PI predicts the $K_{La,5}$), whereas the NO one predicts the Q_a. Five metrics are adopted, the Root Mean Squared Error (RMSE), the Mean Absolute Error (MAE), the Mean Average Percentage Error (MAPE) the determination coefficient (R^2), and

the training time [39]. The RMSE and the MAE tell us how the prediction errors are, that is, if the predictions are close to the expected measurements or not. However, they are absolute metrics in terms of how they do not tell us how big or small these errors are. For that reason, we consider the MAPE, which compares the errors with respect to the expected value. R^2 is considered to determine the correlation between the predicted and expected measurements. Finally, the training time is considered to determine the amount of time to train unique network. Notice that all the prediction metrics are computed considering normalised values, with the exception of the MAPE in order to avoid divisions by zero and the training time. In that sense, the results show that the proposed LSTM-based structures are able to offer a good prediction performance (see Table 1) since both structures yield low RMSE, MAE and MAPE values at the same time they offer a R^2 nearly equal to 1. Therefore, it is corroborated that these structures can be used to implement PI controllers which are mainly based on data.

Table 1. Prediction performance of the DO LSTM-based PI and the NO LSTM-based PI.

	LSTM-Based Prediction Performance				
	RMSE	**MAE**	**MAPE**	R^2	**Training Time**
DO LSTM-based PI	0.026 mg/L	0.018 mg/L	1.347%	0.999	69.91 s
NO LSTM-based PI	0.048 mg/L	0.037 mg/L	6.26%	0.997	98.60 s

3.2. Control Knowledge Transfer Approach

The Control Knowledge Transfer approach corresponds to the stage of the TL-based Control Design devoted to transferring the knowledge of the LSTM-based PI structures of one WWTP control loop into the other. The adoption of this stage is motivated by the fact that we looked for the ease and speed-up of the controller design and implementation process, respectively.

In this manuscript, three different TL approaches are considered to achieve the transfer of the control knowledge between control loops. Two of them are considered to determine which controller, the DO or the NO LSTM-based PI, has to be transferred and then fine-tuned. The third approach mainly consists in the adoption of the controller showing the best performance in the source and target domains and its fine-tuning to adapt its behaviour to the dynamics of the target domain, the control loop where it has been transferred. As a summary, the three considered control approaches are:

- Transfer Learning from DO to NO
  The DO LSTM-based PI structure is transferred directly from the DO to the NO control loop. Here, it is important to notice that the structure is not fine-tuned, that is, the LSTM-based PI controller has been trained to manage the $S_{O,5}$ concentration. Besides, only the normalisation and denormalisation stages are adapted to the NO control loop measurements.
- Transfer Learning from NO to DO
  The NO LSTM-based PI structure is directly transferred from the NO to the DO control loop without performing any change, neither in its structure, nor in its weights and biases. Thus, the knowledge on how to manage $S_{NO,2}$ concentration is transferred into the DO control loop. The unique change performed in this transfer approach corresponds to the normalisation and denormalisation stages. They have been adapted to normalise and denormalise the measurements coming from the NO control loop instead of the DO control loop. Following this, the NO LSTM-based PI will be at least equal to the default PI managing the $S_{NO,2}$ concentration, that is, the NO control loop PI. If Figure 4 is taken into account, one can assure that the NO LSTM-based PI controller will not offer such a good control performance as the DO LSTM-based PI derived from the DO control loop.
- LSTM-based controller Fine-tuning & Transfer

This transfer approach is the most important one since it corresponds to the transfer method performing a fine-tuning process and therefore, adapting the behaviour of the transferred controller to the target domain dynamics. In other words, in this transfer learning approach the LSTM-based controller yielding the best control performance between the Transfer Learning from DO to NO and the Transfer Learning from NO to DO will be considered as the candidate to be fine-tuned. Results in Section 4 show that the best control performance is offered by the DO LSTM-based PI. For that reason, this is the LSTM-based controller considered in the fine-tuning process. Nevertheless, this choice can be done at the very beginning if the performance offered by the conventional PI structures is considered (see Figure 4).

In terms of the three TL classes, the LSTM-based controller Fine-tuning and Transfer approach consists in an inductive transfer learning task: data from the source domain, the DO control loop, is considered to firstly obtain the DO LSTM-based PI structure. Then it is fine-tuned (retrained) with data coming from the PI controlling the target domain, the NO control loop. In other words, the default $S_{NO,2}$ controller whose performance is observed in Figure 4a has been considered to perform the fine-tuning process of the DO LSTM-based PI controller. Thus, the obtained controller, the fine-tuned DO LSTM-based PI (FTDO LSTM-based PI) will know how to correctly manage the desired variable, but adapted to the NO control loop. This clearly shows that an existing controller managing the target control loop is compulsory to obtain the measurements considered in the fine-tuning process. This differs from traditional and conventional TL applications, where labelled data are available.

The main point here is that in the fine-tuning process not all the layers of the DO LSTM-based PI controller will be retrained with measurements of the target domain: the weights of the two LSTM cells are blocked whilst the weights and biases of the two feedforward layers (see Figure 5) are modified in the fine-tuning process. The LSTM cells are the ones that are blocked since they are the layers gathering the information about the time-dependence between measurements. The feedforward layers mainly take this information to adapt the output of the controller to the desired control loop. For that reason, these are the layers which will be retrained just to adapt the outcomes of the LSTM layers to the new domain.

The measurements of the target domain are again obtained by performing a whole-year simulation of the BSM1 behaviour when the three weather profiles, dry, rainy, and stormy, are randomly distributed. The weights and biases of the two retrained feedforward layers are obtained considering the same training parameters as in the case of the DO LSTM-based PI training process: initial learning rate equals to 1×10^{-3}, the weight decay equals to 5×10^{-4} and the early patience is set to 5 epochs.

4. Results

4.1. TL-Based Control Design Results

The performance of the TL-based Control Design approach is determined by means of analysing the control performance of each one of the proposed TL approaches: (i) the Transfer Learning from DO to NO, (ii) the Transfer Learning from NO to DO, and (iii) the LSTM-based controller Fine-tuning and Transfer. In that sense, the two first results will determine which controller, the DO LSTM-based PI or the NO LSTM-based PI, is performing better in both control loops when no fine-tuning process is carried out. Finally, the one performing better is fine-tuned and its control performance is computed in the last TL approach. Results will show which is the best option not only to obtain a complete and good control approach mainly based on data, but also to speed-up the design process of the complete WWTP control strategy.

The control performance has been computed in terms of fix and variable set-points in order to determine if the TL-based Control Design approach is suitable for both types of set-points. Fix set-points are considered since the default control strategy considers them in order to assure that the nitrification and denitrification processes, the ones performing the

pollutant reduction task, are correctly performed [8,27]. They have been set to 2 mg/L and 1 mg/L for the $S_{O,5}$ and $S_{NO,2}$ control loops, respectively. Notwithstanding, variable set-points are the ones of most interest since most of the times the set-points are computed by means of other control strategies or are varied in order to optimise the pollutant reduction process [10,14,40,41]. In this case, the variable DO set-point has been computed accordingly to the Fuzzy Logic adopted in [10], where the Fuzzy controller is considered to determine the $S_{O,5}$ set-point generating the lower $S_{NH,5}$. Moreover, the three different BSM1 weather profiles have also been simulated to determine if the control design approach can be considered regardless of the weather conditions.

4.2. Transfer Learning from DO to NO

The first computed control performance corresponds to the situation where the DO LSTM-based PI is obtained with data from the DO control loop. Then, it is transferred into the NO control loop without performing any fine-tuning process. Results are shown in Table 2, where the first important effect that one can notice is that the control performance in the DO control loop, that is, in the management of $S_{O,5}$, is even better than the control offered by the default PI. This effect is motivated by two situations: (i) the fact that the DO LSTM-based PI has been trained through the simulation of the control strategy when random variations in the set-point are provided, and (ii) the NARX principle which provides the LSTM-based structure with information about the previous predicted outcomes. Thus, the LSTM-based structure has learnt how to correct variations present either in the set-point, or in the measured concentration.

Table 2. Control performance when the DO LSTM-based PI derived from the DO control loop is transferred into the NO control loop.

Transfer Learning from DO to NO Control Loop						
Fix Set-point						
	Dry Weather		Rainy Weather		Stormy Weather	
Structure	*IAE*	*ISE*	*IAE*	*ISE*	*IAE*	*ISE*
PI—$S_{O,5}$	0.148	0.007	0.143	0.007	0.158	0.007
DO LSTM-based PI—$S_{O,5}$	0.006	9.98×10^{-6}	0.006	1.12×10^{-5}	0.006	1.29×10^{-5}
PI—$S_{NO,2}$	1.594	0.691	1.922	0.951	1.874	0.977
DO LSTM-based PI—$S_{NO,2}$	1.008	0.290	1.401	0.578	1.033	0.357
Variable Set-point						
PI—$S_{O,5}$	0.185	0.016	0.155	0.014	0.206	0.020
DO LSTM-based PI—$S_{O,5}$	0.013	2.34×10^{-4}	0.016	4.48×10^{-4}	0.016	4.05×10^{-4}
PI—$S_{NO,2}$	1.792	0.858	2.132	1.089	1.884	0.989
DO LSTM-based PI—$S_{NO,2}$	1.271	0.503	1.672	0.758	1.358	0.593

In terms of the *IAE* and *ISE* metrics, one can observe that they are improved with respect to the default PI control performance when a fixed set-point is considered. In addition, these improvements are achieved regardless of the weather profile. In other words, the *IAE* and *ISE* values were improved by around a 95.98% and a 99.84% in average with respect to the default PI controller, respectively. For instance, the highest *IAE* improvement is achieved when the stormy influent profile is simulated. The *IAE* offered by the default $S_{O,5}$ PI controller is equivalent to 0.158, while it is reduced until 0.006 when the DO LSTM-based PI is considered. This entails that the difference between the measured and the $S_{O,5}$ controller is minimal. In terms of the *ISE*, the highest improvement is obtained when the dry weather is simulated. The achieved improvement equals to 99.86% with respect to the default PI controller. Notwithstanding, this improvement equals to 99.84% and 99.82% when the rainy and stormy weathers are considered, respectively. These results

show that the DO LSTM-based PI is able to be highly improved when a fixed set-point is considered. However, the important results are the ones obtained when a variable set-point is considered, since it corresponds to the most frequently adopted set-point topology.

In such a context, the same effect is observed when a $S_{O,5}$ variable set-point is considered. In this case, the average improvement in terms of the *IAE* and *ISE* equals to 91.67% for the *IAE* and a 97.77% for the *ISE*. Now, the highest improvement is achieved when the dry weather is considered: the *IAE* and the *ISE* are improved by 92.97% and 98.54% with respect to the default PI controller performance. This is motivated by the fact that rainy and stormy influents are derived from the dry weather where the rainy and stormy episodes are included. For that reason, the LSTM-based structure has more often observed the effects of the PI controlling the $S_{O,5}$ when dry episodes are observed rather than stormy or rainy ones. In addition, the control performance clearly shows that the DO LSTM-based PI controller can be adopted as the main controller in the DO control loop (see Figure 6). As it is observed, the output of the controller is much closer to the given set-point of 2 mg/L than the default PI output.

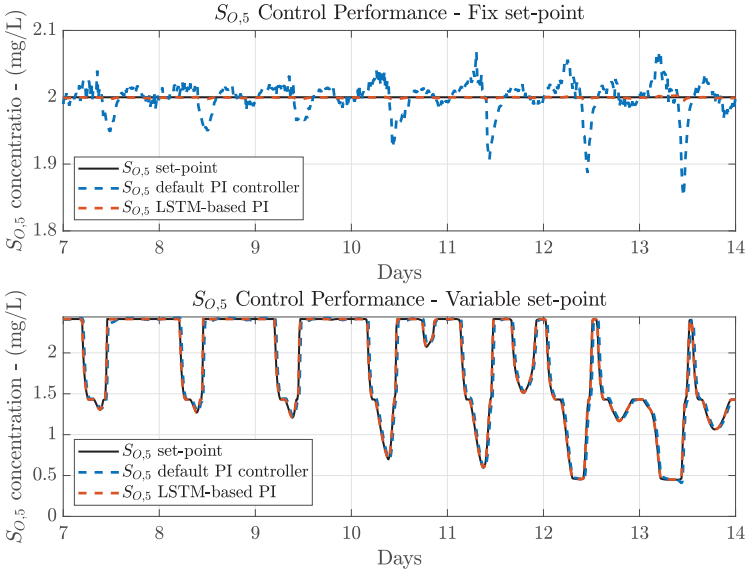

Figure 6. Control performance for the DO control loop when the LSTM-based PI is considered.

However, the most important point is to determine the control performance of the NO control loop, since in this case the DO LSTM-based PI is directly transferred into the NO control loop. The changes performed in the control structure correspond to the normalisation and denormalisation stages, which have been adapted to the range of values involved in the control of $S_{NO,2}$. Results show that the control performance of the DO LSTM-based PI controller can be improved by, on average, 33.07% and 42.94% in the case of the *IAE* and the *ISE*, respectively, when it is managing the $S_{NO,2}$ and considering a fixed set-point. For instance, the highest improvement with respect to the default PI structure is achieved when the stormy weather is considered. The *IAE* and *ISE* obtained in such a situation equal to 1.033 and 0.357, respectively, which in percentage values equal to an improvement of a 44.88% and a 63.46% for the *IAE* and *ISE* respectively. At the same time, this represents a reduction of the *IAE* and *ISE* improvement of 51.32 and 36.36 percentage points with respect to the improvement achieved when the DO LSTM-based PI is managing the $S_{O,5}$. This is clearly motivated by the fact that the DO LSTM-based PI is designed to offer its best performance when managing the DO control loop. When a $S_{O,5}$ variable set-point is chosen, one can observe that the average improvements in the NO control loop

and in terms of the *IAE* and *ISE* are equal to 26.19% and 37.27%, respectively, being the dry weather the one showing the highest improvement (see Figure 7). The *IAE* values go from 1.792 to 1.271 while the *ISE* values go from 0.858 to 0.503, respectively.

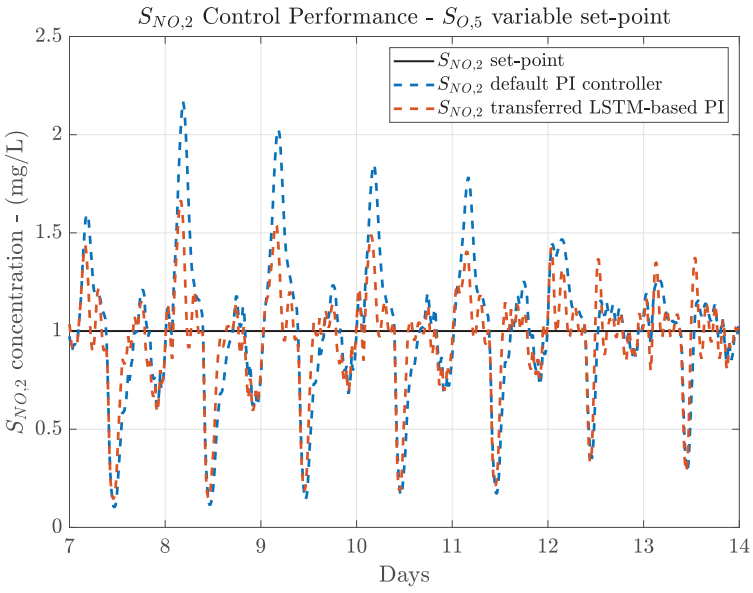

Figure 7. Control performance for the NO control loop when the LSTM-based PI derived from the DO control loop is transferred into it.

These results show that the DO LSTM-based PI controller is able to improve the default PI controllers performance. For that reason, it is considered as a candidate to be fine-tuned in order to adapt its behaviour to the $S_{NO,2}$ control management and therefore, achieve a better improvement in the management of this loop.

4.3. Transfer Learning from NO to DO

Before performing the fine-tuning process, the control performance of the NO LSTM-based PI is also computed to determine its behaviour when managing the NO control loop (its source domain) and its performance when managing the DO loop (its target domain). Results are shown in Table 3 where at first sight it is clearly observed that the *IAE* and *ISE* metrics are improved with respect to the default $S_{NO,2}$ PI controller. When a $S_{O,5}$ fix set-point is considered, the NO control loop *IAE* is improved in average a 24.32% while the corresponding *ISE* is improved around a 39.03% in average. Both with respect to the default NO control loop PI controller. The *ISE* improvement shows that the proposed NO LSTM-based PI controller, which has been derived from the NO control loop, is able to reduce the highest errors between the measured $S_{NO,2}$ and its set-point, with respect to the default PI controller. However, the control performance can be still improved since the improvement achieved in terms of the *IAE* error is still low. For instance, the best improvement is observed when the stormy weather is considered. There, the obtained *IAE* goes from 1.874 to 1.360, whereas the *ISE* goes from 0.977 to 0.543. These values represent an improvement around a 27.43% and a 44.42% when the obtained *IAE* and *ISE* values are compared to the default PI control metrics. In terms of the $S_{O,5}$ control performance, the transferred NO LSTM-based PI shows that the *IAE* performance is degraded instead of improved. For instance, when the NO LSTM-based PI is adopted, the *IAE* is increased from 0.148 to 0.158 when the dry weather is considered. This effect is motivated by the fact that the default PI of the NO control loop is not offering such a good control performance as

the default PI of the DO control loop. Thus, the control performance will not be improved if data from the NO control loop is obtained to derived the NO LSTM-based PI and then transfer it into the DO control loop.

Table 3. Control performance when the NO LSTM-based PI derived from the NO control loop is transferred into the DO control loop.

Transfer Learning from NO to DO Control Loop						
Fix Set-point						
	Dry Weather		Rainy Weather		Stormy Weather	
Structure	*IAE*	*ISE*	*IAE*	*ISE*	*IAE*	*ISE*
PI—$S_{NO,2}$	1.594	0.691	1.922	0.951	1.874	0.977
NO LSTM-based PI—$S_{NO,2}$	1.302	0.486	1.399	0.542	1.360	0.543
PI—$S_{O,5}$	0.148	0.007	0.143	0.007	0.158	0.007
NO LSTM-based PI—$S_{O,5}$	0.158	0.004	0.146	0.004	0.160	0.004
Variable Set-point						
PI—$S_{NO,2}$	1.792	0.858	2.132	1.089	1.884	0.989
NO LSTM-based PI—$S_{NO,2}$	1.266	0.464	1.574	0.662	1.372	0.557
PI—$S_{O,5}$	0.185	0.016	0.155	0.014	0.206	0.020
NO LSTM-based PI—$S_{O,5}$	0.288	0.030	0.239	0.022	0.385	0.049

Visually, one can observe that the $S_{NO,2}$ control performance is slightly improved with respect to the default PI (see Figure 8). The peaks of $S_{NO,2}$ concentration are reduced, however, the desired set-point is not achieved. In terms of the $S_{O,5}$, the control performance is even slightly degraded with respect to the default PI controller. As it can be observed, the measured $S_{O,5}$ does not show variations as the default PI controller, however, there exists an offset which produces the *IAE* increment. For that reason, the *ISE* metric in terms of the $S_{O,5}$ is still reduced, it now equals to 0.004 in average instead of 0.007. Notice that the *ISE* tells if there exists a huge difference between the measured and the desired concentration, whereas the *IAE* tells if the difference is maintained over time.

When a variable set-point is considered, one can observe that the control performance is only improved in terms of the NO control loop. The *IAE* and *ISE* metrics are improved in averages with respect to the default PI controller of 27.56% and 42.94%, respectively. In terms of the DO control loop performance, results show that transferring the NO LSTM-based PI controller derived from the NO loop into the DO loop is not an option, since all the control metrics are degraded. For instance, the *IAE* and *ISE* metrics are nearly doubled with respect to the default PI controller when the stormy weather profile is simulated. These results entail that the NO LSTM-based PI cannot be considered as a candidate to be fine-tuned since it does not improve the control performance of target domain at the same time that the improvement achieved in the source domain is much lower than the one achieved by the DO LSTM-based PI. In addition, this also corroborates one of the main ideas stated before: the better the conventional control performance, the better the LSTM-based one. For that reason, the DO LSTM-based PI is the one considered to perform the fine-tuning process. It is important to notice that the initial training of both structures, the DO LSTM-based PI and the NO LSTM-based PI is not compulsory. In Figure 4b it is clearly observed that the control loop offering the best performance corresponds to the PI managing the DO control loop. Hence, the DO LSTM-based PI can be initially adopted to be trained. Then, it will be transferred into the NO control loop and fined-tuned. As a consequence, there is no need to train or even implement the NO LSTM-based PI.

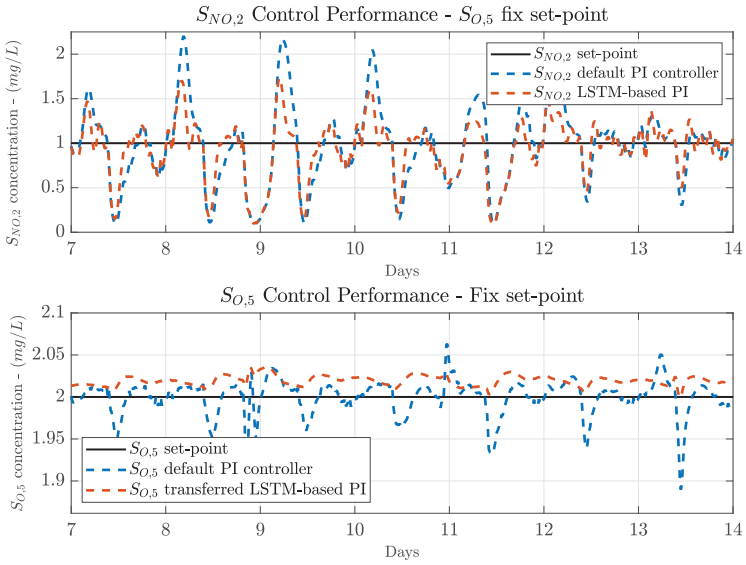

Figure 8. Control performance for the NO and DO control loops when the stormy weather is considered. The LSTM-based PI managing the DO control loop is derived from the NO control loop and transferred into the DO one.

4.4. LSTM-Based Controller Fine-Tuning & Transfer

Once the control performance of the DO and NO LSTM-based PI controllers is computed one can clearly observe that the DO LSTM-based PI is the controller offering the best control performance in both control loops. For that reason, the fine-tuning of the DO LSTM-based PI controller is proposed. To perform this tasks, data coming from the default $S_{NO,2}$ PI controller is considered. In that sense, information about how to control and manage the $S_{NO,2}$ concentration is provided to the DO LSTM-based PI. Thus, the fine-tuned version of the controller, the FTDO LSTM-based PI, should be able to improve a better control performance in terms of the $S_{NO,2}$ managing process.

Now, the prediction performance of the FTDO LSTM-based PI equals to a RMSE of 0.095 mg/L, a MAE of 0.067 mg/L, a MAPE of 6.24% and a R^2 of 0.991. Its training time equals to 20.27 s. At first sight one can observe that prediction performance is degraded with respect to the DO and NO LSTM-based PI controllers. However, this degradation is motivated by the fact that the proposed FTDO LSTM-based PI controller has learnt how to correctly manage the $S_{O,5}$ and $S_{NO,2}$ concentration instead of a unique one. In addition, the training time in this occasion equals to 20.27 s, which means that the time spent in the fine-tuning process is largely reduced with respect to training the LSTM-based structure from scratch. This effect is motivated by the information already present in the LSTM structure, that is, the weights and biases of the blocked LSTM cells. This corroborates that TL techniques can be adopted to simplify and speed up the control design process. Let's suppose that instead of transferring the knowledge of the DO LSTM-based PI into the NO control loop and performing a fine-tuning process, we decide to control each loop with its corresponding LSTM-based PI structure. The amount of time devoted to training the networks correspond to 69.91 and 98.60 s for the DO and NO control loops, respectively. This equals to a total time of 168.51 s only in terms of the training time. Although this time is affordable, if the DO LSTM-based PI is transferred into the NO control loop, only 69.91 s plus the time spent in the fine-tuning process, no more than 21 s is required. Thus, the total amount of time invested in the design process equals to 90.18 s, which represents a reduction of 78.33 s with respect to training two individual nets. Therefore, the reduction of the training time is clearly observed. In addition, it is important to notice that the WWTP

we are dealing with only considers two control loops. However, this reduction of time will be higher in these situations where the number of control loops to design is larger. In that sense, an estimation of the training time reduction can be performed. If we suppose that the training time of the baseline LSTM-based PIs (from scratch) correspond to $t_{baseline}$ and that the time spent in the fine-tuning process on average equals to t_{ft}, the reduction of time (Δt) provided by our approach can be computed as:

$$\Delta t = N \cdot t_{baseline} - [t_{baseline} + (N-1) \cdot t_{ft}] = (N-1)[t_{baseline} - t_{ft}], \quad (9)$$

where $t_{ft} \ll t_{baseline}$. N equals to the number of control loops where the baseline LSTM-based PI is the transfer. As it is observed, the higher the number of control loops to design, the higher the reduction of time and the higher the benefit of the proposed methodology. Not only this, but this methodology can also be applied in those situations where the control of a new WWTP scenario has to be designed. In such a context, the new control structure can be derived by transferring the knowledge of the control structure of an already controlled WWTP. This would involve an even higher reduction of the complexity and time required in the development of the control strategy. All these facts motivate us to consider the TL methods in the design of the WWTP control loops.

In terms of the control performance, results of the FTDO LSTM-based PI control are shown in Table 4, where the *IAE* and *ISE* values are computed for different weather profiles and set-points. It is worth noticing that the $S_{NO,2}$ is now managed by the fine-tuned and transferred DO LSTM-based PI, that is, the FTDO LSTM-based PI, whereas the $S_{O,5}$ concentration is managed by the DO LSTM-based PI.

Table 4. Control performance when the DO LSTM-based PI derived from the DO control loop is transferred into the NO control loop. Then, the NO controller is fine-tuned with data from the default PI controller managing the $S_{NO,2}$.

LSTM-Based Controller Fine-Tuning & Transfer						
Fix Set-point						
	Dry Weather		Rainy Weather		Stormy Weather	
Structure	*IAE*	*ISE*	*IAE*	*ISE*	*IAE*	*ISE*
PI—$S_{O,5}$	0.143	0.007	0.143	0.007	0.158	0.007
DO LSTM-based PI—$S_{O,5}$	0.004	5.12×10^{-6}	0.008	2.43×10^{-5}	0.006	1.76×10^{-5}
PI—$S_{NO,2}$	1.594	0.691	1.922	0.951	1.874	0.977
FTDO LSTM-based PI—$S_{NO,2}$	0.091	0.002	1.150	0.625	0.357	0.151
Variable Set-point						
PI—$S_{O,5}$	0.185	0.016	0.155	0.014	0.206	0.020
DO LSTM-based PI—$S_{O,5}$	0.013	1.99×10^{-4}	0.017	3.91×10^{-4}	0.017	3.72×10^{-4}
PI—$S_{NO,2}$	1.792	0.858	2.132	1.089	1.884	0.989
FTDO LSTM-based PI—$S_{NO,2}$	0.129	0.004	0.643	0.261	0.324	0.122

When a fixed set-point is considered, one can observe that the control performance is hugely improved not only in terms of the $S_{O,5}$, but also in terms of the $S_{NO,2}$. The improvement of the DO control loop with respect to the default PI controller is translated into an average reduction of the *IAE* around a 95.94% and an average reduction in the *ISE* around a 99.78%. Thereby, this is translated in a better tracking process of the $S_{O,5}$ and consequently, a better management of this concentration. In terms of the NO control loop, one can observe that the *IAE* and *ISE* are hugely improved as well. However, there is an exception with the rainy weather. In this case, the $S_{NO,2}$ *IAE* and *ISE* are only improved a 40.17% and a 34.27%, respectively. This is motivated by the fact that the rainy weather profile shows two large perturbation during days 9 and 11. Besides, the fine-tuning process is performed with measurements obtained from the $S_{NO,2}$ default PI controller when a

whole year of randomly distributed weathers is simulated. Thus, this entails that most of the knowledge provided to the DO LSTM-based PI consists in the control actuations to manage the $S_{NO,2}$ concentration when the dry weather is considered (remember that rainy and stormy weathers are equal to the dry weather with the exception of the two rainy and the two stormy episodes). On average, the NO control loop *IAE* and *ISE* are reduced by 73.47% and 72.84% with respect to the default $S_{NO,2}$ PI control performance. The greatest improvement is observed when the dry weather is considered. The *IAE* is reduced from 1.594 to 0.091, whereas the *ISE* is decreased from 0.691 to 0.002 (see Figure 9). In the case of the rainy weather, the reduction of the *IAE* and *ISE* is lower, the *IAE* changes from 1.922 to 1.150 and the *ISE* from 0.951 to 0.625. Nevertheless, this *IAE* value corresponds to the lowest NO control loop *IAE* value of the three TL approaches considered in this work.

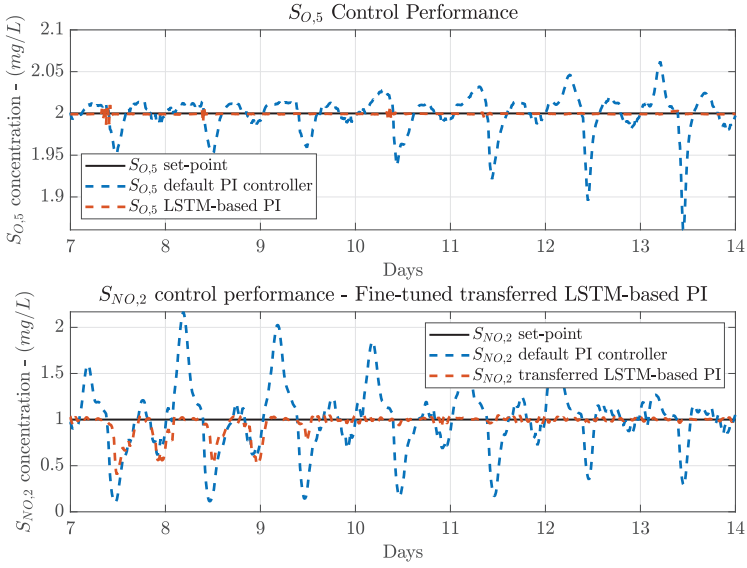

Figure 9. Control performance for the NO and DO control loops when a $S_{O,5}$ fix set-point and dry weather are considered. The LSTM-based PI managing the NO loop is transferred from the DO control loop and fined-tuned with data from the NO control loop.

Results of the control performance when a variable set-point is considered show the same tendency as the fix set-point ones. The *IAE* and *ISE* metrics have been improved for all the weather profiles. Again, the most important results are the ones corresponding to the NO control loop, which is the controller whose control performance improvement is sought with the fine-tuning process. In that sense, the best improvement is now observed when the dry weather is simulated. The *IAE* has been decreased from 1.792 to 0.129, which equals to an improvement of 92.80%. In terms of the *ISE*, it is decreased from 0.858 to 0.004, which represent an improvement of a 99.53%. It is important to notice that the lowest control performance is obtained when the rainy weather is considered, the *IAE* deceases from 2.132 to 0.643 while the *ISE* is reduced from 1.089 to 0.261. Although these improvements are not so high as the ones achieved with the dry weather, they are still much better than the performance obtained when the fine-tuning process is not carried out. For instance, the *IAE* has been improved a 69.84% whilst the *ISE* has been improved a 76.03%. The *IAE* improvement represents an increase of 48.26 and 42.63 percentage points with respect to the improvements achieved in the Transfer Learning from DO to NO and from NO to DO. In terms of the *ISE*, these increments equal to 45.64 and 36.82 percentage points, respectively. Visually, we can observe in Figure 10 that the $S_{NO,2}$ desired value of 1 mg/L is obtained at the same time the $S_{O,5}$ variable set-point is correctly tracked. In

addition, the rainy episodes are plotted to show that the FTDO LSTM-based PI controller requires some more knowledge to finally learn how to manage these events.

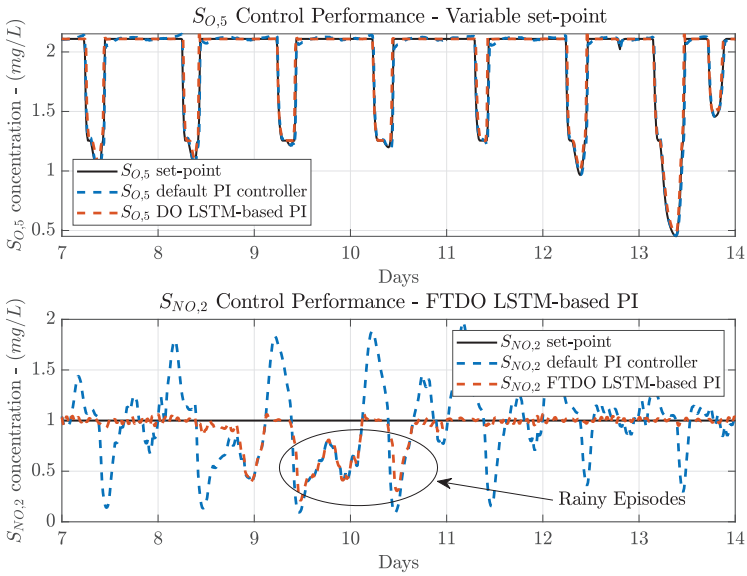

Figure 10. Control performance for the NO and DO control loops when a $S_{O,5}$ variable set-point and rainy weathers are considered. The LSTM-based PI managing the NO loop is transferred from the DO control loop and fined-tuned with data from the NO control loop.

As a summary, the control performance is improved in all terms regardless of the set-point topology and the weather profiles. This entail that the best option to design or improve a control strategy of an industrial plant, and especially a WWTP, is to obtain a first baseline controller, the DO LSTM-based PI, and then transfer its knowledge to the rest of control loops. The main point is to design the baseline controller with data coming from the controller performing better. In our case, this controller corresponds to the $S_{O,5}$ default PI controller. Then, the obtained DO LSTM-based PI is transferred into the remaining control loops and fine-tuned with data coming from controllers actuating in the target domain. Moreover, this approach entail that control loops can be designed without requiring a high knowledge of the different processes carried out in the plant. Only input and output measurements of a control strategy performing well are required. The rest of the control loops will be derived from the implemented one. Thus, the higher the number of control loops, the higher the benefit offered with this design approach. In our case, this benefit is not widely exploded since we have only transferred the LSTM-based PI between two control loops. However, this approach can be adopted in other scenarios where the number of control loops is largely higher than the ones managed here. In that sense, the benefit of this approach should be much higher than the one observed here.

Finally, the results observed in this manuscript motivates us to open a new research line where the transfer learning approach presented here is considered as the initial process of a reinforcement learning based control design. Then, instead of performing the fine-tuning process with measurement coming from a conventional control approach, it could be performed following a reinforcement leaning process. In that sense, the controller would be fine-tuned over time, adapting its output to the incoming measurements.

5. Conclusions

In this work, we presented a new industrial control design process which involves the application of LSTM-based neural networks and transfer learning approaches. The

main purpose was to design and implement the control loops managing a general-purpose WWTP. The application is specific; however, the design approach can be adopted in any kind of industrial environment. The main idea is that TL techniques allow us to derive new control strategies from a baseline one without performing a deep tuning process of each control structure. This reduces the control design complexity, as well as the time invested in the training process of each data-based control structure. Thus, the higher the number of control loops, the higher the improvement achieved.

In our case, the proposed control design approach consists in two main processes: (i) the design of a neural network-based controller with data obtained from an existing control loop and (ii) the transfer of the controller knowledge into the remaining loops. To achieve that, three different design approaches were proposed, two of them mainly consisting in the design of the LSTM-based controller with data from a control loop and then transferring it to the others without retraining the net structure. In that sense, we considered the development of the LSTM-based PI controller either with measurements from the $S_{O,5}$ control loop or from the $S_{NO,2}$ one, both from a general-purpose WWTP. The third option considers the development of the LSTM-based PI with data from the $S_{O,5}$ control loop and the fine-tuning of its transferred version. Results show that there exists a trade-off between deriving the LSTM-based PI with measurement from the $S_{NO,2}$ or the $S_{O,5}$ control loops. If the LSTM-based PI controller is derived with measurements from the $S_{O,5}$ control loop, one can observe that the $S_{O,5}$ control performance is highly improved with respect to the default PI controller regardless of the weather influent and the considered set-point. In addition, the $S_{NO,2}$ control performance experiences a slight improvement as well. On the other hand, the NO control performance experienced an improvement at expense of degrading the $S_{O,5}$ control performance when the LSTM-based PI transferred into the DO control loop is implemented with measurements from the NO control loop. To solve this trade-off, we considered the third option, where the LSTM-based PI derived from the $S_{O,5}$ control loop was adopted and transferred into the DO control loop. Its transferred version was fine-tuned with measurements coming from the default PI controller managing the $S_{NO,2}$ control loop.

Results show that a high improvement is achieved in the $S_{O,5}$ control loop as well as in the $S_{NO,2}$ one. Besides, the lowest *IAE* and *ISE* improvements in terms of the $S_{NO,2}$ when compared to the default $S_{NO,2}$ PI controller equalled to 69.84% and 76.03% for the *IAE* and *ISE*, respectively, which are even higher improvements than in the cases where the fine-tuning process is not considered. This clearly shows that designing a LSTM-based PI in a control loop, transferring it to another different one, and then performing a fine-tuning process is the best option if a high level of improvement of the control performance is sought. Besides, this also entails a speed-up and a complexity reduction of the control design process since only the design and training of one control loop has to be performed. Again, the higher the number of control loops to design, the higher the benefit obtained following this design approach.

Author Contributions: I.P. has designed and trained the artificial neural networks considered in the TL-based methodology adopted in this work. He has also implemented and tested the proposed structures over the BSM1 framework. The manuscript has been also written by I.P., A.M., R.V. and J.L.V. supervised the work. All authors have read and agreed to the published version of the manuscript.

Funding: The APC was funded by the Spanish Government under Project TEC2017-84321-C4-4-R co-funded with European Regional Development Funds of the European Union.

Institutional Review Board Statement: Not applicable.

Informed Consent Statement: Not applicable.

Data Availability Statement: The data considered in this study correspond to the influent and effluent data generated and available in the same BSM1 framework defined in [8,25].

Acknowledgments: This work has received support from the Catalan Government under Projects 2017 SGR 1202 and 2017 SGR 1670, and from the Spanish Government through the MICINN projects PID2019-105434RB-C33 and TEC2017-84321-C4-4-R.

Conflicts of Interest: The authors declare no conflict of interest.

Abbreviations

The following abbreviations are used in this manuscript:

ANN	Artificial Neural Network
ASM1	Activated Sludge Model N.1
BSM1	Benchmark Simulation Model No. 1
BSM1-P	Benchmark Simulation Model No. 1 with Phosphorus processing
BSM2	Benchmark Simulation Model No. 2
$\mathbf{b}_x$	Biases of the xth hidden layer
DO	Dissolved Oxygen in the fifth reactor tank ($S_{O,5}$) control loop
DO LSTM-based PI	LSTM-based PI controller trained with data from the $S_{O,5}$ control loop
FTDO LSTM-based PI	DO LSTM-based PI fine-tuned with data from the $S_{NO,2}$ control loop
IAE	Integrated Absolute Error
ISE	Integrated Squared Error
$K_{La,x}$	Oxygen Transfer Coefficient of the xth reactor tank measured in day^{-1}
LSTM	Long Short-Term Memory
MAE	Mean Absolute Error
MAPE	Mean Average Percentage Error
MLP	Multilayer Perceptron
MPC	Model Predictive Controller
NO	Nitrate and nitrite nitrogen in the second reactor tank ($S_{NO,2}$) control loop
NO LSTM-based PI	LSTM-based PI controller trained with data from the $S_{NO,2}$ control loop
PI	Proportional Integral controller
PID	Proportional Integral Derivative controller
Q_0	Influent flow rate
Q_a	Internal recirculation flow rate
Q_r	External recirculation flow rate
R^2	Determination coefficient
RMSE	Root Mean Squared Error
$S_{NO,x}$	Nitrate and nitrite nitrogen in the xth reactor tank measured in mg/L
$S_{NH,x}$	Ammonium concentration in the xth reactor tank measured in mg/L
$S_{O,x}$	Dissolved oxygen concentration in the xth reactor tank measured in mg/L
TL	Transfer Learning
$\mathbf{U}_x$	Weights affecting the previous output data of the xth hidden layer
WWTP	Wastewater Treatment Plant
$\mathbf{W}_x$	Weights affecting the input data of the xth hidden layer

References

1. Ogata, K. *Modern Control Engineering*; Prentice Hall: Upper Saddle River, NJ, USA, 2010.
2. Wollschlaeger, M.; Sauter, T.; Jasperneite, J. The future of industrial communication: Automation networks in the era of the internet of things and industry 4.0. *IEEE Ind. Electron. Mag.* **2017**, *11*, 17–27. [CrossRef]
3. Ustundag, A.; Cevikcan, E. *Industry 4.0: Managing the Digital Transformation*; Springer: Cham, Switzerland, 2017.
4. Rani, A.; Singh, V.; Gupta, J. Development of soft sensor for neural network based control of distillation column. *ISA Trans.* **2013**, *52*, 438–449. [CrossRef]
5. Pisa, I.; Santín, I.; Vicario, J.L.; Morell, A.; Vilanova, R. ANN-based soft sensor to predict effluent violations in wastewater treatment plants. *Sensors* **2019**, *19*, 1280. [CrossRef] [PubMed]
6. Thennadil, S.N.; Dewar, M.; Herdsman, C.; Nordon, A.; Becker, E. Automated weighted outlier detection technique for multivariate data. *Control Eng. Pract.* **2018**, *70*, 40–49. [CrossRef]
7. Zejda, V.; Máša, V.; Václavková, Š.; Skryja, P. A Novel Check-List Strategy to Evaluate the Potential of Operational Improvements in Wastewater Treatment Plants. *Energies* **2020**, *13*, 5005. [CrossRef]
8. Alex, J.; Benedetti, L.; Copp, J.; Gernaey, K.V.; Jeppsson, U.; Nopens, I.; Pons, M.N.; Rieger, L.; Rosen, C.; Steyer, J.P.; et al. *Benchmark Simulation Model No. 1 (BSM1)*; Technical Report; Department of Industrial Electrical Engineering and Automation, Lund University: Lund, Sweden, 2008.

9. Santin, I.; Pedret, C.; Vilanova, R. Fuzzy control and model predictive control configurations for effluent violations removal in wastewater treatment plants. *Ind. Eng. Chem. Res.* **2015**, *54*, 2763–2775. [CrossRef]
10. Santin, I.; Pedret, C.; Vilanova, R. Applying variable dissolved oxygen set point in a two level hierarchical control structure to a wastewater treatment process. *J. Process Control* **2015**, *28*, 40–55. [CrossRef]
11. Goodfellow, I.; Bengio, Y.; Courville, A. *Deep Learning*; MIT Press: Cambridge, MA, USA, 2016.
12. Pisa, I.; Santín, I.; Morell, A.; Vicario, J.L.; Vilanova, R. LSTM based Wastewater Treatment Plants operation strategies for effluent quality improvement. *IEEE Access* **2019**, *7*, 159773–159786. [CrossRef]
13. Sadeghassadi, M.; Macnab, C.J.; Gopaluni, B.; Westwick, D. Application of neural networks for optimal-setpoint design and MPC control in biological wastewater treatment. *Comput. Chem. Eng.* **2018**, *115*, 150–160. [CrossRef]
14. Hernández-del Olmo, F.; Gaudioso, E.; Dormido, R.; Duro, N. Tackling the start-up of a reinforcement learning agent for the control of wastewater treatment plants. *Knowl.-Based Syst.* **2018**, *144*, 9–15. [CrossRef]
15. Pisa, I.; Morell, A.; Vicario, J.L.; Vilanova, R. Denoising Autoencoders and LSTM-Based Artificial Neural Networks Data Processing for Its Application to Internal Model Control in Industrial Environments—The Wastewater Treatment Plant Control Case. *Sensors* **2020**, *20*, 3743. [CrossRef]
16. Kasireddy, I.; Nasir, A.W.; Singh, A.K. IMC based Controller Design for Automatic Generation Control of Multi Area Power System via Simplified Decoupling. *Int. J. Control Autom.* **2018**, *16*, 994–1010. [CrossRef]
17. Wang, C.; Zhao, W.; Luan, Z.; Gao, Q.; Deng, K. Decoupling control of vehicle chassis system based on neural network inverse system. *Mech. Syst. Signal Prossess.* **2018**, *106*, 176–197. [CrossRef]
18. Souza, F.A.; Araújo, R.; Mendes, J. Review of soft sensor methods for regression applications. *Chemom. Intell. Lab. Syst.* **2016**, *152*, 69–79. [CrossRef]
19. Amirabadi, M.A.; Kahaei, M.H.; Nezamalhosseini, S.A. Novel suboptimal approaches for hyperparameter tuning of deep neural network [under the shelf of optical communication]. *Phys. Commun.* **2020**, *41*, 101057. [CrossRef]
20. Zhuang, F.; Qi, Z.; Duan, K.; Xi, D.; Zhu, Y.; Zhu, H.; Xiong, H.; He, Q. A Comprehensive Survey on Transfer Learning. *Proc. IEEE* **2021**, *109*, 43–76. [CrossRef]
21. Sarkar, D.; Bali, R.; Ghosh, T. *Hands-On Transfer Learning with Python: Implement Advanced Deep Learning and Neural Network Models Using TensorFlow and Keras*; Packt Publishing Ltd.: Birmingham, UK, 2018.
22. Curreri, F.; Patanè, L.; Xibilia, M.G. RNN-and LSTM-Based Soft Sensors Transferability for an Industrial Process. *Sensors* **2021**, *21*, 823. [CrossRef]
23. Miccio, M.; Cosenza, B. Control of a distillation column by type-2 and type-1 fuzzy logic PID controllers. *J. Process Control* **2014**, *24*, 475–484. [CrossRef]
24. Pisa, I.; Morell, A.; Vicario, J.L.; Vilanova, R. Transfer Learning Approach for the Design of Basic Control Loops in Wastewater Treatment Plants. In Proceedings of the 26th IEEE International Conference on Emerging Technologies and Factory Automation (ETFA), Vasteras, Sweden, 7–10 September 2021.
25. Copp, J.B. *The Cost Simulation Benchmark: Description and Simulator Manual (Cost Action 624 and Action 682)*; Office for Official Publications of the European Union: Luxembourg, 2002.
26. Henze, M.; Grady, L., Jr.; Gujer, W.; Marais, G.; Matsuo, T. Activated Sludge Model No 1. *IAWPRC Scientific and Technical Reports*; IAWPRC: London, UK, 1987; Volume 29.
27. Halling-Sørensen, B.; Jorgensen, S.E. *The Removal of Nitrogen Compounds from Wastewater*; Elsevier: Amsterdam, The Netherlands, 1993.
28. Henze, M.; Gujer, W.; Mino, T.; van Loosdrecht, M.C. *Activated Sludge Models ASM1, ASM2, ASM2d and ASM3*; IWA Publishing: London, UK, 2000.
29. Gernaey, K.V.; Jørgensen, S.B. Benchmarking combined biological phosphorus and nitrogen removal wastewater treatment processes. *Control Eng. Prac.* **2004**, *12*, 357–373. [CrossRef]
30. Gernaey, K.V.; Jeppsson, U.; Vanrolleghem, P.A.; Copp, J.B.; International Water Association. Task Group on Benchmarking of Control Strategies for Wastewater Treatment Plants. In *Benchmarking of Control Strategies for Wastewater Treatment Plants*; IWA Publishing: London, UK, 2014.
31. Martin, C.; Vanrolleghem, P.A. Analysing, completing, and generating influent data for WWTP modelling: A critical review. *Environ. Model. Softw.* **2014**, *60*, 188–201. [CrossRef]
32. Modelling & Integrated Assessment, Benchmarking. Available online: http://iwa-mia.org/benchmarking/ (accessed on 9 November 2020).
33. Oliphant, T.E. *A Guide to NumPy*; Trelgol Publishing: Spanish Fork, UT, USA, 2006; Volume 1.
34. Virtanen, P.; Gommers, R.; Oliphant, T.E.; Haberland, M.; Reddy, T.; Cournapeau, D.; Burovski, E.; Peterson, P.; Weckesser, W. SciPy 1.0: Fundamental Algorithms for Scientific Computing in Python. *Nat. Methods* **2020**, *17*, 261–272. [CrossRef] [PubMed]
35. Abadi, M.; Agarwal, A.; Barham, P.; Brevdo, E.; Chen, Z.; Citro, C.; Corrado, G.S.; Davis, A.; Dean, J.; Devin, M.; et al. TensorFlow: Large-Scale Machine Learning on Heterogeneous Systems. 2015. Available online: https://www.tensorflow.org/ (accessed on 5 October 2020).
36. Vilanova, R.; Visioli, A. *PID Control in the Third Millennium—Lessons Learned and News Approaches*; Springer: London, UK, 2012.
37. Da Silva, I.N.; Spatti, D.H.; Flauzino, R.A.; Liboni, L.H.B.; dos Reis Alves, S.F. *Artificial Neural Networks*; Springer International Publishing: Cham, Switzerland, 2017.

38. Boussaada, Z.; Curea, O.; Remaci, A.; Camblong, H.; Mrabet Bellaaj, N. A nonlinear autoregressive exogenous (NARX) neural network model for the prediction of the daily direct solar radiation. *Energies* **2018**, *11*, 620. [CrossRef]
39. Manu, D.S.; Thalla, A.K. Artificial intelligence models for predicting the performance of biological wastewater treatment plant in the removal of Kjeldahl Nitrogen from wastewater. *Appl. Water Sci.* **2017**, *7*, 3783–3791. [CrossRef]
40. Qiao, J.F.; Hou, Y.; Zhang, L.; Han, H.G. Adaptive fuzzy neural network control of wastewater treatment process with multiobjective operation. *Neurocomputing* **2018**, *275*, 383–393. [CrossRef]
41. Santín, I.; Barbu, M.; Pedret, C.; Vilanova, R. Dissolved Oxygen Control in Biological Wastewater Treatments with Non-Ideal Sensors and Actuators. *Ind. Eng. Chem. Res.* **2019**, *58*, 20639–20654. [CrossRef]